ABSTRACT

Title of dissertation: MOLECULAR GAS AND STAR FORMATION AT LOW METALLICITY IN THE MAGELLANIC CLOUDS
Katherine E. Jameson,
Doctor of Philosophy, 2016

Dissertation directed by: Professor Alberto Bolatto
Department of Astronomy

The Magellanic Clouds are two interacting, gas-rich, star-forming, low-mass, nearby satellite galaxies of the Milky Way that afford a unique view of low-metallicty star-forming regions, providing the nearest laboratories to study processes relevant to star formation in the early universe. We use the dust emission from HERITAGE *Herschel* data to map the molecular gas in the Magellanic Clouds, avoiding the known biases of CO emission as a tracer of H_2. On small ($\sim$ few pc) scales in the Small Magellanic Cloud (SMC), we study the effect of metallicity on the structure of photodissociation regions in the outskirts of molecular clouds using [C II] and [O I] spectroscopy combined with new ALMA 7-m array maps of ^{12}CO and ^{13}CO. We estimate the total amount of molecular gas using [C II] to trace H_2 at low-A_V and ^{12}CO to trace H_2 at high-A_V. We find that most of the molecular gas is traced by [C II] emission and that metallicity only affects the relationship between ^{12}CO emission and molecular gas through changes in A_V. Using mid-infrared spectroscopy from *Spitzer* Space Telescope in the SMC, we model the H_2 rotational line emission

to estimate temperatures, column densities, and fractions of warm H_2 gas ($T \geq 100$ K). The temperatures and column densities of warm H_2 gas are similar to nearby galaxies, but the SMC shows somewhat high fractions of warm H_2. The properties of the warm H_2 gas indicate that it is located in photodissociation regions that are more extended in the low metallicity environment of the SMC. We use dust-based molecular gas maps data to evaluate molecular depletion time scales as a function of spatial scale. We compare galaxy-scale analytic star formation models to our observations and find that successfully predicting the trends in the low metallicity environment needs the inclusion of a diffuse neutral medium. The analytic models, however, do not capture the scatter observed, which computer simulations suggest is driven primarily by the time-averaging effect of star formation rate tracers. The averaging of the scatter in the molecular gas depletion time as a function of scale size suggests that the drivers of the star formation process in these galaxies operate on large scales.

MOLECULAR GAS AND STAR FORMATION AT LOW METALLICITY IN THE MAGELLANIC CLOUDS

by

Katherine E. Jameson

Dissertation submitted to the Faculty of the Graduate School of the
University of Maryland, College Park in partial fulfillment
of the requirements for the degree of
Doctor of Philosophy
2016

Advisory Committee:
Professor Alberto Bolatto, Chair/Advisor
Professor Lee Mundy
Professor Massimo Ricotti
Dr. Margaret Meixner
Professor Monica Rubio
Professor Wendell Hill

Preface

My education path towards a Ph.D. has been traditional: I majored in Astronomy & Physics at Boston University, completed my bachelor's degree in four years, went directly into the astronomy graduate program at the University of Maryland, College Park (UMCP) after receiving my bachelor's degree. Since then I have worked towards my Ph.D.. While straightforward, I did not have much support in navigating the path since. My high school was largely arts and humanities focused and not only has no one in my family pursued a Ph.D., but neither of my parents have a background in science or math. One thing has become clear about physics and astronomy after reflecting on my experience, background, and challenges–the general homogeneity of the people that are successful in the fields (in terms of race, gender, sexuality, and family/socioeconomic background).

I have always felt inspired to promote equity and inclusion. At Boston University, I worked with the physics and astronomy clubs to develop and implement a successful solar astronomy outreach program at Boston middle schools. I also worked with astronomy graduate students to implement a new Upward Bound summer program based on astronomy. A few years into the graduate program at UMCP, I led a team of graduate students and department staff and wrote a successful grant proposal for the program named Graduate Resources Advancing Diversity with Maryland Astronomy and Physics (GRAD-MAP; gradmap.astro.umd.edu). GRAD-MAP is a graduate student run diversity initiative with faculty and staff support that strives to give underrepresented minority undergraduates the skills and experience

to successfully pursue graduate degrees in physics and astronomy and build strong ties with mid-Atlantic minority-serving institutions (MSIs). We developed a three-part program consisting of a Collaborative Seminar Series, Winter Workshop, and Spring Symposium. The Collaborative Seminar Series and Spring Symposium are targeted at building better connection between UMCP and the mid-Atlantic MSIs while presenting research and providing information on graduate school. The Winter Workshop brings ~ 10 underrepresented minority students (primarily recruited from our partner MSIs) to UMCP and teaches critical computing skills, research techniques, and strategies for graduate school and summer internship applications; students also begin research projects with UMCP faculty at the Workshop. All of this work is largely grounded in my desire to share my experience and challenges and increase the accessibility of studying astronomy, which I plan to continue in my future academic career.

GRAD-MAP is in it's third year and has received national recognition from the National Society of Black Physicists (NSBP) as a best practice and there were three dedicated sessions to GRAD-MAP at the 2015 Conference of the NSBP that I organized and ran. I was also invited to give a talk on GRAD-MAP in a special session at the 225th American Astronomical Society Meeting. Additionally, I was one of four finalists in 2014 and the recipient of the 2015 Graduate Student Distinguished Service Award at UMCP in recognition of my work to advance equity in the astronomy and physics departments, namely GRAD-MAP.

We have seen that the innovative Winter Workshop helps students early in their college careers build the skills needed to start research and prepare them for

successful summer research experiences. We have successfully hosted three Winter Workshops with a total of $\sim$ 25 alumni, with most having successfully completed summer research projects at various programs and one alumnus currently in the graduate program for astronomy at California State University, Los Angeles. I have personally continued to mentor two of the students from the first Winter Workshop as they were community college students that have since transferred to UMCP. I consider promoting equity and inclusion as a part of who I am as an astronomer. While my work with GRAD-MAP has not directly contributed to my dissertation work, it has helped me develop leadership and mentoring skills while pushing me to evolve into a more independent, confident, and motivated person. I believe this growth played an integral role in my research and I believe it is reflected in this body of work I present as my doctoral dissertation.

Acknowledgments

I am unable to remember all of the names of all of the people that have contributed (in some way) to my education over my 29 years of existence that led me to this point: defending my doctoral dissertation. The ones most responsible for my continued success are my family and close friends. I have learned that my quality of life is largely determined by the quality of the people that surround me. My parents continually supported me in my academic pursuits, as outlandish as it seemed given their claimed deficiencies in science and math. They have never doubted my abilities and have readily shown their willingness to fight anyone or anything that would try to convince me otherwise. They have always listened, and they have always shown interest and pride in my work. They have built within me a strong foundation of confidence; I doubt I would be where I am today without that foundation. If that foundation were that of a house, then my friends (including my brother) would be the remaining walls, windows, doors, and roof. They support me, they shelter me from the elements, and they help me to see the world in new ways.

There should be the obvious acknowledgement of my thesis advisor, Alberto Bolatto. Quite literally, this work would not exist without him and his enviable proposal writing skills that led to the wealth of data available to me upon my arrival. Alberto has continually pushed me to be a better scientist, helped hone my research skills, and shared his advice. He has always taken the time, whether he really could afford to or not, to help me work through problems or to celebrate any number of small victories along the way. Alberto never let me accept defeat and

has guided me through the epic process of proving one's worthiness of a doctorate in astronomy.

I am indebted to all those who helped me become Dr. Jameson. Sláinte!

Table of Contents

List of Figures x

List of Abbreviations xii

1 Introduction 1
1.1 Outline of Thesis . . . 6

2 Dust-based Molecular Gas Estimates for the Magellanic Clouds 7
2.1 Overview . . . 7
2.2 Observations . . . 8
2.2.1 Herschel Data . . . 8
2.2.2 H I Data . . . 9
2.2.3 CO Data . . . 10
2.3 Methodology . . . 11
2.3.1 Modeling Thermal Dust Emission . . . 11
2.3.2 Estimating Molecular Gas from Infrared Dust Emission . . . 13
2.3.2.1 Offsets in H I vs. Dust . . . 20
2.3.2.2 Map Sensitivity and Uncertainty . . . 22
2.3.2.3 Estimating H_2 from CO . . . 26
2.3.3 Convolving to Lower Resolutions . . . 27
2.4 Results . . . 28
2.4.1 Molecular Gas in the Magellanic Clouds . . . 28
2.4.1.1 Structure of the Molecular Gas . . . 32
2.4.1.2 Systematic Uncertainty . . . 33
2.4.1.3 Estimating the Effect of the Optical Depth of H I . . . 36
2.4.1.4 Comparison to Previous Work . . . 38
2.5 Summary and Conclusions . . . 42

3 [C II]-bright and CO-bright Molecular Gas in the SMC 43
3.1 Overview . . . 43
3.2 Observations . . . 48

3.2.1 The Herschel Spectroscopic Survey of the SMC . . . 48
3.2.1.1 Data Reduction . . . 50
3.2.2 ALMA Survey of the Southwest Bar . . . 52
3.2.3 HI Data . . . 53
3.2.4 Additional Data . . . 54
3.2.5 Estimating A_V . . . 55
3.3 Results . . . 56
3.3.1 [C II] and [O I] . . . 56
3.3.2 [N II] and Contribution from Ionized gas . . . 60
3.3.3 [O III] and Highly Ionized Material . . . 66
3.3.4 High Resolution Molecular Gas: ^{12}CO and ^{13}CO . . . 68
3.3.5 Estimating the Optical Depth of ^{12}CO . . . 69
3.3.6 Relationship between ^{12}CO and [C II] . . . 73
3.3.7 ^{12}CO-to-[C II] Ratio . . . 76
3.4 Estimating H_2 using [C II] and ^{12}CO . . . 78
3.4.1 $I_{[C\,II]}$ Contribution from Ionized Gas . . . 80
3.4.2 $I_{[C\,II]}$ Contribution from Atomic Gas . . . 82
3.4.3 Converting $I_{[C\,II]}$ to N_{H_2} . . . 85
3.4.3.1 Method 1: Fixed T, n . . . 86
3.4.3.2 Method 2: W16 PDR Model . . . 87
3.4.4 Converting I_{CO} to N_{H_2} . . . 91
3.4.5 N_{H_2} Estimates . . . 93
3.4.5.1 Uncertainty Estimate . . . 97
3.5 Discussion . . . 101
3.5.1 Comparison to Dust-based H_2 Estimates . . . 102
3.5.2 [C II] as a Tracer of H_2 and Star Formation Rate at Low Metallicity . . . 104
3.5.3 Comparing [C II]-bright and CO-bright H_2 . . . 106
3.5.4 The CO-to-H_2 Conversion Factor in the SMC . . . 109
3.5.5 ^{12}CO and the Molecular to Atomic Transition . . . 114
3.6 Summary and Conclusions . . . 115

4 H_2 Rotational Line Emission in the SMC 119
4.1 Overview . . . 119
4.2 Observations . . . 121
4.2.1 Measuring Line Fluxes . . . 123
4.2.1.1 Difficulty Measuring the H_2 S(3) Line . . . 124
4.3 Modeling the Temperature, Column Density, and Ortho-to-para Ratio of the Warm H_2 Gas . . . 127
4.3.0.1 The Effect of Dust Continuum Emission on the H_2 S(0) 28.2 μm Line Flux . . . 130
4.4 Results . . . 136
4.5 Discussion . . . 142
4.5.1 Excitation Mechanism of the H_2 Rotational Lines . . . 142
4.5.2 Fraction of Warm H_2 . . . 145

4.6 Summary and Conclusions . . . 147

5 Molecular Gas and Star Formation in the Magellanic Clouds 151
5.1 Overview . . . 151
5.2 Observations . . . 152
5.2.1 Hα and 24 μm Data . . . 152
5.2.1.1 Diffuse Hα . . . 153
5.2.2 Distances and Inclination Angles . . . 154
5.2.3 Convolving to Lower Resolutions . . . 156
5.3 Tracing Recent Star Formation . . . 156
5.4 Results . . . 157
5.4.1 Molecular Gas and Star Formation . . . 157
5.4.1.1 Molecular Gas Depletion Time . . . 160
5.4.2 Correlation Between Gas and Star Formation Rate from 20 pc to 1 kpc Size Scales . . . 164
5.5 Discussion . . . 167
5.5.1 $\tau_{\rm dep}^{\rm mol}$ in the Magellanic Clouds . . . 168
5.5.2 Physical Interpretation of the Scatter in $\tau_{\rm dep}^{\rm mol}$ . . . 170
5.5.2.1 Scatter in $\tau_{\rm dep}^{\rm mol}$ as a Function of Size Scale . . . 176
5.5.3 Comparison to Star Formation Model Predictions . . . 180
5.6 Summary and Conclusions . . . 186

6 Conclusion 188
6.1 Future Work . . . 189
6.1.1 What is the nature of the "CO-faint" gas and its effect on star formation? . . . 189
6.1.2 Does Metallicity Affect the Properties of Molecular Clouds and H II regions? . . . 190
6.1.3 Can the Star Formation History of Galaxies Explain Variations in $\tau_{\rm dep}^{\rm mol}$? . . . 192

A SMC PDR Models 194

Bibliography 198

List of Figures

2.1 $N_{\rm H\,I}$ vs. τ_{160} Relationship in the LMC . . . 16
2.2 τ_{160} vs. $N_{\rm H\,I}$ for LMC Quadrants ($\beta = 1.8$) . . . 23
2.3 τ_{160} vs. $N_{\rm H\,I}$ for LMC Quadrants (BEMBB) . . . 24
2.4 LMC H I Offsets . . . 24
2.5 $N_{\rm H_2}$ Map of the LMC . . . 30
2.6 $N_{\rm H_2}$ Map of the SMC . . . 31
2.7 Comparison of $N_{\rm mol}$ Maps . . . 34

3.1 HS^3 regions . . . 57
3.2 [O I]/[C II] vs. A_V . . . 61
3.3 H_2 S(0) and [C II] Images . . . 62
3.4 HS^3 FTS Spectra . . . 63
3.5 [N II] 205 μm[C II]vs. [C II] Intensity . . . 64
3.6 [O III]/[C II] vs. [C II] intensity . . . 67
3.7 ALMA ACA+TP ^{12}CO and ^{13}CO Maps . . . 70
3.8 ^{12}CO/^{13}CO vs. ^{12}COIntensity . . . 71
3.9 [C II] and ALMA ACA+TP ^{12}CO Images . . . 73
3.10 SOFIA GREAT [C II] Spectrum . . . 75
3.11 ^{12}CO/[C II] vs. A_V . . . 77
3.12 PDR Model n and G_0 Results . . . 88
3.13 [C II] Cooling Curve . . . 92
3.14 Comparison of $N_{\rm H_2}$ from [C II] for Method 1 and 2 . . . 95
3.15 $N_{\rm H_2}$ Estimates . . . 96
3.16 Ratio of $N_{\rm H_2}$ from [C II] to the Total $N_{\rm H_2}$ vs. A_V . . . 108
3.17 $N_{\rm H_2}$vs. I_{CO} . . . 110
3.18 X_{CO} vs. A_V . . . 111
3.19 Comparison of the ^{12}CO Emission to the Ratio of Molecular to Atomic Gas . . . 113

4.1 Example IRS Spectrum with PAHFIT Results . . . 125
4.2 Example Excitation Diagram with S(3) RMS Estimate . . . 128
4.3 Example Excitation Diagram and Fit Results . . . 135
4.4 S^{4}MC H_2 S(0) Images . . . 137

4.5 SWBarS H_2 Lines Image . . . 138
4.6 H_2 Line Modeling Results . . . 140
4.7 Warm H_2Compared to N_{H_2} from Dust . . . 148
4.8 Warm H_2Compared to N_{H_2} from [C II] . . . 149

5.1 Σ_{SFR} vs. Σ_{mol} for the LMC and SMC . . . 159
5.2 Σ_{SFR} vs. Σ_{mol} with HERACLES sample . . . 161
5.3 τ_{dep}^{mol} as a Function of Resolution . . . 163
5.4 τ_{dep}^{mol} vs. Metallicity at 1 kpc . . . 165
5.5 Correlation of Σ_{H_2} vs. Σ_{SFR} and Σ_{HI} vs. Σ_{SFR} . . . 166
5.6 Average τ_{dep}^{mol} vs. Σ_* . . . 171
5.7 Scatter in τ_{dep}^{mol} as a Function of Size Scale . . . 179
5.8 Σ_{gas} vs. Σ_{SFR} with OML10 and KMT+ Model Predictions . . . 184

A.1 SMC PDR Model Line Ratios . . . 196
A.2 Results from the High Metallicty PDR Models . . . 197

List of Abbreviations

SMC	Small Magellanic Cloud
LMC	Large Magellanic Cloud
IR	infrared
TIR	total infrared
H_2	molecular hydrogen
ALMA	Atcama Large Millimeter/submillimeter Array
ACA	ALMA $Morita - san$ Compact Array
TP	ALMA Total Power
ATCA	Australian Telescope Compact Array
APEX	Atacama Pathfinder Experiment
SOFIA	Stratospheric Observatory for Infrared Astronomy
GREAT	German Receiver for Astronomy at Terahertz Frequencies
IRAS	Infrared Astronomical Telescope
IRAC	Infrared Camera Array
MIPS	Multi-band Imaging Photometer
IRS	Infrared Spectrometer
PACS	Photoconductor Array Camera and Spectrometer
SPIRE	Spectral and Photometric Imaging Receiver
FTS	Fourier Transform Spectrometer
HIPE	*Herschel* Interactive Process Environment
CASA	Common Astronomy Software Application
SAGE	Surveying the Agents of Galaxy Evolution
HERITAGE	*Herschel* Inventory of the Agents of Galaxy Evolution
MAGMA	Magellanic Mopra Assessment
SINGS	*Spitzer* Infrared Nearby Galaxy Survey
THINGS	The H I Nearby Galaxy Survey
KINGFISH	Key Insights on Nearby Galaxies: A Far-Infrared Survey with *Herschel*
HS^3	*Herschel* Spectroscopic Survey of the SMC
S^4MC	*Spitzer* Spectroscopic Survey of the SMC
PSF	point source function
FWHM	full width at half maximum
FUV	far-ultraviolet
C^+	ionized carbon
[C II]	singly ionized carbon forbidden transition
[C I]	neutral carbon forbidden transition
[O I]	neutral oxygen forbidden transition
[O III]	doubly ionized oxygen forbidden transition
[N II]	singly ionized nitrogen forbidden transition

H I	neutral atomic hydrogen
H II	ionized hydrogen
$M_\odot$	Solar mass
pc	parsec
kpc	kiloparsec
Jy	Jansky
A_V	visual extinction
Z	metallicity
$Z_\odot$	Solar metallicity
B_ν	Planck function
β	thermal dust emission emissivity index
MBB	modified black body
BEMBB	broken emissivity modified black body
SED	spectral energy distribution
τ	optical depth
GDR	gas-to-dust ratio
$\delta_{\rm GDR}$	effective gas-to-dust ratio
N	column density
n	volume density
Σ	surface mass density
PDR	photodissociation region
PAH	polycyclic aromatic hydrocarbons
G_0	FUV radiation field strength
$X_{\rm CO}$	CO-to-H_2 conversion factor
SFR	star formation rate
WNM	warm neutral medium
CNM	cold neutral medium
WIM	warm ionized medium
n_{crit}	critical density
A_{ul}	spontaneous emission rate coefficient from the upper to lower level
R_{ul}	collisional de-excitation rate coefficient from the upper to lower level
EM	emission measure
OPR	H_2 ortho-to-para ratio
BCD	blue compact dwarf galaxy
$\tau_{\rm dep}^{\rm mol}$	molecular gas depletion time
AGN	active galactic nuclei

Chapter 1: Introduction

Star formation plays a critical role in shaping how galaxies form and evolve. Understanding the molecular gas content of low-mass, low-metallicity galaxies and its relationship to the star formation rate is necessary to understand how the gas mass fractions evolve with redshift (e.g., Tacconi et al. 2010; Genzel et al. 2012) and how the star formation efficiency depends on galaxy mass and metallicity (e.g., Bolatto et al. 2011; Saintonge et al. 2011; Krumholz et al. 2011). Both are critical to understanding the "galaxy mass function" and drivers of the star formation history of the universe.

Our current knowledge of the extragalactic relationship between gas and star formation comes from studies of mostly high-metallicity, high-mass nearby galaxies that use ^{12}CO to trace the molecular gas. The original work to quantitatively compare the star formation rate to the gas density by Schmidt (1959) found a power law relationship, generally referred to as the "star formation law." More recent studies of the extragalactic star formation law follow the work of Kennicutt (1989, 1998), which used primarily disk-averaged measurements of the surface density of total gas ($\Sigma_{\rm gas} = \Sigma_{\rm H_2} + \Sigma_{\rm HI}$) and star formation rate ($\Sigma_{\rm SFR}$). They found that the relationship between $\Sigma_{\rm gas}$ and $\Sigma_{\rm SFR}$ follows a power law distribution ($\Sigma_{\rm SFR} \propto {\Sigma_{\rm gas}}^{1+p}$). Studies

at higher resolution found that the general power law trend continued, but only within the molecular-dominated regimes and that $\Sigma_{\rm mol}$ and $\Sigma_{\rm SFR}$ follow an approximately linear power law relation (Bigiel et al. 2008; Schruba et al. 2011; Bigiel et al. 2011; Rahman et al. 2012). At lower gas surface densities, where H I dominates the total gas budget, they see a steep fall off in the relationship. Resolved galaxy studies show that while the total gas continues to be correlated with the star formation rate within galaxies, the molecular gas correlates best with the star formation rate.

Due to the nearly linear power law slope of the relationship between $\Sigma_{\rm mol}$ and $\Sigma_{\rm SFR}$, a convenient way to quantify the relationship is the molecular gas depletion time: $\tau_{\rm dep}^{\rm mol} = \Sigma_{\rm mol}/\Sigma_{\rm SFR}$. The depletion time can be thought of as the amount of time it would take to deplete the current reservoir of molecular gas given the current star formation rate. Most of the resolved data for samples of galaxies achieve resolutions of several hundred parsecs to ~ 1 kpc (Bigiel et al. 2008; Leroy et al. 2008; Bigiel et al. 2011; Rahman et al. 2012; Leroy et al. 2013a) and all find similar values for the average molecular gas depletion time of $\tau_{\rm dep}^{\rm mol} \sim 2$ Gyr. The weak dependence of $\tau_{\rm dep}^{\rm mol}$ on the galactic properties and environment (Leroy et al. 2013a) suggests that star formation is a local process based on the conditions within giant molecular clouds (GMCs).

The conclusions from studies of mostly high-mass, high-metallicity disk galaxies may not extend to lower metallicity star-forming dwarf galaxies where the ISM is dominated by atomic gas. The lack of metals produce different physical conditions that potentially affect the molecular gas fraction and how star formation proceeds within the galaxy. For example, the galaxies will have lower dust-to-gas ratios,

which results in lower extinctions and higher photodissociation rates. The Large and Small Magellanic Clouds (LMC, SMC) provide ideal laboratories to study the physics of star formation at low mass, $M_{*,\rm LMC} = 2 \times 10^9\ M_\odot$ and $M_{*,\rm SMC} = 3 \times 10^8\ M_\odot$ (Skibba et al. 2012), and low metallicity, $Z_{\rm LMC} \sim 1/2\ Z_\odot$ (Russell & Dopita 1992) and $Z_{\rm SMC} \sim 1/5\ Z_\odot$ (Dufour 1984; Kurt et al. 1999; Pagel 2003), due to their proximity and our ability to achieve high spatial resolution (~ 10 pc).

Tracing the molecular gas at low-metallicity is difficult because CO, the most common tracer of H_2, emits weakly and is often undetected. The Magellanic Clouds have been studied extensively in ^{12}CO with the earliest surveys completed using the Columbia 1.2m (Cohen et al. 1988; Rubio et al. 1991). The early survey of both Clouds completed by Israel et al. (1993) using the Swedish-ESO Submillimetre Telescope (SEST) showed the CO emission to be under-luminous compared to the Milky Way by a factor of ~ 3 in the LMC and ~ 10 in the SMC. Since then, many large-scale surveys have been completed for the LMC (Fukui et al. 2008; Wong et al. 2011) and SMC (Rubio et al. 1993a; Mizuno et al. 2001; Muller et al. 2010). The H_2 gas is expected to be more prevalent than CO at low metallicity due to increased ability of H_2 to self-shield against dissociating UV photons compared to CO. Both observations and modeling suggest that $\sim 30\% - 50\%$ of the H_2 in the Solar Neighborhood resides in a "CO-faint" phase (e.g., Grenier et al. 2005; Wolfire et al. 2010; Planck Collaboration et al. 2011), similar to the estimated fraction in the LMC (e.g., Roman-Duval et al. 2010; Leroy et al. 2011). Studies of the SMC find this phase to encompass $80\% - 90\%$ of all the H_2 (Israel 1997; Pak et al. 1998; Leroy et al. 2007, 2011; Bolatto et al. 2011), likely dominating the molecular reservoir

available to star formation.

Two ways to trace the total amount of molecular gas are to use thermal dust emission and combine CO and [C II] emission. Dust is mixed with the gas; by knowing the total amount of dust and either assuming or self-consistently determining the gas-to-dust ratio, we can determine the total amount of gas and from that the total amount of molecular gas–including molecular gas faint in CO emission. The CO-faint molecular gas can also be traced by [C II] emission as most of the carbon exists as C^+ while H_2 remains molecular since it is strongly self-shielding (Tielens & Hollenbach 1985; Wolfire et al. 1989; Kaufman et al. 1999; Wolfire et al. 2010). The [C II] 158 μm emission is the dominant coolant of the neutral atomic gas (Wolfire et al. 2003). The gas is heated by electrons ejected from small dust grains and polycyclic aromatic hydrocarbons (PAHs) by the photoelectric effect. The 158 μm transition has an energy above ground of $\Delta E/k = 91$ K and emits in ionized, neutral, and molecular gas. The critical density for collisions with H_2 is $n_{crit} \sim 4000$ cm^{-3}, which is the density required for the rate of collisions to balance the rate of spontaneous emission. The outer layers of molecular clouds illuminated by far-ultraviolet (FUV) radiation, referred to as photodissociation regions (PDRs), where carbon exists as primarily C^+ emits brightly in the 158 μm since the warm, dense conditions are comparable to the energy and critical density of the transition. Combining the molecular gas traced by [C II] emission with the molecular gas traced by ^{12}CO emission yields an estimate of the total amount of molecular gas.

The H_2 molecule also has rotational quadrupole transitions in the warm, dense conditions of PDRs. These transitions were observable using the *Spitzer IRS*

and allow us to directly study the conditions of the warm molecular gas. Modeling of the rotational quadrupole transitions allows us to quantify the column density and temperature of the warm molecular gas. Assuming local thermodynamic equilibrium (LTE), the total column density in the upper level can be determined using $N_u/g_u = N_{gas}\left[e^{-E_u/kT_{gas}}/Z(T_{gas})\right]$ where $Z(T_{gas})$ is the partition function. Herbst et al. (1996) found the analytic expression for the partition function of $Z(T_{gas}) \sim 0.024T_{gas}/1 - e^{-6000K/T_{gas}}$ is an good approximation to the true partition function evaluated by summing all transitions with upper level energy $\lesssim 25000$ K. The difference in the emission between the ortho and para transitions, quantified by the ortho-to-para ratio (OPR), can give some insight into the conditions and/or excitation mechanism. Since the quadrupole transitions change by $\Delta J = 2$, all radiative decay and collisional (de-)excitation conserve ortho or para state. For H_2 in LTE, the expected OPR depends on the temperature: $OPR \sim 2$ for $T \sim 100$ K and $OPR \sim 3$ for $T > 200$ K (Burton et al. 1992). H_2 gas with temperatures of ~ 100 K are only expected to contribute to the lowest energy transition, $J = 2-0$ or S(0), which has temperature-equivalent energy of $E_u/k = 510$ K. The next transitions all have temperature-equivalent energies of $\gtrsim 1000$ K and will be primarily produced by warm, $T > 200K$ gas, which would result in an LTE $OPR \sim 3$. Departures from the LTE $OPR \sim 3$ value can be produced by cooler gas, emission that is produced by non-LTE scenarios, or fluorescence. By combining estimates of the total amount of molecular gas with the amount of warm H_2, we can begin to understand the properties of molecular gas at low metallicity in the SMC, particularly whether or not more of the total molecular gas is warm.

1.1 Outline of Thesis

Chapters 2 and 3 are devoted to estimating the total amount of molecular gas at low metallicity in the Magellanic Clouds. Chapter 2 presents our work that uses dust emission to trace the molecular gas through both the Large and Small Magellanic Clouds and compares the new estimates to previous estimates. Chapter 3 presents new *Herschel* [C II] (and other far-infrared line observations) and ALMA CO observations of a selection of star-forming regions in the Small Magellanic Cloud (SMC). We estimate the total amount of molecular gas using the combination of [C II] and ^{12}CO, which are similar to the dust-based estimates, and use this estimate to explore how CO emission traces the molecular gas at low metallicity. In Chapter 4 we model the H_2 rotational line emission to understand the temperature, amount of warm molecular gas, and in what regions the line emission is produced. By comparing to the other estimates of the total amount of molecular gas, we estimate the fraction of warm molecular gas and compare to other nearby galaxies. Taking the dust-based molecular gas maps created in Chapter 2, we compare the total molecular gas to the star formation in Chapter 5 to determine whether star formation proceeds differently at low metallicity. Chapter 6 provides the conclusion to the thesis and discusses what future work would be interesting to explore. Chapters 2 and 5 are published in Jameson et al. (2016). Chapter 3 is currently a paper at an advanced draft stage that has received comments from one co-author. Chapter 4 is not yet in paper form, but will be in the near future.

Chapter 2: Dust-based Molecular Gas Estimates for the Magellanic Clouds

2.1 Overview

Using dust emission to estimate the molecular gas in low metallicity systems avoids the biases of CO and can trace "CO-faint" molecular gas. This method of tracing the molecular gas using dust emission in the Magellanic Clouds was first applied by Israel (1997) using *IRAS* data, and later by Leroy et al. (2007, 2009) in the SMC and Bernard et al. (2008) in the LMC using *Spitzer* data. Bolatto et al. (2011) further refined the methodology and created a map of H_2 in the SMC using dust continuum emission from *Spitzer* and studied the spatial correlation between the atomic gas, molecular gas, and star formation rate.

In this work, we produce an estimate of the molecular gas using dust emission traced by *Herschel* in the LMC and SMC. In Sections 5.2 and 2.3 we outline the observations and how we convert them to physical quantities. Section 5.4 presents our molecular gas estimates and compare them to previous observations. Finally, we summarize the conclusions from this study of the molecular gas in the LMC and SMC in Section 5.6.

2.2 Observations

2.2.1 Herschel Data

The far-infrared images come from the HERschel Inventory of The Agents of Galaxy Evolution in the Magellanic Clouds key project (HERITAGE; Meixner et al. 2013). HERITAGE mapped both the Large Magellanic Cloud (LMC) and Small Magellanic Cloud (SMC) at 100, 160, 250, 350, and 500 μm with the Spectral and Photometric Imaging Receiver (SPIRE) and Photodetector Array Camera and Spectrometer (PACS) instruments. Information on the details of the data calibration, reduction, and uncertainty can be found in Meixner et al. (2013).

For this work, we apply further background subtraction. First, we remove the foreground Milky Way cirrus emission. Following Gordon et al. (2014) (based on Bot et al. 2004), we estimate the foreground cirrus emission by using the relationship between IR dust emission and H I from Desert et al. (1990) and scaling the integrated H I intensity map over the velocities of the Milky Way emission in the direction of the LMC by applying the conversion factors 1.073, 1.848, 1.202, 0.620 (MJy sr^{-1}/10^{20} cm^{-2}) for 100 μm, 160 μm, 250 μm, and 350 μm, respectively. The median estimated cirrus emission was 5.7, 9.9, 6.4, and 3.3 MJy sr^{-1} for the 100 μm, 160 μm, 250 μm, and 350 μm images.

Second, we set the images to comparable zero-points: the outskirts of the PACS images were set to the COBE and IRAS data emission levels while the outskirts of the SPIRE images were set to zero due to the lack of similar large-scale

coverage at the longer wavelengths. After subtracting the cirrus emission, we chose 6 regions in the outskirts of the LMC with no emission in the *Herschel* or H I images, fit a plane to the median values of the regions and subtract the plane. The cirrus-subtraction and background-subtraction had primarily minor effects on the images, with the final image values being lower by 7%, 9%, 2%, and 2% on average for the 100 μm, 160 μm, 250 μm, and 350 μm images in regions with $S/N > 3$.

2.2.2 H I Data

The neutral atomic gas data come from 21 cm line observations of H I. We use the LMC H I map from Kim et al. (2003) and the SMC H I map from Stanimirović et al. (1999), both combined Australian Telescope Compact Array (ATCA) and Parkes 64m radio telescope data. The interferometric ATCA data set the map resolution at $1'$ ($r \sim 20$ pc in the SMC and $r \sim 15$ pc in the LMC), but the data are sensitive to all size scales due to the combination of interferometric and single-dish data.

The observed brightness temperature of the 21 cm line emission is converted to H I column density ($N_{\rm HI}$) assuming optically thin emission using

$$N_{\rm HI} = 1.823 \times 10^{18} \frac{\rm cm^{-2}}{\rm K\ km\ s^{-1}} \int T_B(v)\ {\rm d}v\,. \tag{2.1}$$

We find RMS column densities of 8.0×10^{19} cm^{-2} in the LMC map and 5.0×10^{19} cm^{-2} in the SMC map. We convert column density to surface mass density ($\Sigma_{\rm HI}$) using

$$\Sigma_{\rm HI} = 1.4 \cos i \left(8.0 \times 10^{-21} \frac{M_\odot\ {\rm pc}^{-1}}{\rm cm^{-2}} \right) N_{\rm HI}\,, \tag{2.2}$$

where the factor of 1.4 accounts for He and i is the inclination angle.

While the assumption of optically thin H I emission is likely appropriate throughout much of the galaxies, there are regions with optically thick emission, which would cause $N_{\rm HI}$ to be underestimated. While a statistical correction for H I optical depth in the SMC exists (Stanimirović et al. 1999), none exists for the LMC. Additionally, nearby surveys of H I (i.e., THINGS; Walter et al. 2008) make no optical depth corrections. We chose not to make any optical depth corrections to the H I maps as the statistical corrections in the SMC are generally small (increases the total H I mass by 10%; Stanimirović et al. 1999) and an accurate optical depth correction would require assuming a spin temperature.

2.2.3 CO Data

We use integrated ^{12}CO $(1-0)$ intensity maps from the 4m NANTEN radio telescope (half power beam width of 2.6′ at 115 GHz) for the LMC (Fukui et al. 2008) and SMC (Mizuno et al. 2001). The LMC and SMC velocity integrated maps have typical 3σ noise of ~ 1.2 K km s^{-1} and ~ 0.45 K km s^{-1}, respectively. For the LMC, there is also the higher resolution and sensitivity MAGellanic Mopra Assessment (MAGMA) Survey, which used the 22m Mopra telescope of the Australia Telescope National Facility to follow-up the NANTEN survey with 40″ angular resolution and 1σ sensitivity of 0.2 K km s^{-1} (Wong et al. 2011). However, the MAGMA survey is not complete as they only mapped regions with detected CO in the NANTEN map. Because the CO maps are only used to identify molecular regions and do not affect the final resolution of our molecular gas maps, we use the higher coverage NANTEN

maps in our molecular gas mapping process and then, in the LMC, we compare the final dust-based molecular gas maps to the higher resolution MAGMA data.

2.3 Methodology

2.3.1 Modeling Thermal Dust Emission

The dust emission modeling done in this work used a modified blackbody with a fixed emissivity index, β, to fit the dust temperature T_d pixel-by-pixel to the 100, 160, 250, and 350 μm HERITAGE images. Excluding the 500 μm image avoids the issue of possible "excess" dust emission at $\lambda > 400$ μm observed in the SMC and LMC (Planck Collaboration et al. 2011; Gordon et al. 2014). From the fitted T_d, we calculate, τ_{160} for all 3σ fits to T_d using

$$\tau_{160} = \frac{S_{160}[\mathrm{MJy/sr}]}{B_\nu(T_{dust}, 160\mu\mathrm{m})} \, .$$

All images are convolved to the resolution of the 350 μm data, the lowest resolution ($25''$), using the kernels from Aniano et al. (2011). We fix β in the model to avoid the degeneracy between T_d and β, which can occur when the correlated errors between the *Herschel* bands are not taken into account. Fixing β also follows the previous work in the SMC (Leroy et al. 2009; Bolatto et al. 2011). We adopt $\beta = 1.8$ for our fiducial molecular gas map because that is the approximate average value of β_1 found in the broken emissivity modified blackbody (BEMBB) modeling by Gordon et al. (2014) and similar to $\beta = 1.7$ found for M33 using the *Planck* data (F. Israel, private communication). We also create maps using $\beta = 1.5$ and $\beta = 2.0$ to see how

that affects the H_2 estimate since $\beta \sim 1-2$ for carbonaceous grains (Jager et al. 1998) and $\beta \sim 2$ for silicate grains (Coupeaud et al. 2011).

The second map uses the BEMBB dust emission modeling results from Gordon et al. (2014), which uses the same *Herschel* data, but includes the 500 μm image and accounts for correlated uncertainty between the different bands. All images are convolved to the resolution of the 500 μm data (35″), and thus lower resolution than our first method of dust modeling. The implementation of the correlated uncertainties in Gordon et al. (2014) eliminates the degeneracy between T_d and β, allowing both to be fit by the models. Gordon et al. (2014) fit three different modified blackbody models to the data: a simple modified blackbody, one that allows two temperatures, and one with broken emissivity index (fits two β values and the break wavelength). We use the surface mass density of dust ($\Sigma_{\rm dust}$) from the broken emissivity model (with $0.8 < \beta_1 < 2.5$) because it produces the smallest residuals and the gas-to-dust ratio falls within the range allowed by elemental abundances. To be comparable to the dust modeling done in this work, we convert $\Sigma_{\rm dust}$ map to τ_{160}:

$$\tau_{160} = \kappa_{\rm eff,\ 160} \Sigma_{\rm dust}$$

where $\kappa_{\rm eff,\ 160} = 11.6$ [cm^2 g^{-1}], which Gordon et al. (2014) finds by calibrating the broken emissivity model to reproduce the diffuse Milky Way SED (Compiègne et al. 2011) with a gas-to-dust ratio of 150, based on the depletion measurements from Jenkins (2009).

2.3.2 Estimating Molecular Gas from Infrared Dust Emission

We combine the dust emission with a self-consistently estimated gas-to-dust ratio to estimate the total amount of gas. By removing the atomic gas, we are left with an estimate of the amount of molecular gas. The benefit of this method, particularly at low metallicity, is its ability to trace H_2 where CO has photo-dissociated. This method is based on the previous work by Israel (1997) and Leroy et al. (2011) in both Magellanic Clouds, Dame et al. (2001) in the Milky Way, Bernard et al. (2008) in the LMC, and Leroy et al. (2007, 2009) and Bolatto et al. (2011) in the SMC, all of which have demonstrated that dust is a reliable tracer of the molecular gas. In Figure 2.1, we show that the optical depth of the dust correlates well with $N_{\rm HI}$, which represents the majority of the gas, and the 1σ scatter in the distribution is comparable to the uncertainty of τ_{160} of $\sim 1 \times 10^{-5}$, suggesting there is intrinsically a tight relationship. The variation in the relationship between $N_{\rm HI}$ and τ_{160} that is observed in nearby clouds (see below) could contribute to the observed scatter. The dust is also well correlated with the molecular gas traced by ^{12}CO, which is shown for the SMC in Figure 4 in Lee et al. (2015a) using the HERITAGE and MAGMA data. We summarize the specific steps in our methodology, which closely follow the methodology by Leroy et al. (2009) for the SMC, but with improvements allowed by the increased IR coverage and resolution from *Herschel*.

Following Leroy et al. (2009) and Bolatto et al. (2011), we model the dust emission in order to get the optical depth of the dust emission at 160 μm (τ_{160}). We use the results from two different dust emission fitting techniques for the LMC,

one presented in this paper and another from Gordon et al. (2014), both based on the assumption of modified blackbody emission, $S_\nu \propto \nu^\beta B_\nu\left(T_d\right)$. We describe the fitting techniques in more detail in Section 2.3.1. For the SMC, we only produce one molecular gas map using the modeling results from Gordon et al. (2014) since Bolatto et al. (2011) produced a molecular gas map using a fixed β simple modified blackbody model and a similar methodology. The Gordon et al. (2014) dust modeling may produce a more accurate measure of T_d since it allows β to vary while reducing the amount of degeneracy between T_d and β (Dupac et al. 2003; Shetty et al. 2009) by accounting for the correlated errors between the *Herschel* bands.

While the dust temperature along the line of sight throughout the Magellanic Clouds likely has a distribution of temperatures (Bernard et al. 2008; Galliano et al. 2011; Galametz et al. 2013), the assumption of a single dust temperature on the small spatial scales we cover ($\sim$ 20 pc) is reasonable since temperature mixing is restricted. Leroy et al. (2011) ran both simple modified black body fits and more complex dust models from Draine & Li (2007) to find τ_{160} using the *Spitzer* data for the LMC and SMC and found both produced similar results. A future follow-up study of Gordon et al. (2014) will run more complex dust modeling of the HERITAGE *Herschel* data.

This study focuses on using dust emission as a means to estimate the amount of molecular gas, which does not require a measurement of the dust mass. By only using τ_{160} we avoid making any assumptions about the conversion to dust mass, which would introduce a further layer of uncertainty. We define our effective gas-

to-dust ($\delta_{\rm GDR}$) ratio in terms of τ_{160},

$$\delta_{\rm GDR} = \Sigma_{\rm HI}/\tau_{160},$$

such that any proportionality constant between the infrared intensity and τ_{160} will be incorporated into $\delta_{\rm GDR}$ and not affect our final results.

We expect, in principle, that the relationship between $N_{\rm HI}$ and τ_{160} should go through the origin, but our measurements show indications of an offset (see Figure 2.1). We regionally fit and then remove the offset and find that the relationship has a positive and roughly constant offset in $N_{\rm HI}$ in both the LMC ($N_{\rm HI} \sim 4 \times 10^{20}$ cm^{-2}) and SMC ($N_{\rm HI} \sim 1.5 \times 10^{21}$ cm^{-2}). A similar offset is observed by Leroy et al. (2011), Bolatto et al. (2011), and Roman-Duval et al. (2014). As opposed to Bolatto et al. (2011), we remove the offset to avoid overestimates when creating maps of the gas-to-dust ratios, which would result in higher estimates of the total amount of gas. This offset could be due to a layer of H I gas with little to no dust, it could be due to the issues with background subtraction with the *Herschel* images (particularly in the LMC where the HERITAGE maps to not extend much past the main part of the galaxy), or some combination of the two effects. Another possibility is that the relationship between $N_{\rm HI}$ and τ_{160} is non-linear and the slope (gas-to-dust ratio) decreases at low $N_{\rm HI}$, which we explore as part of the systematic uncertainty estimation (see Section 2.3.2.2 and 2.4.1.2). Determining the true nature of the offset is beyond the scope of this work, but warrants further investigation. We subtract the offset in $N_{\rm HI}$ from the H I map and use the offset-subtracted map for the rest of the analysis. For further discussion on the offset subtraction see Section 2.3.2.1.

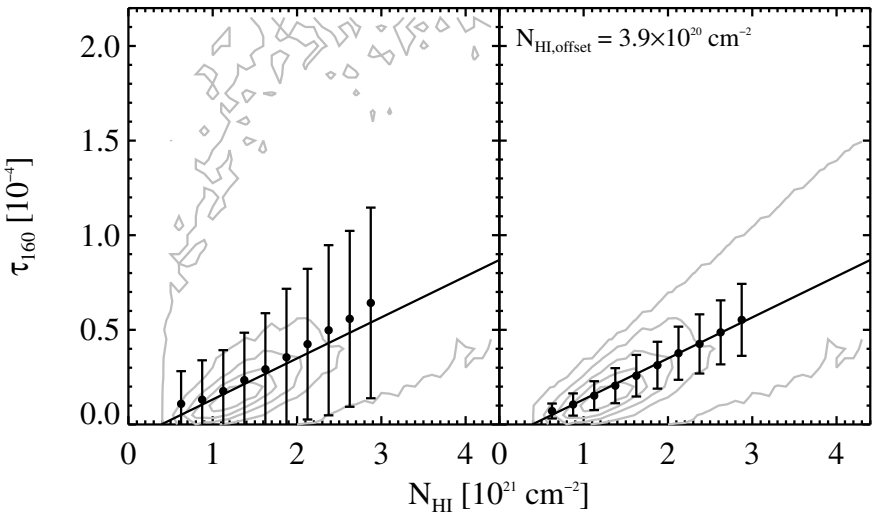

Figure 2.1 Both plots show the relationship between $N_{\rm H\,I}$ and τ_{160} (from the BEMBB dust modeling) in the LMC with the right plot showing the best representation of the relationship between $N_{\rm H\,I}$ and τ_{160} as the lines of sight with molecular gas have been removed. The contours levels correspond to the full extent of the distribution, 20%, 40%, 60%, and 80% of the maximum density of points. The black points show the medians in 2.5×10^{20} cm^{-2} $N_{\rm H\,I}$ bins with error bars showing 1σ of the distribution of measurements within the bin. The plots show the two-stage iteration used to fit the offset in the distribution: the *left* plot has points near bright CO emission masked and the *right* plot has masked points near bright CO and points with estimated $N_{\rm mol} > 0.5 N_{\rm H\,I}$ based on the first iteration. The typical error on τ_{160} is $\sim 1 \times 10^{-5}$ in regions with predominately H I gas, which is similar to the 1σ spread in the distribution in the bins. This suggest that the correlation between $N_{\rm H\,I}$ and τ_{160} is intrinsically very tight and approximately linear, showing that the dust is a good tracer of the gas. We find the offset in $N_{\rm H\,I}$ from the fit to the medians in the second iteration. The $N_{\rm H\,I}$ offset is $\sim 5 \times 10^{20}$ cm^{-2} throughout most of the LMC.

Steps to Produce Molecular Gas Map

1. Model the dust emission in the Herschel images to get τ_{160} (see Section 2.3.1 for more details).

2. Fit the H I offset in the $N_{\rm HI}$ vs. τ_{160} distribution regionally (see Section 2.3.2.1 for more details).

3. Produce first iteration map of the spatially varying effective gas-to-dust ratio ($\delta_{\rm GDR}$) at 500 pc scales determined from the diffuse regions ($\Sigma_{\rm gas} = \Sigma_{\rm HI}$)

   (a) Compute $\delta_{\rm GDR}$ for each pixel.

   (b) Mask all pixels that likely have molecular gas: all regions within 2′ of bright CO emission ($I_{\rm CO} > 3\sigma$)

   (c) Use averaging of nearest neighbors to iteratively fill in the masked (molecular) regions in the map.

   (d) Convolve map with symmetric Gaussian with FWHM = 500 pc.

4. Estimate $\Sigma_{\rm mol}$ using the first iteration of the smoothed effective $\delta_{\rm GDR}$:

$$\Sigma_{\rm mol} = (\delta_{\rm GDR}\Sigma_{\rm dust}) - \Sigma_{\rm HI}.$$

5. Produce second iteration of map of spatially varying $\delta_{\rm GDR}$ smoothed to 500 pc. Same as Step 4 with the modification that both regions within 2′ of bright CO emission ($I_{\rm CO} > 3\sigma$) and points that have estimated $\Sigma_{\rm mol} > 0.5\Sigma_{\rm HI}$ are masked.

6. Produce final map of $\Sigma_{\rm mol}$ map using the second iteration of the smoothed $\delta_{\rm GDR}$ map.

The final steps in producing the molecular gas maps remove unphysical artifacts. First, we remove small regions of estimated H_2 that are likely spurious by masking pixels that have positive molecular gas in less than 50% of the pixels surrounding them within a $4' \times 4'$ box (12×12 pixels in the modified black body map from this work and 4×4 pixels in the maps from Gordon et al. (2014); $\sim 60 \times 60$ pc in the LMC and $\sim 70 \times 70$ pc in the SMC). Generally, this removes emission smaller than $\sim 2'$ ($r \sim 30$ pc in the LMC and $r \sim 35$ pc in the SMC)–two times the beam size of the lower resolution H I data–and regions of negative values (from under-estimated total gas). Second, we median-filter the map over 3 pixels ($\sim 1'$ in the LMC map from this work) to smooth out the $\Sigma_{\rm mol}$ map and remove spikes that are unphysical and below the resolution of the H I map, largely due to the residual striping from the HERITAGE PACS images (Meixner et al. 2013).

There are a few caveats to this methodology that can potentially bias our molecular gas estimate. In addition to tracing the molecular gas (including any "CO-faint" component), our methodology may also trace optically thick and/or cold H I gas that emits disproportionately to the optically thin H I. Stanimirović et al. (1999) takes a statistical approach and estimates the optical depth correction in the SMC based on column density using the absorption line measurements from Dickey et al. (2000) and finds the correction only changes the total H I mass by $\sim 10\%$. Lee et al. (2015b) takes a similar approach to estimate an optical depth

correction in the Milky Way and finds that the correction only increases the mass of H I in the Perseus molecular cloud by $\sim 10\%$. Braun (2012) attempted to measure the H I optical depth from the flattening of the line profile in M31, M33, and the LMC, and found non-negligible optical depth corrections for high column densities ($22 < \log N_{\rm HI} < 23$) in compact ($\sim 100$ pc) regions, which increases the total H I mass by $\sim 30\%$. The Braun (2012) estimate relies on the assumption of gaussian line profiles to look for flattening of the H I line due to optical depth, which is a difficult measurement in the low signal-to-noise data. McKee et al. (2015) find $\sim 30\%$ to be the appropriate H I optical depth correction for the Solar neighborhood based on the average correction factors found using absorption line measurements in the plane of the Milky Way. Fukui et al. (2015), on the other hand, find more extreme opacity correction factors, as high as a factor of ~ 2 in the plane of the Milky Way using a relationship between $N_{\rm HI}$ and the optical depth at 353 GHz from *Planck*. The possible H I opacity corrections coming from a variety of methods and data show that the factors are uncertain.

The manner in which the optical depth correction will affect our molecular gas estimates is complex. It can increase the H I column density in the regions used to estimate the gas-to-dust ratio, leading to an increase in the total gas estimated in the molecular regions, and/or in the molecular regions, resulting in a decrease in the amount of molecular gas. We choose to use the H I statistical opacity corrections from Stanimirović et al. (1999) and Lee et al. (2015b) to explore how correcting for optical depth effects our methodology in Section 2.4.1.3.

We note that, in Perseus where the structure of the molecular cloud is resolved,

Lee et al. (2015b) compares their map of H I with the statistical optical depth correction to their inferred "CO-faint" gas, observing that the structures are not spatially coincident (see Figure 2.7 and Lee et al. 2015b). This suggests that the "CO-faint" gas cannot be explained by optically thick H I alone. Additionally, Lee et al. (2015b) comment that their opacity corrected H I map does not show the the sharp peaks seen in maps from Braun (2012).

Our methodology also relies on the assumption that the gas-to-dust ratio in the diffuse, atomic gas is the same in the molecular regions; we only measure the relationship between gas and dust in the atomic phase. There is observational evidence that the gas-to-dust ratio may vary from the diffuse to the dense gas in the Magellanic Clouds (Bot et al. 2004; Roman-Duval et al. 2014). In the Milky Way, *Planck* results show an factor of 2 increase in the FIR dust optical depth per unit column density (τ_{250}/N_H) from the diffuse to the dense gas (Planck Collaboration et al. 2011), which would could indicate a lower gas-to-dust ratio in the dense gas. Both optically thick H I and a decrease in the gas-to-dust ratio from the diffuse to the dense gas would mimic the effect of molecular gas and would result in our methodology overestimating the amount of molecular gas. We explore how these factors could affect our measurement of H_2 in our systematic uncertainty estimate.

2.3.2.1 Offsets in H I vs. Dust

The H_2 mapping method assumes that the gas-to-dust ratio in the diffuse, atomic ISM is the same as in the dense, molecular regions. As part of the mapping,

we investigated the global and regional relationship between $N_{\rm HI}$ and τ_{160}. The global relationship between $N_{\rm HI}$ to τ_{160} is primarily defined by one linear relationship (equivalent to a single dust-to-gas ratio) with a large amount of scatter (see Figure 2.1). We split the galaxies into quadrants to fit the offset in H I. For the LMC, we split the Southeast quadrant into 16 smaller regions due to the complexity of this part of the galaxy: the Molecular Ridge and an H I streamer that extends to become part of the Magellanic Bridge. Figure 2.4 shows the fitted offsets in $\Sigma_{\rm HI}$ in the LMC, with the offsets typically being $\sim 5\ M_{\odot}\ {\rm pc}^{-2}$.

By splitting up the LMC into four equal quadrants and looking at the regional relationships between $N_{\rm HI}$ and τ_{160}, we found that the offset distribution is coming from the SW quadrant. We further checked for smaller regional variation within the different molecular gas complexes and found the majority of offset points to be coming from the Molecular Ridge. Possible explanations for an offset at higher $N_{\rm HI}$ compared to the dust include: issues with the background subtraction in the *Herschel* data or a constant layer of H I gas with little to no dust along the line of sight. We note that variations in the gas-to-dust ratio would only change the slope of the distribution, and not just the offset. An issue with background subtraction seems unlikely since the excess offset appears to be correlated with a physical complex and there is no obvious gradient across the quadrant. A layer of low-dust or dust-free H I is possible since there is an H I streamer extending out of the galaxy in this area that becomes part of the Magellanic Bridge. It is possible the stripped gas could have little to no dust.

Steps to Finding H I Offset

1. Mask all points that likely have molecular gas given the CO map (all regions within $2'$ of bright CO emission ($I_{\rm CO} > 3\sigma$ detections)

2. First fit a linear equation to the binned medians of the diffuse gas ($N_{\rm HI} < 3{\times}10^{21}$ cm^{-2}); the slope represents the effective GDR ($\delta_{\rm GDR}$) and offset gives the H I offset.

3. Use the fitted $\delta_{\rm GDR}$ to estimate the total gas using the dust map ($\Sigma_{\rm gas} = \delta_{\rm GDR}\Sigma_{\rm dust}$), subtract $\Sigma_{\rm HI}$ to get first iteration estimate of H_2 ($\Sigma_{\rm mol} = (\delta_{\rm GDR}\Sigma_{\rm dust}) - \Sigma_{\rm HI}$).

4. Mask all points near bright CO and any points that have estimated $\Sigma_{\rm mol} > 0.5\Sigma_{\rm HI}$.

5. Refit a linear equation to the binned medians of the diffuse gas with the new mask.

6. Remove the $\Sigma_{\rm HI}$ offset from the second iteration of fitting from the H I map and use this subtracted H I map in the rest of the analysis.

2.3.2.2 Map Sensitivity and Uncertainty

We use a Monte Carlo method to estimate the uncertainty in our molecular gas maps and determine the sensitivity levels. For the maps produced with the dust fitting from this work, we select three sub-regions (shown in Figure 2.5) with different

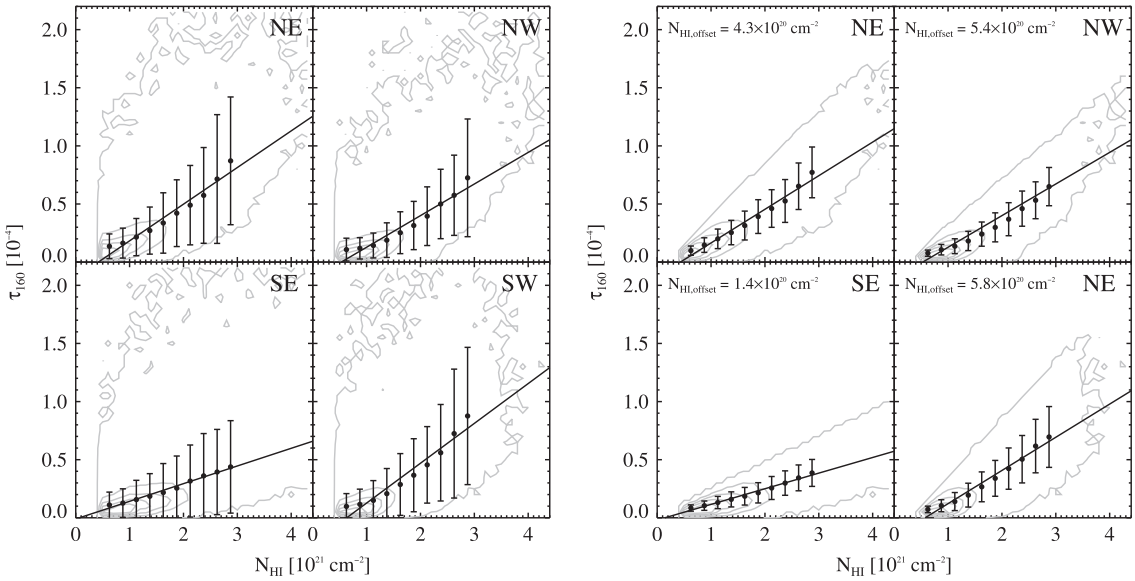

Figure 2.2 Relationships between τ_{160} and the column density of H I for the quadrants of the LMC using our fiducial $\beta = 1.8$ dust modeling results. The contours show the density of points at 80%, 60%, 40%, and 20% of the maximum with the outer contour showing the full extent of the distribution. The black points show the median τ_{160} values with 1σ in 2.5×10^{20} cm^{-2} bins from $1 - 3 \times 10^{21}$ cm^{-2} (chosen to avoid low number of values and the threshold where CO-dark H_2 can exist). The black lines show the fit to the medians, which are used to make rough estimates of the H_2 and to determine the H I offset. The left set of plots have only regions near bright CO masked. The right set of plots have additional regions with significant estimated H_2 masked (see Section 2.3.2) based on the quadrant fits to the binned median values of the distribution shown in the plots on the left.

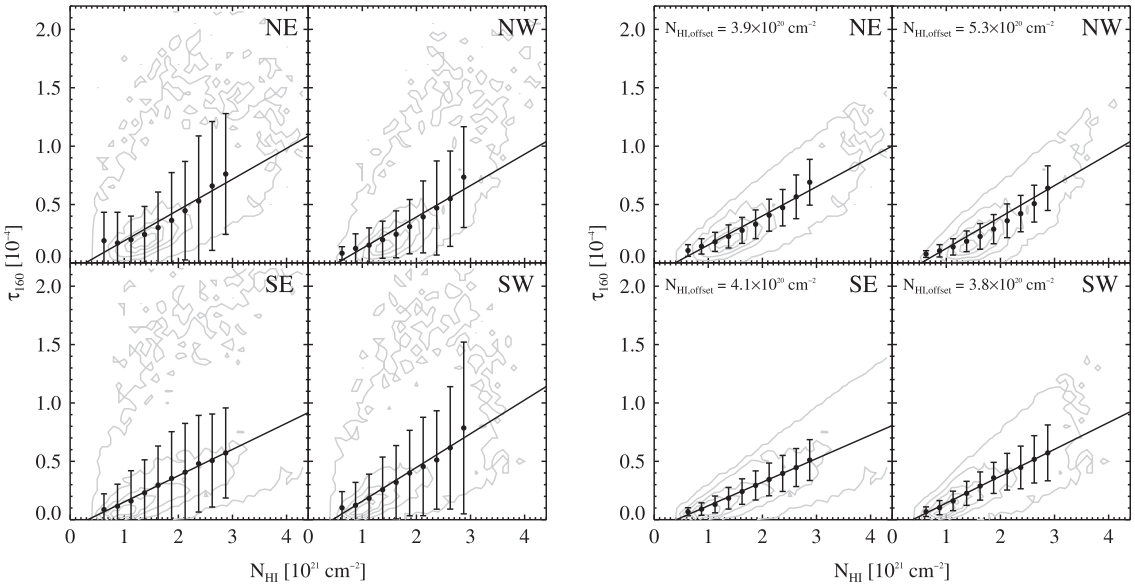

Figure 2.3 Same as Figure 2.2 but with τ_{160} from the Gordon et al. (2014) dust modeling results.

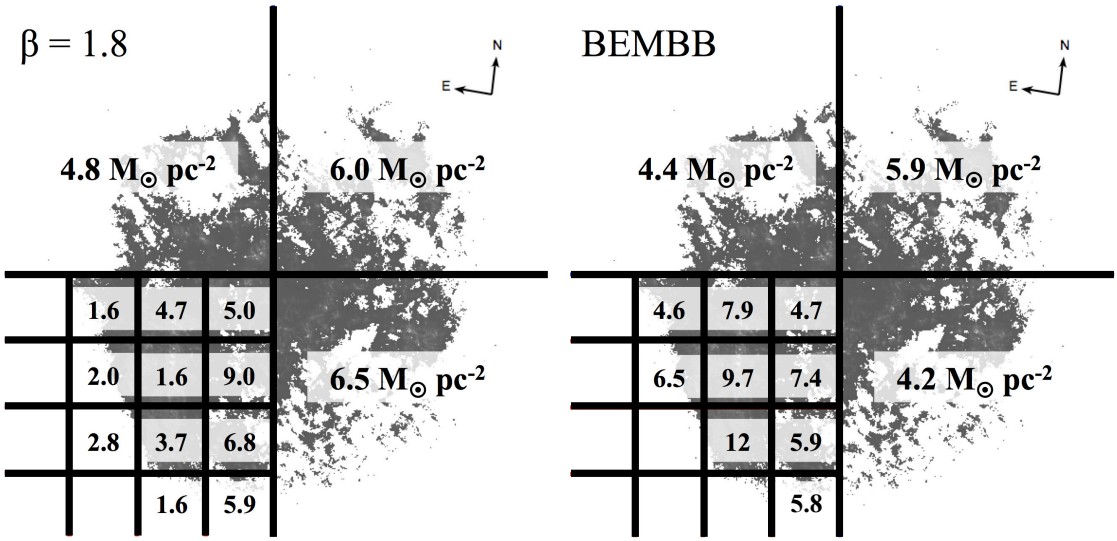

Figure 2.4 The H I offset fit for each region in the LMC for the fiducial β=1.8 dust modeling in this work (*left*) and Gordon et al. (2014) (*right*).The background grey-scale shows the tau_{160} map from the Gordon et al. (2014) modeling.

levels of molecular gas (high, moderate, and low). We add normally distributed noise with an amplitude equal to the uncertainty to each of the *Herschel* bands and fit T_d for a fixed β for each sub-region and then calculate τ_{160}. For the dust modeling results from Gordon et al. (2014), we add normally distributed noise to the τ_{160} maps with amplitude equal to the uncertainty estimates from Gordon et al. (2014). Finally, we add noise to the H I map and create new $\Sigma_{\rm mol}$ maps. The process is repeated 100 times for each of the different maps. We use the distribution of $\Sigma_{\rm mol}$ for each pixel from the Monte Carlo realizations to estimate a realistic uncertainty. The sensitivity of the maps is estimated by finding the lowest $\Sigma_{\rm mol}$ that is consistently recovered at $\geq 2\sigma$.

We know that the systematic uncertainty from the methodology will dominate the uncertainty in our molecular gas maps (Leroy et al. 2009; Bolatto et al. 2011). To estimate the level of systematic uncertainty, we see how changes to various aspect of the mapping methodology affect the estimated total molecular mass $M_{\rm mol}$ (which includes the factor of 1.4 to account for He). We explore the effects of different assumptions in the dust modeling and determination of the gas-to-dust ratio and produces maps that:

- change the value of β in our dust modeling and re-run the fitting with $\beta = 1.5$ and $\beta = 2.0$;
- do not remove an H I offset, which explores the idea that the relationship between $N_{\rm HI}$ and τ_{160} may not be linear a low column densities;
- apply a single gas-to-dust ratio using the high and low values from Roman-

Duval et al. (2014) (as opposed to using the map of $\delta_{\rm GDR}$);

- scale the $\delta_{\rm GDR}$ map down by a factor of 2 in the molecular regions to account for a possible change in the gas-to-dust ration from the diffuse to the dense gas, where we define the dense gas as regions in the map that are likely to have molecular gas (Step 5 in Section 2.3.2);

- apply a single gas-to-dust ratio for the diffuse gas and a lower value for the dense gas using the values from Roman-Duval et al. (2014), where the dense gas value is applied to regions with bright CO emission (as in Roman-Duval et al. 2014).

For the versions of the maps where we use gas-to-dust ratios found in Roman-Duval et al. (2014), we use the maps of $\Sigma_{\rm dust}$ in place of τ_{160}. We use the range in $M_{\rm mol}$ values to estimate the amount of systematic uncertainty in our molecular gas estimate.

2.3.2.3 Estimating H_2 from CO

For the purposes of this work, we want to compare the amount of H_2 traced by detected, bright ^{12}CO emission to the molecular gas traced by the dust emission. To convert the CO intensity ($I_{\rm CO}$) into column density of mass, we use the following equations:

$$N({\rm H_2}) = X_{\rm CO}\ I_{\rm CO} \tag{2.3}$$

$$M_{\rm mol} = \alpha_{\rm CO}\ L_{\rm CO}, \tag{2.4}$$

where proportionality constants appropriate for Galactic gas are $X_{\rm CO} = 2 \times 10^{20}$ cm^{-2} (K km s^{-1})$^{-1}$ and $\alpha_{\rm CO} = 4.3\ M_{\odot}$ (K km s^{-1} pc^2)$^{-1}$, $I_{\rm CO}$ is the integrated intensity of the ^{12}CO $J = 1 \rightarrow 0$ transition (in K km s^{-1}), and $L_{\rm CO}$ is the luminosity of the same transition (in K km s^{-1} pc^2). On small spatial scales and in CO-bright regions, using the Galactic values is a good approximation (Bolatto et al. 2008).

2.3.3 Convolving to Lower Resolutions

To produce the lower resolution molecular gas maps, we first convolve the maps from the *Herschel* beam to a gaussian with FWHM of 30″ for the $\beta = 1.8$ map (appropriate for the 350 μm image resolution) and 40″ for the BEMBB map (appropriate for the 500 μm image resolution) using the kernels from Aniano et al. (2011). We then produce the range of lower resolution maps (from 20 pc to $\sim$ 1 kpc) by convolving the images of $\Sigma_{\rm SFR}$, $\Sigma_{\rm mol}$, and $\Sigma_{\rm HI}$ with a gaussian kernel with FWHM $= \sqrt{(r^2 - r_0^2)}$, where r is the desired resolution and r_0 is the starting resolution of the image. The images are then resampled to have approximately independent pixels (one pixel per resolution element). To mitigate edge effects from the convolution, we remove the outer two pixels (two beams) for all resolution images of the LMC. In the SMC, we remove two outer pixels for $r \leq 600$ pc and remove one pixel from the edges for $r \geq 700$ pc due to the small size of the images.

Table 2.1. Total Molecular Gas Mass Estimates for the LMC and SMC

	Data	Dust Fitting[a]	Method	$M_{\rm mol}$ $[10^7 M_\odot]$[b]
		LMC		
1	*Herschel* 100-350μm	MBB, $\beta = 1.8$	$\delta_{\rm GDR}$ map[c]	9.9
2	*Herschel* 100-500μm	BEMBB, $0.8 < \beta < 2.5$	$\delta_{\rm GDR}$ map[c]	6.3
3	*Herschel* 100-350μm	MBB, $\beta = 1.5$	$\delta_{\rm GDR}$ map[c]	6.8
4	*Herschel* 100-350μm	MBB, $\beta = 2.0$	$\delta_{\rm GDR}$ map[c]	10.1
5	*Herschel* 100-500μm	BEMBB, $0.8 < \beta < 2.5$	$\delta_{\rm GDR}$ map[c], no H I offset	13.4
6	*Herschel* 100-500μm	BEMBB, $0.8 < \beta < 2.5$	GDR = 540[d]	3.9
7	*Herschel* 100-350μm	MBB, $\beta = 1.8$	$\delta_{\rm GDR}$ map[c], $\delta_{\rm GDR,dense} = 0.5\delta_{\rm GDR,map}$	4.5
8	*Herschel* 100-500μm	BEMBB, $0.8 < \beta < 2.5$	$\delta_{\rm GDR}$ map[c], $\delta_{\rm GDR,dense} = 0.5\delta_{\rm GDR,map}$	4.0
		SMC		
9	*Herschel* 100-500μm	BEMBB, $0.8 < \beta < 2.5$	$\delta_{\rm GDR}$ map[c]	2.0

[a]MBB = Modified Black Body, BEMBB = Broken Emissivity Modified Black Body

[b]assuming $d_{\rm LMC} = 50$ kpc and $d_{\rm SMC} = 62$ kpc

[c]map of spatially varying $\delta_{\rm GDR}$, see Section 2.3.2

[d]does not include factor of 1.36 contribution from helium

2.4 Results

2.4.1 Molecular Gas in the Magellanic Clouds

We find molecular gas fractions that are comparable to the Milky Way in the LMC (17%), but much lower in the SMC (3%). These molecular gas fractions come from our new estimates of the total molecular gas mass: we find a total molecular gas mass (including He) in the LMC of $M^{\rm mol}_{\rm LMC} = 6.3^{+6.3}_{-3.2} \times 10^7\ M_\odot$ and $M^{\rm mol}_{\rm SMC} = 1.3^{+1.3}_{-0.65} \times 10^7\ M_\odot$ in the SMC. These values are the sums (with no cuts) of our fiducial molecular gas maps that use the BEMBB dust modeling results from Gordon et al. (2014) with a spatially varying $\delta_{\rm GDR}$ and include a factor of 2 systematic uncertainty. Table 2.1 shows the results from our exploration of varying the map making methodology to estimate the systematic uncertainty combined with estimates of the molecular gas mass from the literature. In Table 5.1 we list the

integrated properties of both galaxies. The molecular gas maps are sensitive to $\Sigma_{\rm mol} \sim 15\ M_\odot\ {\rm pc}^{-2}$ ($\sim 7 \times 10^{20}\ {\rm cm}^{-2}$) based on the Monte Carlo estimates, which is comparable to the sensitivity of the SMC map from Bolatto et al. (2011). Our molecular gas fraction in the SMC is lower than previous estimates (Leroy et al. 2007; Bolatto et al. 2011), but is consistent with the factor of ~ 2 estimate of systematic uncertainty for all of the estimates (see Section 2.4.1.4 for further discussion).

The fiducial molecular gas maps ($\beta = 1.8$ and BEMBB dust modeling) were produced using maps of the effective dust-to-gas ratio ($\delta_{\rm GDR}$) that had average values of $N_{\rm HI}/\tau_{160}$ of $1.8 \pm 0.6 \times 10^{25}\ {\rm cm}^{-2}$ (LMC $\beta = 1.8$), $1.3 \pm 0.3 \times 10^{25}\ {\rm cm}^{-2}$ (LMC BEMBB), and $4.8 \pm 0.9 \times 10^{25}\ {\rm cm}^{-2}$ (SMC BEMBB). In the Milky Way, Planck Collaboration et al. (2014) found $N_{\rm HI}/\tau_{160} = 1.1 \times 10^{25}\ {\rm cm}^{-2}$ in the diffuse ISM. Our $N_{\rm HI}/\tau_{160}$ values are on average a factor of ~ 1.5 (LMC) and ~ 4.4 (SMC) times higher than the diffuse Milky Way ISM, which is consistent with the expectation that the gas-to-dust ratio should increase with decreasing metallicity.

Given the total NANTEN CO luminosities of $L({\rm CO})_{\rm LMC} = 7 \times 10^6$ K km s^{-1} pc^2 and $L({\rm CO})_{\rm SMC} = 1.7 \times 10^5$ K km s^{-1} pc^2 (using no sensitivity cuts), we find $\alpha_{\rm CO}^{\rm LMC} = 10^{+9}_{-6}$ and $\alpha_{\rm CO}^{\rm SMC} = 76^{+77}_{-38}$, where all units for $\alpha_{\rm CO}$ are given in $M_\odot$ (K km s^{-1} pc^2)$^{-1}$. Compared to the Milky Way value of $\alpha_{\rm CO} = 4.3$ (Bolatto et al. 2013), the conversion factor for the LMC is ~ 2 times higher and the SMC is ~ 17 times higher. Our $\alpha_{\rm CO}$ values are comparable to the dust-based $\alpha_{\rm CO}$ found by Leroy et al. (2011) of 6.6 (K km s^{-1} pc^2)$^{-1}$ and $53 - 85$ (K km s^{-1} pc^2)$^{-1}$ for the LMC and SMC, respectively.

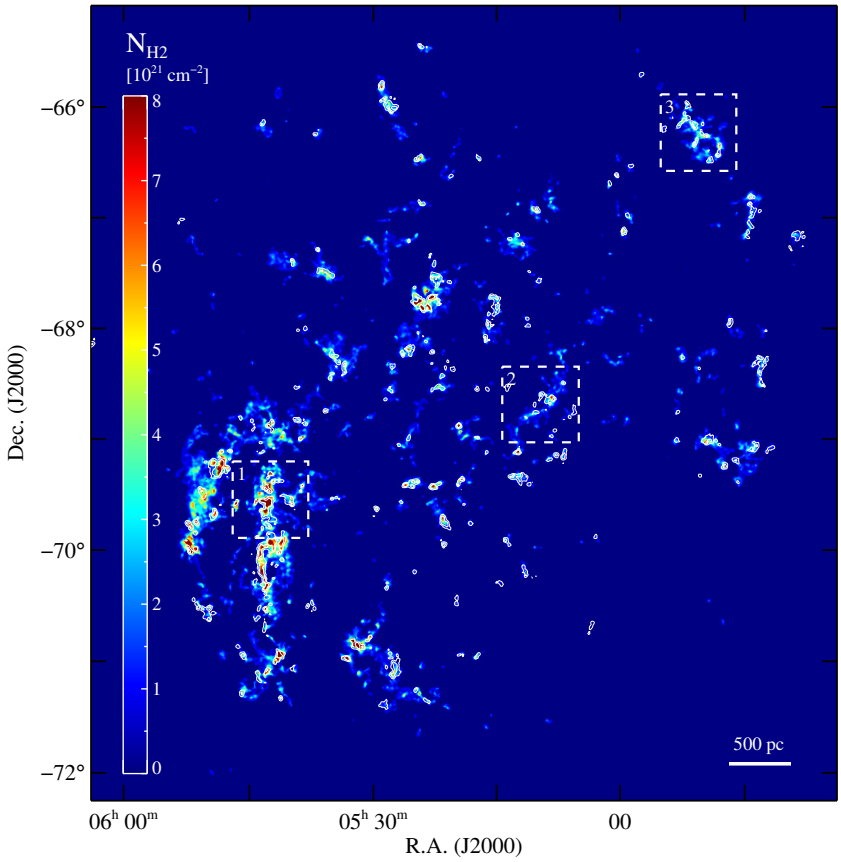

Figure 2.5 H_2 column density (N_{H_2}) map of the LMC at $\sim$ 5 pc resolution ($\theta = 20''$, 1 beam per pixel sampling) produced by modeling the dust continuum emission from *Herschel* 100 μm, 160 μm, 250 μm, and 350 μm observations from HERITAGE (Meixner et al. 2013) using a modified black body. The white contours show the 1.2 K km s^{-1} (3σ) and 5 K km s^{-1} levels of the MAGMA DR3 CO map ($\theta = 40''$), which covered regions with prior CO detection. Assuming a Galactic conversion factor of $X_{CO} = 2 \times 10^{20}$ cm^{-2} (K km s^{-1})$^{-1}$, the contour levels correspond to column densities of 2.4×10^{20} cm^{-2} and 1×10^{21} cm^{-2}. The dashed white boxes indicate the three regions in Figure 2.7. There is excellent agreement between the dust-based molecular gas map and the CO map even though the CO is not directly used to produce the map.

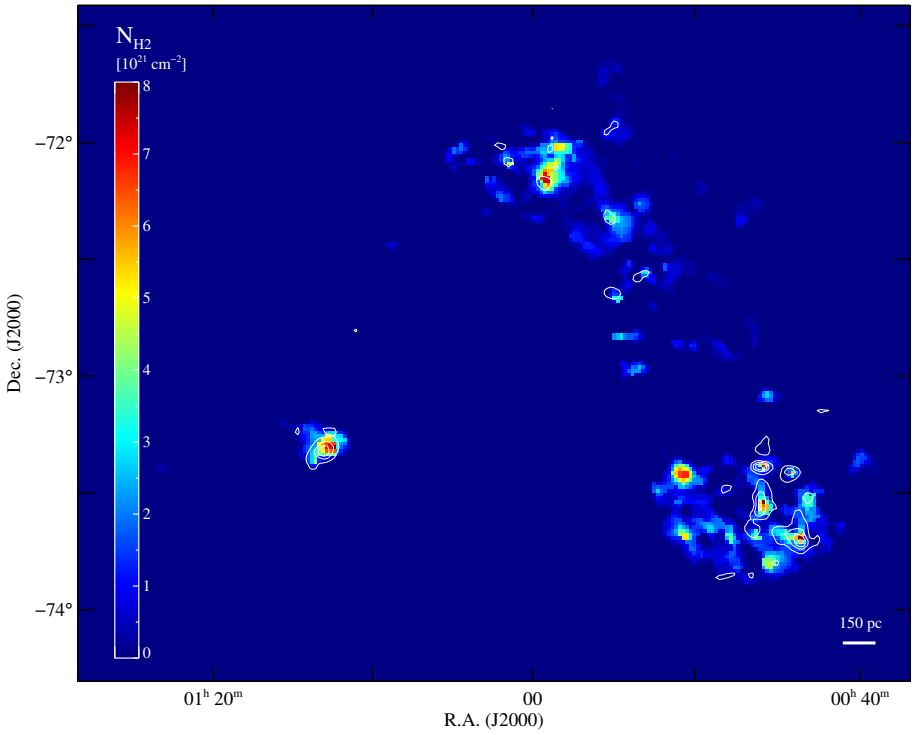

Figure 2.6 H_2 column density (N_{H_2}) map of the SMC at $\sim$ 10 pc resolution ($\theta = 40''$, 1 beam per pixel sampling) produced by modeling the dust continuum emission from *Herschel* 100 μm, 160 μm, 250 μm, 350 μm, and 500 μm observations from HERITAGE (Meixner et al. 2013) using the BEMBB dust modeling results from Gordon et al. (2014). The white contours show the 0.45 (3σ), 1, 1.5, and 2 K km s^{-1} levels of the NANTEN CO map ($\theta = 1'$).

2.4.1.1 Structure of the Molecular Gas

One of the most striking results is the similarity of the structure of the molecular gas traced by dust to that traced by CO throughout the entire LMC (see Figure 2.5 and Figure 2.7). Since our methodology only indirectly uses the CO map as a mask (see Section 2.3.2) the similarity is confirmation that our methodology traces the structure of the gas. Figure 2.7 shows that both dust modeling techniques produce maps with similar structure, although the BEMBB map tends to predict systematically lower amounts of H_2.

The details of the structures traced by CO are different from the dust-based molecular gas map. All of the regions shown in Figure 2.7 show molecular gas traced by dust, but not by CO at the 3σ level. This is likely a layer of self-shielded H_2 where CO has mostly dissociated, as expected from models (Wolfire et al. 2010; Glover & Mac Low 2011). The same is generally true for the SMC, but having only the lower resolution full coverage NANTEN ^{12}CO map ($r = 2.6'$) makes detailed comparison of the structure difficult. Conversely, Region 2 in Figure 2.7 shows a molecular gas cloud traced by CO and not by the dust-based method. As discussed in Leroy et al. (2009), one possible explanation is that the dust is cold and faintly emitting in the far infrared, below the sensitivity of the HERITAGE *Herschel* images. The peak in the CO emission of this cloud is detected from 250-500 μm, but only weakly detected at 160 μm and marginally detected ($\sim 3\sigma$) at 100 μm, consistent with the interpretation of cold dust. There are a few other detections of CO without a dust-based molecular gas counterpart, although the cloud in Region 2 is the clearest

example with the strongest CO emission.

2.4.1.2 Systematic Uncertainty

The systematic uncertainty comes from the different possible assumptions that can be made in the dust modeling and the method of measuring the gas-to-dust ratio. Because the statistical errors are typically small, the systematic uncertainty dominates the total uncertainty in the molecular gas mapping methodology (Leroy et al. 2009; Bolatto et al. 2011). We present the range of our total molecular gas mass estimates ($M_{\rm mol}$) in Table 2.1 (we list all $M_{\rm mol}$ estimates alongside estimates from the literature in Table 3.6 in Section 2.4.1.4). We use the range of as a means to gauge the amount of total systematic uncertainty and we look at the variation between the two fiducial molecular gas maps (Table 2.1 rows 1 and 2) with different dust modeling assumptions to determine the amount of systematic uncertainty due to assumptions in the dust modeling.

The two lowest $M_{\rm mol}$ estimates that we found use a single gas-to-dust ratio of 380 from Roman-Duval et al. (2014) and use the upper estimates for the gas-to-dust ratios for the diffuse and the dense gas from Roman-Duval et al. (2014) of $\rm GDR_{diffuse} = 540$ and $\rm GDR_{dense} = 330$ (see rows 6 and 10 in Table 3.6 in Section 2.4.1.4). These maps have large regions of negative values from where the estimated total gas is less than the H I, which causes only small areas of estimated H_2 and the low $M_{\rm mol}$ values, which would be due to using too low a value of the gas-to-dust ratio. The value for $M_{\rm mol}$ with GDR = 380 is less than the total molecular gas you

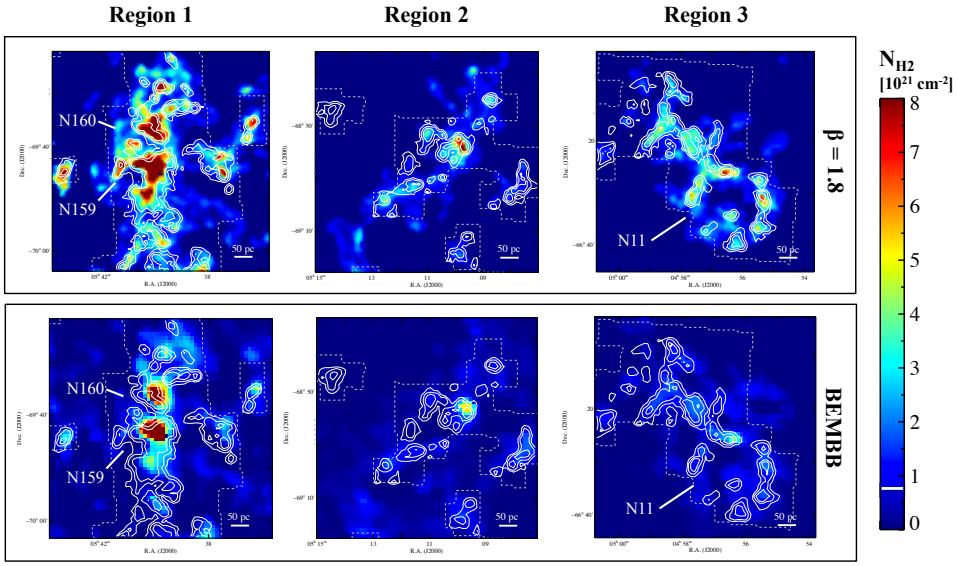

Figure 2.7 The top and bottom rows of images respectively show the enlarged regions of the $N_{\rm mol}$ maps (identified in Figure 2.5) for the dust modeling with $\beta = 1.8$ and the BEMBB model from Gordon et al. (2014) at the same color scale as show in Figure 2.5. The contours show the MAGMA ^{12}CO intensity at levels of 0.6 (3σ), 2, and 5 K km s^{-1} with the dashed grey line showing the survey coverage in the regions. The white line on the color bar indicates the estimated sensitivity level of $N_{\rm mol} \sim 7 \times 10^{20}$ cm^{-2} ($\Sigma_{\rm mol} \sim 15$ $M_\odot$ pc^{-2}). Both dust-based molecular gas maps show similar structure. The dust-based estimate tends to show more extended molecular gas than that traced by ^{12}CO. The only clear example of a CO cloud (with strong CO emission) with no dust-based molecular gas counterpart (in both the LMC and SMC) is found in the NE of Region 2. The difference in intensity demonstrates the systematic uncertainty in the methodology.

would get by applying a Galactic CO-to-H_2 conversion factor to the low resolution NANTEN CO map, which is a lower limit on the total molecular gas since a higher conversion factor should be appropriate when the CO structure is unresolved. We do not consider these values of $M_{\rm mol}$ when estimating the systematic uncertainty in the total molecular gas mass.

The difference between the highest (row 5) and lowest (row 6) molecular gas mass is ~ 3.5. The minimum $M_{\rm mol}$ estimate (row 6) comes from assuming a single gas-to-dust ratio of 540, which is the highest value found by Roman-Duval et al. (2014). This $M_{\rm mol}$ estimate is only a factor of ~ 1.5 lower than using a spatially varying $\delta_{\rm GDR}$ applied to the same BEMBB dust modeling results. The maximum value comes from using the BEMBB modeling that does not remove an H I offset (row 5), which allows for a possible non-linear relationship in $N_{\rm HI}$ vs. τ_{160} (see Section 2.3.2.2 and Section 2.3.2.1). This would be an overestimate if the relationship between $N_{\rm HI}$ vs. τ_{160} is linear since it will artificially increase the $\delta_{\rm GDR}$ values in the maps. Allowing for a difference in the gas-to-dust ratio in the diffuse and dense gas by scaling down $\delta_{\rm GDR}$ in the dense gas reduces $M_{\rm mol}$ by a factor of ~ 2 for the $\beta = 1.8$ map and ~ 1.5 for the BEMBB map. We conclude that our molecular gas estimate is good to within a factor of ~ 2, which agrees with the estimates from similar methodologies by Leroy et al. (2009, 2011) and Bolatto et al. (2011).

We compare the effects of different dust modeling techniques by using $\beta = 1.8$ and BEMBB maps while keeping all other aspects of the methodology the same (using a spatially varying $\delta_{\rm GDR}$). Figure 2.7 shows the difference between the molecular gas maps using the $\beta = 1.8$ and BEMBB modeling (top and bottom rows,

respectively). The BEMBB map is a factor of ~ 2 lower molecular gas column density estimates than using the fits from the $\beta = 1.8$ model. The difference in values between the two maps show no variation as a function of τ_{160}, which indicates that the dust models do not produce systematically different results in the dense gas as compared to the diffuse. The τ_{160} values from the BEMBB modeling (Gordon et al. 2014) tend to be higher than from the $\beta = 1.8$ modeling largely due to differences in the fitted dust temperatures (T_d). The BEMBB modeling tends to fit higher T_d, which is a result of the range of β values combined with the degeneracy between β and T_d (Dupac et al. 2003; Shetty et al. 2009): fitting a lower β value to the same data will result in an increase in T_d. An increase in τ_{160} produces lower effective gas-to-dust ratio ($\delta_{\rm GDR}$) and a lower estimate of the amount molecular gas. Our adopted factor of ~ 2 systematic uncertainty is consistent with the variation seen between the two maps.

2.4.1.3 Estimating the Effect of the Optical Depth of H I

We apply the statistical optical depth corrections from Stanimirović et al. (1999) for the SMC and Lee et al. (2015b) for the Milky Way to $N_{\rm HI}$ maps to estimate how accounting for optically thick H I could affect our molecular gas estimate. There is no comparable optical depth correction for the LMC, so we apply the statistical corrections for the lower metallicity SMC and higher metallicity Milky Way to estimate a range of possible effects. Applying the Lee et al. (2015b) correction to the LMC H I produces a maximum correction factor of 1.43 and shifts the top 5%

of $N_{\rm H\,I}$ from $> 3.1 \times 10^{21}$ cm^{-2} to $> 4.0 \times 10^{21}$ cm^{-2}, whereas the Stanimirović et al. (1999) correction produces a maximum correction factor of 1.36 and shifts the top 5% to $> 3.3 \times 10^{21}$ cm^{-2}. Applying the Stanimirović et al. (1999) correction to the SMC produces a maximum correction factor of 1.48 and shifts the top 5% of the $N_{\rm H\,I}$ from $> 4.4 \times 10^{21}$ cm^{-2} to $> 5.2 \times 10^{21}$ cm^{-2}. In the LMC, both of the statistical optical depth corrections decrease the total molecular gas mass estimate by $\sim 5\%$ while in the SMC it increases the total molecular gas mass by a factor ~ 2, both are within our estimate of the systematic uncertainty.

The molecular gas estimate changes because the amount of H I in the diffuse regions, where we determine the effective gas-to-dust ratio, increases or decreases with respect to the amount of H I in the molecular regions. Optical depth corrections in the diffuse gas will increase the effective gas-to-dust ratio and increase the estimate of the total amount of gas. If the optical depth corrections in the molecular regions are similar to the corrections in the diffuse regions, as is the case in the SMC, the total amount of gas will increase and the molecular gas estimate will increase. If the optical depth corrections in the molecular regions are larger than in the diffuse, more of the total gas estimate will be due to H I as opposed to H_2 and the molecular gas estimate will decrease, as is the case in the LMC. Ultimately, the decrease in the molecular gas mass estimate in the LMC is negligible, which indicates that optical depth effects do not significantly contribute to our molecular gas estimate.

2.4.1.4 Comparison to Previous Work

The molecular gas maps we present are improvements upon previous dust-based H_2 estimates given the availability of the *Herschel* data with increased sensitivity and coverage of the far-infrared combined with improvements in the methodology and more extensive estimation of the systematic uncertainty. Table 2.1 includes the existing dust-based molecular gas mass estimates for LMC and SMC from the literature. While some of the total molecular mass values are out of the range of the estimate from this work, they can all be reconciled and explained by differences in methodology and limitations in the data.

Table 2.2. Comparison of Total Molecular Gas Mass Estimates for the LMC and SMC

	Data	Dust Fitting[a]	Method	$M_{\rm mol}$ $[10^7 M_\odot]$[b]	Reference
			LMC, this work		
1	*Herschel* 100-500μm	BEMBB, $0.8 < \beta < 2.5$	$\delta_{\rm GDR}$ map[c]	6.3	1
			LMC, literature		
2	*Herschel* 100-500μm,	BEMBB, $0.8 < \beta < 2.5$	$\rm GDR_{diffuse} = 380$, $X_{\rm CO} = 2 \times 10^{20}$	2.7	2
3	MAGMA ^{12}CO				
4	*IRIS*, *Spitzer* 3-160μm	Desert et al. (1990)	lowest 5% $\delta_{\rm GDR}$	33	3
5	*IRAS* 12-100μm	···	reference $N_{\rm H}/\mu_{\rm FIR}$	15.4	4
6	NANTEN ^{12}CO	···	Galactic $\alpha_{\rm CO} = 4.3$	1.25	5
7	NANTEN ^{12}CO	···	$X_{\rm CO} = 7 \times 10^{20}$	5	5
			SMC, this work		
8	*Herschel* 100-500μm	BEMBB, $0.8 < \beta < 2.5$	$\delta_{\rm GDR}$ map[c]	2.0	1
			SMC, literature		
9	*Herschel* 100-500μm,	BEMBB, $0.8 < \beta < 2.5$	$\rm GDR_{diffuse} = 1200$, $X_{\rm CO} = 1 \times 10^{21}$	0.2	2
	NANTEN ^{12}CO				
10	*Spitzer* 70-160μm	MBB, $\beta = 1.5$	$\delta_{\rm GDR}$ map[c]	2.2	6
11	*IRIS* 100,*Spitzer* 160μm	Dale & Helou (2002)	regional GDR	3.2	7
12	*IRAS* 12-100μm	···	reference $N_{\rm H}/\mu_{\rm FIR}$	10.5	4
13	NANTEN ^{12}CO	···	Galactic $\alpha_{\rm CO} = 4.3$	0.07	8
14	NANTEN ^{12}CO	···	$X_{\rm CO} = 2.5 \times 10^{21}$	0.42	8

References. — (1) this work, (2) Roman-Duval et al. (2014), (3) Bernard et al. (2008), (4) Israel (1997), (5) Fukui et al. (2008), (6) Bolatto et al. (2011), (7) Leroy et al. (2007), (8) Mizuno et al. (2001)

[a]MBB = Modified Black Body, BEMBB = Broken Emissivity Modified Black Body

[b]assuming $d_{\rm LMC} = 50$ kpc and $d_{\rm SMC} = 62$ kpc

[c]map of spatially varying $\delta_{\rm GDR}$, see Section 2.3.2

The early estimates from Israel (1997) for both the LMC and SMC were based on low resolution *IRAS* data, did not directly model the dust emission (using instead a scaled far-infrared surface brightness, $\mu_{\rm FIR}$, based on the difference in dust temperature relative to a fiducial value), and used one effective gas-to-dust ratio for each galaxy based on a few reference positions. These early estimates are likely high due to the lack of long wavelength data, which causes a bias towards higher dust temperature, and therefore high effective gas-to-dust ratios; regardless, the estimates are still with a factor of ~ 2 for the LMC and ~ 5 for the SMC.

Bernard et al. (2008) produced a dust-based estimate of the molecular gas for the LMC using the *Spitzer* SAGE data and found a total molecular mass of 3.3×10^8 $M_\odot$. They chose a single $\delta_{\rm GDR}$ equal to the value at the lowest 5% level of the $\delta_{\rm GDR}$ distribution, $\tau_{160}/N_{\rm HI} = 8.8 \times 10^{-26}$ cm^2 (or $N_{\rm HI}/\tau_{160} = 1.1 \times 10^{25}$ cm^2). This value of gas-to-gas ratio is consistent with the average values we find in our maps of the gas-to-dust ratio, but our maps have a wide range of values. Bernard et al. (2008) takes this value of the gas-to-dust ratio and applies it to the entire galaxy. The primary difference that drives the higher molecular gas mass estimate is that Bernard et al. (2008) fits lower dust temperatures (median $T_{\rm d} \sim 18$ K) to the *Spitzer* 160 μm and *IRIS* 100 μm data. The dust modeling used in this work includes more infrared bands and longer wavelength data and we find a higher average dust temperature of $T_{\rm d} = 23$ K. Changing $T_{\rm d}$ from 18 K to 23 K (and holding I_{160} constant) results in a decrease in τ_{160} of a factor of ~ 3. When the similar gas-to-dust ratio is applied to the map of higher values of τ_{160}, the total gas, and therefore molecular gas mass estimate is higher. Scaling our τ_{160} up by a factor of 3 yields a total molecular gas

mass of 2.1×10^8 $M_\odot$, which is comparable to the Bernard et al. (2008) estimate. The $M_{\rm mol}$ estimate from Bernard et al. (2008) can serve as an upper limit to the amount of gas associated with the excess far-infrared emission.

The most recent estimates for the molecular gas masses come from Roman-Duval et al. (2014), which also used the dust modeling from Gordon et al. (2014). While this work focuses on creating maps of the molecular gas, Roman-Duval et al. (2014) studies the global relationship between the gas and dust in the different gas phases and does not explore any spatial variations. The molecular gas mass estimate we show in Table 2.1 combines the estimate of the molecular gas traced by bright CO emission (using the fiducial $X_{\rm CO} = 2 \times 10^{20}$ cm^{-2} (K km s^{-2})$^{-1}$) in the LMC $X_{\rm CO} = 1 \times 10^{21}$ cm^{-2} (K km s^{-2})$^{-1}$) in the SMC) with the estimate of the amount of molecular gas not traced by bright CO emission ("CO-dark" or "CO-faint"). They estimate the amount of molecular gas not traced by CO by applying the diffuse gas-to-dust ratio (GDR$^{\rm dif}$ = 380 in the LMC and GDR$^{\rm dif}$ = 1200) to the regions where molecular gas is expected, based on the dust surface density, but no CO is detected. The total molecular gas mass estimates for the LMC and SMC are significantly lower than the estimates from this work. Roman-Duval et al. (2014) uses a constant gas-to-dust ratio while we use a map of the gas-to-dust ratio, the average gas-to-dust ratios from our maps are $\sim 50\%$ larger than the average values by Roman-Duval et al. (2014), and they use CO to estimate part of the molecular gas. The main factor driving the lower molecular gas is the low gas-to-dust ratio applied uniformly across the galaxies. The difference in gas-to-dust ratio is largely due to the difficulty in fitting a linear relation to a noisy distribution ($\Sigma_{\rm gas}$-$\Sigma_{\rm dust}$);

Roman-Duval et al. (2014) finds a range in the fitted global GDR^{dif} of $380 - 540$ depending on the fitting method.

The new estimate for the SMC using the *Herschel* data is lower than the estimates based on *Spitzer* data: $\sim 40\%$ lower than the estimate from Bolatto et al. (2011), and $\sim 60\%$ from Leroy et al. (2007). This is well within the factor of $2-3$ estimated systematic uncertainty from Bolatto et al. (2011). Given the differences in methodology used in all of the previous estimates and their respective levels of uncertainty, we find all of the molecular gas mass estimates to be consistent.

2.5 Summary and Conclusions

We create H_2 maps for the LMC and SMC by using dust emission from HERITAGE *Herschel* images as a tracer of the total column density of gas and subtracting off the atomic component, which avoids the known biases of using CO as a tracer of the molecular gas at lower metallicity. Our dust-based methodology has the potential to include optically thick and/or very cold H I, but we see no evidence of this and assume that all of the gas in our maps is molecular. We find total molecular gas masses of $M^{mol}_{LMC} = 6.3^{+6.3}_{-3.2} \times 10^7\ M_\odot$ and $M^{mol}_{SMC} \sim 1.3^{+1.3}_{-0.65} \times 10^7\ M_\odot$ including the estimated systematic uncertainty. The structure of the molecular gas maps show good agreement with the structure of the MAGMA ^{12}CO map in the LMC, with the main difference that more extended H_2 is seen using our dust-based method.

Chapter 3: [C II]-bright and CO-bright Molecular Gas in the SMC

3.1 Overview

Molecular clouds are the sites of the first stages of star formation. The structure of molecular clouds and the transition from atomic to molecular gas can affect what fraction of the gas participates in star formation. The effects of metallicity on the structure and properties of molecular clouds (Rubio et al. 1993a; Bolatto et al. 2008; Heyer et al. 2009; Hughes et al. 2010; Schruba et al. 2012), and the resulting effects on star formation, are not well understood due to the difficulty in observing H_2 and the molecular-to-atomic transition at low metallicity. Without knowledge of these effects, simulations of molecular clouds and star formation at low metallicity are largely unconstrained. Galaxy evolution simulations, particularly at the very early times when metallicities are low, rely on an accurate understanding of the fraction of gas available for star formation. At a metallicity of $Z \sim 1/5\ Z_\odot$ (Dufour 1984; Kurt et al. 1999; Pagel 2003) and a distance of $D \approx 63$ kpc, the Small Magellanic Cloud (SMC) provides an ideal laboratory to study the effects of low metallicity on the molecular gas and the molecular to atomic transition.

While the SMC allows us to study the conditions of the molecular gas in a low-mass galaxy, the exact three-dimensional structure of the SMC is uncertain.

Scowcroft et al. (2016) used Cepheids to trace the 3D structure of the stellar population of the SMC and found it appears to be a cylindrical shape viewed from one end with a line-of-sight depth of $\sim$ 20 kpc, consistent with other total depths estimated from Cepheids and RR Lyrae distance estimates (Subramanian & Subramaniam 2012), with the northeast being closer than the southwest. It is unclear if the gas structure follows that of the stars. Stanimirović et al. (2004) see evidence in the H I profiles of the SMC of differential rotation from a disk. Assuming the SMC neutral gas exists in a disk, Stanimirović et al. (2004) assume a scale height of 1 kpc, based on the typical sizes of large H I shells, and find an inclination angle of 40°. However, Jameson et al. (2016) report that new fitting of the H I line profiles as an inclined disk could indicate a much higher inclination angle of up to 70° Teuben et al. (2016). While we do not know the exact structure of the SMC, we are still able to use the low-metallicity environment to study the local conditions of the molecular clouds throughout the galaxy.

The transition from atomic to molecular gas occurs at the outer edges of the molecular cloud, where the shielding is lower and molecules are more easily dissociated. These edges are referred to as photodissociation regions (PDRs). Studying the molecular gas structure requires understading the distribution of H_2 from the dense cloud cores to the diffuse outer layers of the clouds. The most common tracer of molecular gas is ^{12}CO. The H_2 gas, however, is expected to be more prevalent than CO at low metallicity due to the ability of H_2 to effectively self-shield against dissociating far-UV photons. Both observations and modeling suggest that $\sim 30\% - 50\%$ of the H_2 in the Solar Neighborhood resides in a "CO-faint" phase (e.g., Grenier et

al. 2005; Wolfire et al. 2010; Planck Collaboration et al. 2011). Studies of the SMC suggest this phase to encompass $80\% - 90\%$ of all the H_2 (Israel 1997; Pak et al. 1998; Leroy et al. 2007, 2011; Bolatto et al. 2011), likely dominating the molecular reservoir available to star formation.

In regions where CO is photo-dissociated, the carbon is present as neutral carbon, C^0, and singly ionized carbon, C^+. Given the CO dissociation energy of 10.6 eV and the C ionization potential of 11.3 eV, a large fraction of the carbon will be ionized throughout the interstellar medium (ISM). The [C II] 158 μm line (arising from the $^2P^0_{3/2} \rightarrow ^2 P^0_{1/2}$ fine structure transition), with an energy above ground of $\Delta E/k = 91$ K, originates from the "CO-faint" H_2 gas as well as the neutral atomic and ionized gas. The [C II] line thus offers the potential to estimate the amount of molecular gas not traced by bright CO emission, particularly in low metallicity environments where a significant fraction of the H_2 may not be traced by bright CO emission: after removing the contributions to [C II] from atomic and ionized gas, the remaining emission can be attributed to molecular gas. To then convert the [C II] emission to a molecular gas column density requires some knowledge of the conditions of the gas (namely volume density and temperature, which determine the [C II] excitation). Early [C II] observations of low metallicity environments from the *Kuiper Airborne Observatory* have shown bright emission and high [C II]/CO ratios that are best explained by a significant amount of H_2 not traced by CO emission in star-forming regions of the Magellanic Clouds (Poglitsch et al. 1995; Israel et al. 1996; Israel & Maloney 2011) and IC 10 (Madden et al. 1997). Even at higher metallicity in the Milky Way, spectral decomposition of the [C II] line using the

GOT C+ survey shows that molecular gas not associated with bright CO emission (called "CO-dark" or "CO-faint" molecular gas) accounts for $\sim 30\%$ of the total molecular mass (Pineda et al. 2013).

To estimate the total amount of molecular gas we need both [C II] and CO observations: the [C II] emission traces the molecular gas at low A_V into the PDR, while the CO emission traces the remaining molecular gas at high A_V. The Magellanic Clouds have been studied extensively in CO with the first major survey completed by Israel et al. (1993) using the Swedish-ESO Submillimetre Telescope (SEST). Since then, several surveys have taken place in the SMC (Rubio et al. 1993a; Mizuno et al. 2001; Muller et al. 2010). Their typical angular resolution of $\sim 30''$ (~ 10 pc), however, make it difficult to use them to study individual star-forming regions.

In this study, we present new *Herschel* far-infrared line observations, including Photoconductor Array Camera and Spectrometer (PACS) [C II] and [O I] observations, from the *Herschel* Spectroscopic Survey of the SMC (HS^3), together with new ALMA *Morita-san* Compact Array (ACA) ^{12}CO, ^{13}CO, and C^{18}O observations of the Southwest Bar of the SMC, all at a resolution of $\sim 5-10''$ ($\sim 1.5-3$ pc). The ACA resolution is similar to that of the PACS spectroscopy, which allows us to produce estimates of molecular gas from [C II] and CO at comparable resolutions and investigate how the "[C II]-bright" molecular gas relates to the "CO-bright" molecular gas at low metallicity.

In Section 5.2 we describe the details of the HS^3 and ALMA SMC observations and data reduction, as well as ancillary data used for this study. We present the main

Table 3.1. HS^3 [C II] and [O I] Map Properties

Region	Center Position R. A. (J2000)	Dec. (J2000)	Size	P. A.	1σ Uncertainty (10^{-9} W m^{-2} sr^{-1}) [C II]	[O I]
SWBarS	00h45m27.1s	-73d21m00.0s	$1.7' \times 6.1'$	10°	1.2	4.1
N22	00h47m58.103s	-73d16m52.13s	$1.7' \times 6.1'$	20°	1.4	3.5
SWBarN	00h48m26.882s	-73d06m04.36s	$1.7' \times 6.1'$	145°	1.5	3.9
SWDarkPK	00h52m23.7s	-73d14m49.0s	$1.2' \times 1.2'$	48°	1.3	3.4
N83	01h14m19.280s	-73d15m09.04s	$1.7' \times 8.0'$	30°	1.4	3.5

Table 3.2. HS^3 [N II] and [O III] Map Properties

Region	Center Position R. A. (J2000)	Dec. (J2000)	Size	P. A. [N II]	[O III]	1σ Uncertainty (10^{-9} W m^{-2} sr^{-1}) [N II]	[O III]
SWBarS	00h45m21.85s	-73d22m49.36s	$1.5' \times 1.5'$	75°	10°	0.34	2.8
N22	00h47m54.35s	-73d17m27.69s	$1.5' \times 1.5'$	65°	40°	0.36	2.8
SWBarN	00h48m26.30s	-73d06m04.28s	$1.5' \times 1.5'$	75°	55°	0.27	2.4
SWDarkPK	00h52m56.11s	-73d12m17.25s	$1' \times 1'$	55°	40°	0.33	2.8
N83	01h14m03.28s	-73d17m06.81s	$1.5' \times 1.5'$	50°	65°	0.29	3.0

results of the two surveys in Section 5.4. Our methodology to estimate molecular gas using [C II] and ^{12}CO emission is described in Section 3.4. We discuss the results of our new molecular gas estimates in Section 5.5, including a comparison to previous dust-based estimates and converting our estimates to CO-to-H_2 conversion factor values to compare to models and simulations of molecular clouds at low metallicity. Finally, Section 5.6 summarizes our work and outlines the main conclusions of this study.

3.2 Observations

3.2.1 The Herschel Spectroscopic Survey of the SMC

The *Herschel* Pilbratt et al. (2010) Spectroscopic Survey of the SMC (HS^3) map the key far-infrared (far-IR) lines of [C II] 158 μm, [O I] 63 μm, [O III] 88 μm, and [N II] 122 μm with the PACS spectrometer Poglitsch et al. (2010) and obtain Spectral and Photometric Imaging Receiver (SPIRE, Griffin et al. 2010) Fourier Transform Spectrometer (FTS) observations (that include [N II] 205 μm) in five regions across the SMC with varying star formation activity and ISM conditions. These targets were covered using strips oriented to span the range from the predominantly molecular to the presumably atomic regime. The strips are fully sampled in [C II] and [O I], while only a few pointings where observed for [N II] and [O III].

The HS^3 targeted regions with a range of star formation activity, overlapping with the *Spitzer* Spectroscopic Survey of the SMC (S^4MC; Sandstrom et al. 2012) whenever possible, and spanning a range of "CO-faint" molecular gas fraction using dust-based molecular gas estimates Bolatto et al. (2011) going from the peaks out to the more diffuse gas. The main survey covers 5 star-forming areas which we refer to as 'N83' (also includes N84), 'SWBarN' (covers N27), 'SWBarS' (covers N13), 'N22' (also include N25, N26, H36, and H35) and a smaller square region called 'SWDarkPK' that covers a region with a dust-based peak in the molecular gas without any associated CO emission as seen in the NANTEN ^{12}CO map (Mizuno et al. 2001). The 'N' numbered regions refer to H II regions from the catalog by

Henize (1956), and the 'H' numbered regions are from the catalog of Hα structures by Davies et al. (1976).

The [C II] and [O I] maps are strips that encompass the peaks in CO, star formation, and "CO-faint" H_2 as traced by dust. Using the PACS spectrometer $47'' \times 47''$ field of view, the strips were sampled using rasters with sizes $33'' \times 11$ ([C II]) and $24'' \times 15$ ([O I]) by $23.5'' \times 3$. Both [O III] and [N II] observations were targeted at the location of the main ionizing source in each region and sampled with $23.5'' \times 2$ by $23.5'' \times 2$ raster. The PACS maps used the unchopped scan mode with a common absolute reference position placed south of the SMC "Wing" and observed at least once every two hours. The PACS spectrometer has a beam FWHM of $\theta \sim 9.5''$ at the wavelength for [O I] (63 μm), [O III] (88 μm), $\theta \sim 10''$ at [N II] (122 μm), and $\theta \sim 12''$ at [C II] (158 μm), which have corresponding spectral resolutions of $\sim$ 100, 120, 320, and 230 km s^{-1} (Poglitsch et al. 2010). Tables 3.1 and 3.2 list the positions and uncertainties for all the PACS spectroscopy line images. The SPIRE FTS observations were "intermediate sampling" single-pointing at high resolution at the star-forming peak, which is typically close to the peak in ^{12}CO, for the N83, SWBarN, SWBarS, N22 regions. In addition to the main survey regions FTS observations, one single-pointing covered the brightest H II region N66, which has PACS [C II] and [O I] observations as part of Guaranteed Time Key Project SHINING and is included in the *Herschel* Dwarf Galaxy Survey (DGS; Madden et al. 2013).

3.2.1.1 Data Reduction

PACS spectral observations were obtained in the Un-Chopped mapping mode and reduced using the Herschel Interactive Processing Environment (HIPE) version 12.0.2765 (Ott 2010). Reductions applied the standard spectral response functions, flat field corrections, and flagged instrument artifacts and bad pixels (see Poglitsch et al. 2010; Croxall et al. 2012). The dark current, determined from each individual observation, was subtracted during processing as it was not removed via chopping. *Herschel's* baseline exhibits significant baseline drifts and distinctive instrumental transients are common occurrences. These instabilities result in a variable non-astrophysical continuum, which is dominated by emission from *Herschel* itself.

Transient signals are strongly correlated with motions of the PACS grating and of *Herschel*. Using fits of the Draine & Li (2007) dust model to spectral energy distributions of galaxies in the KINGFISH sample we estimate the expected astrophysical continuum is less than 2% of the spectral continuum detected at [C II] 158μm. Given that the other spectral lines were located farther from the peak of the dust-continuum than the [C II] line, we assume that thermal dust emission is undetected in the PACS spectra. Thus, the continuum adjacent to the expected locations of the observed fine-structure-lines should be constant and is used to correct for transients. This has significantly improved our ability to detect line emission.

The averages of the clean off-observations obtained were subtracted from observations to correct for the thermal background contributed by *Herschel*. Subsequently, all spectra within a given spatial element were combined. Final spectral

Table 3.3. ALMA ACA+TP Map Properties

Region	Map Center R. A. (J2000)	Dec. (J2000)	Map Size	P. A.
SWBarS	00h45m24.54s	-73d21m42.63s	$2.3' \times 3.5'$	10°
N22	00h47m54.28s	-73d17m46.76s	$2.3' \times 3.5'$	20°
SWBarN	00h48m15.53s	-73d04m56.41s	$2.3' \times 3.5'$	145°
SWDarkPK	00h52m56.07s	-73d12m17.08s	$3' \times 3'$	48°

cubes with 2.06″ spatial pixels were created by combining individual pointings using the Drizzle algorithm implemented in HIPE. In-flight flux calibrations[1] were applied to the data. These calibrations resulted in absolute flux uncertainties on the order of 15% with relative flux uncertainties between each *Herschel* pointing on the order of ∼10%.

The long and short wavelength SPIRE-FTS arrays (FWHMs of 34″ and 19″, respectively) are arranged in concentric circles and are dithered 4 times to provide complete coverage of the mapped region. The FTS data reduction started with level 0.5 data, which was temperature drift corrected, detector clipped, and time shift corrected using HIPE (version 12). A semi-extended-source correction Wu et al. (2013) was applied to the individual bolometer (level 1) data before mapping. Spectral cubes are produced using the corrected bolometer fluxes.

Table 3.4. ALMA ACA+TP Map Properties (continued)

Region	$\theta_{maj}('') \times \theta_{min}('')$			RMS (K)		
	^{12}CO	^{13}CO	C^{18}O	^{12}CO	^{13}CO	C^{18}O
SWBarS	6.60×6.06	6.92×6.05	6.76×6.18	0.17	0.16	0.10
N22	6.39×5.56	6.59×5.83	7.01×6.41	0.24	0.22	0.13
SWBarN	7.08×5.74	7.25×5.33	7.40×5.66	0.12	0.16	0.08
SWDarkPK	6.95×5.55	8.39×5.63	7.42×5.72	0.18	0.16	0.10

3.2.2 ALMA Survey of the Southwest Bar

We mapped four regions in the Southwest Bar of the SMC in ^{12}CO, ^{13}CO, and C^{18}O $(2-1)$ using Band 6 of the ALMA Atacama Compact Array (ACA; 7m-array consisting of 11 antennas) and Total Power array (TP; 12m single-dish) during Cycle 2. Three of these regions were previously mapped in ^{12}CO and ^{13}CO $(2-1)$ using the Swedish ESO-Submillimeter Telescope (SEST) (Rubio et al. 1993a,b, 1996), but at a resolution of $22''$. The ACA maps were observed using a mosaic with $22.1''$ spacing of 47 pointings for the N22, SWBarS, and SWBarN regions and 52 pointings for the SWDarkPK with 25.5 s integration time per pointing. Both ^{12}CO and ^{13}CO were observed with 117.2 MHz (152 km s^{-1}) bandwidth and 121.15 kHz (0.2 km s^{-1}) spectral resolution. We chose a somewhat broader bandwidth for C^{18}O of 468.8 MHz (642 km s^{-1}) and corresponding 0.24 MHz (0.3 km s^{-1}) spectral resolution, and used the fourth spectral window for continuum (1875.0 MHz bandwidth, 7.81 MHz resolution). During the early ALMA cycles the fast-mapping capabilities of the array are fairly limited, and so we decided to cover only half of the strips mapped by

[1]Calibration Version 65

HS[3]. The coverage of the maps overlaps approximately with the main CO emission known to be present in the strips, except for SWDarkPK where the PACS map is small and we covered its entire area.

We use the Common Astronomy Software Applications (CASA) package version 4.2.2 to reduce, combine, and image the data. After creating the reduced measurement set using the script provided with the delivered ACA data, we clean the ACA data and image it using the TP image as the model image in clean. Due to the short integration times and the arrangement of the 7m-array, we use conservative masks for cleaning to reduce the effects of the poor $u-v$ coverage of the ACA-only data. The data are imaged at 0.3 km s^{-1} spectral resolution and synthesized beam sizes of $\sim 7'' \times 5.5''$ (2.1 pc $\times$ 1.7 pc) for ^{12}CO $(2-1)$. The previously published single-dish SEST ^{12}CO $(2-1)$ data from Rubio et al. (1993a) overlaps with the SWBarN region, which they refer to as LIRS49. They found a peak temperature of 2.56 K in a $43''$ beam at $\alpha(1950) = 00:46:33$, $\delta(1950) = -73:22:00$ and we find a peak temperature of 2.55 K in the same aperture in the SWBarN ACA+TP data when convolved to $43''$ resolution. The combination of the ACA and TP data make the observations sensitive to all spatial scales. The positions, beam sizes, and sensitivities of the observations are listed in Table 3.3.

3.2.3 HI Data

The neutral atomic gas data come from 21 cm line observations of H I. We use the H I map from Stanimirović et al. (1999) that combined Australian Telescope

Compact Array (ATCA) and Parkes 64m radio telescope data. The interferometric ATCA data set the map resolution at $1'$ ($r \sim 20$ pc in the SMC), but the data are sensitive to all size scales due to the combination of interferometric and single-dish data. The observed brightness temperature of the 21 cm line emission is converted to H I column density ($N_{\rm H\,I}$) assuming optically thin emission. The observed brightness temperature of the 21 cm line emission is converted to H I column density ($N_{\rm H\,I}$) using:

$$N_{\rm H\,I} = 1.823 \times 10^{18} \frac{\rm cm^{-2}}{\rm K\ km\ s^{-1}} \int T_B(v)\ {\rm d}v\,.$$

The SMC map has an RMS column density of 5.0×10^{19} cm^{-2}.

3.2.4 Additional Data

We use mid-infrared data for the SMC from *Spitzer* both IRAC and MIPS as part of the SMC-SAGE (Gordon et al. 2011) and S^{3}MC (Bolatto et al. 2007) surveys and spectroscopic *IRS* data, particularly H_2 rotational lines, from the S^{4}MC (Sandstrom et al. 2012) survey. The maps of the H_2 rotational line images were produced by fitting and removing the baseline near the line and then calculating the total line intensity. We also use a velocity-resolved [C II] spectrum from SOFIA GREAT heterodyne instrument (Heyminck et al. 2012) from the SMC survey presented in Herrera-Camus et al. (2016b).

Since the ALMA Survey focuses on the Southwest Bar of the SMC, there is no comparable map of CO from ALMA for N83. However, there are new APEX maps of ^{12}CO $(2-1)$ that overlap the N83 HS^3 region (PI: Rubio). We use the

APEX data for the N83 region to be able to make similar comparisons to the HS3[3] data, but note the lower resolution ($\sim 25''$) limits the analysis. To do this, we take the additional step of convolving and re-gridding the *Herschel* spectroscopic maps ([O I], [C II]) to match that of the APEX ^{12}CO $(2-1)$ map.

3.2.5 Estimating A_V

We investigate the structure of the photodissociation region and molecular cloud by using the visual extinction (A_V) as an indicator of the total column through the cloud, and as means to gauge the depth within the cloud associated with the observations. To match the high resolution of the [C II], [O I], and ALMA CO data, we use the optical depth at 160 μm (τ_{160}) and the HERITAGE 160 μm map of the SMC (Meixner et al. 2013) as the basis for producing a map of A_V. Lee et al. (2015) fit a modified blackbody with $\beta = 1.5$ to the SMC HERITAGE 100 μm, 160 μm, 250 μm, and 350 μm data for the SMC. We resample their map of fitted dust temperatures at the lower resolution of the 350 μm *Herschel* map ($\sim 30''$) to the higher resolution 160 μm map ($\sim 12''$) in order to estimate τ_{160} at a resolution comparable to the [C II] and ALMA CO maps. We convert from τ_{160} to A_V using $A_V \sim 2200\tau_{160}$ from Lee et al. (2015), which is based on measurements in the Milky Way and provides similar A_V values as those found using UV/optical and NIR color excess methods (see Figure 1 in Lee et al. 2015).

3.3 Results

We present the first high resolution imaging ($\sim 10''$ ~ 3 pc) of a suite of far-IR cooling lines from the *Herschel* Spectroscopic Survey of the SMC (HS^3) and CO from the ALMA ACA in the SMC. [C II] and [O I] lines were detected in all of the regions targeted, and [C II] is detected throughout all of the regions. The ALMA ACA+TP data shows clear detections of ^{12}CO and ^{13}CO $(2-1)$ emission in all of the regions, but C^{18}O is not detected. In this section we discuss the comparison of the [O I], [C II], and ^{12}CO emission.

3.3.1 [C II] and [O I]

The [C II] 158 μm dominates the cooling of the warm ($T \sim 100$ K) neutral gas because of the high carbon abundance, its lower ionization potential of 11.26 eV, and its excitation temperature of 92 K. Ionized carbon, C^+, exists throughout most phases of the ISM except in the dense molecular gas where most of the carbon is locked in CO. The [O I] 63 μm line also contributes to the gas cooling, but with an excitation temperature of 228 K and a high critical density ($\sim 10^5$ cm^{-3}), this line dominates over the [C II] emission only in the densest gas. Indeed, the bright "blue" knots of [O I] emission in Fig. 3.1 are coincident with bright knots of Hα emission (in black contours) associated with very recent massive star formation in dense and presumably warm structures bathed by intense radiation. In warm PDRs subjected to radiation fields larger than 10^3 Habings and due to the difference in critical densities, the [O I] to [C II] ratio is a good indicator of density, but in colder

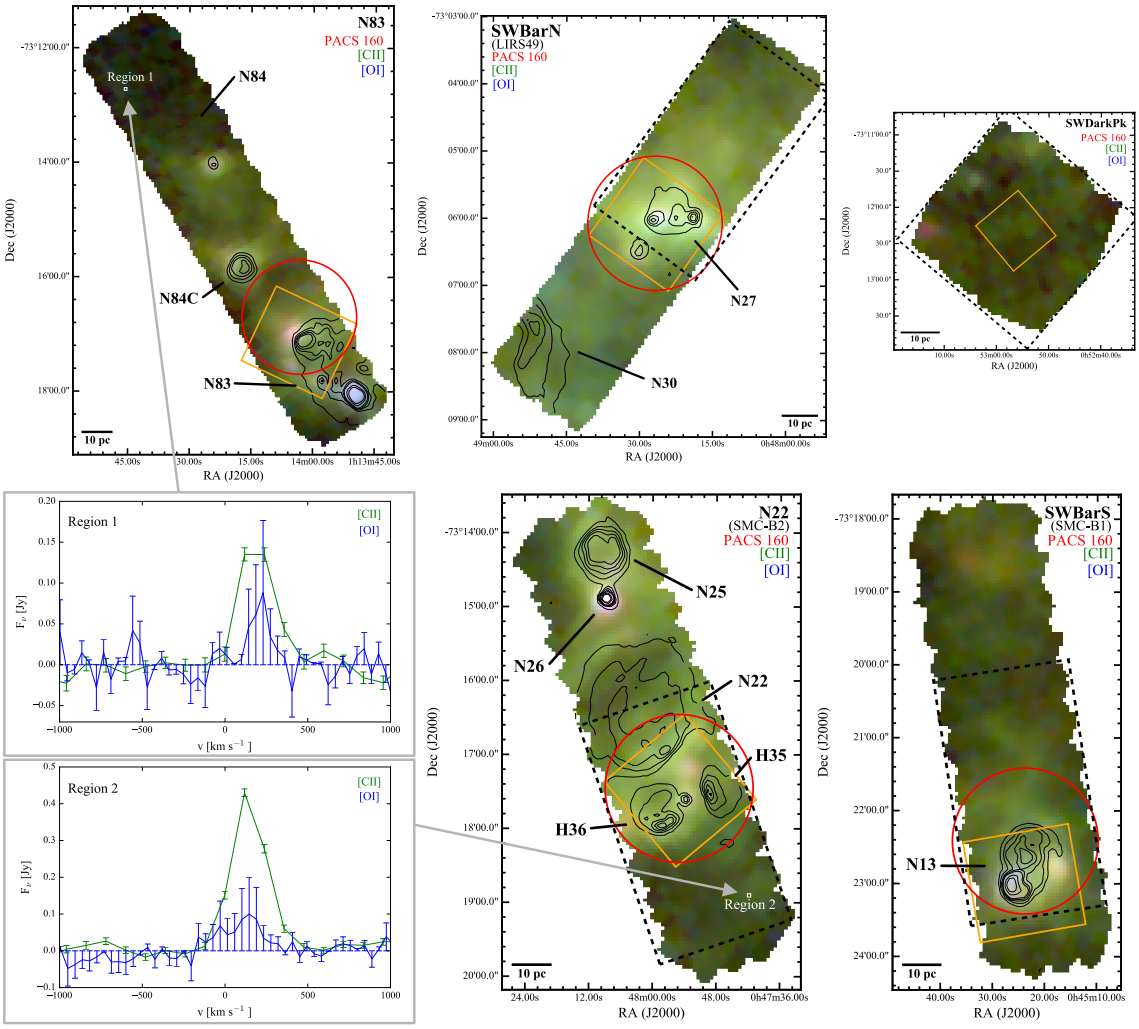

Figure 3.1 RGB composites of the five HS^3 regions. The [C II] (green) and [O I] (blue) are on the same intensity scale from 0 to 3×10^{-7} W m^{-2} sr^{-1}, whereas the PACS 160 μm image (red) is shown on a scale from 0 to 2×10^{-5} W m^{-2} sr^{-1}. All images are displayed using a logarithmic stretch. The black contours show MCELS Hα intensity (Smith & MCELS Team 1999) at linear intervals (1, 2, 3, 4, 5, 10, 15 10^{-14} ergs cm^{-2} s^{-1}) to show the location of massive star formation throughout the regions with the region designations based on Hα from Henize (1956) and Davies et al. (1976) indicated. The names of overlapping regions from Rubio et al. (1993a,b, 1996) SEST surveys are listed in parentheses. The orange squares show the coverage of the [O III] observations ([N II] has approximately the same coverage) and the red circles show the area covered by the FTS observations. The black dashed line rectangles show the approximate coverage of the ALMA maps. The two inset spectra, labeled Region 1 and 2, show spectral extractions from the PACS cube in some of the faintest regions covered by the strips. We clearly detect [C II] emission throughout the faint areas and, somewhat unexpectedly, also [O I] 63 μm.

gas and particularly below $n \lesssim 10^4\,\mathrm{cm}^{-3}$ it is mostly sensitive to temperature and the incident radiation field (e.g., Kaufman et al. 1999).

Figure 3.1 shows the [O I] and [C II] integrated intensity images in combination with the 160 μm PACS image showing dust continuum emission. The differences in the local star formation, shown by Hα in black contours, produce different structures and varying intensities of [C II], [O I], and dust emission. In many faint regions in the diffuse gas the [O I] line is detected (see inset spectra in Figure 3.1). In principle it is possible for [O I] 63 μm to be a very important coolant for the warm neutral phase (WNM) of the ISM (Wolfire et al. 1995, 2003). Despite the high critical density of this transition, the high temperature of the WNM excites [O I] making it an efficient coolant even in $n \sim 1\,\mathrm{cm}^{-3}$ gas.

A challenge with interpreting velocity unresolved observations of [O I] 63 μm, such as ours, is the potential effect of self-absorption or absorption from cold gas along the line of sight, a phenomenon originally identified through anomalous [O I] 145 μm to 63 μm integrated line ratios. Indeed some Milky Way massive star-forming regions show significant self-absorption and absorption by foreground cold clouds containing O^0 in velocity-resolved observations of [O I] (Poglitsch et al. 1996; Leurini et al. 2015). It is unknown how widespread this phenomenon is in the SMC, where 145 μm observations do not exist and velocity-resolved observations are very limited.

In the Milky Way heavy [O I] self-absorption is usually accompanied by [C II] absorption. There is no indication of absorption in recent [C II] velocity-resolved profiles (Requena-Torres et al. 2016; Herrera-Camus et al. 2016b), and no clear ev-

idence of self-absorption in [O I] velocity-resolved profiles (Y. Okada, private communication) in the star-forming regions N25 (located in the north end of the HS[3] "N22" region), N66, and N88 in the SMC. Given the high radiation fields and low A_V throughout much of the SMC, this suggests that in the SMC there is a dearth of high A_V cold material that may absorb [O I] along the line of sight, while absorption contamination is likely more common in the Milky Way (e.g., Leurini et al. 2015). As mentioned above, another indicator of optical depth or absorption in the [O I] 63 μm line is anomalously high [O I] 145 μm to 63 μm ratios (Stacey et al. 1983). While there are no *Herschel* PACS observations of [O I] 145 μm in the SMC, three regions were observed in [O I] 145 μm to 63 μm in the LMC Cormier et al. (2015). Only one of these regions, N159 (the site of the brightest CO emission in the LMC; Israel et al. 1993), has a high 145 μm to 63 μm ratio of 0.11, which is not much higher than the theoretical limit of 0.1 for the expected ratio for optically thin emission for $T > 300$ K (Tielens & Hollenbach 1985). If the line were self-absorbed in our observations, we would expect to see lower [O I]/[C II] ratios in high density regions at higher A_V, but we see the opposite. We conclude that it is unlikely that the [O I] 63 μm line is significantly affected by absorption in our SMC observations.

What is the origin of the observed [C II] emission? Figure 3.2 shows the integrated intensity ratio of [O I] to [C II]. The observed ratio is approximately constant with a value of [OI]/[CII] $\sim$ 0.3. This is also the typical value observed in the disks of the KINGFISH sample of nearby galaxies (Herrera-Camus et al. 2015). Using the [C II] and [O I] cooling curves calculated for diffuse gas under SMC conditions (Wolfire et al. 2016), a ratio [OI]/[CII] $\sim$ 0.3 is indicative of densities of $\sim$

$10^2 - 10^3$ cm^{-3}, which are consistent with dense CNM and/or molecular gas. Figure 4.4 shows the similarity between the mid-infrared H_2 S(0) quadrupole rotational line at 28.8 μm and the [C II] emission. This clearly demonstrates that molecular gas is associated with the [C II]-emitting material, strongly suggesting that most of the [C II] emission in our mapped regions has a PDR origin and it arises from the surfaces of molecular clouds.

3.3.2 [N II] and Contribution from Ionized gas

The HS^3 data set includes sparsely sampled FTS spectra for the SWBarN, SWBarS, N22, and N83 regions, as well as a pointing towards the most active star-forming region in the SMC, the giant HII region N66. In Figure 3.4 we show the long wavelength array (SLW) spectra in red and the short wavelength array (SSL) in blue with the positions of the ^{12}CO, [C I], and [N II] lines indicated. We see clear detections of the lower rotational transitions of ^{12}CO and the [N II] 205 μm lines, as well as weak detections of [C I].

We do not detect the [N II] 122 μm line in any of the regions, while the [N II] 205 μm line is detected in all regions in the FTS spectra (see Figure 3.4). Because the ionization potential of nitrogen of 14.5 eV is higher than hydrogen, ionized nitrogen traces the ionized gas. The [N II] 122 μm and 205 μm lines result from the fine-structure splitting of the ground state of ionized nitrogen and are primarily excited by collisions with electrons. Their critical densities differ and the ratio can be used to estimate the electron density (n_e). The [N II] 122 μm line has a higher

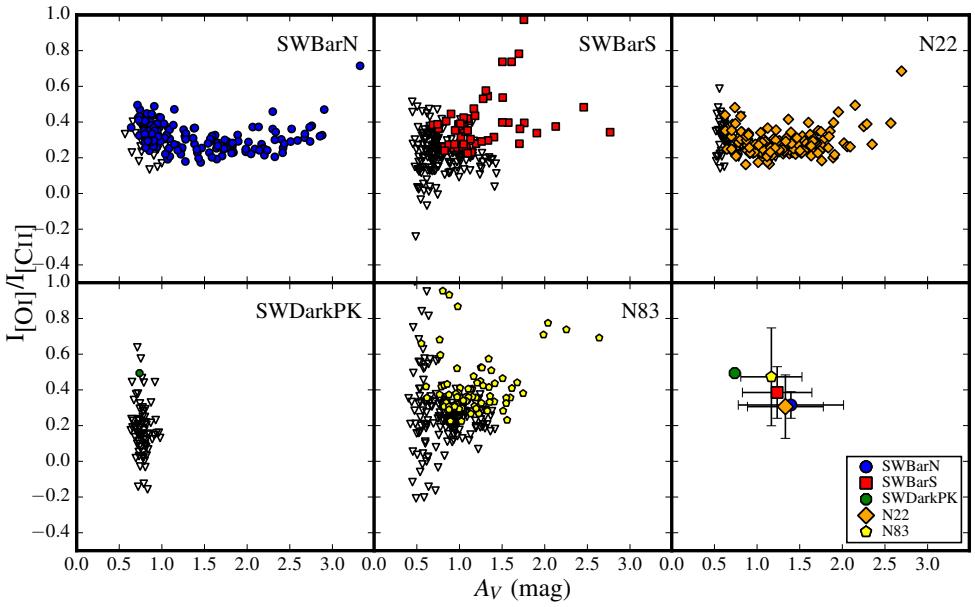

Figure 3.2 The ratio of the integrated intensity of [O I] to that of [C II] as a function of A_V for the HS^3 regions. The colored symbols show independent measurements detected at $> 3\sigma$ in both [O I] and [C II] with the downward pointing triangles indicating upper limits (where $I_{[OI]} < 3\sigma$). The bottom right panel shows the average values with the error bars showing 1σ on mean for each of the regions except for SWDarkPK, for which we show the one measurement $> 3\sigma$. The [O I]/[C II] ratio is mostly constant across the regions and independent of A_V and has a typical value of ~ 0.3.

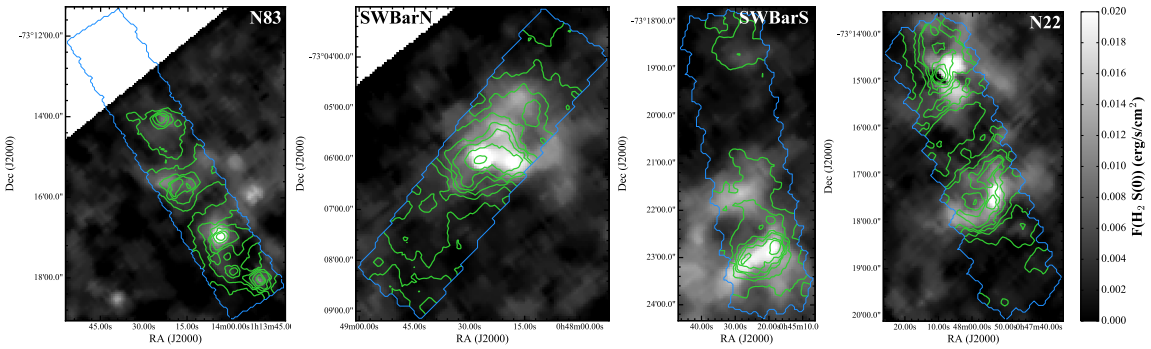

Figure 3.3 Images of the H_2 S(0) 28.2 μm line from S^{4}MC (Sandstrom et al. 2012) resampled to match the HS^3 [C II] images. Contours show the [C II] integrated intensity at levels of 0.3, 0.5, 0.7, 0.9, 1.2, 1.5, 2.0, 3.0×10^{-7} W m^{-2} sr^{-1}, with the blue line showing the [C II] map coverage. The excellent correspondence between the structures provides evidence that [C II] is tracing the molecular gas in the PDRs.

critical density for collisions with electrons ($n_e \sim 300$ cm^{-3}) compared to the 205 μm line, which has a critical density similar to that for exciting the [C II] 158 μm line with collisions with electrons. Thus the ratio of [C II]/[N II] 205 μm in ionized gas is independent of density, and it depends only on the relative abundances of the ions which are likely similar to the elemental abundances.

The sensitivity of the [N II] 122 μm observations is $\sim 3 \times 10^{-10}$ W m^{-2} sr^{-1}, while the range of detected [N II] 205 μm intensities is $\sim 2 - 5 \times 10^{-10}$ W m^{-2} sr^{-1}. Based on these measurements, the [N II] 122/205 ratio is $\lesssim 1$ in regions where the [N II] 205 μm line is detected. Using the the electron collision strengths from Tayal (2011), this translates to an upper limit to the electron density of $n_e \sim 20$ cm^{-3}. In other words, our measurements are consistent with a relatively low density for the

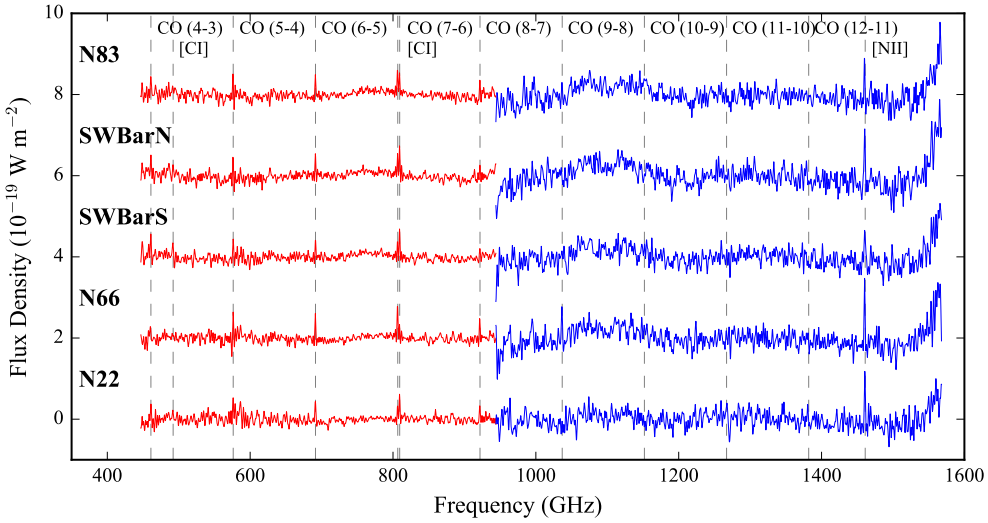

Figure 3.4 FTS SLW (red) and SSW (blue) spectra averaged over all the bolometers for HS^3 regions SWBarN, SWBarS, N22, and N83, plus N66 (the target of PACS observations from the *Herschel* GTKP SHINING project) with each spectra being offset by 2×10^{-19} W m^{-2} sr^{-1}. The SLW and SSW spectra have a second-order polynomial fit and subtracted to remove the baseline. The grey dashed lines indicate the positions of possible spectral lines. There are no detections of the CO ladder in the SSW except for CO (9–8) in N66, which also displays CO (8–7) in the SLW, showing that gas associated with the molecular complex in this giant H II region is warm and highly excited.

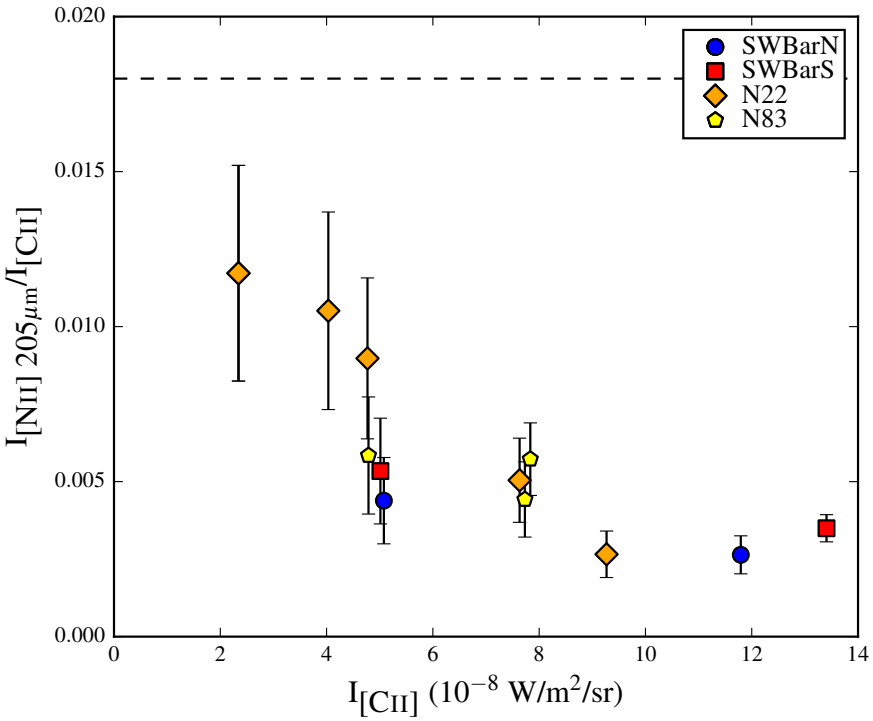

Figure 3.5 Ratio of integrated intensities of [N II] 205 μm ($I_{[NII]\ 205\mu m}$) to [C II] ($I_{[CII]}$) as a function of the [C II] intensity for FTS bolometer measurement of [N II] 205 μm that is $> 3\sigma$ for each of the regions. The error bars show the 1σ uncertainty on the line ratio, which is dominated by the uncertainty in the [N II] 205 μm flux (the uncertainty in $I_{[CII]}$ is smaller than the symbols). The FTS pointings for each of the regions targeted the star-forming peak, which tends to coincide with the peak CO emission. The ratios are low and naturally peak towards higher values at lower [C II] intensities. The black dashed line shows the lowest observed ratio of [NII] 205 μm/[CII] ~ 0.018 in the KINGFISH sample (Croxall et al. 2016).

ionized material, somewhat lower than the mean ionized gas density observed in the KINGFISH sample of galaxy disks of $n_e \sim 30\,\mathrm{cm}^{-3}$ (Herrera-Camus et al. 2016a).

In Figure 3.5, we show the [N II] 205 μm/[C II] ratio for all of the pointings where [N II] 205 μm is detected at $> 3\sigma$, and where the [C II] intensity found for the central FTS bolometer position after convolving the map to the FTS resolution ($\sim 17''$). We see that the [N II] 205 μm emission ranges from 0.2%$-$1.2% of the [C II] emission. For carbon emission arising from ionized gas with a ratio $C^+/N^+ \approx C/N$ similar to Galactic we would expect a [N II] 205 μm/[C II]$\sim$ 0.2, mostly independent of density due to the similarity in the critical densities (Tayal 2008, 2011). Because the [N II] emission can only arise from ionized gas, the fact that we measure over $\sim$ 20 times fainter [N II] relative to [C II] suggests that the contribution of ionized gas to the latter is at most 5%.

These ratios represent the maximum ratios throughout the regions since the FTS observations targeted the bright CO emission, which tend to be near H II regions, and as such will have the highest fraction of [C II] emission arising from ionized gas. The observed [N II] 205μm/[C II] ratios are lower than the typical values found in the KINGFISH survey of 0.057 (Croxall et al. 2016). Similarly, Cormier et al. (2015) find depressed [N II] 122 μm/[C II] in dwarf galaxies, suggesting that ionized gas only produces a small fraction of the [C II] emission in low metallicity environments.

3.3.3 [O III] and Highly Ionized Material

The [O III] 88 μm line traces ionized gas as the second ionization potential of oxygen is $\sim$ 35 eV, much higher than hydrogen. HS[3] obtained [O III] observations toward the dominant HII region in each strip. We observe bright [O III] emission from all of these pointings. Figure 3.6 shows the [O III]/[C II] ratios for the SMC regions, which reach as high as [OIII]/[CII] $\sim$ 4. Observations of the [O III]/[C II] ratio for higher metallicity galaxies based on ISO data presented by (Brauher et al. 2008) found lower ratios that ranged from [OIII]/[CII] $\sim 0.1 - 1.5$. The higher values in the SMC are similar to the ratios found for dwarf galaxies observed with *Herschel* PACS as part of the Dwarf Galaxy Survey (DGS) with a median and range of [OIII]/[CII] $= 2.0^{13.0}_{0.52}$ (Cormier et al. 2015). These comparisons to measurements in other galaxies should be tempered somewhat by the fact that the SMC observations are pointings toward H II regions obtained at high spatial resolution, while the comparison work typically samples larger scales and therefore a mix of ionized and neutral material. The critical density for [N II] 122 μm line is similar to [O III], but the [O III] ionization potential is much higher as is the energy above ground for excitation. Cormier et al. (2015) suggest that the hard radiation fields found at lower metallicity in dwarf galaxies could explain the high [O III] emission. Note that we failed to detect [N II] 122 μm emission toward these same pointings. A combination of hard radiation fields and low density ionized gas may explain the high [O III] to [N II] 122 μm ratios present in the SMC.

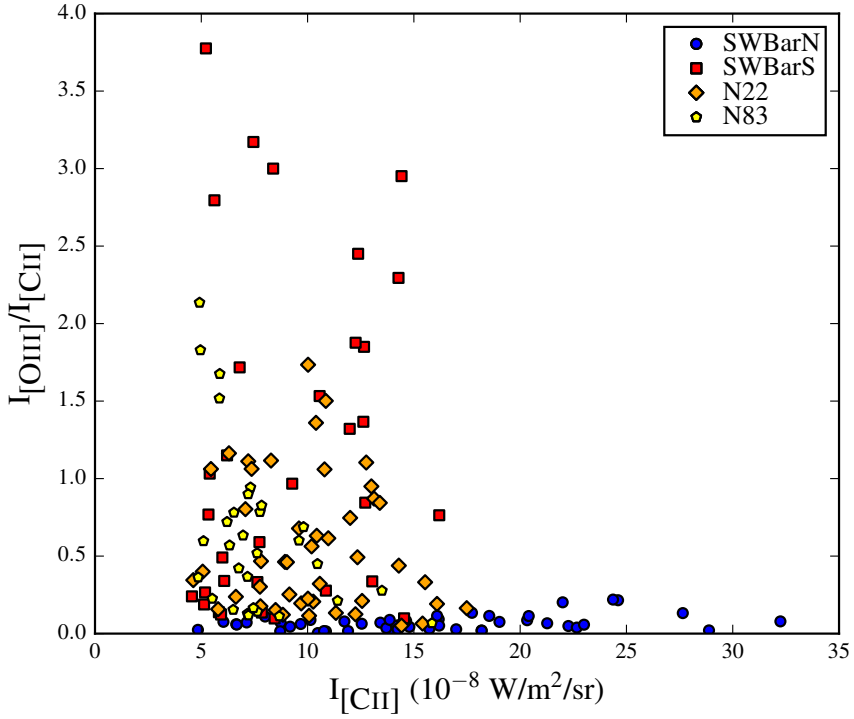

Figure 3.6 Ratio of integrated intensities of [O III] 88 μm ($I_{[OIII]}$) to [C II] ($I_{[CII]}$) as a function of the [C II] intensity where [O III] is detected at $> 3\sigma$ for each of the regions. The [O III] maps cover the main H II regions in the HS^3 regions. We see high $I_{[OIII]}/I_{[CII]}$ ratios in all of the regions except SWBarN where there is no large H II region and likely less ionized gas.

Table 3.5. ALMA CO Properties

Region	$\Delta v_{\rm LSR}$ (km s^{-1})	T_{peak} (K)[a]		Map Sensivity (K km s^{-1})[b]		
		^{12}CO	^{13}CO	^{12}CO	^{13}CO	C^{18}O
SWBarS	104 – 133	18.6	4.9	2.1	1.7	1.2
N22	113 – 133	15.9	2.6	2.1	2.4	1.0
SWBarN	104 – 140	14.6	4.3	1.8	2.2	1.2
SWDarkPK	137 – 160	12.1	3.0	1.9	1.8	1.3

[a]in 0.3 km s^{-1} channels

[b]defined as $3 \times RMS$ away from line emission

3.3.4 High Resolution Molecular Gas: ^{12}CO and ^{13}CO

We mapped and detected ^{12}CO and ^{13}CO $(2-1)$ in all of the regions targeted by ALMA, shown in Figure 3.7. We do not detect C^{18}O with our current observations, which had the minimum integration time allowed per pointing to increase the coverage of the mosaics. Despite the lower metallicity and less dust-shielding, ^{12}CO and ^{13}CO form and emit brightly in small clumps. Our high resolution ALMA ACA data show that the bright CO emission is found in small structures, which were mostly unresolved by previous observations. For most of the regions, a large fraction of the flux comes from the high resolution ACA maps. In the SWBarS and SWBarN regions, the ACA flux represents $\sim 60\%$ of the flux in the combined ACA+TP ^{12}CO maps. In the SWDarkPK, nearly 100% of the flux is from the high resolution imaging, whereas in the N22 region most of the emission is diffuse with only $\sim 30\%$ of the flux found at high resolution. The higher fraction of diffuse ^{12}CO emission in N22, less in SWBarS and SWBarN, and none in SWDarkPK is likely due

to their varying evolutionary stages: N22 is the most evolved region with multiple large H II regions around the CO emission, SWBarS and SWBarN both are actively forming stars and have one prominent H II region, and SWDarkPK has no signs of active star formation.

Figure 3.8 shows the comparison between the ^{12}CO and ^{13}CO $(2-1)$ emission. We find average ^{12}CO/^{13}CO $(2-1)$ ratios of $\sim 5-7.5$ (in units of K km s^{-1}). These ratios are consistent with previous measurements in the SMC toward emission peaks (Israel et al. 2003) and in nearby galaxies (e.g., Paglione et al. 2001; Krips et al. 2010). In the Milky Way the ratios are similar to what we obtain for the SMC, with an average of ~ 5 (Solomon et al. 1979) in the inner Galaxy, and somewhat higher ratios of ~ 7 for large parts of the plane (Polk et al. 1988) and in the outer Galaxy clouds (Brand & Wouterloot 1995). This suggests that once high enough density and shielding is reached, the conditions in a low metallicity molecular cloud may approach that higher metallicity clouds.

3.3.5 Estimating the Optical Depth of ^{12}CO

The linear trend with no turnover observed between ^{12}CO and ^{13}CO indicates that while the ^{12}CO $(2-1)$ transition is optically thick where there is ^{13}CO, the ^{13}CO likely remains optically thin for these observations. Using the ^{13}CO to ^{12}CO ratios, we can estimate the optical depth of the ^{12}CO $(2-1)$ observations. The Rayleigh-Jeans radiation temperature of the CO line emission is

$$T_R = J_R(T_{ex})(1 - e^{-\tau}) \tag{3.1}$$

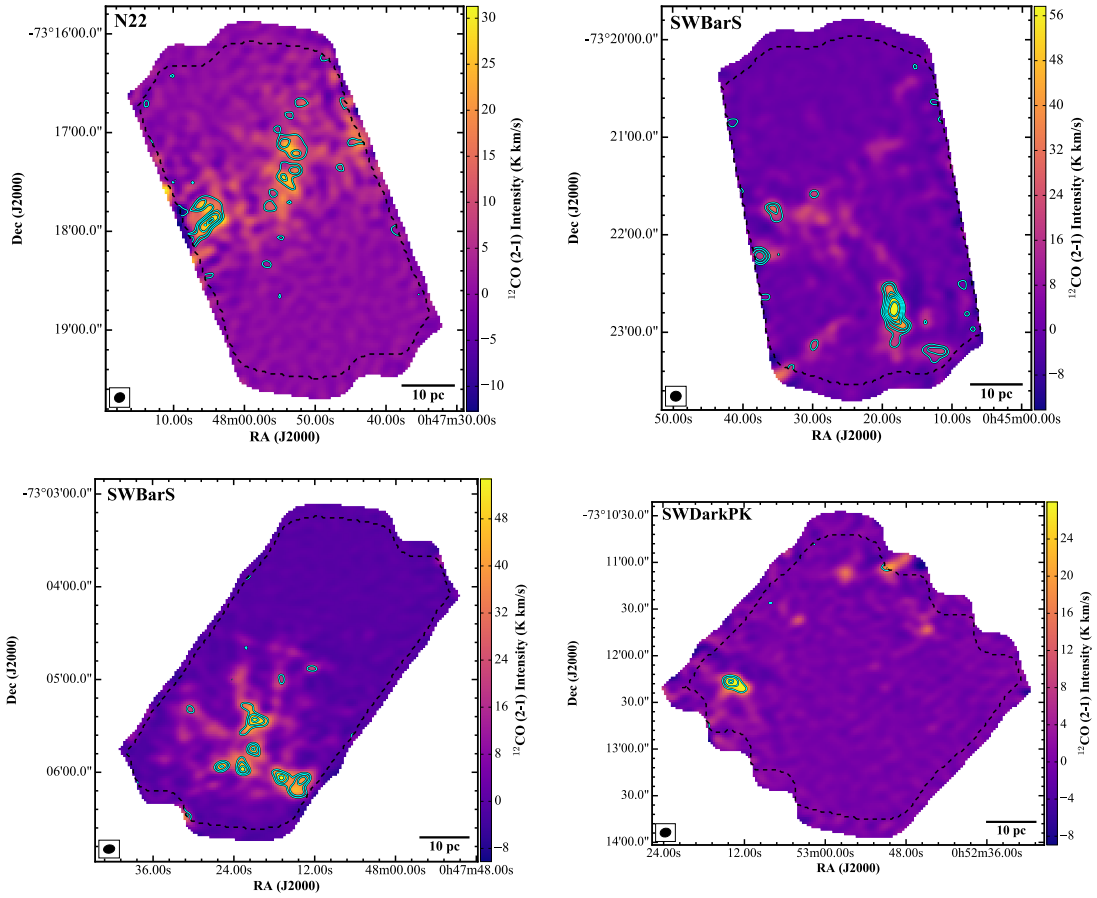

Figure 3.7 Integrated intensity map of ALMA ACA+TP ^{12}CO $(2-1)$ with contours showing ALMA ACA+TP ^{13}CO $(2-1)$ at levels of 2.5, 4, 6, 8, 10, 15 K km s^{-1}. The black dashed line shows the coverage of the ^{13}CO $(2-1)$ image. The sensitivities of the maps are listed in Table 3.5.

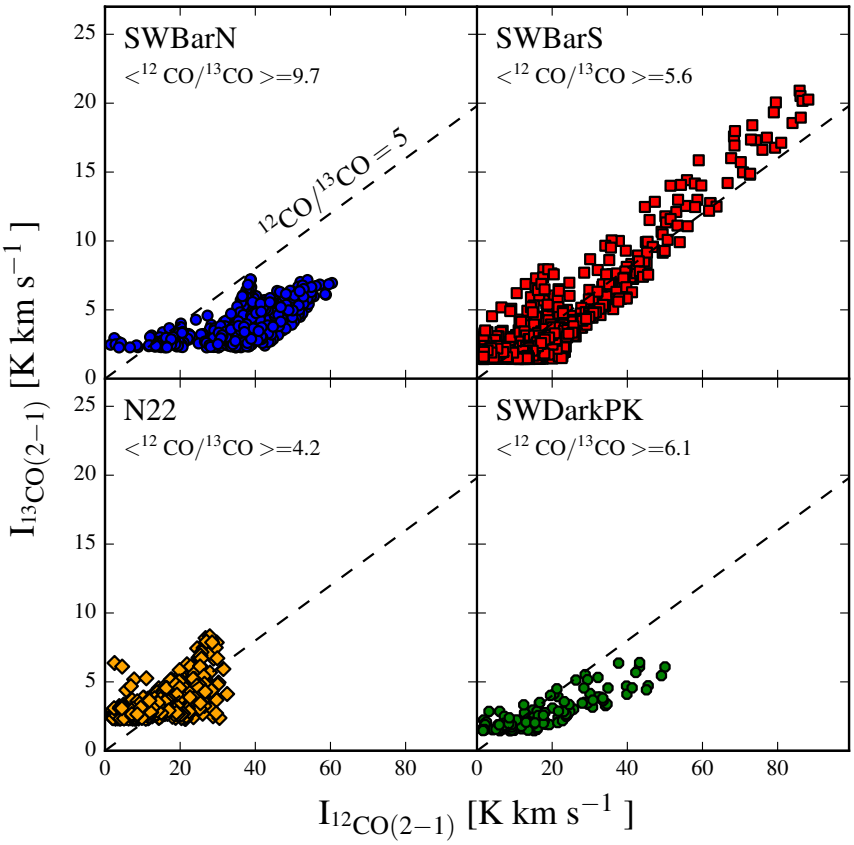

Figure 3.8 Ratio of integrated intensity of ^{12}CO $(2-1)$ to ^{13}CO where both are detected at $> 3\sigma$. The mean ^{12}CO/^{13}CO are listed for each region. The dashed line shows a typical ratio found in the Milky Way of ^{12}CO/^{13}CO = 5.

where T_{ex} is the excitation temperature and τ is the optical depth of the line. The observed intensity is,

$$J_R(T_{ex}) = \frac{h\nu}{k}\left(\frac{1}{e^{(h\nu/kT_{ex})}-1} - \frac{1}{e^{(h\nu/kT_{bg})}-1}\right) \tag{3.2}$$

where T_{bg} is the background temperature (take to be the Cosmic Microwave background of 2.73 K). The ratio of the line temperatures for different isotopic species line brightness temperatures can be used to estimate the optical depth of the more abundant species if we assume both lines share the same excitation temperature. This is strictly correct only in the high-density regime ($n \gg n_{cr}$, where $n_{cr} \sim 10^4\,\mathrm{cm}^{-3}$ is the critical density of the CO 2–1 transition considered), where the level populations will follow a Boltzmann distribution at the kinetic temperature of the gas. For ^{12}CO and ^{13}CO $(2-1)$,

$$\frac{T_{R,^{12}\mathrm{CO}(2-1)}}{T_{R,^{13}\mathrm{CO}(2-1)}} = \frac{1-e^{-\tau_{^{12}\mathrm{CO}}}}{1-e^{-\tau_{^{12}\mathrm{CO}}/X}} \tag{3.3}$$

where X is the abundance ratio of ^{12}CO/^{13}CO. Assuming that $\tau_{^{12}\mathrm{CO}} \gg 1$, we can solve for the optical depth of ^{12}CO:

$$\tau_{^{12}\mathrm{CO}} = -X \ln\left(1 - T_{R,^{13}\mathrm{CO}(2-1)}/T_{R,^{12}\mathrm{CO}(2-1)}\right) \tag{3.4}$$

Taking the abundance ratio $X = 70$ for the Milky Way (Wilson & Rood 1994), the average ^{12}CO/^{13}CO values (where $I_{^{13}\mathrm{CO}} > 3\sigma$) indicate optical depths of $\tau_{^{12}\mathrm{CO}} =$ 11.9, 13.8, 12.5, and 19.0 for the SWBarN, SWBarS, N22, and SWDarkPK regions, respectively. In practice ^{12}CO is likely to be more highly excited than ^{13}CO due to radiative trapping, which would result in smaller ^{13}CO/CO ratios and somewhat underestimating the optical depth by this method.

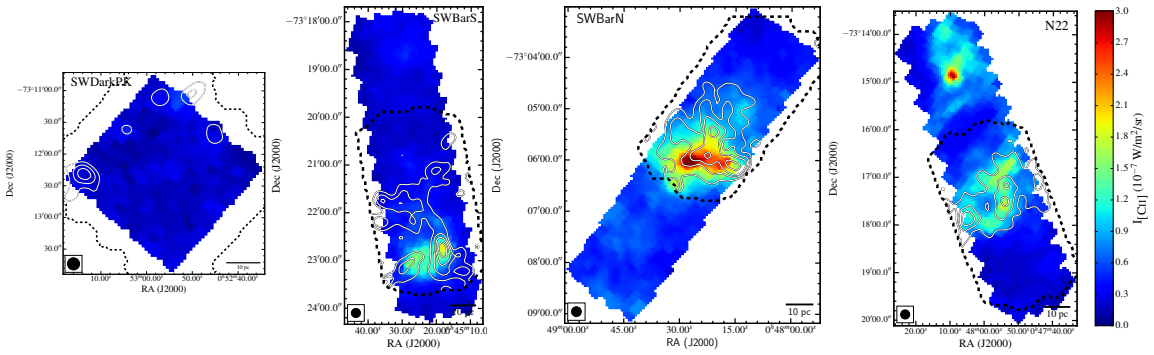

Figure 3.9 Maps of the [C II] integrated intensity with black contours showing the integrated intensity of ALMA ACA+TP ^{12}CO $(2-1)$ map convolved to the [C II] resolution ($\theta = 12''$) at levels of 0.3, 1, 2, 4, 6 $\times$ 10^{-10} W m^{-2} sr^{-1} (2, 8, 16, 32, 48 K km s^{-1}). The dashed black lines show the coverage of the ACA maps. There is generally good agreement between the peaks in the [C II] and the ^{12}CO emission and the faint [C II] emission tends to trace the faint ^{12}CO structure, strongly suggesting that most of the [C II] is originating from PDRs and is associated with molecular gas.

3.3.6 Relationship between ^{12}CO and [C II]

[C II] emission can arise from neutral atomic gas, molecular gas, and ionized gas. Our comparison of [C II] to [N II] shows that only a small fraction of the [C II] emission arises from ionized gas. While [C II] emission is an important coolant of the cold neutral medium (Dalgarno & Black 1976; which we explore in Section 3.4.2), photodissociation regions (PDRs) are expected to produce bright [C II] emission (Hollenbach & Tielens 1999, and references therein). The carbon will exist as CO in the dense parts of the molecular gas, but at the edges of the cloud the lack of

shielding will dissociate CO and much of the carbon will exist as C^+ while there can still be molecular (H_2) gas (e.g., Israel et al. 1996; Bolatto et al. 1999; Wolfire et al. 2010). This leads to a layer of molecular gas surrounding the molecular cloud associated with [C II] but no ^{12}CO emission. Studying the ^{12}CO to [C II] ratio can determine whether the [C II] emission is primarily associated with the PDR and provide insight into the structure of the molecular cloud and its associated faint CO gas.

What is the origin of the [C II] emission in our SMC regions? Figure 3.9 shows the [C II] integrated intensity maps with the ALMA ^{12}CO (2−1) integrated intensity shown with contours. There is a striking similarity between the structure, at both high and low intensity, but the [C II] extends through the mapped region whereas the CO emission is more localized. The similarity in integrated intensity emission structure suggests that the [C II] emission predominately traces the molecular gas. This is reinforced by the velocity-resolved observations. Recent observations of the [C II] 158 μm line using the GREAT instrument on SOFIA for individual pointings throughout some of the HS^3 show that the velocity ranges covered by the [C II] and ^{12}CO (2 − 1) emission are similar, although in a FWHM sense the [C II] line can be up to $\sim$ 50% wider than the ^{12}CO line (Herrera-Camus et al. 2016a). Other SOFIA GREAT observations of SMC star-forming regions N66, N25/26 (covered in the HS^3 'N22' region), and N88 show that the [C II] profile is similar to the ^{12}CO profile and with the [C II] profile up to $\sim$ 50% wider (Requena-Torres et al. 2016). We show one example GREAT [C II] spectrum for one pointing in the SWBarN region compared with the beam-matched ALMA ^{12}CO (2 − 1) profile and the H I

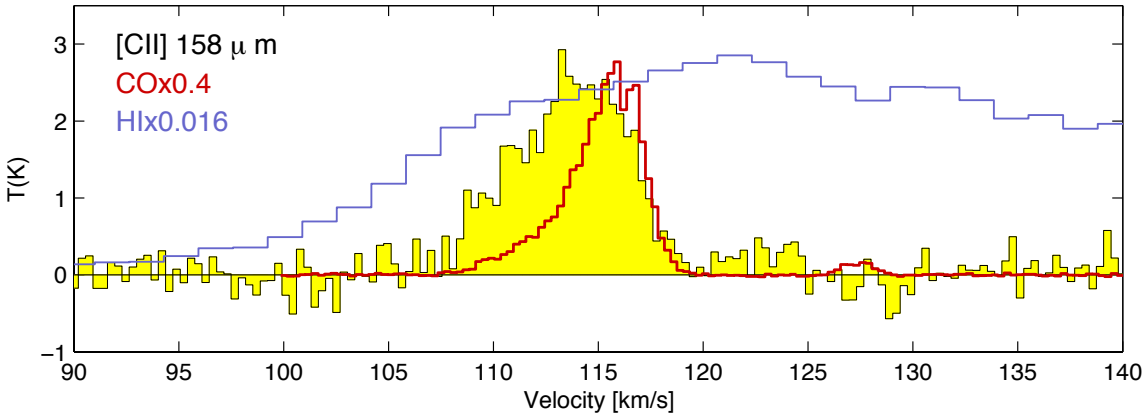

Figure 3.10 Spectrum of [C II] from one pointing observed with SOFIA GREAT from (Herrera-Camus et al. 2016b) with the yellow filled histogram showing the data in 0.3 km s^{-1} bins with scaled spectra of the ALMA ^{12}CO $(2-1)$ in red and H I in purple for the same area in the SWBarN region. The black and red lines show the Gaussian fits to the [C II] and ^{12}CO lines, respectively, with the fit parameters listed. This illustrates that the velocity profile of the [C II] emission is most similar to the ^{12}CO and not the H I, suggesting that a significant fraction of the emission comes from molecular gas, and that the [C II] emission profile is can be wider (typically by at most $\sim 50\%$) than the ^{12}CO line profile.

emission (at a resolution $\sim 1'$) toward the same point in Figure 3.10. As mentioned above, the CO and [C II] cover a very similar velocity range, which is much more restricted than that of the H I emission. This strongly suggests that toward these molecular regions [C II] is dominated by emission arising from molecular gas rather than atomic gas.

Furthermore, there is a clear similarity between the [C II] map and the map of the H_2 rotational line emission at 28.2 μm (see Figure 4.4). This line requires warm gas ($T \gtrsim 100$ K) to be excited, so it is a poor tracer of the bulk of the molecular mass. But the spatial coincidence between these two transitions together with the [C II]-^{12}CO agreement above provide strong evidence that a majority of the [C II] emission arises from molecular gas.

3.3.7 ^{12}CO-to-[C II] Ratio

In Figure 3.11 we show the ratio of ^{12}CO/[CII] emission as a function of A_V estimated from dust emission (see §3.2.5), which indicates the total column density through the molecular cloud along the line-of-sight. The ratios are typically much lower at low A_V and increase with A_V. At higher A_V and deeper within the cloud, there is enough shielding from FUV radiation for significant amounts of ^{12}CO to exist, with an increasing fraction of the carbon is in the form of CO as opposed to C or C^+. The values of this ratio in the outskirts of the clouds are typically $\sim 1/5$ the fiducial value for the Milky Way of ^{12}CO/[CII] $\sim 1/4400$ (Stacey et al. 1991). Towards the centers of the clouds, at high A_V, the ratio tends to reach the Milky

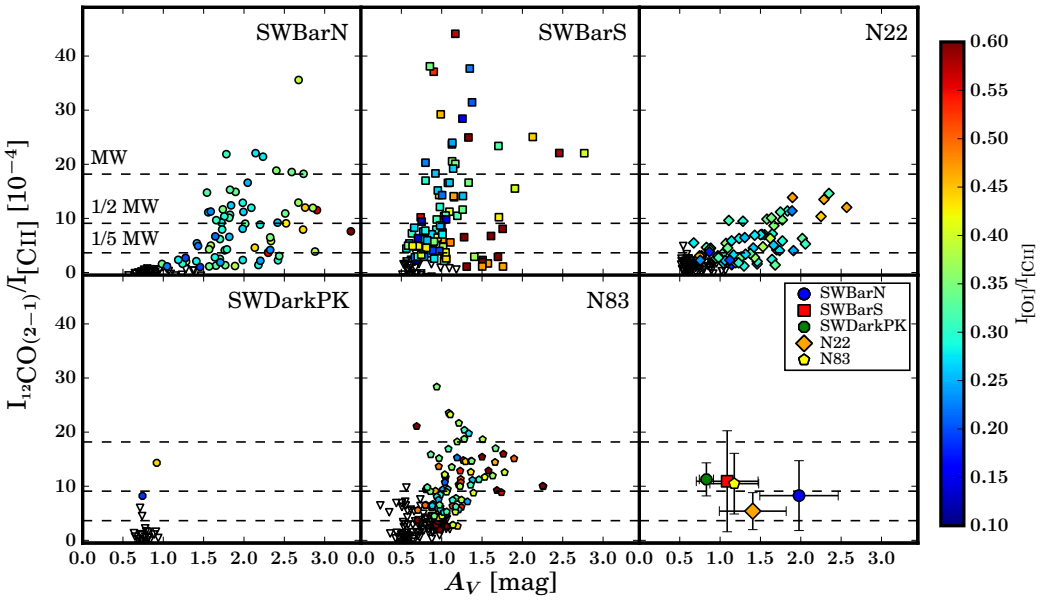

Figure 3.11 The ratio of the integrated intensity of ALMA ACA+TP ^{12}CO $(2-1)$ to that of [C II] as a function of A_V for the HS^3 regions. The colored symbols show independent measurements detected at $> 3\sigma$ in both ^{12}CO and [C II] the downward pointing triangles indicate upper limits (where $I_{\rm CO} < 3\sigma$). The over plotted dashed lines show scalings of the canonical [C II] to ^{12}CO $(1-0)$ ratio translated to $(2-1)$ assuming thermalized emission for the Milky Way of $\sim 1/4400$ (Stacey et al. 1991). The bottom left panel shows the mean ^{12}CO $(2-1)/$[C II] ratios for each region. We see a trend of ^{12}CO $(2-1)/$[C II] starting at values much lower than the Milky Way value at low A_V and increasing ^{12}CO $(2-1)/$[C II] towards higher A_V. The [O I]/[C II] ratios also show an increase towards higher A_V, which is consistent with increasing density producing more [O I] emission and/or less [C II].

Way value or higher as in the case of the SWBarN and SWBarS regions which show compact, bright peaks in the ^{12}CO and ^{13}CO emission. The lower ^{12}CO-to-[C II] ratios at lower A_V suggest that there is a reservoir of H_2 gas that is not traced by bright CO emission.

The low range of A_V in the SWDarkPK region and the high ^{12}CO-to-[C II] values seen at low A_V (e.g., in the SWBarS region) are probably in part due to the geometry of the sources, as well as physical differences in density and radiation field (see §3.4.3.2). Limitations in how we estimate A_V likely also play a role. In order to derive a dust temperature from the dust SED we need to include the longer wavelength data, which have poorer resolution. To obtain our A_V estimate we have thus applied the dust temperature fit on larger ($\sim 40''$) scales, which smooth out any dust temperature variations on small scales, particularly those likely present towards smaller CO clouds or cores. Associated with this, the simple one dust temperature modified blackbody fit is also biased toward the higher dust temperatures that will dominate the emission. A high dust temperature results in underestimating τ_{160} and A_V. This combination of inability to resolve small structures and bias toward underestimating A_V should be taken into account when interpreting Figure 3.11.

3.4 Estimating H_2 using [C II] and ^{12}CO

Models of molecular clouds predict a layer where hydrogen exists primarily as H_2 while carbon exists as C^+ instead of CO. At low A_V, in the outer layers of the molecular cloud, the molecular gas will be associated with [C II] emission. As the

shielding increases deeper within the cloud at high A_V, the molecular gas will be traced by CO emission. The expectation at low metallicity based on PDR models, existing CO and [C II] observations, and the dust-based molecular gas estimates, is that the majority of the molecular gas exists in regions that are "CO-faint". These regions, where CO is easily photo-dissociated, should be visible in [C II] emission (Tielens & Hollenbach 1985; Sternberg & Dalgarno 1995; Wolfire et al. 2010). Observations targeted at tracing this "CO-faint" gas using *Herschel* [C II] observations in the Milky Way show that this component is $30-40\%$ of the molecular gas (Pineda et al. 2013; Langer et al. 2014). We can estimate the total amount of molecular gas by evaluating the [C II] emission coming from H_2 gas at low A_V, and combining it with the H_2 traced by CO emission at high A_V:

$$N_{H_2} = N_{H_2,[C\,II]} + X_{CO}\, I_{CO}, \tag{3.5}$$

To convert the [C II] intensity to a column of H_2 gas we have to estimate and remove any possible contribution to the [C II] emission from ionized and atomic gas:

$$I_{[C\,II],mol} = I_{[C\,II]} - I_{[C\,II],ionized} - I_{[C\,II],atomic}, \tag{3.6}$$

leaving only [C II] emission arising from molecular hydrogen. This methodology is based on many previous studies that estimate molecular gas based on [C II] emission, with the most recent from Langer et al. (2014) in the Milky Way, Okada et al. (2015) in the LMC, and Requena-Torres et al. (2016) in the SMC. However, those studies relied primarily on [C II], [C I], and ^{12}CO, lacking any observations that would give them an indication of the temperature and/or density of the [C II]-emitting gas. Our [O I] observations allow us to use the [O I]/[C II] line ratios to constrain the

conditions of the [C II]-emitting gas and better estimate the amount of molecular gas.

The integrated [C II] line intensity ($I_{[\mathrm{C\,II}]}$) from collisional excitation assuming optically thin emission is

$$I_{[\mathrm{C\,II}]} = 2.3 \times 10^{-24} \left[\frac{2e^{-91.2/T}}{1 + 2e^{-91.2/T} + n_{\mathrm{crit}}/n} \right] N_{\mathrm{C^+}}, \tag{3.7}$$

where $I_{[\mathrm{C\,II}]}$ is in units of W m^{-2} sr^{-1} , T is the kinetic gas temperature in K, n is the volume density of the collisional partner (H, H_2, of e^-) in cm^{-3}, $N_{\mathrm{C^+}}$ is the column density of C^+ in cm^{-2}, and n_{crit} is the critical density for collisions with a given partner in cm^{-3} (Crawford et al. 1985). We assume a carbon abundance ($(\mathrm{C^+/H})_{\mathrm{SMC}}$) that is the Milky Way abundance scaled by the metallicity of the SMC, such that $(\mathrm{C^+/H})_{\mathrm{SMC}} = \mathrm{Z'_{SMC}}\ (\mathrm{C^+/H})_{\mathrm{MW}} = 2.8 \times 10^{-5}$, taking $Z'_{\mathrm{SMC}} = 0.2$ and $(\mathrm{C^+/H})_{\mathrm{MW}} = 1.4 \times 10^{-4}$ (Sofia et al. 1997), which agrees with the available measurements in the SMC (Kurt et al. 1999).

3.4.1 $I_{[\mathrm{C\,II}]}$ Contribution from Ionized Gas

We estimated a very low contribution to the total [C II] emission from ionized gas based on our [N II] 205 μm measurements (§3.3.2). Here we also estimate the possible contribution using the narrow-band Hα data for the SMC to estimate the electron volume density (n_e) and column density (N_e), and assuming a ionized gas temperature to calculate $I_{[\mathrm{C\,II}]}$ using Equation 3.7. The Hα observations provide the emission measure (EM), which can be used to estimate n_e:

$$\mathrm{EM} = \int n_e^2 dl = 2.75 \left(\frac{T}{10^4 \mathrm{K}} \right)^{0.9} \left(\frac{I_{\mathrm{H}\alpha}}{1\mathrm{R}} \right) \mathrm{pc\ cm^{-6}}, \tag{3.8}$$

which we can then solve for n_e using

$$n_e = \left(\frac{2.75}{l} \left(\frac{T}{10^4 \mathrm{K}} \right)^{0.9} \left(\frac{I_{\mathrm{H}\alpha}}{1 \mathrm{R}} \right) \right)^{1/2} \mathrm{cm}^{-3}. \tag{3.9}$$

where $I_{\mathrm{H}\alpha}$ is the Hα intensity (1 R $= 10^6\ (4\pi)^{-1}$ photons cm^{-2} s^{-1} sr^{-1} $= 2.409 \times 10^{-7}$ ergs s^{-1} cm^{-2} sr^{-1} at $\lambda = 6563$ Å), T is the electron temperature, and l is the length over which n_e^2 is integrated (Reynolds 1991). This procedure is uncertain and known to be biased toward overestimating n_e since the highest densities dominate the EM, but it provides an independent check on the conclusions in §3.3.2, and it also gives us the ability to correct the [C II] maps at higher resolution.

We assume $T_e = 8000$ K, appropriate for Galactic H II regions and the warm ionized medium (WIM). While the temperature of H II regions is a strong function of metallicity and is likely higher in the SMC, Kurt & Dufour (1998) measures $T_e \approx 12000$ K in N66, Goldsmith et al. (2012) calculates the [C II] critical density for collisions with electrons only up to 8000 K, and reports $n_{\mathrm{crit},e} = 44$ cm^{-3}. The [C II] emission from ionized gas is not expected to dominate the total [C II] emission (see Section 3.3.2), so the effect of assuming a lower temperature will be minimal. The most uncertain quantities are the assumed lengths: the distance l over which n_e^2 is integrated, and the distance used to convert the volume density to a column density. For simplicity, we assume both to be 20 pc, which is approximately the diameter of the largest H II region (N22) found within the survey regions and likely to be the size scale that produces the majority of the measured integrated n_e^2. This assumption, along with the fact that the emission measure will be most sensitive to regions of high n_e make it likely that the actual amount [C II] emission from ionized

gas is lower than our estimates. The maximum n_e we estimate from the Hα emission is $\sim 20 - 25$ cm^{-3}, which is consistent with the upper limit on n_e determined from the [N II] 122 μm/205 μm values (see Section 3.3.2).

The overall change after correcting for the contribution from ionized gas is small. We list the average percentages of [C II] intensity estimated to originate from the ionized gas in Table 3.6. The amount of emission from ionized gas can be as high as $\sim 50\%$, but this is only found within the H II region where the [C II] surface brightness is low. The effect of correcting for the ionized gas mainly effects the structure of [C II] emission in and near the H II regions where we expect little to no molecular gas.

3.4.2 $I_{[\mathrm{C\,II}]}$ Contribution from Atomic Gas

We estimate the amount of [C II] emission from H I by using the typical temperature and density for the conditions of the gas and assume that the column density of ionized carbon scales with the carbon abundance such that $N_{\mathrm{C}^+} = (\mathrm{C}^+/\mathrm{H})_{\mathrm{SMC}} \mathrm{N}_{\mathrm{H\,I}}$. The [C II] emission from atomic hydrogen gas arises from a combination of the warm neutral medium (WNM), with typical temperatures of $6000 - 12000$ K, and the denser cold neutral medium (CNM), which has temperatures of $50 - 120$ K. Some or all of the CNM component may be directly associated with the molecular gas as a shielding layer surrounding and mixed with the outer part of the molecular cloud in the photodissociation region. Given the differences in conditions, we make separate estimates for the [C II] emission coming from the WNM and CNM and

remove both contributions from $I_{[\mathrm{CII}]}$.

To estimate the possible H I associated with the [C II] emission, we want to select only the H I with velocities in the observed range of the [C II] emission. However, the spectral resolution of the PACS spectrometer is $\sim$ 240 km s^{-1}, which encompasses almost all of the H I emission and is a much larger range of velocities than the $\sim 15 - 50$ km s^{-1} widths of the ^{12}CO line observations. We use the velocity-resolved observations of [C II] from the SOFIA GREAT receiver Herrera-Camus et al. (2016b) as guidance to estimate the relationship between the velocity profile of the [C II] emission and the ^{12}CO throughout all our regions.

Figure 3.10 shows an example [C II] spectrum from a pointing in the SWBarN region with the ALMA ACA ^{12}CO $(2-1)$ and H I line profiles for the same region. The [C II] line is clearly resolved, and shows a profile similar to the ^{12}CO and much narrower than the H I, but the [C II] emission is $\sim$ 50% wider. The region we show in Figure 3.10 has the greatest width difference between [C II] and ^{12}CO for all the regions observed with GREAT from Herrera-Camus et al. (2016a). A recent study be Requena-Torres et al. (2016) of the N66, N25/N26, and N88 star-forming regions in the SMC using velocity-resolved [C II] GREAT observations show similarity between [C II] and ^{12}CO line profiles and find the [C II] emission to be at most 50% wider than ^{12}CO. Similarly, comparison of the dynamics of [C II], H I, and CO on larger scales show that the [C II] line widths agree better with the CO than H I (de Blok et al. 2016). To select the H I associated with the strong [C II] emission and the molecular cloud, we created integrated intensity maps of H I for each of the ALMA regions using a velocity range that is centered on the ^{12}CO line velocity, but $\pm$25%

wider than the range of velocities with observed ^{12}CO throughout the region (not for individual lines-of-sight). We use these H I maps to estimate the amount of [C II] emission associated with neutral atomic gas.

To estimate the [C II] emission attributable to atomic gas we assume a single temperature and density for the WNM and CNM. The H I emission will be dominated by the WNM component, which we assume to have a temperature of ≈ 8000 K (Wolfire et al. 2003) and a typical density range of $0.1 - 1$ cm^{-3} (Velusamy et al. 2012). We set $n_{\rm WNM} = 1$ cm^{-3} for our estimate to ensure we do not underestimate the [C II] contribution from the WNM. The C^+ excitation critical density for $T \approx 8000$ K of the WNM from hydrogen atoms is $n_{\rm crit}(H^0) = 1600$ cm^{-3} (Goldsmith et al. 2012). For the CNM, we assume $n_{\rm CNM} = 100$ cm^{-3} and $T = 40$ K based on the values found from H I absorption line study by Dickey et al. (2000). For collisions with electrons, we take $n_{{\rm crit},e} = 6$ cm^{-3}. We calculate the critical density for collisions with hydrogen atoms for the CNM temperature using $n_{\rm crit} = A_{ul}/R_{ul}$, where A_{ul} is the spontaneous emission rate coefficient and R_{ul} the collisional de-excitation rate coefficient. Using $A_{ul} = 2.36 \times 10^{-6}$ s^{-1} and the fit to R_{ul} for 20 K $\leq T^{\rm kin} \leq 2000$ K from Barinovs et al. (2005), we find $n_{\rm crit}({\rm H}^0) \approx 3000$ cm^{-3}.

We calculate $I_{\rm [CII]}$ using Equation 3.7 for both collisions with hydrogen atoms and electrons in the WNM and CNM and collisions with hydrogen for the CNM and add them to produce our estimate. We take an ionization fraction in neutral gas to be $n_{e^-}/n_{\rm H} = 4.3 \times 10^{-4}$ (Draine 2011). In order to calculate this we need the fraction of WNM and CNM in our lines of sight, which is unknown. We assume that 50% of $N_{\rm H\,I}$ associated with the CO emission is associated with the CNM and

the other 50% with the WNM when calculating $I_{[\mathrm{CII}]}$. Dickey et al. (2000) find the fraction of cool H I to be $\sim 15\%$ of the total H I in the SMC along a few lines of sight, however locally it may be much higher. Assuming a higher fraction of CNM will generate a higher estimate of the associated [C II] emission, decreasing the likelihood of underestimating the [C II] emission from H I. Table 3.6 shows the average amount of total [C II] emission for each region. We find that H I typically only accounts for $\lesssim 5\%$. The SWDarkPK region has the highest fraction of [C II] emission coming from H I, likely because it is not actively forming stars and is more atomic-dominated (as also suggested by the lower CO emission indicating less molecular gas at $A_V > 1$ than the other regions). These low fractions of [C II] emission from atomic gas are consistent with the theoretical study by Nordon & Sternberg (2016), who find that most of the C^+ column would be associated with H_2 gas for all relevant conditions.

3.4.3 Converting $I_{[\mathrm{C\,II}]}$ to $N_{\mathrm{H_2}}$

After removing the contributions from ionized and neutral atomic gas, we assume the remainder of the [C II] emission originates from molecular gas. We estimate the amount of H_2 gas from the remaining [C II] emission in two ways:

1. Assuming a fixed T and n representative of PDR regions and converting $I_{[\mathrm{CII}]}$ to $N_{\mathrm{H_2}}$using Equation 3.7.

2. Using PDR models tuned to the SMC conditions (Wolfire et al. 2016, henceforth W16) to estimate n and the FUV radiation field intensity from the observed combination of [C II], [O I], and FIR continuum, determining $N_{\mathrm{H_2}}$

from the cooling curve.

We explain both methods in the following sections.

3.4.3.1 Method 1: Fixed T, n

Using Equation 3.7, we can solve for the H_2 column density given the [C II] intensity:

$$N_{H_2} = \frac{4.35 \times 10^{23}}{(C^+/H)_{SMC}} \left[\frac{1 + 2e^{-91.2/T} + n_{crit}(H_2)/n}{2e^{-91.2/T}} \right] I_{[C\,II],H_2}. \tag{3.10}$$

To estimate N_{H_2}, we need only assume a temperature and volume density and calculate the appropriate critical density for collisions with H_2 using the latest collisional de-excitation rate fits by Wiesenfeld & Goldsmith (2014) as a function of temperature, which includes H_2 spin effects in LTE:

$$n_{crit} = \frac{A_{ul}}{R_{ul}} = \frac{2.36 \times 10^{-6}}{(4.55 + 1.6e^{(-100.0\ K/T)}) * 1 \times 10^{-10}} \tag{3.11}$$

Our assumption is that all of the [C II] emission associated with H_2 comes from the photodissociation regions where the gas is warm and moderately dense. We can then make the simplifying assumption that this region has a single average temperature of $T = 90$ K and density of $n = 4000$ cm^{-3} (consistent with the PDR modeling results in §3.4.3.2). These are chosen as similar to the excitation temperature and critical density of the transition, and thus at about the point in which the gas emits most efficiently (e.g. Leroy et al. 2016). For reference, the exact critical density for collissions with H_2 at $T = 90$ K is $n_{crit}(H_2) = 4648$ cm^{-3}. This choice of temperature and density results in a conservative estimate of the

Table 3.6. Properties of H_2 Estimates from [C II]

Region	Average % $I_{[CII]}$ from H I	from H^+	$\bar{N}_{H_2,[CII]}$ [10^{21} cm^{-2}] Fixed T, n	W16	$M_{H_2,[CII]}$ [10^4 $M_\odot$] Fixed T, n	W16	$M_{H_2,^{12}CO}$[a][10^4 $M_\odot$]
SWBarS	3%	6%	1.2	0.97	5.05	4.15	1.3
N22	2%	15%	1.6	1.1	5.64	4.13	1.0
SWBarN	2%	7%	2.9	2.5	8.60	7.21	1.7
SWDarkPK	7%	9%	0.48	0.63	0.90	1.16	0.10

[a]total mass above the RMS level ($\gtrsim$ 5 K km s^{-1})

amount of molecular gas associated with the [C II] emission. Assuming a lower temperature or density would decrease the amount of [C II] emission per H_2 molecule and increase the amount of molecular gas needed to explain the observed emission, while increasing the temperature or density will not change our results significantly. The benefit of this methodology is its simplicity and straightforward calculation. The drawback is that it over simplifies the conditions of the [C II] emitting gas by assuming only one constant temperature and volume density throughout each region and across all regions.

3.4.3.2 Method 2: W16 PDR Model

We can constrain the physical conditions of the gas in the photodissociation regions by modeling the [C II], [O I], and total far-infrared (FIR) emission from the *Spitzer* and *Herschel* imaging. We use new PDR models generated using the elemental abundances and grain properties for SMC conditions that are presented in Appendix A. The models solve the equilibrium chemistry, thermal balance, and radiation transfer through a PDR layer characterized by a constant H nucleus volume density (n in units of cm^{-3}) and incident far-ultraviolet (FUV; 6 eV $<$ E $<$ 13.6

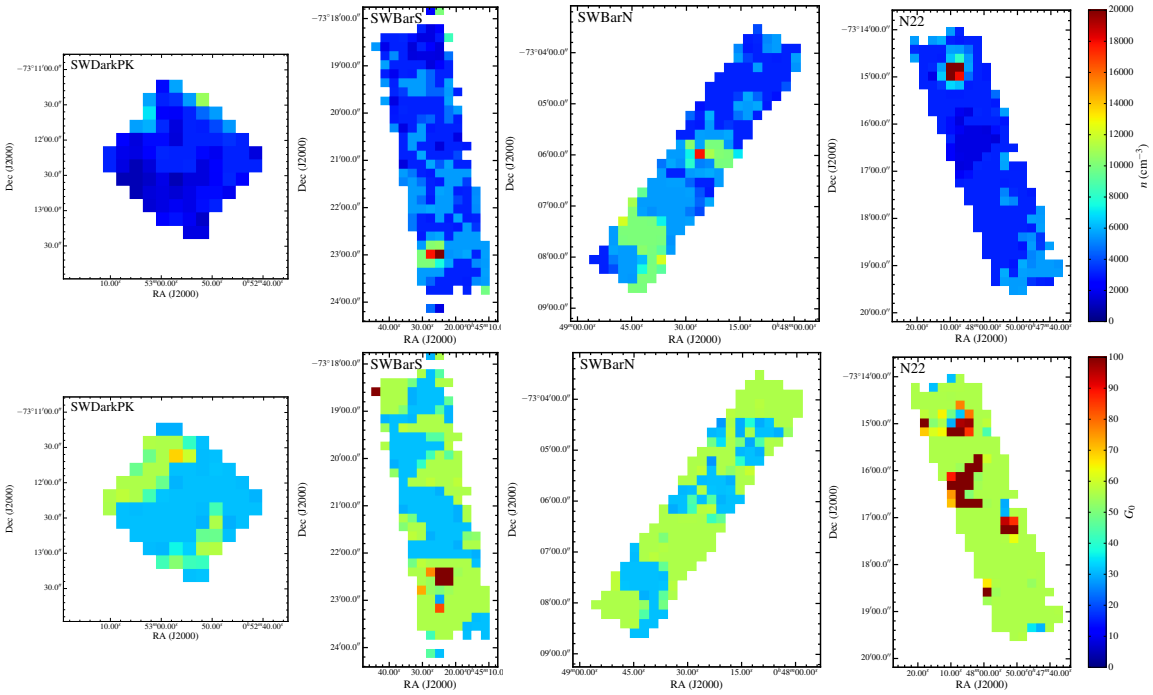

Figure 3.12 Density and radiation field for each of the regions with HS^3 and ALMA data, obtained from physical PDR modeling developed for the conditions in the SMC (abundances, cosmic ray rates, dust to gas ratio, etc; Wolfire et al. 2016). The top row shows volume density (n). The bottom row shows FUV radiation field strength (G_0).

eV) radiation field (G_0 in units of the local Galactic interstellar FUV field found by Habing, 1.6×10^{-3} erg cm^{-2} s^{-1}). The models are based on Kaufman et al. (2006) but are updated for gas and grain surface chemistry as described in Wolfire et al. (2010) and Hollenbach et al. (2012). We also modify the grain properties and abundances as appropriate for the SMC (see Appendix A) which makes it tailored to modeling the emission from the HS^3 regions.

We use the [C II], [O I], and total-infrared (TIR) intensity images as inputs to determine the nearest volume density and FUV radiation field strength in the model grids using a version of the PDR Toolbox (Pound & Wolfire 2008) that is updated with the SMC models. While the PDR Toolbox and models call for far-infrared (FIR) intensity as the input, the term FIR is meant to represent all of the FUV and optical emission absorbed by dust and re-radiated in the infrared, which makes the current definition of TIR the most appropriate to compare to the models. We calculate the TIR intensity using the *Spitzer* 24 μm and 70 μm (no *Herschel* 70 μm map exists) combined with *Herschel* 100 μm, 160 μm, and 250 μm images, all convolved to the lowest resolution of the *Spitzer* 70 μm image ($\sim 18''$), following the prescription by Galametz et al. (2013):

$$S_{\rm TIR} = \sum c_i S_i, \tag{3.12}$$

all in units of W kpc^{-2}, where the coefficients (c_i) are 2.013, 0.508, 0.393, 0.599, and 0.680 for 24 μm, 70 μm, 100 μm, 160 μm, and 250 μm, respectively. We convolve the [C II] and [O I] images to the resolution of the TIR. We run the PDR Toolbox for the intensities at each matched pixel in the images and produce maps of n and

G_0. The images are then sampled with $\sim$ 1 pixel per beam, matching the [C II] beam-sampled images. While the limiting resolution of the TIR map is lower at a resolution $\sim 18''$ than the [C II] ($\sim 12''$), it is not significantly lower and we expect n and G_0 to vary smoothly. The initial images of n and G_0 show artifacts from the FIR image (due mostly to the strong beam patterns from the point sources). We take one final step and mask out regions in the images with unphysical values of n or G_0 that are due to the artifacts and use a linear interpolation to replace the masked values. The results of model fits are shown in Figure 3.12. The PDR models suggest that the typical volume densities are $n \sim 10^3 - 10^4$ cm^3, which is consistent with most of the gas being molecular in order to reproduce the observed far-infrared emission.

Using the maps of n and G_0, we convert the [C II] emission to $N_{\rm H_2}$. We use [C II] cooling rates as a function of n from Wolfire et al. (2016) that are adapted from Wolfire et al. (2003) to account for the conditions of the SMC, which we show in Figure 3.13. We use the same abundances as for the PDR model. The [C II] rates are calculated for a fiducial FUV radiation field strength of $G_0 = 5.5$, which is approximately the average in diffuse gas in the SMC Southwest Bar based on the maps from (Sandstrom et al. 2010) and the cooling rates were primarily intended for use in diffuse gas. While the [C II] cooling rate is only determined for a single G_0 in Wolfire et al. (2016), the effect of different G_0 is to change the the photoelectric heating rate, which to first order is proportional to G_0 (Bakes & Tielens 1994, equation 42). If [C II] dominates the cooling, then the [C II] line intensity is proportional to G_0. The appropriate [C II] cooling rate per H_2 molecule

for each pixel is determined by taking the [C II] cooling rate appropriate for the specific value of n and then scaling it linearly by the ratio of estimated G_0 to the fiducial G_0 for diffuse gas. We then use this local [C II] cooling rate to calculate a H_2 column density and produce the final map. The benefit of this method is that it can account for the variations in density and radiation field in the [C II]-emitting gas throughout the regions. The weakness is that the gas conditions are estimated using "single component" models based on plane-parallel PDRs that do not account for complex geometries, or for distributions of n or G_0 within a spatial resolution element. This is alleviated by the fact that our physical resolution is 4 pc, thus we expect the conditions in a beam to be relatively uniform and simple "single component" models to be more applicable than they would be if applied to data on much larger scales.

3.4.4 Converting $I_{\rm CO}$ to $N_{\rm H_2}$

Once enough shielding from dissociating radiation is built up at high A_V, carbon will mostly exist in the form of CO. Since emission from low-J ^{12}CO transitions are almost always optically thick, the luminosity is determined the emitting area, brightness temperature, and velocity spread, and is not affected by lower abundances of C or O. The exact amount of H_2 traced by the ^{12}CO emission (and not [C II]) cannot be easily calculated theoretically and relies on empirical calibrations of the conversion factor, $X_{\rm CO}$, typically calibrated in terms of ^{12}CO $(1-0)$ emission. To convert from ^{12}CO $(2-1)$ to the equivalent ^{12}CO $(1-0)$ integrated intensity we

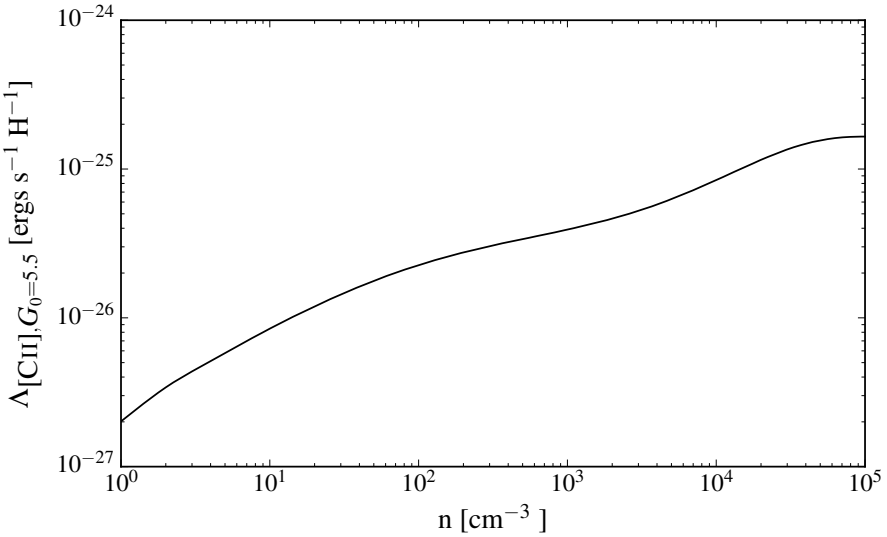

Figure 3.13 [C II] cooling rate ($\Lambda_{[\mathrm{C\,II}]}$) as a function of density for the conditions in the SMC from Wolfire et al. (2016) used to convert the [C II] emission to a column density of H_2. The cooling curve is calculated assuming $G_0 = 5.5$.

assume thermalized emission. This is equivalent to assuming constant integrated intensity in K km s^{-1} units, or to divide the 2–1 emission in units of W m^{-2} Hz^{-1} by $J_u^3 = 8$. Numerical simulations of low metallicity molecular clouds show that the conversion factor reaches Galactic, high-metallicity values in the CO-bright regions (Shetty et al. 2011; Szűcs et al. 2016), suggesting that regardless of metallicity, CO traces a similar amount of H_2 at high A_V. Therefore, we use a Galactic CO-to-H_2 conversion factor $X_{CO} = 2 \times 10^{20}$ cm^{-2} (K km^{-1} s^{-1})$^{-1}$ (Bolatto et al. 2013), to estimate the amount of molecular gas present in regions at high A_V where most of the carbon is in the form of CO. This is consistent with an underlying picture where most of the difference in the conversion factor observed in low metallicity systems is due to the shrinking of the high A_V CO-emitting cores and the growth of the outer layer of H_2 coextensive with C^+ (e.g., Wolfire et al. 2010; Bolatto et al. 2013).

3.4.5 N_{H_2} Estimates

Overall, the two different methods to estimate N_{H_2} based on [C II] emission produce similar results. Table 3.6 shows that average column densities and total H_2 masses for both methods are different by at most a factor of $\sim$ 1.5 The total mass estimates from Method 1, assuming $T = 90$ K and $n = 4000$ cm^{-3}, are higher than the estimates from Method 2, using the SMC PDR models and W16 [C II] cooling rates, except for the SWDarkPK region. The fixed temperature and density produce higher estimates because they fail to account for the presence of higher density regions that have a higher emission of [C II] per unit H_2 mass, as

we show in the example in Figure 3.14. The opposite is true for the SWDarkPK where the densities from the PDR modeling are somewhat lower than those in other regions, and the assumed $n = 4000$ cm^{-3} in Method 1 appears to be too high. This is consistent with the observed lower level of CO emission in that very quiescent region, which is suggestive of less dense molecular gas.

The Method 1 results produce structure that is similar to the [C II] emission, with the peak in the N_{H_2} occurring at the peaks in [C II] emission, which are nearly coincident with the peaks in the CO emission. When the variations in density and radiation field strength are accounted for in the estimate in Method 2, then the peaks in the N_{H_2} maps occur around the peak in the CO emission (see Figure 3.14), consistent with our understanding that [C II] emission should trace the H_2 gas in the photodissociation regions surrounding the dense molecular gas traced by bright CO. We prefer the N_{H_2} estimates from Method 2 because it incorporates additional information, and use them for the remaining analysis and discussion.

Figure 3.15 shows the H_2 maps derived from [C II] alone, from CO alone, and the total corresponding to their sum for each region. The H_2 estimated from [C II] is more extended than that derived from CO and wraps around it, which agrees with the idea that the [C II] should be primarily tracing the H_2 in the low A_V portion of the molecular cloud. The CO emission traces between $\sim 5\% - 70\%$ of the total molecular gas in this methodology, with a typical percentage of only 20%. Note, however, that there are no H_2 column density peaks without CO emission.

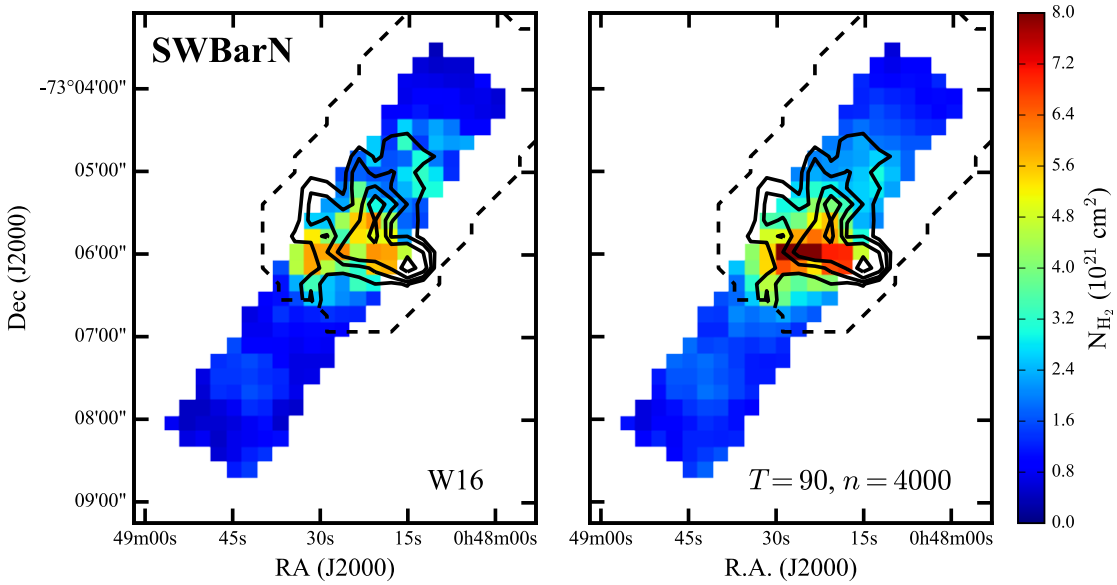

Figure 3.14 Images of the estimate of $N_{\rm H_2}$ from the [C II] emission for the SWBarN region using Method 2 using W16 models (left) and Method 1 with a fixed $T = 90$ K and $n = 4000$ cm^3 (right), shown at the same scale. The black contours show the estimate of $N_{\rm H_2}$ from ^{12}CO (using $X_{CO} = 2 \times 10^{20}$) at levels of 0.4, 0.8, 1.4, and 2.4×10^{21} cm^{-2} and the black dashed line shows the coverage of the ^{12}CO map. Both $N_{\rm H_2}$ estimates from [C II] produce similar average estimates of $N_{\rm H_2}$, but the structures are different. When taking into account the local T and n using the W16 results, there is less H_2 needed to explain the [C II] emission at the center of the cloud (the peak of the ^{12}CO emission). The estimated $N_{\rm H_2}$ peaks away from the ^{12}CO peak, which is consistent with the [C II] emission tracing the CO-faint H_2 in the photodissociation region, suggesting that the H_2 estimates using the new models are more accurate.

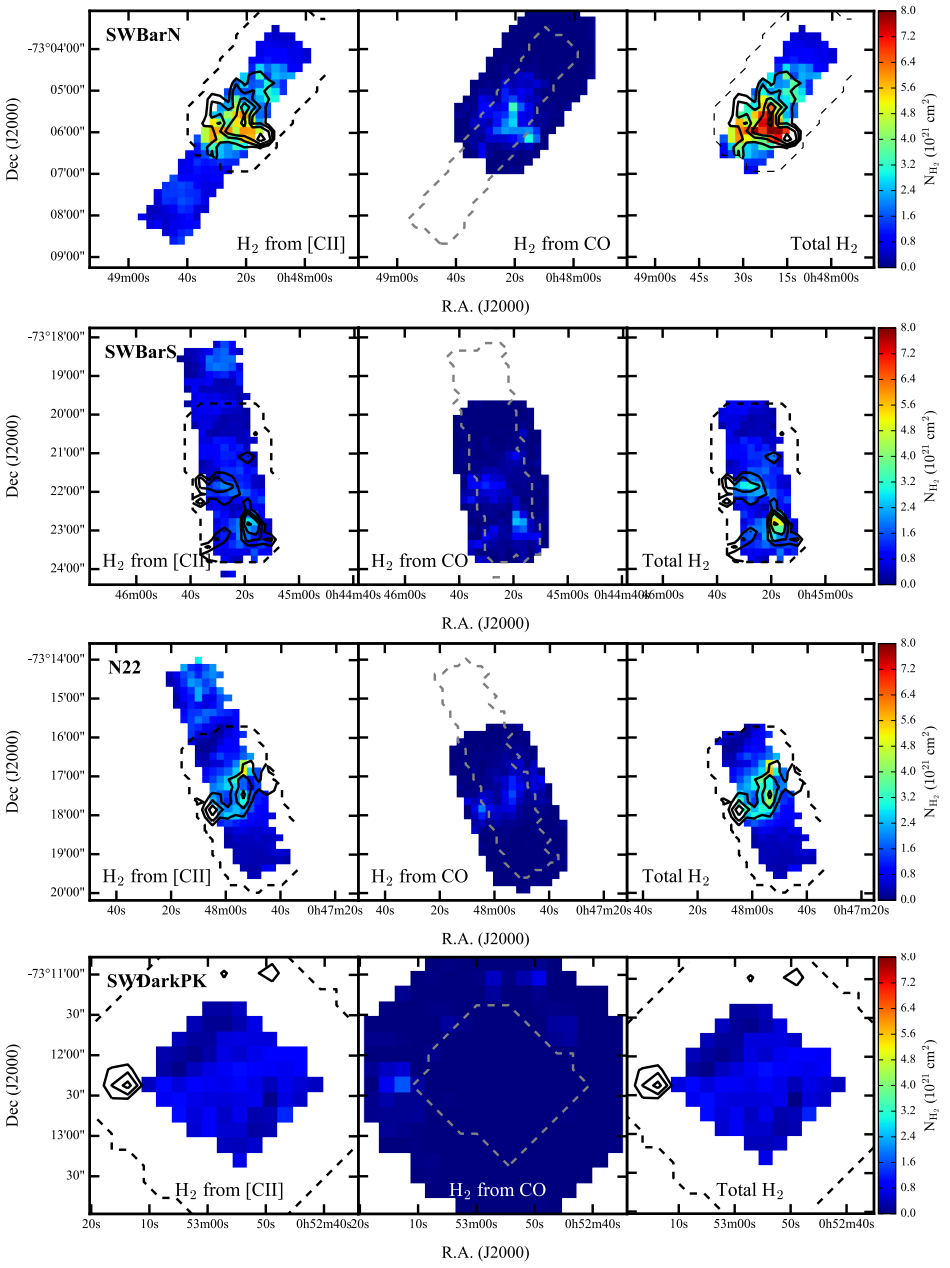

Figure 3.15 Images of $N_{\rm H_2}$ for each of the regions with *Herschel* and ALMA data. The images on the left shows the estimate of $N_{\rm H_2}$ from the [C II] emission using Method 2 (W16 n, G_0) described in Section 3.4.3.2. The middle images shows $N_{\rm H_2}$ traced by ^{12}CO, with the ALMA $(2-1)$ converted to $(1-0)$ assuming thermalized emission, and assuming a Galactic X_{CO} of 2×10^{20} cm^{-2} (K km s^{-1})$^{-1}$. The images on the right show total $N_{\rm H_2}$ found by combining the estimate from [C II] with the estimate from ^{12}CO. The black contours show the estimate of $N_{\rm H_2}$ from ^{12}CO at levels of 0.4, 0.8, 1.4, and 2.4 $\times$ 10^{21} cm^{-2} and the black dashed line shows the coverage of the ^{12}CO map. The grey dashed line shows the HS^3 ([C II] and [O I]) coverage. All maps are shown at the same color scale.

3.4.5.1 Uncertainty Estimate

In this section we explore the effects of different potential sources of uncertainty that could affect the H_2 column density estimates. We explore in detail how [O I] absorption and [C II] optical depth could affect our adopted values of G_0 and n from the models, as well as the difference between the results using the SMC PDR models and the higher metallicity models. In general, increasing n and/or G_0 will increase the [C II] cooling rate, which decreases the amount of H_2 needed to account for the observed [C II] emission. The amount of increase in [C II] cooling depends on the specific value of n since it is not a linear function of n (see Figure 3.13), whereas the [C II] cooling scales linearly with G_0.

The values of G_0 appear to be robust to the choice of PDR model since the results using the SMC PDR models are similar to those found using the high metallicity models from Kaufman et al. (2006) (see Appendix A). The G_0 values are also consistent with the values found by Israel & Maloney (2011) for the N22 and SWBarN (N27) regions using Lyman continuum and dust emission and by Sandstrom et al. (2010) from modeling the mid-IR SED. The results for n using the new SMC PDR models are a factor of ~ 10 higher than what would have been obtained using a high metallicity PDR model (e.g., Kaufman et al. 1999). The increase in density at lower metallicity is due to the result that for a given G_0 and n the grains will be more charged at low metallicity due to fewer free electrons, and the photoelectric heating efficiency will decrease. Higher density (lower G_0/n) is required to reach the same heating efficiency at higher metallicity. See Appendix A for a

description of the changes in the new models. This increase in density translates to an increase in the total H_2 mass from [C II] ($M_{H_2,[CII]}$) by factors of $\sim 1.5 - 3.0$.

There are uncertainties associated with the interpretation of the available observations; in particular, the possibility of [O I] self-absorption, of optically thick [C II] emission, and the spread in the available carbon abundance measurements. We already discussed the likelihood of [O I] absorption or self-absorption in Section 3.3.1, and found no evidence that there is significant absorption present in our observations. To explore how much a low level of absorption would affect our results, we assume 30% of the integrated [O I] intensity is absorbed leading to a 30% underestimate in the real [O I] flux. We find that if we allow for 30% larger [O I] flux, the model density increases by a factor of ~ 3 while the radiation field G_0 decreases by a similar factor of ~ 3. The increase in density increases the cooling rate, which decreases the amount of H_2 needed to explain the [C II] emission. Conversely, decreasing G_0 also decreases the cooling rate, which increases the amount of H_2. At the moderate densities in the regions ($\sim 10^3 - 10^4$ cm^{-3}), the cooling rate does not increase much with n, whereas the cooling rate will scale linearly with G_0. As a result, the effect of increasing the amount of H_2 from the change in G_0 dominates over the decrease due to the change in n and the estimated $M_{H_2,[CII]}$ decreases by $\sim 30\%$.

We have no evidence that the [C II] 158 μm emission is optically thick in our SMC regions. Measurements of [^{13}C II] and [^{12}C II] in dense, Galactic PDRs find optical depths $\tau_{[CII]} \approx 0 - 3$ (Ossenkopf et al. 2013). A moderate optical depth of $\tau_{[CII]} = 1$ seen in Galactic regions scaled to account for the lower carbon abundance

in the SMC gives $\tau_{[\mathrm{CII}]} = 0.2$. This level of optical depth is also possible in the higher $N_{\mathrm{H_2}}$ regions; using the equation for $\tau_{[\mathrm{CII}]}$ from Crawford et al. (1985) with $N_{\mathrm{H_2}} = 10^{22}$ cm^{-2} (values found in the peaks of our $N_{\mathrm{H_2}}$ estimates), $T = 100$ K, and $n = 5000$ cm^{-3} produces $\tau_{[\mathrm{CII}]} = 0.2$. To explore how this level of moderate optical depth would affect our H_2 estimates by correcting the [C II] emission by a factor of $\tau/(1 - \exp(-\tau)) = 1.1$. We find that this has little effect on the model values of n and G_0, and only increasing n by a factor of $\lesssim 2$ in some of the denser ($n \sim 5000 - 10000$ cm^{-3}) regions and decreasing G_0 by the same factor. Since n and G_0 remain largely the same, the [C II] cooling rate is the same as for the uncorrected, lower [C II] intensity while the optical depth correction increases amount of [C II] emission, which increases the amount of H_2. The correction for $\tau_{[\mathrm{CII}]} = 0.2$ increases the mass estimates by $\sim 10\%$.

Additionally sources of uncertainty include the carbon abundance, absolute flux calibration of the PACS spectrometer, and the [C II] intensity attributed to ionized and neutral gas. The measurements of the gas-phase carbon abundance in the SMC range from C/H$\sim 1.4\times10^{-5}-3.4\times10^{-5}$ (Kurt et al. 1999). This introduces a factor of $\sim 30\%$ uncertainty on our assumed value of 2.8×10^{-5}, which translates into a factor of $\sim 30\%$ uncertainty in the H_2 estimate as it scales linearly with carbon abundance. The absolute flux calibration of the PACS spectrometer is an additional source of uncertainty on the order of 30% (Poglitsch et al. 2010). Finally, there is uncertainty involved in our estimates of the [C II] intensity attributed to neutral and ionized gas. Our estimate of [C II] emission from ionized gas would likely only overestimate the actual contribution, and the ultimate contribution is small ($\lesssim 10\%$)

in the regions in and around the molecular cloud and does not significantly affect the total H_2 mass estimate. The contribution from neutral gas is more uncertain. Changing the amount of H I associated with the WNM has little effect on on the estimated [C II] intensity due to the high temperature and low density (compared to the critical density) of the gas, but the high temperature causes the H I emission from the WNM to dominate over the CNM. Changing the amount of H I in the CNM has a stronger effect on the attributed [C II] intensity due to the density being closer to the critical density (see Equation 3.7). Varying the fraction of the H I associated with the CNM from our assumed value of 50% to 25% and 75% changes the fraction of the [C II] intensity from neutral gas by ±2%, which would ultimately have a similar effect on the mass as the optical depth correction. Since a correction to $I_{[\mathrm{CII}]}$ of +10% had an effect of $\sim +10\%$ on the mass, a $\sim 2\%$ correction to $I_{[\mathrm{CII}]}$ will cause a $\sim 2\%$ increase of the H_2 mass, which is negligible compared to the other sources of uncertainty discussed.

Each of the main factors tend to contribute $\leq 30\%$ in uncertainty: $\sim \pm 30\%$ from the PACS spectrometer calibration, $\sim \pm 30\%$ from the carbon abundance measurements, and $\sim \pm 20\%$ from the combination of the effects of [O I] absorption and [C II] optical depth. Adding the results in quadrature produces a total uncertainty estimate of $\sim \pm 50\%$. This uncertainty neglects the factor of ~ 2 difference in the H_2 masses measured using the higher metallicity PDR models from Kaufman et al. (2006). The difference in the PDR models is driven by the different assumptions about dust grains compared to the Milky Way. One factor is the PAH abundance, which the SMC PDR models assume is 1/7.7 times the Milky Way value based on

the results from modeling of the mid-infrared spectra PAH band rations using the Draine & Li (2007) models in the SMC from Sandstrom et al. (2010). However, there is a large amount of scatter in the estimated PAH abundance in the SMC ranging from 1/2 to 1/10 times the Milky Way value and the regions we mapped in the Southwest Bar show the highest PAH abundances. A higher PAH abundance in our regions would cause the the estimated H_2 masses to be higher and closer to the ones produced using the higher metallicity PDR models. In addition to the PAH abundance, there are a number of other assumptions used for the SMC PDR models that are uncertain and the high metallicity PDR model results that are a factor of ~ 2 higher likely offer an upper limit on the H_2 mass estimates. Taking this into consideration, we choose to adopt an uncertainty of a factor of ~ 2 for the mass of H_2 associated with [C II] emission.

3.5 Discussion

We have presented the results of our new far-IR emission line data, focusing primarily on the [C II] 158 μm and [O I] 63 μm lines from *Herschel* PACS observations, and ALMA ACA CO $(2-1)$ data for a sample of star-forming regions in the SMC. Using the [C II] and ^{12}CO line emission, we estimated the total amount of molecular gas in a low metallicity environment and found that the bulk of the molecular gas is traced by [C II]. Here, we compare the [C II]-based molecular gas estimates to previous dust-based estimates, discuss the implications of [C II] molecular gas estimates and how it relates to CO, and use the [C II]-based estimates to

Table 3.7. Total Gas Masses

Region	M_{H_2} [10^5 $M_\odot$] [C II]+CO	M_{H_2} [10^5 $M_\odot$] Dust	M_{HI} [10^5 $M_\odot$] Δv_{CO}[a]	M_{HI} [10^5 $M_\odot$] Δv_{total}
SWBarS	$0.52^{+0.52}_{-0.26}$	$2.33^{+2.33}_{-1.17}$	3.42	6.53
N22	$0.48^{+0.48}_{-0.24}$	$1.23^{+1.23}_{-0.62}$	3.15	7.30
SWBarN	$0.86^{+0.86}_{-0.43}$	$1.61^{+1.61}_{-0.81}$	4.64	9.00
SWDarkPK	$0.11^{+0.11}_{-0.06}$	$1.79^{+1.79}_{-0.90}$	1.46	3.08
N83	$0.48^{+0.48}_{-0.24}$	$2.96^{+2.96}_{-1.48}$	4.67	6.16

[a]using the H I integrated intensity only around the velocity channels with CO emission

estimate the CO-to-H_2 conversion factor (X_{CO}) and compare to simulations and models of molecular clouds at low metallicity.

3.5.1 Comparison to Dust-based H_2 Estimates

Another method that can trace "CO-faint" molecular gas is to use dust emission and a self-consistently determined gas-to-dust ratio in atomic regions using H I emission (Dame et al. 2001; Israel 1997; Leroy et al. 2009; Bolatto et al. 2011). We compare our molecular gas estimates using [C II] and CO to the recent dust-based molecular gas estimates for the SMC presented in Jameson et al. (2016). Table 3.7 shows the [C II]+CO and dust-based molecular gas estimates over the area with both [C II] and ALMA ^{12}CO coverage, where we make a cut at the RMS level before calculating the total mass from CO.

The [C II]+CO estimates are consistent with the dust-based estimates from Jameson et al. (2016) in the SWBarS, N22, and SWBarN regions, given the factor of ~ 2 uncertainty in both methods. The [C II]+CO estimates for the SWDarkPK and N83 regions, on the other hand, are significantly lower than the result of the dust method. All of the [C II]+CO estimates are systematically lower than the dust-based H_2 mass estimates. The systematically lower [C II]+CO estimates can be the result of our [C II] methodology underestimating the amount of H_2 and/or the dust methodology overestimating the total molecular gas mass.

When estimating the amount of H_2 associated with [C II], we have been conservative in our estimates of the contribution to [C II] from the ionized and neutral gas and the conditions of the gas (n and G_0), which may cause our estimates to underestimate the total H_2. The dust-based method relies on self-consistently calibrating the gas-to-dust ratio in the atomic gas assuming that it only varies smoothly on large scales (500 pc). This methodology could overestimate the molecular gas if the gas-to-dust ratio is an overestimate of the actual gas-to-dust ratio, which could be the case if the gas-to-dust ratio decreases in molecular regions. Jameson et al. (2016) finds that scaling down the gas-to-dust ratio by a factor of 2 in the dense gas leads to a similar factor of ~ 2 decrease in the total molecular gas mass estimate. If the dust-based molecular gas estimates were lower by a factor of ~ 2 then all of the estimates would be consistent with the [C II]+CO estimates and there would be one region (SWBarN) where the [C II]+CO molecular gas estimate would be higher than the dust-based estimate. Similarly, if we used the density and radiation field estimates from the higher metallicity PDR models, the [C II]+CO estimates

would be ~ 2 higher (caused largely by the assumption of more neutral dust grains at higher metallicity) and would no longer be systematically below the dust-based estimates. Roman-Duval et al. (2014) finds no strong evidence of a change in the gas-to-dust ratio between the diffuse and molecular gas in the SMC while Sandstrom et al. (2012) finds evidence that the small dust grains (PAHs) are more neutral in the SMC, which would suggest that it could be likely that the systematic difference higher dust-based estimates are due to [C II]+CO underestimates. However, both of these results are based on difficult measurements and rely on a number of assumptions, particularly those of the dust models,

3.5.2 [C II] as a Tracer of H_2 and Star Formation Rate at Low Metallicity

On larger scales and in high-metallicity environments, [C II] acts as a calorimeter as it is the main coolant of the ISM. The heating comes from far-UV (FUV) photons causing electrons to be ejected from dust grains due to the photoelectric effect. Most recently De Looze et al. (2014) and Herrera-Camus et al. (2015) have shown that [C II] emission correlates well with other star formation rate tracers, specifically Hα and 24 μm, on kiloparsec scales in nearby galaxies. On smaller scales Kapala et al. (2015) found that the correlation between [C II] and star formation rate holds, although much of the [C II] emission in M31 comes from outside of star-forming regions, as the FUV photons that heat the gas travel long distances diffusing throughout the gas disk. When the M31 observations are averaged over kiloparsec scales, Kapala et al. (2015) recovers the relationship between [C II] and

star formation rate observed in other galaxies.

Both De Looze et al. (2014) and Herrera-Camus et al. (2015) show that the scatter in the correlation between [C II] and star formation rate (SFR) increases as the metallicity decreases. The breakdown in the tight [C II]SFR relationship can be understood in terms of a decrease in the photoelectric heating efficiency and/or an increase in the FUV photon escape fraction. In a low-metallicity environment there is less dust, allowing FUV photons to propagate farther through the gas and potentially escape the region or even the galaxy. The increase in the propagation distance causes the [C II] emission to be less co-localized with the recent massive star formation. If the FUV propagation distance is longer than the scale on which the [C II] emission is compared to other star formation indicators, that increases the scatter in the [C II]-SFR relationship. When the propagation distance is larger than the scale of the gas disk a fraction of the FUV photons escape the galaxy. The [C II] emission will then underestimate the star formation rate even when considering integrated properties. This is consistent with the lower [C II] emission per unit star formation rate (estimated combined from FUV and 24 μm emission) observed at lower metallicities by De Looze et al. (2014).

On small scales, [C II] traces the H_2 by reflecting the cooling of the gas, through accounting for the amount of emission attributed to collisions with H_2 molecules. This requires removing the contribution to the emission due to the cooling of the atomic gas, and understanding the conditions (temperature and density) that account for the [C II] excitation. In this context, the star formation rate is only important in that it is the source of FUV photons that ionize the carbon and heats

the PDR. Because this takes place on the scale of individual H II regions, the fraction of FUV photons that ultimately escape the galaxy does not enter in the estimates. The fact that at lower metallicity the PDR region at $A_V \lesssim 1$ is physically very extended makes [C II] an excellent tracer of "CO-faint" molecular gas. The excellent correspondence between the H_2 S(0) line emission and [C II] emission (see Figure 4.4), and the general correspondence between the [C II] and ^{12}CO emission (see Figure 3.9) demonstrates that [C II] traces the structure of the molecular gas at low metallicity.

3.5.3 Comparing [C II]-bright and CO-bright H_2

We estimated the amount of molecular gas using [C II] to trace the "CO-faint" molecular gas at low A_V ("[C II]-bright" molecular gas) and ^{12}CO to trace the molecular gas at high A_V using a Galactic X_{CO} to convert the observed emission to molecular gas ("CO-bright" molecular gas). Figure 3.16 shows the fraction of the total molecular gas coming from [C II] as a function of A_V estimated from dust. We see that at the low metallicity of our mapped SMC regions most of the molecular gas is traced by [C II], not CO, with $\sim$ 70% of the molecular gas coming from [C II]-bright regions on average. The data also shows the expected trend of a higher fraction of the total molecular gas being traced by CO as A_V increases, although with a lot of scatter. The scatter is in part due to the fact that our A_V estimate uses data with lower resolution than the [C II] or the CO observations, and in part due to our limitations at estimating the physical conditions from the available data. But

more fundamentally, much of the scatter must arise from the fact that the relevant A_V for photodissociation is not the line-of-sight extinction that we measure, but the A_V toward the dominant sources of radiation. Note that given methodology the molecular gas estimate from [C II] is more likely to underestimate than overestimate, suggesting that the "[C II]-bright" molecular fractions may be preferentially higher.

In the SWBarN and N22 regions CO traces at most $\sim 50\%$ of the molecular gas at our maximum A_V. The trend in the SWBarS region is considerably steeper, and around $A_V \sim 1$ it reaches "CO-bright" fractions of $\sim 70\%$. This is consistent with the fact that this region hosts the brightest ^{12}CO and ^{13}CO emission. The range of observed "[C II]-bright" molecular gas fractions are consistent with the estimated fractions for regions in the SMC with velocity-resolved [C II] spectra by Requena-Torres et al. (2016), who find 50% to $\sim 90\%$ of the molecular gas is traced by [C II] emission. The fractions of "CO-faint" molecular gas in the SMC are much higher than fractions found in local Galactic clouds ($f_{\rm CO-faint} = 0.3$, Grenier et al. 2005), and fractions in dense molecular clouds estimated from [C II] emission ($f_{\rm CO-faint} = 0.2$; Langer et al. 2014). The fractions in the SMC are more similar to those found using [C II] emission in diffuse Galactic clouds ($f_{\rm CO-faint} = 0.75$ for clouds with no detectable ^{12}COemission, Langer et al. 2014). Overall, the high fractions of [C II]-bright gas suggest that most of the H_2 gas in the SMC is found within PDRs or in regions with PDR-like conditions.

Figure 3.17 shows that, despite the fact that most molecular gas is related to [C II] rather than CO emission, our estimates for $N_{\rm H_2}$ are correlated with the ^{12}CO integrated intensity. The black dashed line in Figure 3.17 shows the estimated

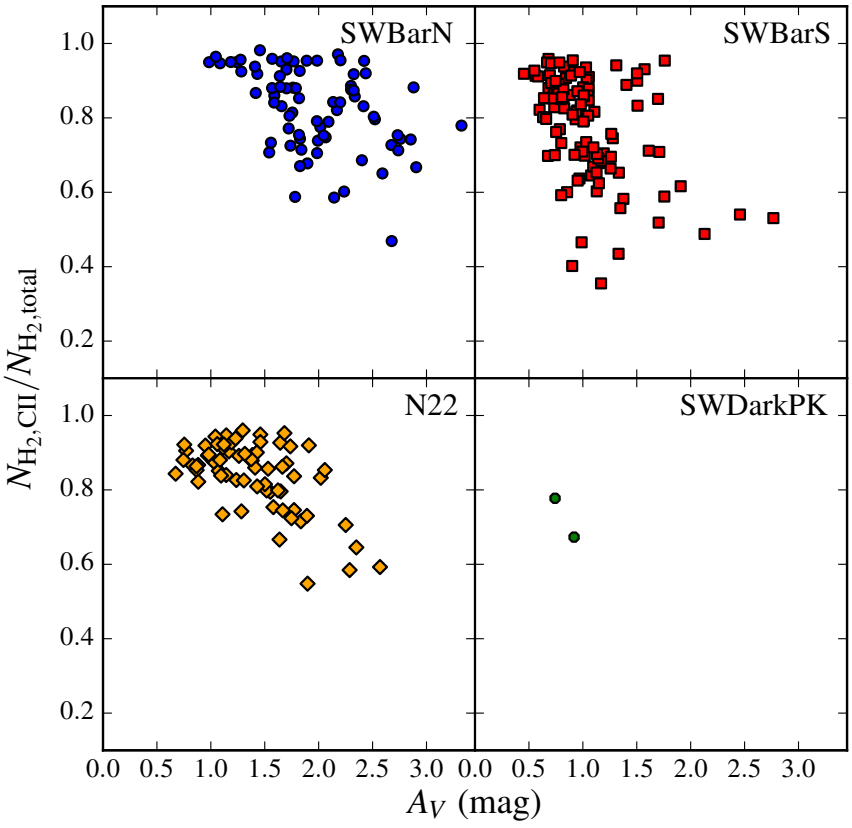

Figure 3.16 Relationship between the ratio of $N_{\mathrm{H_2,[CII]}}$ to $N_{\mathrm{H_2,total}}$ as a function of A_V for the ALMA regions where $N_{\mathrm{H_2,total}}$ is the combined estimate of H_2 from [C II] and H_2 from CO, the latter using a Galactic CO-to-H_2 conversion factor $X_{CO} = 2 \times 10^{20}$ cm^{-2} (K km s^{-1})$^{-1}$. The colored symbols show independent measurements with $I_{^{12}\mathrm{CO}} > 3\sigma$.

amount of $N_{\rm H_2}$ associated with CO using a Milky Way conversion factor of $X_{CO} = 2\times10^{20}$ cm^{-2} (K km s^{-1})$^{-1}$. There is a clear offset between the results from assuming a Galactic X_{CO} and our estimate for $N_{\rm H_2}$. This offset is due to the presence of molecular gas traced primarily by [C II] emission (at low A_V). Interestingly, we see that the relations are steeper than that in the Milky Way. The steeper slopes indicate that molecular gas builds up faster with CO intensity than it does in the Milky Way. This is due to the presence of "[C II]-bright" H_2 along the line-of-sight toward CO emission: simply the result of the fact that "CO-bright" regions still have substantial [C II] emission associated with them at the resolution of our measurements.

3.5.4 The CO-to-H_2 Conversion Factor in the SMC

We use our $N_{\rm H_2}$ determination to estimate the values of X_{CO} throughout the mapped regions, accounting for both "[C II]-bright" and "CO-bright" molecular gas. Figure 3.18 shows our estimates of X_{CO} as a function of A_V, where there is a trend of decreasing X_{CO} with increasing A_V albeit with significant scatter. The trend in X_{CO} matches the expectation of extended envelopes of "[C II]-bright" molecular gas, and it compares well with similar trends seen in low metallicity molecular cloud simulations (Shetty et al. 2011; Szűcs et al. 2016). The scatter can be explained as due to the "breakdown" of a single value of X_{CO} on small scales in simulations and even observed clouds, due to the clumpy nature of molecular clouds (Glover & Mac Low 2011; Shetty et al. 2011; Bolatto et al. 2013).

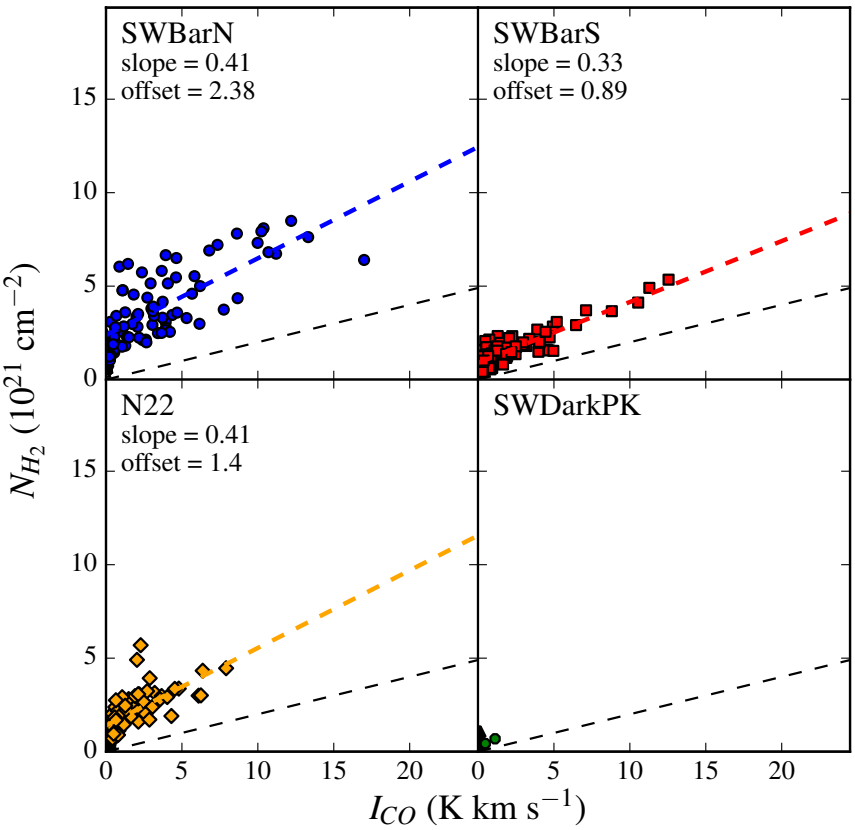

Figure 3.17 Relationship between I_{CO} and $N_{\rm H_2}$ for the ALMA regions where $N_{\rm H_2}$ is the combined estimate of H_2 from [C II] and from CO using the Galactic CO-to-H_2 conversion factor $X_{CO} = 2 \times 10^{20}$ cm^{-2} (K km s^{-1})$^{-1}$. The colored symbols show independent measurements detected at $> 3\sigma$ in ^{12}CO. There is good correlation between CO and H_2, and the slope of the relationship is X_{CO}. The thick dashed colored lines show the linear fits to the data; the slope steeper slopes correspond to higher values of X_{CO}. The over plotted black dashed lines shows the Galactic conversion factor (X_{CO}) appropriate for the Milky Way and resolved measurements (Bolatto et al. 2013).

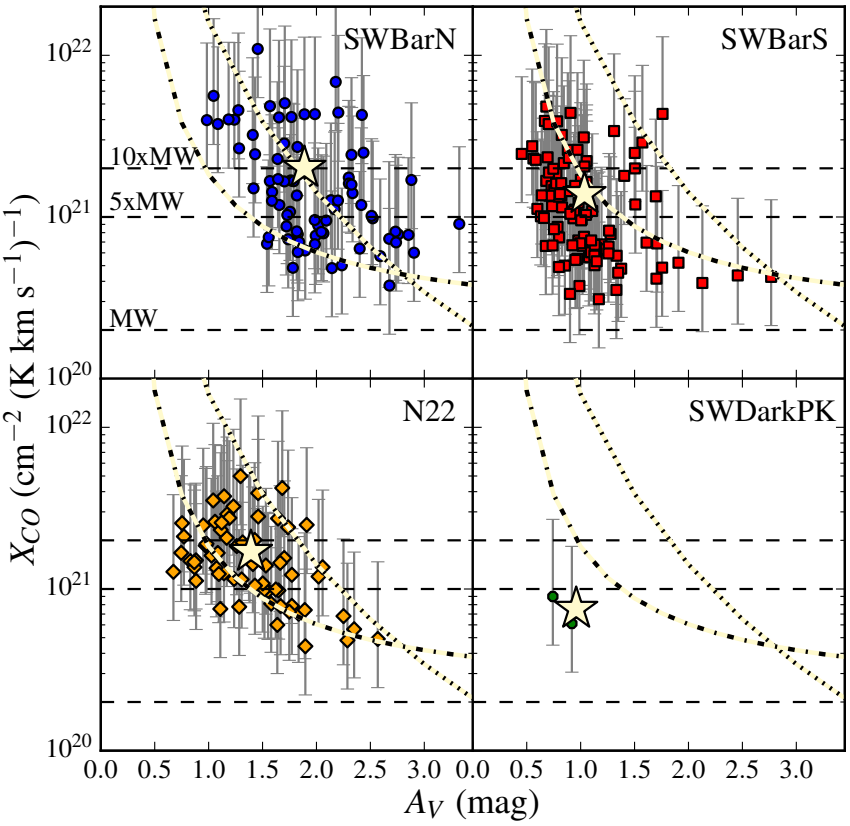

Figure 3.18 The CO-to-H_2 conversion factor (X_{CO}) as a function of A_V for the ALMA regions where the H_2 used is the combined estimate of H_2 from [C II] and H_2 from CO using a Galactic of $X_{CO} = 2 \times 10^{20}$ cm^{-2} (K km s^{-1})$^{-1}$. The colored symbols show independent measurements detected at $> 3\sigma$ in ^{12}CO with the error bars showing the factor of 2 uncertainty in N_{H_2}, with the star symbols showing the mean A_V and X_{CO} for each region. The over plotted dashed lines show scalings of the Galactic conversion factor appropriate for the Milky Way and resolved measurements (Bolatto et al. 2013). The dotted line shows the estimate of X_{CO} based average CO luminosity, the average N_{H_2}, and the average A_V over the entire cloud for the simulations of molecular clouds by Glover & Mac Low (2011). The dash-dotted line shows similar cloud-averaged estimate of X_{CO} as a function of A_V from the PDR models from Wolfire et al. (2010) for the SMC metallicity and radiation field strength of 40 G_0, the approximate mean radiation field found in the regions (see Section 3.4.3.2).

The values we find for our regions have on average a conversion factor of $X_{CO} \sim 5\, X_{CO,\mathrm{MW}}$. For the entire SMC, and using the dust-based molecular gas estimates, Jameson et al. (2016) find a CO-to-H_2 conversion factor ~ 17 times higher than the average Milky Way value. The difference between these two results can be mostly ascribed to the bias in our chosen HS^3 fields. Our survey selected actively star-forming regions with bright CO emission, whereas most of the SMC is faint in CO: in fact our regions contain some of the peaks of CO emission in the SMC. But even within our observed regions many lines of sight have high fractions of H_2 not traced by "bright-CO" emission (see Figure 3.16). The higher global measurement is simply a statement of the fact that the extinction in a typical molecular line-of-sight in the SMC is probably $A_V \sim 0.5 - 1$. Accounting for the dust-to-gas ratio of 1/5-1/7 the Galactic value, the same line-of-sight would have $A_V \sim 2.5 - 7$ in the Milky Way and emit brightly in CO. Even in our highly biased regions bright in CO we barely reach $A_V \sim 2.5$ in the SMC (Figure 3.18).

We can compare our estimates of X_{CO} versus A_V with theoretical studies of the relation between CO and H_2 at low metallicity. Wolfire et al. (2010) present a model of molecular clouds in order to understand the fraction of H_2 not traced by bright CO emission as a function of metallicity. They assume spherical clouds with r^{-1} density profile, predicting the fraction of "CO-faint" gas based on their mean volume density, external radiation field, mean A_V ($\langle A_V \rangle$), and metallicity relative to Galactic (Z'). Glover & Mac Low (2011) and more recently Szűcs et al. (2016) create simulations of molecular clouds with varying conditions, including metallicity, finding an empirical relationship for the mean X_{CO} value as a function

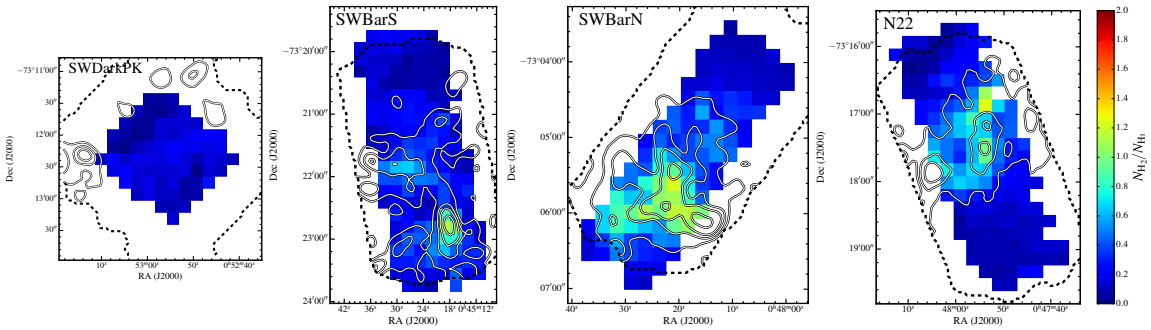

Figure 3.19 Ratio of the estimate of the total molecular gas column (using [C II] and ^{12}CO) to $N_{\rm HI}$ estimated to be associated with the molecular cloud (see Section 3.4.2). The black contours show the ALMA ^{12}CO (2-1) integrated intensity (convolved to [C II] resolution of 12″) at levels of 1.6 ($\sim 3\sigma$), 8, 16, 32, and 48 K km s^{-1}. We see that faint CO emission extends to $N_{\rm H_2}/N_{\rm HI} \sim 0.5$, which is beyond the estimated molecular to atomic transition.

of the mean A_V for the simulated clouds. The trend predicted by the Wolfire et al. (2010) calculations is

$$X_{CO} = X_{CO,0} \exp\left(\frac{4\Delta A_V}{\langle A_V \rangle}\right) \exp\left(\frac{-4\Delta A_V}{\langle A_V \rangle / Z'}\right) \tag{3.13}$$

where

$$\Delta A_V = 0.53 - 0.045 \log\left(\frac{G_0}{n}\right) - 0.097 \log\left(Z'\right), \tag{3.14}$$

while Glover & Mac Low (2011) find

$$X_{CO} = \begin{cases} X_{CO,0} \left(\langle A_V \rangle / 3.5\right)^{-3.5} & \text{if } \langle A_V \rangle < 3.5 \text{ mag} \\ X_{CO,0} & \text{if } \langle A_V \rangle \geq 3.5 \text{ mag} \end{cases} \tag{3.15}$$

where $X_{CO,0}$ is the mean value for the Milky Way.

In Figure 3.18 we overplot the predicted X_{CO} trend from Wolfire et al. (2010) using the metallicity of the SMC ($Z' = 0.2$), an average $n = 5000$ cm^{-3}, and $G_0 = 40$

based on the PDR modeling we did (see Section 3.4.3.2). We also overplot the empirical fit from the simulations by Glover & Mac Low (2011). Both predictions are close to the data for both individual lines of sight and for the averages within a region (indicated by the star), although Wolfire et al. (2010) seems to do a better job overall. As both the Wolfire et al. (2010) model and Glover & Mac Low (2011) simulations suggest, the main effect driving the relationship between X_{CO} and A_V is not metallicity itself, but how metallicity (and environment) affect the FUV shielding in the molecular gas. In particular, the critical element is the dust-to-gas ratio in the medium.

3.5.5 ^{12}CO and the Molecular to Atomic Transition

It is interesting to look at the molecular-to-atomic transition using our new measurements. We estimate the molecular to atomic ratio using our total molecular gas estimate, $N_{\rm H_2}$, and the H I column density map associated with the molecular cloud. The $N_{\rm H\,I}$ map is the same that we used to determine the amount of [C II] emission associated with H I gas (see Section 3.4.2), which was produced by only integrating the H I emission over a velocity range that is centered on the ^{12}CO line velocity, but $\pm$25% wider than the range of velocities with observed ^{12}CO emission throughout each the region. Figure 3.19 shows the maps of the $N_{\rm H_2}/N_{\rm H\,I}$ ratio with overlaid ALMA ^{12}CO contours. As expected for the atomic-dominated SMC, we observe peak molecular-to-atomic ratios of $N_{\rm H_2}/N_{\rm H\,I} \sim 1.5$ that show that the amount of molecular gas does not greatly exceed the amount of H I gas along the line-

of-sight due to the large amount of atomic gas. We also see ^{12}CO emission out $N_{\rm H_2}/N_{\rm HI} \sim 0.5$, which is beyond where we estimate the molecular gas to dominate over the atomic gas. The observation of ^{12}CO emission out to the region where we estimate the molecular-to-atomic transition occurs indicates that the molecular gas is truly "CO-faint" and not "CO-dark." We note, however, that trying to use CO to estimate molecular masses at low metallicities rapidly runs into the problem of the fast growth in the conversion factor and its steep dependence on local conditions, nominally A_V or column density.

3.6 Summary and Conclusions

We present results from the *Herschel* Spectroscopic Survey of the SMC (HS^3), a survey that mapped far-IR cooling lines in five star-forming regions. These data are complemented by APEX CO observations in the SMC Wing region N83, ALMA ACA observations of the Southwest Bar of the SMC that mapped four of the five HS^3 regions in ^{12}CO, ^{13}CO, and C^{18}O, and by SOFIA GREAT observations that will be presented fully in a forthcoming paper. The main results from these new observations are:

1. The [C II] 158 μm line is detected throughout the entirety of the regions. The [O I] 63 μm emission is also very widespread, and detected throughout large portions of the regions including faint diffuse areas (§3.3.1, Figure 3.1).

2. The [O I]/[C II] ratio is fairly uniform throughout all the regions with an average value of [OI]/[CII] ~ 0.3 (§3.3.1, Figure 3.2).

3. We do not detect the [N II] 122 μm line, but we do detect the [N II] 205 μm line in every region with FTS spectroscopy. Using the upper limit on the [N II] 122 μm observations, the observed [N II] 122 μm/205 μm ratio is consistent with an electron density $n_e \lesssim 20$ cm^{-3} (§3.3.2, Figure 3.5).

4. We find [O III]/[C II] ratios in the H II regions that are high compared to more massive, higher metallicity galaxies (§3.3.3, Figure 3.6).

5. Our ALMA ACA ^{12}CO maps include the total power correction and show small (few pc), bright structures with bright ^{13}CO surrounded by more diffuse, faint emission. We do not detect C^{18}O in any of the regions. We find ^{12}CO/^{13}CO $\sim 7-13$, which translates to ^{12}CO optical depths of $\tau_{^{12}\mathrm{CO}} \sim 4.5-11$ assuming the ^{13}CO emission is optically thin (§3.3.4, Figures 3.7 and 3.8).

6. The ^{12}CO/[C II] ratios are $\sim 1/5$ the average ratio found for the Milky Way and increase with A_V, reaching the Milky Way ratio or higher. The low ^{12}CO/[C II] ratios at low A_V suggests that there is a layer of molecular gas not traced by bright ^{12}CO emission, which is confirmed by our modeling (§3.3.6, Figures 3.9 and 3.11).

We see evidence that the [C II] emission traces molecular gas in regions where the CO is expected to be photo-dissociated from the low ^{12}CO/[C II] ratios and good correspondence between the [C II] structure and the H_2 S(0) and ^{12}CO emission. We use the [C II] and ^{12}CO emission to estimate the total molecular gas assuming that the bright [C II] emission traces molecular gas at low A_V and ^{12}CO traces gas at high A_V. We first remove the possible [C II] emission from the ionized and atomic

gas (both CNM and WNM), and assume the remaining [C II] emission arises from molecular gas. We convert this emission to N_{H_2} using two different methods: the first assumes a fixed temperature and density of $T = 90$ K and $n = 4000$ cm^{-3}, and the second uses the n and G_0 from new SMC PDR models (see Appendix A) for the [C II], [O I], and total-IR combined with new [C II] cooling rates from Wolfire et al. (2016). The two methods produce similar results, but we choose to use the second method to account for variations in the conditions throughout the regions. We convert the ^{12}CO emission to a molecular gas estimate applicable in the high A_V regions of the clouds using a Milky Way conversion factor of $X_{CO} = 2 \times 10^{20}$ cm^{-2} (K km s^{-1})$^{-1}$. We estimate a factor of 2 uncertainty in our molecular gas estimates, but note that given our assumptions for the carbon abundance and PDR models that we are more likely to underestimate H_2.

Using our estimates of N_{H_2} using [C II] and ^{12}CO, we find that:

1. Our H_2 estimated from [C II] and ^{12}CO is mostly consistent with (although systematically lower than) larger-scale dust-based estimates from Jameson et al. (2016).

2. We find average fractions of the molecular gas traced by [C II] of $\sim 70\%$ and show that most of the molecular gas in the SMC is not traced by bright ^{12}CO emission, which is expected for low metallicity environments where H_2 is able to self-shield while CO is photodissociated.

3. We use the N_{H_2} estimated from [C II] and ^{12}CO to evaluate the CO-to-H_2 conversion factor (X_{CO}), and find X_{CO} decreases with increasing A_V. The

relationship between X_{CO} and A_V is consistent with models from Wolfire et al. (2010) and simulations from Glover & Mac Low (2011) and Szűcs et al. (2016), which suggests that the main effect of lowering the metallicity is to decrease A_V and the amount of shielding for a given gas column density.

4. Despite the fact that most of the molecular gas in the SMC is not traced by bright CO emission, we do observe faint ^{12}CO emission out to the estimated location of the molecular-to-atomic transition. Using the aggregate CO emission to obtain total molecular mass in a low metallicity environment suffers from the problem that it is very sensitive to the local A_V or column density.

Chapter 4: H_2 Rotational Line Emission in the SMC

4.1 Overview

While molecular hydrogen (H_2) is the most abundant molecule in the universe, H_2 line emission only traces warm gas or gas pumped by ultraviolet (UV) radiation. Generally, CO line emission is used to trace to cold, dense molecular gas associated with star formation owing to its brightness at low temperatures, which results from its available dipole transitions at lower rotational energies (due to the strong chemical bond between carbon and oxygen that makes the nuclear separation extremely small). While the H_2 molecule lacks a permanent dipole moment due to its symmetry, it has observable quadrupole rotation-vibration transitions that are visible in the near- and mid-infrared. The lowest energy transitions for the H_2 molecule is the pure rotational quadrupole ground transition, $J = 2 - 0$ or S(0), which has a temperature-equivalent energy of $E_u/k = 510$ K and critical density of $n_{crit,H} \sim 1000$ cm^{-2}, which are low enough to allow warm ($T \gtrsim 100$ K) molecular gas to emit. At low metallicity, most of the H_2 is in a "CO-faint" phase at low A_V that is largely associated with [C II] emission within photodissociation regions (PDRs; see Chapter 4). In the SMC, we have seen that the total molecular gas estimates from dust emission and the combination of [CII] $+^{12}$ CO emission shows

more extended molecular gas than the bright CO emission. With the H_2 rotational line emission, we can determine how much of this extended H_2 is warm. The conditions of this "CO-faint" molecular gas determines whether or not it can contribute directly to star formation.

The *Spitzer IRS* instrument provided a wealth of observations of the mid-infrared H_2 rotational lines, which are accessible only from space. Roussel et al. (2007) studied the H_2S(0) to S(7) lines in 57 galaxies as part of the SINGS survey, which represents a range in galaxy types from lower metallicity dwarf galaxies to normal star-forming disk galaxies to galaxies dominated by AGN emission. By modeling the line emission of the rotational transitions, Roussel et al. (2007) find warm H_2 ($T \geq 100$ K) column densities similar to those in resolved PDR regions and fractions of the warm molecular gas compared to the cold molecular gas traced by CO of $\sim 1 - 30\%$. For normal galaxies, they find evidence that the H_2 emission is consistent with excitation in PDR regions. Hunt et al. (2010) presents H_2 line observations from *IRS* spectra for 22 low metallicity ($12 + \log(\mathrm{O/H}) = 7.4 - 8.3$) blue compact dwarf galaxies (BCDs), but only $\sim 1/3$ have one or more of the S(0)-S(4) lines detected. Using the galaxies with at least two H_2 lines detected, they find high warm molecular gas masses compared to the SINGS galaxies and up to the same mass of warm molecular gas as neutral atomic gas. Additionally, they find no trend in the estimated mass of warm H_2 with metallicity, suggesting that metallicity and warm H_2 rotational line emission are not strongly linked. The SMC provides a unique laboratory to examine the conditions of the warm H_2 gas at low metallicity while being close enough that we can explore individual star-forming regions.

In this chapter, we present the results of our study of the warm H_2 gas and how it relates to the total molecular gas. In Section 4.2 we present the *Spitzer IRS* spectra and summarize the data reduction and the H_2 line flux extraction using PAHFIT. We then describe our simple modeling technique for the rotational H_2 line emission in Section 4.3 and the temperatures, column densities, and ortho-to-para ratio are presented in 4.4. Section 4.5 discusses the excitation mechanism of the H_2 gas line emission and the fraction of warm H_2 using the dust-based H_2 estimate (Chapter 2;Jameson et al. 2016) and H_2 estimate using [C II] and ^{12}CO from Chapter 3 and compare the fractions to other galaxies. Finally, we summarize the work and conclusions in Section 4.6.

4.2 Observations

The data come from the *Spitzer* Spectroscopic Survey of the SMC (S^4MC; Sandstrom et al. 2009, 2010, 2012), which used the Infrared Spectrograph (*IRS*) in the low resolution mode ($\lambda/\delta\lambda \approx 60 - 130$) to map six star-forming regions: N22, N66, N76, N83, SWBarN (named 'SW Bar 1' in the original observations), and SWBarS ('SW Bar 3'). The N22, SWBarN, and SWBarS region coverage overlaps (and exceeds) the *Herschel* Spectroscopic Survey of SMC coverage. The low resolution *IRS* spectra cover wavelengths from 5.5 μm to 38.0 μm, including the rotational quadrupole H_2 line transitions S(0) through S(7). The full spectral range is observed separately over the short-low (SL) and long-low (LL) orders. Each mapping observation included an "off" position outside of the SMC with minimal emission, which

was used to subtract foreground emission and reduce the effect of rogue pixels (pixels with abnormally high dark current and/or photon responsivity that changed during the mission). Using Cubism, additional bad pixels were removed and the spectral cubes were produced. Due to increasing numbers of "hot" pixels at wavelengths beyond ~ 35 μm, the LL spectra beyond 35 μm were removed. The details of the data reduction are described in Sandstrom et al. (2009, 2010, 2012).

Due to the varying point-spread function (PSF) with wavelength, all spectral frames are convolved to the resolution of the 38 μm wavelength ($\theta \approx 10''$) using convolution kernels based on the theoretical IRS PSFs determined using the modeling software sTinyTim. Before combining the four separate spectral order maps, SL2 ($5.2 - 7.6$ μm), SL1 ($7.5 - 14.5$ μm), LL2 ($14.5 - 20.75$ μm), and LL1 ($20.5 - 38.5$ μm), we scale the LL1 spectra to match the MIPS 24 μm flux using the SAGE maps (Gordon et al. 2011) that are convolved to the resolution of the *IRS* 38 μm PSF using the PSFs determined by Gordon et al. (2008). The individual orders are then stitched together by aligning the images, determining an average scale factor over the overlapping wavelength range, and then linearly interpolating over the overlap range. While Sandstrom et al. (2012) further refines the method for combining the spectra by accounting for temporally and spatially varying dark current, analogous to the "dark settle" seen in high resolution *IRS* spectra, we do not correct for this effect because it has only a minor impact on the overall result and none of our lines of interest occur in the overlap regions.

4.2.1 Measuring Line Fluxes

We re-sample each cube to have $\sim$ 1 pixel per 10″ beam. We extract the spectra in each pixel with full spectral order coverage and fit each spectrum using PAHFIT (Smith et al. 2007), which allows us to measure the fluxes from emission lines that are heavily blended with PAH emission lines (i.e. the H_2 S(4) line; see Figure 4.1). PAHFIT uses a model, consisting of starlight, thermal dust continuum, resolved dust features and feature blends (from PAHs), prominent emission lines, as well as simple fully-mixed or screen dust extinction, dominated by the silicate absorption bands at 9.7 and 18 μm. The PAHFIT routine fits the model (the combination of all the emission and absorption components) to the observed IRS spectrum using the Levenberg-Marquadt algorithm to minimize the global χ^2. The routine reports the formal statistical uncertainties from the IRS pipeline ramp fitting and the full uncertainties in combined quantities, such as integrated line intensities, from the full covariance matrices. Upper limits include additional uncertainty estimated based on the the residuals of the observed flux intensity from the best-fitting model.

Given the low metallicity and therefore low gas-to-dust ratio in the SMC, there is little dust extinction. We ran PAHFIT twice for each region: once with the fit for dust extinction turned on and once with the dust extinction fit turned off. As expected, the results from fitting for the dust extinction found low to no extinction. For our analysis, we use the results with no dust extinction due to the fact that the extinction curve used by PAHFIT is for the Milky Way, and there are known differences in the extinction curve in the SMC (Gordon et al. 2003) which

may introduce more uncertainty in the line intensities than the lack of an extinction correction.

In addition to the beam-sampled maps of the H_2 line intensity, we also create images of the lines by locally fitting the continuum and summing the flux. These maps are made at the native pixel scale of the LL1 spectral cubes of $\sim 1.5''$ and the maps are made for the full spectral order cube spatial coverage. PAHFIT is run for the combined cubes across all spectral orders (SL1, SL2, LL1, LL2), which have smaller spatial coverage than the individual order cubes because the SL and LL modules do not completely overlap in the sky (see Figure 4.4). When running PAHFIT the routine does not always find emission in some or all of the H_2 lines, probably because of a combination of the complexity of the models, the low signal-to-noise in some of the wavelength ranges, and the faintness of the lines compared to the continuum and other dust emission and absorption features. The locally-fitted continuum will not produce reliable line fluxes due to the complexity of the spectrum, but it does provide a way to investigate the emission directly. We use these maps to look at the structure of the line emission.

4.2.1.1 Difficulty Measuring the H_2 S(3) Line

In many of the regions, the S(3) line is not detected at the nominal $> 3\sigma$ while the S(1), S(2), and S(4) lines (as well as occasionally some higher energy level transitions) are detected at $> 3\sigma$. The spectral orders in the *IRS* spectra are joined at $\sim 14 - 15$ μm and $\sim 20 - 21$ μm, so the difficulty extracting the S(3) 9.7 μm

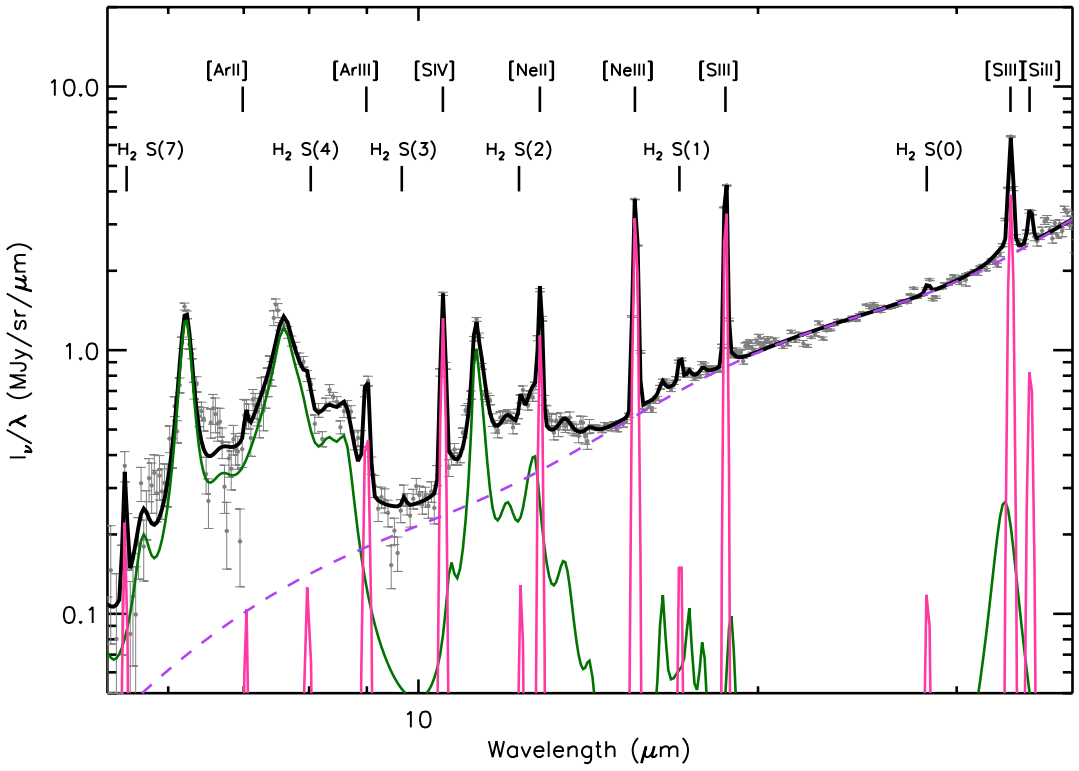

Figure 4.1 Example IRS spectrum, black boxes, from the SWBarS region with the PAHFIT result, shown in green. Purple, blue, and red lines show the emission line, PAH feature, and continuum fits, respectively. All of the emission lines fitted by PAHFIT are labeled (not shown, but included as possible emission lines: H_2 S(5) and S(6)).

line flux is not a result of the merging of the separate spectra. However, there is a silicate PAH absorption feature at 9.7 μm. While the overall extinction in the SMC is low, it is possible that there is more silicate dust than carbon dust given that the lines-of-sight with measured ultraviolet to near-infrared extinction curves show little to no 2175 Å "bump," which is attributed to graphite. The lack of the graphite feature has been explained by a different silicate-to-carbon dust ratio compared to the Milky Way (Pei 1992) or grain size distributions (Weingartner & Draine 2001), which may arise from small carbonaceous dust being preferentially ejected from the galaxy during the most recent starburst (Bekki et al. 2015) or from fundamental differences in the dust growth and destruction mechanisms at high and low metallicity. A possible explanation for the low S(3) line detections is difficulty in the PAHFIT routine fitting the absorption feature combined with the lower signal-to-noise at the shorter wavelengths (see Figure 4.1).

Figure 4.2 shows the H_2 line transitions fluxes in terms of the level populations and transition energy, also referred to as an excitation diagram (see Section 4.3). We expect that the upper levels of the transitions, particularly the pairs S(1), S(3) and S(2), S(4) will be populated by the same gas with a given temperature and column density. This results in a linear relationship between the pairs, with the slope indicating the temperature and the normalization the column density. Since radiative decay of the quadrupole transition changes by $\Delta J = 2$, these pairs are unaffected by variations in the ortho-to-para ratio. For the line-of-sight in Figure 4.2, the S(3) line flux is $\sim 1.5\sigma$, and represents an upper limit, shown by the green arrow. This low value for the upper limit of S(3) is much lower than what

would be expected for the ortho and para transitions coming from gas of a similar temperature: the possible slope between S(1) and S(3) is much steeper than that of the S(2) and S(4), which would indicate the gas is much colder. The uncertainty in the line flux reported by PAHFIT takes into account only the uncertainty at the line wavelength and the residuals from the model. However, the spectrum tend to have appreciable RMS levels near the S(3) transition that PAHFIT does not consider. When we estimate the RMS level in the spectrum near the S(3) line (± 0.25 μm), we find that the value is higher than the uncertainty from PAHFIT. When the RMS level of the spectrum is taken as the upper limit for the S(3) line flux, shown with the red downward triangle in Figure 4.2, the upper limit is consistent with a similar linear trend between between the S(1), S(2), and S(4) transition, which is what is expected and observed in other studies of H_2 rotational lines (e.g., Fuente et al. 1999; Habart et al. 2003; Roussel et al. 2007).

4.3 Modeling the Temperature, Column Density, and Ortho-to-para Ratio of the Warm H_2 Gas

With the H_2 line fluxes from PAHFIT, F_{ul}, we use excitation diagrams to visualize the distribution of level populations; it shows the column densities in the upper level of each transitions N_u, normalized by its statistical weight g_u, as a function of the of the energy of the transition E_{ul}. The level column densities are calculated using the measured fluxes of the line transitions:

$$N_u = \frac{4\pi F_{ul}}{h\nu_{ul} A_{ul} \Omega}, \tag{4.1}$$

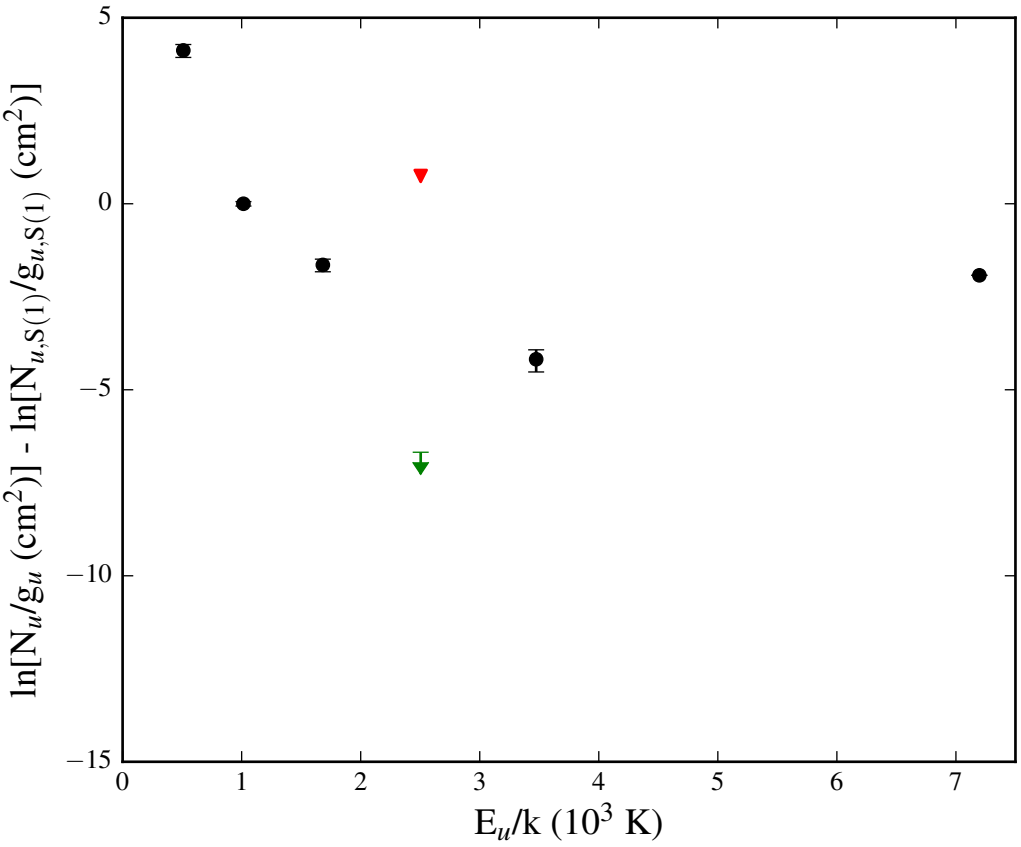

Figure 4.2 An example of an excitation diagram from the SWBarS region for a spectrum where PAHFIT reports a detection of the S(3) line at $< 3\sigma$ or upper limit. The black points with error bars show the line transitions detected at $< 3\sigma$, which are the S(0), S(1), S(2), and S(4) lines. The S(3) upper limit using the values reported by PAHFIT is shown with the green arrow, and falls significantly below the S(1), S(2), and S(4) line intensities. The red downward arrow shows the estimated upper limit based on the RMS in the spectrum ± 0.25 μm around the S(3) line at 9.66 μm, which makes the measurement consistent with the S(3) intensity following the approximate linear relationship seen for the other transitions.

where A_{ul} is the spontaneous emission probability for the $u \rightarrow l$ transition, $h\nu_{ul}$ is the transition energy ($E_{ul} = E_u - E_l$), and Ω is the beam solid angle. Figure 4.3) shows an example of a typical excitation diagram for one line-of-sight (i.e., pixel) in the SWBarS region.

We follow the basic methodology of Roussel et al. (2007) for the SINGS galaxies, which builds off of previous work by Rigopoulou et al. (2002) and Higdon et al. (2006), and assume there are two discrete gas components along the line of sight: a cool and a warm component. Assuming local thermodynamic equilibrium (LTE), we use the Boltzmann Equation:

$$\frac{N_u}{g_u} = N_{gas}\left[\frac{e^{-E_u/kT_{gas}}}{Z(T_{gas})}\right], \text{ where } Z(T_{gas}) \sim \frac{0.024T_{gas}}{1 - e^{-6000K/T_{gas}}} \tag{4.2}$$

Since we only consistently detect the S(0) ($J = 2-0$), S(1) ($J = 3-1$), S(2) ($J = 4-2$), and S(4) ($J = 5-3$) transitions, we chose four free parameters: warm gas column density (N_{warm}), cool gas column density (N_{cool}), warm gas temperature (T_{warm}), and the ortho-to-para ratio (OPR) to scale the warm component of S(1) to S(2) and S(4). We adopt the following methodology to determine the four parameters.

1. We assume the S(2) and S(4) emission come solely from the warm gas component and use them to fit T_{warm} and N_{warm} simultaneously:

$$\frac{N_{u,2}}{g_{u,2}} = N_{warm}\frac{e^{-E_u/kT_{warm}}}{Z(T_{warm})}, \frac{N_{u,4}}{g_{u,4}} = N_{warm}\frac{e^{-E_u/kT_{warm}}}{Z(T_{warm})}. \tag{4.3}$$

   When put in terms of $ln(N_u/g_u)$ as a function of E_u/k, the slope between the S(2) and S(4) emission gives T_{warm} and the offset gives N_{warm}.

2. We assume that all of the emission in the S(0) transition originates in the cool

gas. Instead of fitting T_{cool}, as in Roussel et al. (2007), we fix the cool gas temperature to $T_{cool} = 100$ K, consistent with the cool component temperatures found for the SINGS galaxies, and use S(0) to calculate N_{cool}:

$$\frac{N_{u,0}}{g_{u,0}} = N_{cool}\frac{e^{-E_u/k*100\mathrm{K}}}{Z(100\mathrm{K})}, \tag{4.4}$$

3. The last parameter, OPR, is the scaling factor for the warm component of S(1) to account for potential deviations from the high temperature LTE ratio of $OPR = 3$, including non-equilibrium conditions between ortho and para transitions:

$$\frac{N_{u,1}}{g_{u,1}} = N_{cool}\frac{e^{-E_u/k*100\mathrm{K}}}{Z(100\ \mathrm{K})} + OPR \times N_{warm}\frac{e^{-E_u/kT_{warm}}}{Z(T_{warm})}. \tag{4.5}$$

4.3.0.1 The Effect of Dust Continuum Emission on the H_2 S(0) 28.2 μm Line Flux

The H_2 S(0) 28.2 μm line is at long enough wavelengths that it occurs in a part of the spectrum that begins to be dominated by thermal emission from warm dust in the ISM ($T \sim 50 - 100K$). For the H_2 line emission, the solution to the equation of radiative transfer is

$$I_{obs} = I(0)e^{-\tau_{\mathrm{H_2}}} + S_{\mathrm{H_2}}(1 - e^{-\tau_{\mathrm{H_2}}}) \tag{4.6}$$

where $I(0)$ is the intensity of background radiation, $S_{\mathrm{H_2}}$ is the source function from the H_2 gas, $\tau_{\mathrm{H_2}}$ is optical depth of the H_2, and I_{obs} is the emergent intensity that we observe. The correction from the effect of thermal dust emission on the S(0) line intensity has not been explored by recent H_2 studies. In the following section, we explore what effect the dust emission might have on the observed H_2 line intensity.

While in reality the dust is dispersed throughout the gas, most of the gas in the SMC is neutral hydrogen traced by H I emission. The H I profiles in the SMC are wide and the multiple peaks indicate a complex velocity structure Stanimirović et al. (2004). While Stanimirović et al. (2004) see evidence for differential rotation based on the H I velocity structure across the SMC, the assumed scale height of neutral gas is set to 1 kpc based on the typical sizes of large H I shells, which is a significant fraction of the observed $\sim$ 4 kpc projected size in the plane of the sky. The molecular, star-forming gas represents only a small fraction of the total gas (Jameson et al. 2016) and the observed ^{12}CO and [C II] line profiles are narrow and overlap over a small range of the velocities with H I emission (see Chapter 3, Figure 3.10). Given that the observations suggest the H_2 gas spatial extent is likely small compared to that of the H I, most of the emission from dust will either be foreground or background.

Expanding shells in the H I gas appear to be the most likely mechanism that can explain complex, multi-peaked H I emission profiles (Hindman 1967; Staveley-Smith et al. 1997). Assuming that the wide and multiple-peaked H I profiles are due to expanding shells in the gas, we use that framework to determine whether the majority of the gas, and therefore dust, is in front of or behind the H_2 gas. In general, the SMC is moving towards the MW and has positive H I line velocity in the range $v_{heliocentric} \sim 120 - 200$ km s^{-1} (Stanimirović et al. 2004). The tendency for the ^{12}CO emission, particularly in the Southwest Bar, to be found at the lower end of the H I velocities would correspond to the molecular gas being located in the more distant side of the H I shell where the line emission is red-shifted to smaller

velocities compared to the average velocity of the gas. Conversely, we see that the velocity of the ^{12}CO emission in the N76 region is near the higher end of the H I velocity range (past the main peak in the emission) and is likely found behind much of the H I gas such that the dust would act as a foreground emission.

Given that we see evidence for some regions that the dust emission is likely to be background and in others foreground, we explore what correction factors would be necessary to compensate for either situation. We first make the assumption that the thermal dust emission acts as background radiation source. Assuming that the optical depth of the H_2 emission is low ($\tau_{H_2} \ll 1$), the relationship becomes

$$I_{obs} = I_{dust}(0)(1 - \tau_{H_2}) + \tau_{H_2} S_{H_2}, \tag{4.7}$$

which can be rearranged to be

$$I_{obs} - I_{dust}(0) = \tau_{H_2}(S_{H_2} - I_{dust}(0)). \tag{4.8}$$

Ultimately, we are interested in the source emission of the H_2 and need to correct for the dust emission. The PAHFIT routine accounts for the contribution of the dust emission to the observed emission, such that

$$I_{H_2,\mathrm{PAHFIT}} = I_{obs} - I_{dust}(0) = \tau_{H_2}(S_{H_2} - I_{dust}(0)), \tag{4.9}$$

where

$$I_{H_2,\mathrm{intrinsic}} = \tau_{H_2} S_{H_2} \text{ and } I_{dust}(0) = \tau_{\mathrm{dust}} S(T_{\mathrm{dust}}) \tag{4.10}$$

However, this intensity still includes a contribution from the dust emission that reduces the observed line intensity. Assuming LTE, S_{H_2} and $S(T_{\mathrm{dust}})$ are determined

by the Planck function and the H_2 flux from PAHFIT compared to the intrinsic H_2 flux scales such that

$$\frac{F_{\rm H_2,PAHFIT}}{F_{\rm H_2,intrinsic}} \propto 1 - \frac{\tau_{\rm dust,28\mu m} B(T_{\rm dust,28\mu m})}{B(T_{\rm H_2})} = 1 - \frac{\tau_{\rm dust,28\mu m}(e^{h\nu/kT_{\rm H_2}} - 1)}{(e^{h\nu/kT_{\rm dust,28\mu m}} - 1)} \tag{4.11}$$

and the correction factor (f_{corr}) to the line flux measured from PAHFIT for background dust emission is

$$f_{corr,bg} = \left[1 - \frac{\tau_{\rm dust,28\mu m}(e^{h\nu/kT_{\rm H_2}} - 1)}{(e^{h\nu/kT_{\rm dust,28\mu m}} - 1)}\right]^{-1} \tag{4.12}$$

If the dust emission is the foreground source, then the emission measured by PAHFIT becomes

$$I_{\rm H_2,PAHFIT} = (\tau_{\rm H_2} S_{\rm H_2})(1 - \tau_{\rm dust,28\mu m}), \tag{4.13}$$

and the correction factor is

$$f_{corr,fg} = [1 - \tau_{\rm dust,28\mu m}]^{-1}\,. \tag{4.14}$$

Estimating the additional correction due to dust continuum emission requires knowing the dust temperature and optical depth at the wavelength of the H_2 S(0) line at 28 μm. While the majority of the dust in the SMC have low equilibrium temperatures of $T_{\rm dust} \sim 20 - 30$ (Gordon et al. 2014; Lee et al. 2015a), this cold dust is unlikely to contribute much, if any, emission to the thermal dust continuum at 28 μm. The main continuum dust emission at 28 μm is likely due to warm dust. PAHFIT uses a combination of up to 8 thermal dust continuum components composed of modified blackbodies with at fixed temperatures of $T_{\rm dust}$ = 35, 40, 50, 65, 90, 135, 200, 300 K to fit the dust continuum in the IRS spectra.

While the PAHFIT results are not intended to measure the properties of the warm dust, it does provide an indication of the temperature of the emitting dust. We use the temperature of the warm dust component contributing the most emission at 28 μm as the dust temperature to compute the blackbody emission from dust in the correction factor. We use the map of dust temperature in the SMC from Lee et al. (2015a) (re-gridded to match the H_2 S(0) image) to convert to the dust optical depth at 160 μm (τ_{160}) using the HERITAGE 160 μm map and then scale the values to estimate the dust optical depth at 28 μm (τ_{28}) assuming $\tau_\lambda \propto (\lambda/\lambda_0)^2$ (Draine 2003). This essentially provides a worst-case scenario for the impact of dust continuum on the measurements of H_2, since it is equivalent to assuming that all the dust contributing at 160 μm is causing the emission near 28 μm.

We find warm dust temperatures at 28 μm from PAHFIT of 65 K and 90 K throughout the regions and the maximum estimated dust optical depth of $\tau_{28} \sim 0.1$ K. Combining these produces a maximum possible correction to the S(0) line flux of $f_{corr,bg} \sim 5\%$ if the dust is a background source and $f_{corr,fg} \sim 10\%$ if the dust is a foreground source. These small possible correction factors are within the uncertainty on the measurement. As a result, we do not apply any correction factor to the S(0) line fluxes extracted using PAHFIT.

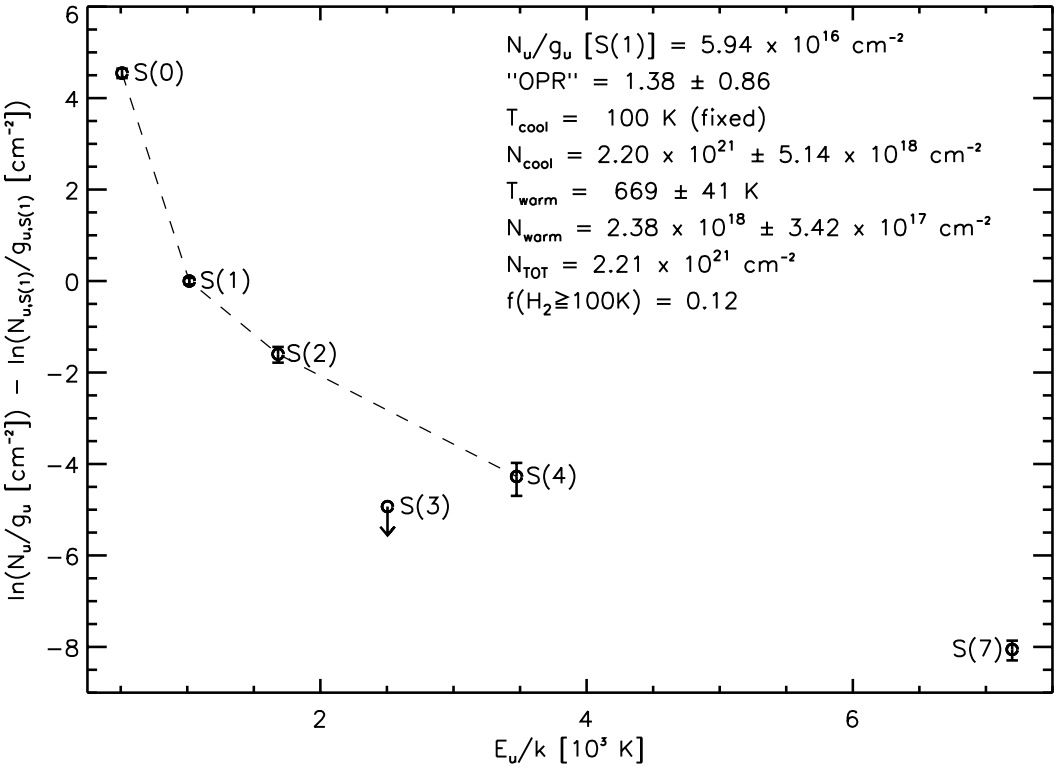

Figure 4.3 Representative excitation diagram from the SWBarS region for the same spaxel shown in Figure 4.1. The S(3) point shows the upper limit based on the PAHFIT results and is excluded in the analysis. The dashed line shows the fitted fluxes, with the fit parameters listed. The warm temperature, OPR, and f($H_2 \geq$ 100K) using the dust-based estimate (see Section 4.5.2) are all within the range of values found for SINGS galaxies (Roussel et al. 2007).

4.4 Results

Figure 4.4 shows the H_2 S(0) line emission found by fitting the local continuum with contours showing the Hα (Smith & MCELS Team 1999), tracing H II regions and site of recent massive star formation, and ^{12}CO emission, tracing the colder, high A_V regions of the molecular gas. The S(0) is expected to trace the cooler H_2 gas with $T \sim 100$ K given the lower equivalent temperature of $E_u/k = 510$ K and critical density of $n_{crit,H} \sim 1000$ cm^{-2}. The images show that the H_2 S(0) line emission generally follows the structure of the CO emission and the bright line emission is found around the H II regions. This morphology suggests that the S(0) line emission is associated with the photodissociation region (PDR) and that it traces the warm molecular envelope surrounding the cooler, denser, molecular cloud.

We observe that the spatial structure of the H_2 rotational line emission varies depending on the transition. Figure 4.5 shows the S(0) through S(4) line images for the SWBarS region using the line fluxes extracted from the *IRS* spectral cube using PAHFIT. The cube has been convolved and re-sampled to approximately one pixel per beam ($\sim 10'' \sim 3$ pc). The S(0) and S(1) lines are clearly detected throughout much of the region and generally show similar structure. The structure of the line emission begins to change with the higher energy transitions, likely tracing hotter gas. The main regions with S(3) emission are located around the peak in the S(0) line, which is consistent with what would be expected if the higher level transitions are tracing the hotter gas in the outer part of the PDR that is exposed to higher radiation field intensities.

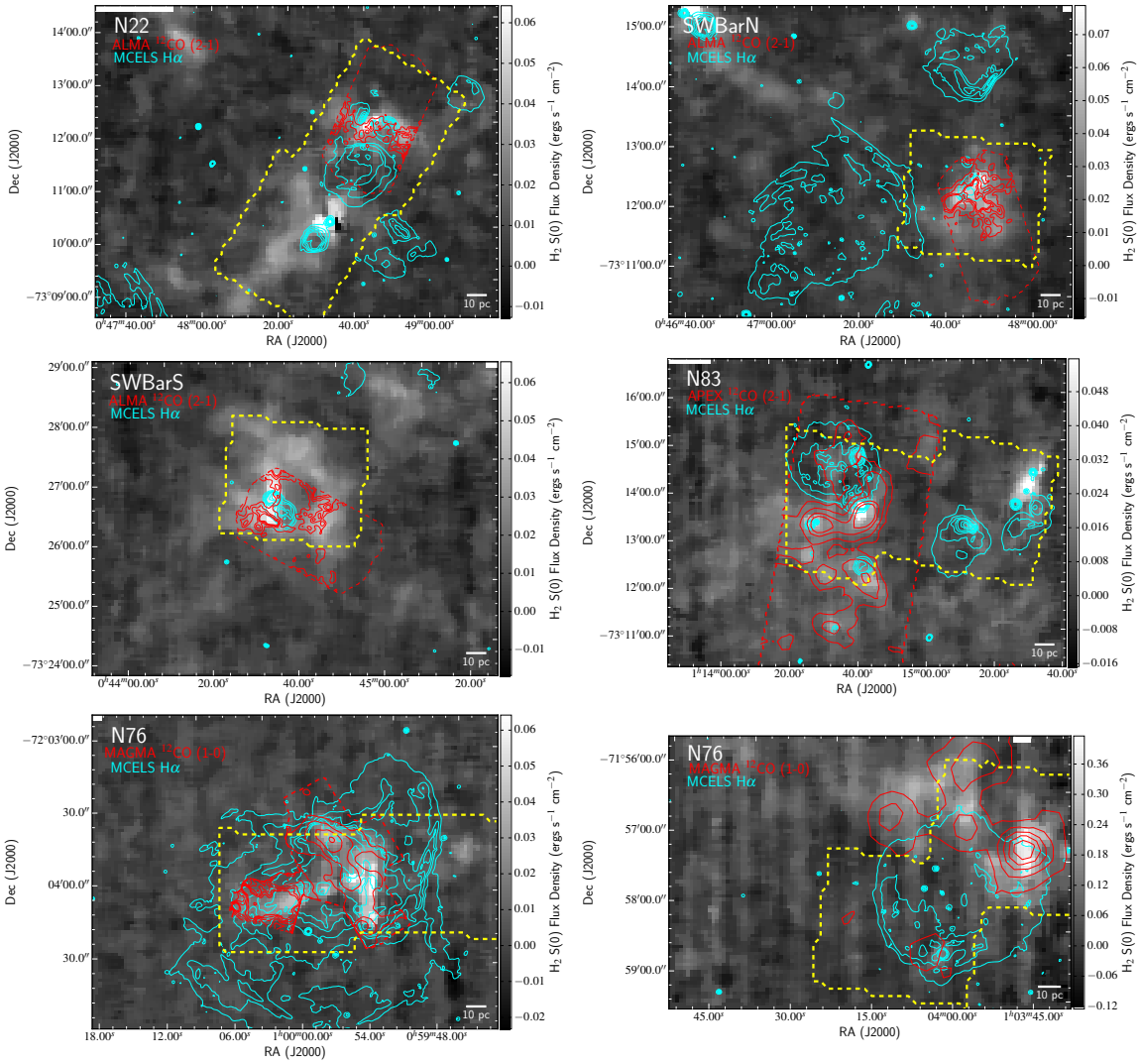

Figure 4.4 Maps of the H_2 S(0) line (measured by fitting and removing the continuum near the line) shown over the full coverage of the LL1 spectral cube with the native pixel scale of $\sim 1.5''$. The yellow dashed line shows the coverage of the final spectral cubes where all of spectral order cubes overlap. The red contours for N22, SWBarN, and SWBarS show the integrated ALMA ACA ^{12}CO $(2-1)$ ($\theta \sim 5''$) at levels of 10, 15, 25, 35 K km s^{-1}; for N83 they show APEX ^{12}CO $(2-1)$ ($\theta \sim 25''$) at levels of 10, 15, 25, 35 K km s^{-1}; for N66 they show SEST ^{12}CO $(2-1)$ ($\theta \sim 33''$; Rubio et al. 1996) The red dashed line showing the ^{12}CO map coverage. The cyan contours show MCELS Hα flux density (Smith & MCELS Team 1999) at levels of 1, 2, 3, 4, 5, 10, 15 10^{-14} ergs cm^{-2} s^{-1}.

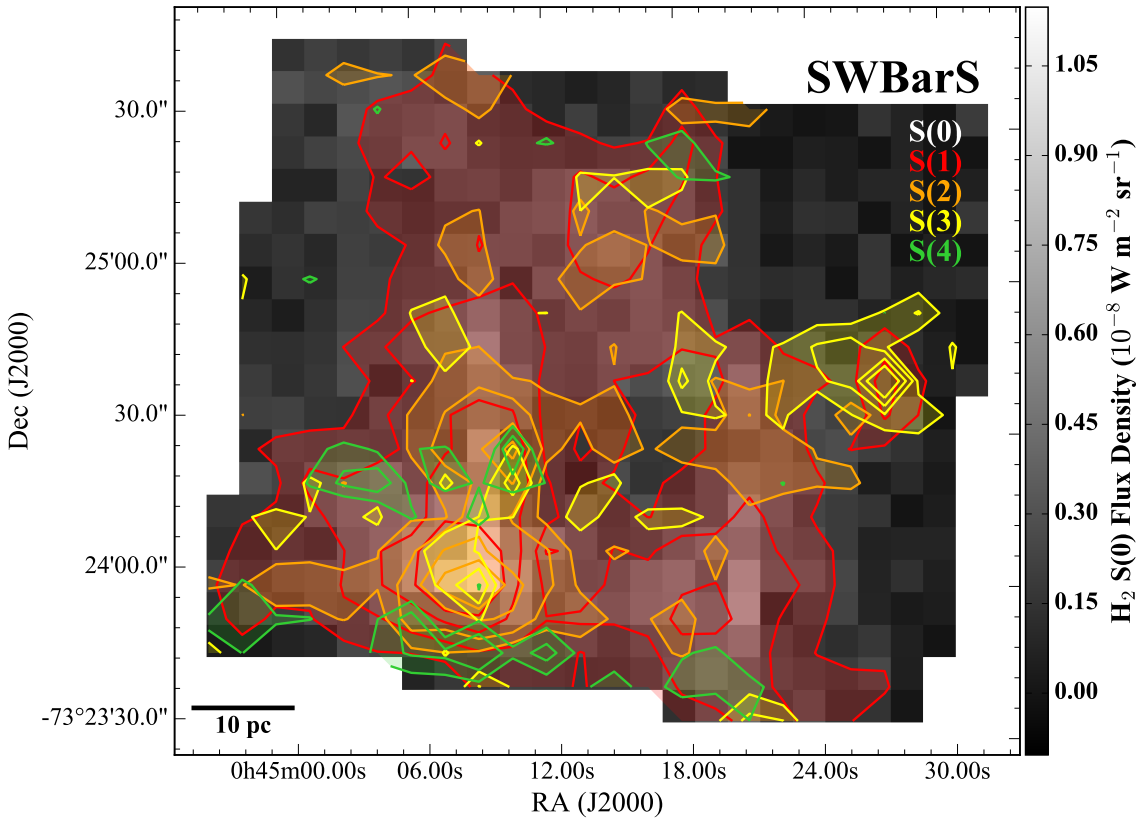

Figure 4.5 Maps of the H_2 S(0) line in the SWBarS region shown in greyscale with the red, orange, yellow, and green contours showing the S(1), S(2), S(3), and S(4) line fluxes, respectively. The line fluxes shown were measured using PAHFIT and the images are approximately beam-sampled with $\sim 10''$ (3 pc) pixels. The contour levels are 0.4, 0.6, 0.9, and 1.2×10^{-8} W m^{-2} sr^{-1} with the exception of the S(4) that has levels of 1.6 and 2.0×10^{-8} W m^{-2} sr^{-1}, due to the higher noise in the fitted line fluxes. The mean uncertainties in the S(0), S(1), S(2), S(3), and S(4) line fluxes from PAHFIT throughout the region are 0.8, 0.6, 1.3, 1.4, and 3.1×10^{-9} W m^{-2} sr^{-1}, respectively. The orientation of this image is the same as for the SWBarS region in Figure 4.4.

For the regions with the S(0), S(1), S(2), and S(4) H_2 rotational lines detected by PAHFIT at $\geq 3\sigma$ we model the line emission to estimate the column density of a cool ($T = 100$ K) component ($N_{\rm cool}$) associated with the S(0) transition, the column density of the warm ($T > 100$ K) component ($N_{\rm warm}$), the temperature of the warm component ($T_{\rm warm}$) associated with primarily the S(2) and S(4) line emission, and the ortho-to-para ratio (OPR) determined from the difference in the S(1) emission compared to the S(2) and S(4). Figure 4.6 shows results from the modeling of the rotational line emission, displayed as kernel density estimates for the probability distribution function or the physical parameters for each region. The general shapes of the distributions for each region are similar with typical values of $N_{\rm cool} \sim 10^{21}$ cm^{-2}, $N_{\rm warm} \sim 10^{18}$ cm^{-2}, $T_{\rm warm} \sim 800$ K, and OPR ~ 1.

Roussel et al. (2007) uses a similar modeling technique to derive the conditions of the H_2 gas for kiloparsec-scale regions in the centers of 57 galaxies using *Spitzer IRS* spectra that are part of the SINGS survey. The exact method of determining the temperatures and column densities of the gas from the H_2 line intensities differs slightly from our method and they extract H_2 line intensities by locally fitting the pseudocontinuum of the spectra. They assume that the $OPR = 3$, which is the value for a thermalized system at high temperature ($T \geq 200$K), and only fit a different OPR when the fitted temperatures between the transitions does not monotonically increase. Our modeling method allows the OPR to be fit and assumes the cool component temperature is fixed. We made this choice because the cool component

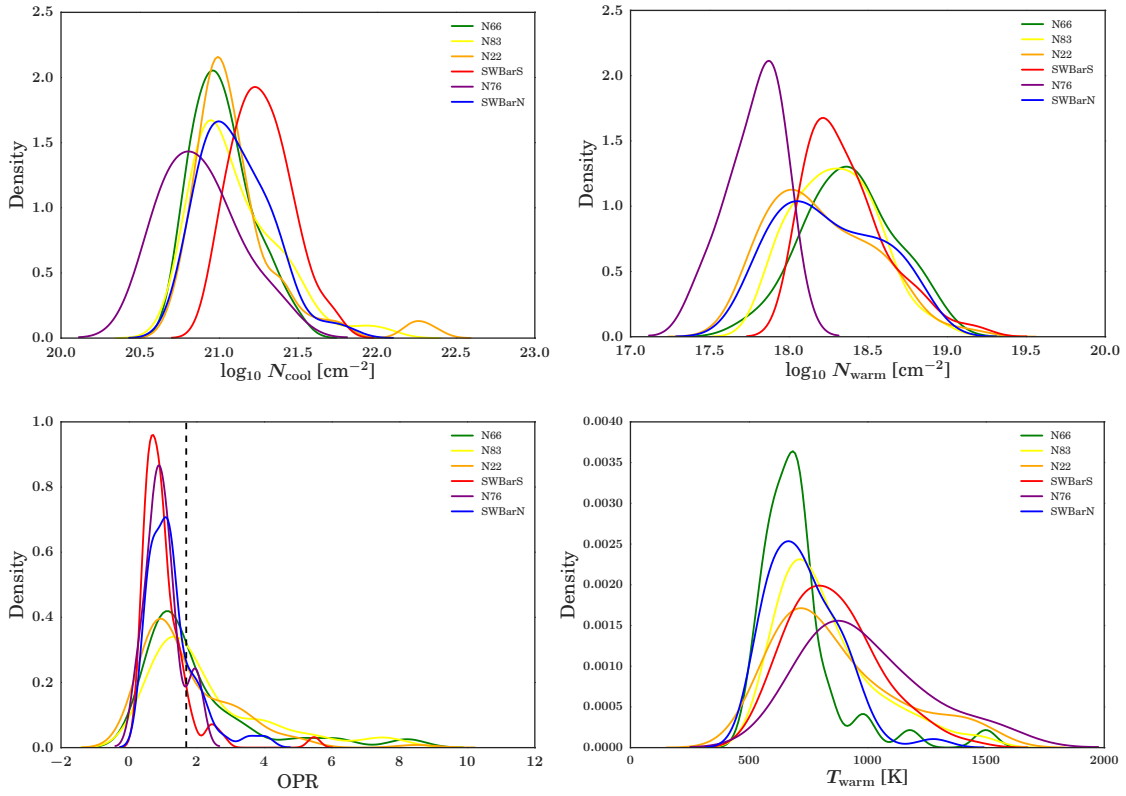

Figure 4.6 Kernel density estimates (KDE) of the fitted parameters N_{cool} (top left), N_{warm} (top right), OPR (bottom left), and T_{warm} (bottom right). The KDE were computed using gaussian kernels and using a "rule of thumb" bandwidth estimate. The black dashed line indicates $OPR = 1.7$, which would be the observed OPR of LTE H_2 gas if the ortho-para conversion timescale is longer than the other relevant timescales (e.g., in the case of FUV-pumping of the optically thicker ortho absorption lines).

mainly contributes to the S(0) intensity, whereas the OPR can be constrained with the S(1) compared to the S(2) and S(4) intensity. Hunt et al. (2010) also presents H_2 rotational line emission using *Spitzer IRS* spectra for low metallicity blue compact dwarf (BCD) galaxies on ∼kpc scales, but have many fewer detections than Roussel et al. (2007). As a result, they adopt the methodology of Roussel et al. (2007) but fix $OPR = 3$ and only derive "reliable" (detecting two transitions at $\geq 2.5\sigma$) temperatures and column density estimates for 4 out of the 22 galaxies.

Our choice of $T_{\rm cool} = 100$ K is consistent with fitted values from for the SINGS galaxies from Roussel et al. (2007), which have a median temperature of $T = 154$ K, when the fits are constrained to $T = 97 - 300$ K. For the BCD galaxies, Hunt et al. (2010) also finds temperature estimates for the low energy H_2 transitions of $T \sim 100 - 120$ K for the 4 galaxies with two measured H_2 rotation transition line intensities. The range in column densities for the total warm H_2 ($T \geq T_{\rm cool}$) for the SINGS galaxies are similar to our results, with values ranging from $10^{19} - 2 \times 10^{21}$ cm^{-2}. Hunt et al. (2010) reports warm H_2 column densities of $N_{\rm H_2} \sim 3 \times 10^{21}$, determined for the $T \sim 100$ K gas. The warmer gas component temperatures from Roussel et al. (2007) range from $T \sim 350 - 1000$ K and result in column densities of $\sim 10^{17} - 10^{19}$ cm^{-2}, which are also comparable to our estimates except that our warm gas temperature tends to be on the higher end of the range of temperatures. For the galaxies where OPR is treated as a free parameter, they find values of $OPR \sim 0.9 - 2.5$ with approximately half of the galaxies being set to the assumed $OPR = 3$. Overall, the range of estimated conditions of the warm H_2 gas in the SMC on small ($\sim$ 3 pc) size scales is comparable to that of normal star-forming

galaxies and low metallicity BCDs on kiloparsec size scales.

4.5 Discussion

4.5.1 Excitation Mechanism of the H_2 Rotational Lines

There are a variety of mechanisms that can excite the rotational and vibrational transitions in the H_2 molecule: FUV photons from massive stars that pump the H_2 molecules into an excited state and/or heat the gas through the ejection of photoelectrons from dust, shocks from molecular outflows or supernovae, or x-rays from AGN or supernovae that heat the gas by photoionization through large column densities. For normal star-forming galaxies, the main source of H_2 line excitation is expected to FUV radiation in PDRs (Hollenbach & Tielens 1997). H_2 gas that is UV-pumped will produce fluorescent spectra only if the radiative cascade through vibration-rotation levels is not significantly altered by collisions, which would thermalize the gas. Because the critical densities of the pure rotation H_2 lines are low, $\sim 10^3$ cm^{-3} for the S(0) to S(3) transitions, they are expected to be populated mainly by collisions and thermalized. The vibrational transitions, which emit lines in the near-infrared, are more likely to be produced by fluorescence due to their higher critical densities. Our observation regions are targeted at star-forming regions unlikely to be dominated by supernova remnants; our resolution is high enough to distinguish individual supernovae, which we do not observe in our regions. The effects of shocks from molecular outflows would be over smaller size-scales than our observations at ~ 3 pc and produce temperatures of a few thousand degrees. Thus

the H_2 emission must be attributed to the FUV-radiated H_2 gas in PDRs. Figure 4.4 shows the similarity between the H_2 line and CO line emission with the brightest H_2 line emission located at the edges of H II regions, which consistent with the warm H_2 being located in PDRs: the outer, UV-irradiated layers of molecular clouds.

The remaining question is whether the observed rotational line emission is thermalized by collisions or produced by fluorescence. Burton et al. (1992) showed that the lower rotation levels, particularly S(0) and S(1), of H_2 will be thermalized across wide range of conditions due to the low critical densities. In Chapter 3, we showed that the PDR models indicate gas densities in these regions of $\sim 10^3 - 10^4$ cm^{-3} based on the [C II] and [O I] emission in a subset of the S^{4}MC regions (N22, N83, SWBarN, and SWBarS), which should be sufficient for the rotational levels of the H_2 gas to be in collisional equilibrium (Burton et al. 1992). The OPR expected for thermalized gas a high ($T \gtrsim 200$ K) is $OPR = 3$, based on the statistical weights of the even and odd transitions, but it can be lower at lower temperatures (e.g., $OPR = 2$ for $T \gtrsim 100$ K). In the SMC regions, we typically observe ratios of $OPR \sim 1$ between the S(1) and S(2) and S(4) transitions. Given that the temperatures associated with these transitions are high, ~ 800 K, an $OPR \sim 1$ is below the expected value of 3 for high temperatures. While we measure $OPR < 3$ for the warmer component of the gas, it is still possible that the S(0) and S(1) states are thermalized.

Because the radiative decay and collisional (de-)excitation conserve ortho or para state ($\Delta J = 2$), the conversion from one state to the other can only occur by H_2 dissociation followed by reformation on dust grains or reactions with protons and

hydrogen atoms. The initial ortho-to-para ratio for H_2 molecules after formation is uncertain. This OPR could be lower if the H_2 molecule remains on the dust long enough after formation to reach equilibrium at the dust temperature, and then that lower OPR could be preserved if the H_2 molecular is destroyed before reaching the equilibrium $OPR = 3$ for the gas temperature. Another possible explanation for the OPR in emission from a PDR is that the H_2 gas states have not reached equilibrium, which could happen if the photodissociation front is advancing into cold gas (where the equilibrium $OPR < 3$) and the recently heated gas has not had time to reach equilibrium. This scenario is the preferred explanation for the $OPR < 3$ observed in the Galactic PDRs NGC 7023 (Fuente et al. 1999) and ρ Ophiuchi (Habart et al. 2003). Finally, The lower OPR values could be explained by fluorescent emission as the UV absorption lines have higher optical depth in the ortho states so that ortho states are pumped less. Fluorescence is predicted to shift the expected $OPR = 3$ in LTE (between the ortho and para states) to $OPR = \sqrt{3} = 1.7$ (Sternberg & Dalgarno 1995), which is still higher than our typical $OPR \sim 1$. Given the current data, it is difficult to distinguish which situation(s) may be driving the lower OPR, but using images of the near-infrared ro-vibrational line emission, which mainly arises due to fluorescence, would help determine if flourescence contributea to the rotational line emission from the warmer H_2 gas and could explain the low OPR values observed in the SMC.

4.5.2 Fraction of Warm H_2

Assuming that the S(0) line emission is thermally excited and traces the warm molecular gas, we can use the column density associated with the $T = 100$ K component to compare the warm molecular gas to the total molecular gas estimates from dust (Chapter 2; Jameson et al. 2016) and from [C II] and ^{12}CO (Chapter 3). The column density of the $T = 100$ K gas from the S(0) emission dominates the column when compared to the warmer $T \sim 800$ K component that is a factor of $\sim 10^3$ lower, and approximately represents the total column density of the molecular gas emitting in the rotational quadrupole transitions.

In Figures 4.7 and 4.8, we show the ratio of the column density of the warm $H_2$to the total H_2 estimated using dust and [C II] and ^{12}CO respectively. The dust-based H_2 map has a resolution of $\sim 45''$ (set by the *Herschel* 500 μm image resolution), but we resample it to match the beam-sampled H_2 line images that have pixel sizes of $\sim 10''$. While we only have [CII]+^{12}CO H_2 estimates for 3 of the S^{4}MC regions, the resolution of $\sim 12''$ (set by the *Herschel* PACS [C II] image) is comparable to that of the H_2 line images. The over-sampling of the dust-based H_2 map allows us to get a sense of the trend in the ratio at $\sim 10'' \sim 3$ pc, but likely causes the column density to be underestimated as the original map would not be sensitive to smaller scale peaks. This explains the points where $N_{H_2,T=100K}/N_{H_2,dust} > 1$ ($\log_{10} N_{H_2,T=100K}/N_{H_2,dust} > 0$), since the dust-based estimate should account for all H_2 gas and the N_{H_2} associated with warm H_2 should not exceed this value. However, we also see some high ratios when using the [CII]+^{12}CO H_2 estimate (particularly in

the SWBarS region), which is obtained at higher resolution (12″). This may suggest that either the total molecular gas is underestimated, or that the temperature of the cool component is higher than the assumed 100 K and the warm H_2 is overestimated along some lines-of-sight.

Overall, we see a trend of higher fraction of warm H_2 at low column densities that decreases and flattens at higher N_{H_2} when using the dust-based estimates. The trends are similar using the [CII]$+^{12}$CO, but with a larger scatter in the distribution that makes it difficult to distinguish between a slight decreasing trend and a flat value. A higher fraction of warm H_2 at lower column densities is consistent with our interpretation that the H_2 rotational line emission arises in PDRs, which would consist of more warm H_2 on the outskirts of the clouds and lower column density regions. The flatter distributions in the warm gas fraction using the [CII] $+^{12}$ CO is also consistent with the PDR scenario, since most of the molecular gas is traced by the [C II] emission in the PDR and is likely in a similar region as the warm H_2.

The warm fractions in the SMC are mostly found within the range of warm gas fractions for the SINGS galaxies estimated by Roussel et al. (2007) of $f_{\rm warm} = 0.01 - 0.45$. These were found by comparing to the H_2 obtained from using ^{12}CO assuming a Galactic conversion factor of $X_{CO} = 2.3 \times 10^{20}$ cm^{-2} (K km s^{-1})$^{-1}$. Generally, the warm H_2 fractions are higher in the SMC regions than the average of ~ 0.1 for the SINGS galaxies. A key difference between the SMC observations and the SINGS galaxy observations are the size scales: the *IRS* resolution is 3 pc in the SMC, and $\gtrsim 1$ kpc for the more distant galaxies. Another difference is that we targeted preferentially star-forming regions in the SMC. While we are able to resolve

the PDR and estimate the fraction of warm H_2, the SINGS observations average over multiple PDRs with a wide range of conditions and include more gas that is quiescent and non-star forming. Finally, it is possible that there is a tendency for a higher fraction of warm H_2 at lower metallicities. This would be consistent with our observations of more extended PDR regions based on the comparison [C II] and ^{12}CO emission: essentially more of the H_2 gas exists in low A_V regions that are bathed by a higher radiation field and are thus warmer than more shielded layers.

4.6 Summary and Conclusions

In this study, we used the rotational H_2 line emission from the *Spitzer IRS* spectra from the S^{4}MC survey (Sandstrom et al. 2009) to study the properties of the emitting H_2 gas at low metallicity in star-forming regions in the SMC. We extracted the H_2 line intensities using PAHFIT to be able to measure the lines that overlap with extended PAH emission features. Assuming that the mid-infrared dust emission is either a foreground or background source, we estimate that the correction is $\lesssim 5-10\%$ for the S(0) line. We model the H_2 line emission assuming that two components can explain the S(0) through S(4) emission: a cool component at $T = 100$ K that is constrained by the S(0) emission, and a warm component that dominates the S(2) and S(4) transitions. We fit for the column density of the cool component and the warm component ($N_{\rm cool}$ and $N_{\rm warm}$), the temperature of the warm component

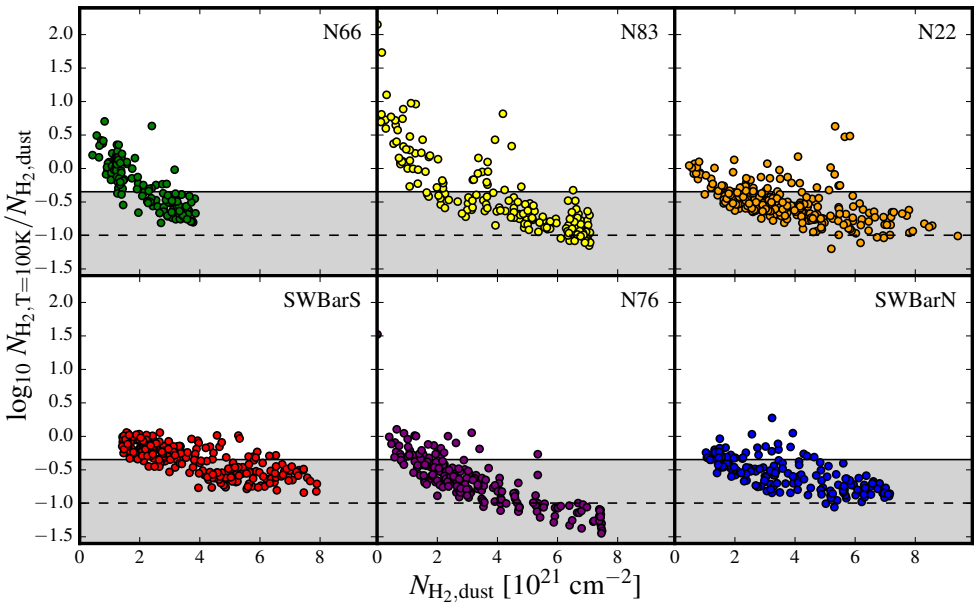

Figure 4.7 Fraction of warm H_2 ($T = 100$ K) using the total molecular gas estimate from dust (with a resolution of $\sim 45''$ re-sampled to match the H_2 image with $\sim 10''$ pixels). The black dashed line shows the mean fraction of warm H_2 ($T \geq 100$ K) gas to cold molecular gas of $f_{\rm warm} \sim 0.1$, traced using ^{12}CO emission and converted using a Galactic X_{CO}, found for a sub-sample of star-forming SINGS galaxies (excluding the measurements for LINER galaxies) from Roussel et al. (2007). The grey shaded area shows the range in integrated measurements of the fraction of warm H_2 of $f_{\rm warm} = 0.01 - 0.45$.

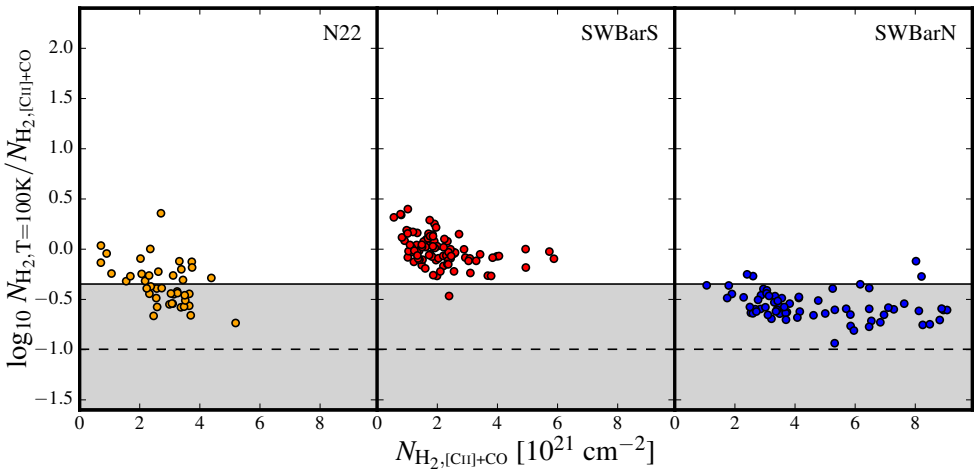

Figure 4.8 Same as Figure 4.7 except the total molecular gas estimate comes from [C II] and ^{12}CO instead of dust.

($T_{\rm warm}$), and the ortho-to-para ratio (OPR). We find similar distributions across the six different star-forming regions with typical values of $N_{\rm cool} \sim 10^{21}$ cm^{-2}, $N_{\rm warm} \sim 10^{18}$ cm^{-2}, $T_{\rm warm} \sim 800$ K, and $OPR \sim 1$.

The conditions we find in the SMC at parsec-scales are comparable to those found for nearby galaxies in the SINGS survey and blue compact dwarf galaxies on kiloparsec-scales using a similar model (Roussel et al. 2007; Hunt et al. 2010). The H_2 line emission is consistent with being emitted from photodissociation regions (PDRs) when the excitation is due to the FUV photons from massive stars that either heat the gas and collisionally excite the H_2 rotational line and/or pump the H_2 to excited states. The low OPR values compared to the expected $OPR = 3$ for gas in LTE between the ortho and para states may be due to a difference in H_2 formation, the gas being out of equilibrium due to the PDR front moving into cold gas, or a contribution from fluorescence. Using the warm H_2 column density estimates,

we measure the fraction of warm H_2 and find that the fractions in the SMC range from $\sim 1 - 0.1$, which is somewhat higher than the SINGS galaxies. Ultimately, the H_2 line emission is consistent with originating from PDRs with conditions similar to those found in nearby "normal" galaxies. While the temperatures and column densities are similar, the higher fractions of warm H_2 gas in the SMC suggest that more of the H_2 gas resides in PDR regions–consistent with the results from our study of the [C II] emission that shows extended PDRs due to the lower amount of dust shielding at low metallicity.

Chapter 5: Molecular Gas and Star Formation in the Magellanic Clouds

5.1 Overview

Using dust emission to estimate the molecular gas in low metallicity systems avoids the biases of CO and can trace "CO-faint" molecular gas. Using a dust-based molecular gas estimate based on *Spitzer* data, Bolatto et al. (2011) found that molecular gas depletion time ($\tau_{\rm dep}^{\rm mol} = \Sigma_{\rm mol}/\Sigma_{\rm SFR}$) in the SMC is consistent with the values seen in more massive disk galaxies. Combining the dust-based molecular gas estimate with the atomic gas traced by H I showed that the analytic star formation models of Krumholz et al. (2009) and Ostriker et al. (2010) predicted the trend in the data. While the SMC is lower metallicity, the geometry is poorly constrained and it shows clear signs of disturbance from interaction with the LMC and the Milky Way, which makes it problematic for comparisons against models created for galactic disks. We adopt a higher inclination angle for the SMC than was used in Bolatto et al. (2011) to explore how that affects the results. The LMC is nearly face-on with a well-constrained inclination angle and has a clear disk morphology, which minimizes the uncertainty in the analysis.

We compare the new dust-based molecular gas estimates and atomic gas (presented in Chapter 2) to the star formation rate in both galaxies and compare to the

existing studies of large disk galaxies. In Section 5.2 and 5.3 we outline the Hα and 24 μm observations and how we convert them to a star formation rate. Section 5.4 presents the main results of this study, focusing on the relationship between molecular gas and star formation and the effect of scale. We discuss the implications of the results and compare the observations to star formation model predictions in Section 5.5. Finally, we summarize the conclusions from this study of the LMC and SMC in Section 5.6.

5.2 Observations

5.2.1 Hα and 24 μm Data

We combine images of Hα and 24 μm dust emission to trace recent star formation. For the LMC we use the calibrated, continuum-subtracted Hα map from the Southern Hα Sky Survey Atlas (SHASSA; Gaustad et al. 2001) at 0.8′ resolution. We correct the Hα maps for the line-of-sight Milky Way extinction using A_V(LMC) = 0.2 mag and A_V(SMC) = 0.1 mag (Schlafly & Finkbeiner 2011). We found background emission outside the LMC, on the order of 10% of the total flux observed in the main part of the galaxy, likely from the diffuse Milky Way Hα emission. We apply additional background subtraction by removing a polynomial fit to the regions outside of the galaxy. In the SMC, we use the continuum-subtracted Hα map from the Magellanic Cloud Emission Line Survey (MCELS; Smith & MCELS Team 1999) at 2.3″ resolution. For both the SMC and LMC we use the Multiband Imaging Photometer (MIPS) 24 μm map from the *Spitzer* Survey "Surveying the

Agents of Galaxy Evolution" (SAGE; Meixner et al. 2006; Gordon et al. 2011).

5.2.1.1 Diffuse Hα

The Hα images of the Magellanic Clouds clearly show extended, low-level of emission throughout the galaxies, which traces the ISM component referred to as diffuse ionized gas (DIG) or the warm ionized medium (WIM). In the Milky Way, the filling factor of the WIM ranges from $0.1 - 0.4$, with evidence that it increases with distance from the mid-plane (Berkhuijsen et al. 2006), and contribute $\sim 10 - 15\%$ of the total H II emission (Reynolds 1993). More detailed studies of the WIM in the Milky Way find that physical conditions differ from conditions in classical H II regions vary widely (Haffner et al. 2009). Early work by Kennicutt & Hodge (1986) demonstrated that an extended Hα component accounts for $\sim 15\%$ of the flux in the LMC. Later, Kennicutt et al. (1995) found that the diffuse component of the Hα emission, found by comparing the total flux to the integrated flux from H II regions, is $\sim 25 - 35\%$ in the LMC and $\sim 34 - 40\%$ in the SMC. These fractions of diffuse or extended emission are consistent with what is found for Magellanic Irregulars (Kennicutt 1989) and in spirals, including the $20 - 40\%$ fraction found in M31 (Walterbos & Braun 1994). The diffuse Hα component is similar to other star-forming galaxies and a significant fraction of the total emission.

While widespread amongst galaxies, the origin of the diffuse ionized gas is unclear–is it all escaped Hα photons from star-forming regions or is the gas ionized within the diffuse ISM (Rahman et al. 2011 and references therein)? If the gas

is primarily ionized within the diffuse ISM by mechanisms not directly related to star formation and not accounted for in the star formation rate calibration, then including the diffuse emission would overestimate the star formation rate. Pellegrini et al. (2012) studied the optical depth of H II regions in the Magellanic Clouds and found that the luminosity of escaped ionizing radiation provides enough power to ionize the diffuse gas, suggesting that the diffuse Hα emission in the Magellanic Clouds could all be escaped radiation from young, massive stars in H II regions. Even if all of the diffuse Hα emission can be attributed to star formation, the appropriateness of including the emission in the star formation rate depends on the details of the star formation rate conversion calibration. The calibration by Calzetti et al. (2007) was done on scales of $200-600$ pc, which likely includes some extended emission. We include the diffuse Hα emission in our analysis and convert the Hα maps to star formation rate assuming that massive stars are responsible for all of the Hα flux.

5.2.2 Distances and Inclination Angles

To convert observational measurements to surface mass density (Σ), we need both the distance to the galaxy and inclination angle (i). For the LMC, we use an inclination angle of $i = 35°$, which is the approximate intermediate value of the three fits to stellar proper motions and line-of-sight velocity measurements in van der Marel & Kallivayalil (2014), which range from $i = 26.2° \pm 5.9°$ to $i = 39.6° \pm 4.5°$, and is consistent with their previous work that found $i = 34.7° \pm 6.2°$ (van der Marel

& Cioni 2001). We assume that the inclination of stellar disk is comparable to the gas disk given the disk-like morphology of the LMC. While Kim et al. (1998) fit an inclination angle to the H I kinematics, they found it was unreliable and much higher than the morphological fit ($i = 22° \pm 6°$). Ultimately, Kim et al. (1998) adopt the inclination angle found from the stellar dynamics.

The inclination of the SMC is poorly constrained due to its irregular morphology. Recent work by Scowcroft et al. (2016) shows that assuming a disk with an inclination angle inaccurately represents the detailed morphology of the SMC. However, comparing the SMC to the LMC and studies of other galaxies requires knowing the mass surface densities and adopting the simple model of an inclined disk. Bolatto et al. (2011) adopted $i = 40° \pm 20°$ based on the analysis of the H I rotation curve by Stanimirović et al. (2004). The recent estimate of the SMC inclination based on three dimensional structure traced by cepheid variable stars finds $i = 74° \pm 9°$ (Haschke et al. 2012), which is consistent with the previous studies using cepheids (Caldwell & Coulson 1986; Groenewegen 2000). While cepheids, as old stars, may not trace the gaseous disk, a new analysis of the H I rotation also indicates a higher possible inclination of $i \approx 60 - 70°$ (private communication, P. Teuben). A higher inclination angle scales the surface mass densities to lower values. We adopt $i = 70°$ for the inclination of the SMC and compare to the previous results in Bolatto et al. (2011) to determine how the higher inclination angle affects the results.

5.2.3 Convolving to Lower Resolutions

We produce the range of lower resolution maps (from 20 pc to $\sim$ 1 kpc) by convolving the images of $\Sigma_{\rm SFR}$, $\Sigma_{\rm mol}$, and $\Sigma_{\rm HI}$ with a gaussian kernel with FWHM $= \sqrt{(r^2 - r_0^2)}$, where r is the desired resolution and r_0 is the starting resolution of the image. The images are then resampled to have approximately independent pixels (one pixel per resolution element). To mitigate edge effects from the convolution, we remove the outer two pixels (two beams) for all resolution images of the LMC. In the SMC, we remove two outer pixels for $r \leq 600$ pc and remove one pixel from the edges for $r \geq 700$ pc due to the small size of the images.

5.3 Tracing Recent Star Formation

We use Hα, locally corrected for extinction using 24 μm emission, to trace the star formation rate surface density ($\Sigma_{\rm SFR}$). Following Bolatto et al. (2011), we use the star formation rate (SFR) calibration by Calzetti et al. (2007) to convert Hα and 24 μm luminosities:

$$\mathrm{SFR}(M_\odot\ \mathrm{yr}^{-1}) = 5.3 \times 10^{-42}[L(\mathrm{H}\alpha) + \ (0.031 \pm 0.006)L(24\mu\mathrm{m})], \qquad (5.1)$$

where luminosities are in erg s^{-1} and $L(24\mu\mathrm{m})$ is expressed as $\nu L(\nu)$. The average contribution from 24 μm to the total star formation rate is $\sim$ 20% in the LMC and $\sim$ 10% in the SMC. A significant fraction ($\sim$ 40%) of the Hα emission in both the LMC and SMC is diffuse. We include all of the Hα emission in this analysis since Pellegrini et al. (2012) showed that all of the ionizing photons could have originated

from H II regions from massive stars (see Appendix **??** for further discussion). The RMS background value of the SFR map is 1×10^{-4} $M_{\odot}$ yr^{-1} kpc^{-2} in the LMC and 4×10^{-4} $M_{\odot}$ yr^{-1} kpc^{-2} in the SMC.

This conversion to star formation rate assumes an underlying broken power-law Kroupa initial mass function (IMF) and was calibrated against Paschen-α emission for individual star-forming regions. Ideally, Hα and 24 μm emission would only be used for size scales that fully sample the IMF and sustain star formation for > 10 Myr; for smaller scales, pre-main sequence stars are more appropriate and a better indicator of the current star formation rate. Hony et al. (2015) find that the star formation rate from pre-main sequence stars matches that from Hα at scales of $\sim$ 150 pc in the N66 region in the SMC. Our highest resolution of $\sim$ 20 pc resolves H II regions, and the mapping of the star formation rate on these scales is questionable. Nonetheless, we apply the star formation rate conversion even to our highest resolution data to allow us to compare to other studies and investigate the relationships in terms of a physical quantity, although it is important to keep these limitations in mind when interpreting the results.

5.4 Results

5.4.1 Molecular Gas and Star Formation

Understanding whether or not metallicity and galaxy mass affect the conversion of gas into stars is important for understanding galaxy evolution throughout cosmic time. The relationship between molecular gas and star formation rate has

Table 5.1. Global Properties

Property	LMC	SMC
$M_{\rm mol}^{\rm dust}$	$6.3^{+6.3}_{-3.2} \times 10^7\ M_\odot$	$2.0^{+2.0}_{-1.0} \times 10^7\ M_\odot$
$L_{\rm CO}$	7×10^6 K km s^{-1}[a]	1.7×10^5 K km s^{-1}[b]
$M_{\rm HI}$	$4.8 \times 10^8\ M_\odot$[c]	$3.8 \times 10^8\ M_\odot$[d]
M_*	$2 \times 10^9\ M_\odot$[e]	$3 \times 10^8\ M_\odot$[f]
SFR[d]	$0.20\ M_\odot$ yr^{-1}	$0.033\ M_\odot$ yr^{-1}
$\tau_{\rm dep}^{\rm mol}$	$0.37^{+0.37}_{-0.19}$ Gyr	$0.61^{+0.61}_{-0.31}$ Gyr

[a]Fukui et al. (2008), no sensitivity cuts

[b]Mizuno et al. (2001), no sensitivity cuts

[c]Staveley-Smith et al. (2003)

[d]Stanimirović et al. (1999)

[e]Skibba et al. (2012)

[f]assuming A_V(LMC) = 0.2 mag and A_V(SMC) = 0.1 mag

been studied extensively in nearby, high-metallicity, star-forming galaxies. With the dust-based molecular gas estimates of the nearby Magellanic Clouds, we are in a unique position to probe how the relationship between the molecular gas and star formation rate behave as a function of metallicity and the size scale considered. Figure 5.1 shows the relationships for the LMC and SMC using the new dust-based molecular map at the highest resolution of 20 pc, 200 pc (scale where multiple star forming regions are being averaged), and 1 kpc (comparable to the ^{12}CO surveys of nearby galaxies).

We compare the relationship between the molecular gas and star formation rate in the SMC and LMC to that for the HERACLES sample of nearby galaxies by

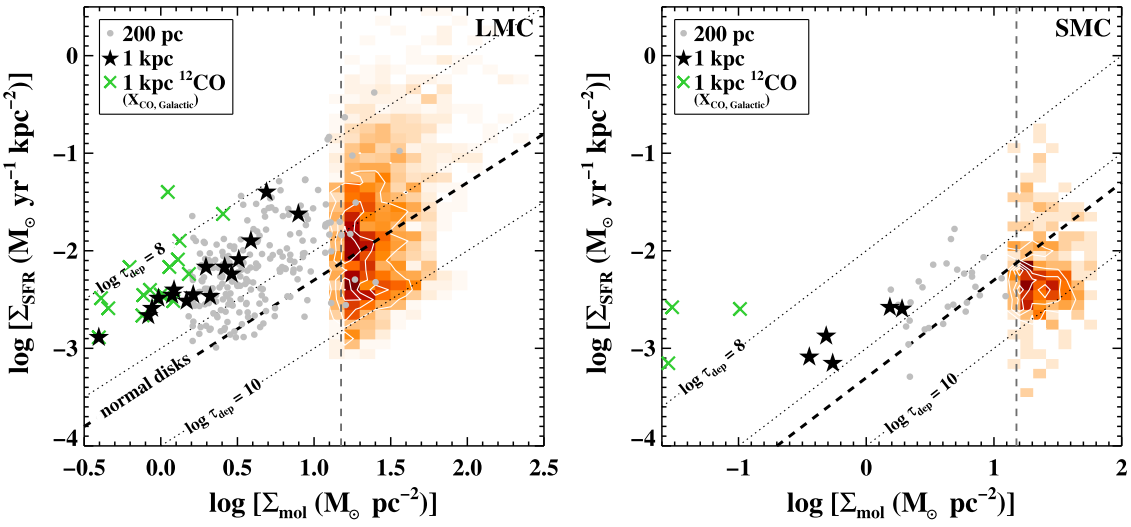

Figure 5.1 $\Sigma_{\rm SFR}$ as a function of $\Sigma_{\rm mol}$ for the LMC (left) and SMC (right) at various resolutions. The red color scale shows the two-dimensional distribution at a resolution of $r = 20$ pc with the white contours indicate levels that are 20%, 40%, 60%, and 80% of the maximum density of points. The vertical gray dashed line indicates the estimated 2σ sensitivity cut of the $r = 20$ pc data ($\Sigma_{\rm mol} \sim 15\ M_\odot\ {\rm pc}^{-2}$). The grey circles and black stars show the data at resolutions $r = 200$ pc and $r = 1$ kpc, respectively. The green stars show $\Sigma_{\rm mol}$ derived from NANTEN CO data at a resolute of $r = 1$ kpc using a Galactic CO-to-H_2 conversion factor. Here we present the SMC data corrected by a higher inclination angle of $i = 70°$, as opposed to results from Bolatto et al. (2011) that used $i = 40°$, which results in a diagonal shift to lower surface densities.The dotted lines indicate constant molecular depletion times $\tau_{\rm dep}^{\rm mol} = 0.1$, 1, and 10 Gyr. The dashed line shows the typical depletion time for normal galaxies $\tau_{\rm dep}^{\rm mol} \sim 2$ Gyr (Bigiel et al. 2008, 2011; Rahman et al. 2012; Leroy et al. 2013a).

Leroy et al. (2013a). The HERACLES sample resolves the galaxies and compares the gas and star formation at a resolution of $\sim$ 1 kpc. Figure 5.2 shows that the LMC and SMC data (convolved to a comparable resolution of 1 kpc) lie within the scatter in the data for high-metallicity, star-forming galaxies, although above the main cluster of data points for a given molecular gas surface density.

5.4.1.1 Molecular Gas Depletion Time

A convenient way to quantify the relationship between molecular gas and star formation is in terms of the amount of time it would take to deplete the current reservoir of gas given the current rate of star formation, the molecular gas depletion time:

$$\tau_{\rm dep}^{\rm mol} = \Sigma_{\rm mol}/\Sigma_{\rm SFR}. \tag{5.2}$$

The data for the LMC and SMC appear consistent with a well-defined depletion time. We find average molecular gas depletion times at 1 kpc scales of $\sim$ 0.4 Gyr in the LMC and $\sim$ 0.6 Gyr in the SMC. Weighting the average of $\tau_{\rm dep}^{\rm mol}$ by the molecular gas mass and star formation rate does not significantly affect the averages at 1 kpc scales; at 200 pc scales, weighting of the average typically changes the value of $\tau_{\rm dep}^{\rm mol}$ by $\sim$ 20%. The main exception is for the star formation rate weighted $\tau_{\rm dep}^{\rm mol}$ average in the LMC, which is shorter by $\sim$ 50% and likely due to the significant contribution of 30 Doradus at these scales. The range of possible molecular gas depletion times given the factor of up to $\sim$ 2 systematic uncertainty in the molecular gas estimate is $\sim 0.2 - 1.2$ Gyr. This is shorter than the molecular gas depletion time found for the

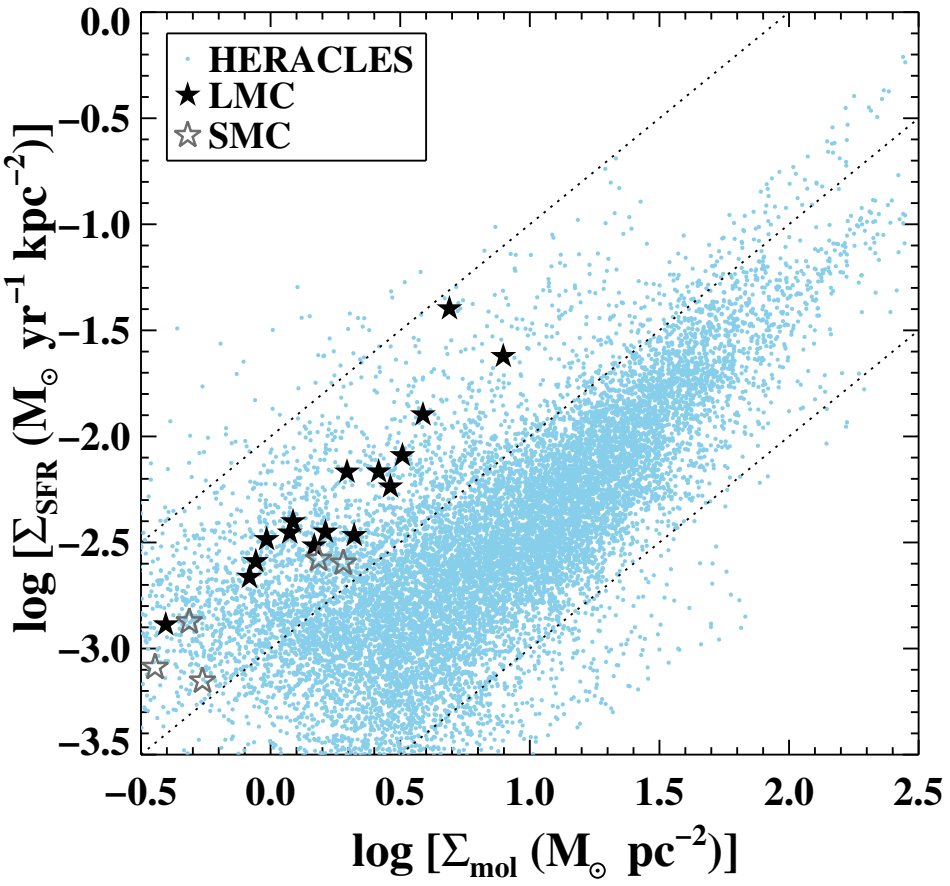

Figure 5.2 $\Sigma_{\rm SFR}$ vs. $\Sigma_{\rm mol}$ for the $r \sim 1$ kpc data from the HERACLES sample of nearby star-forming galaxies (Leroy et al. 2013a) (blue), where the $\Sigma_{\rm mol}$ is estimated using ^{12}CO with a Galactic CO-to-H_2 conversion factor. The $r \sim 1$ kpc data for the LMC (filled stars) and SMC (open stars) are over plotted. The LMC and SMC points fall within the full distribution for the HERACLES sample, but offset above the main distribution.

SMC by Bolatto et al. (2011) of $\tau_{\rm dep}^{\rm mol} \sim 1.6$ Gyr at 1 kpc resolution, but within the factor of 2 systematic uncertainty on both estimates. The molecular gas depletion time found in the Magellanic Clouds is lower than the average value of ~ 2 Gyr for nearby normal disk galaxies at comparable ~ 1 kpc size scales, but within the range of observed values for the STING sample (Rahman et al. 2012) and the larger HERACLES sample (Bigiel et al. 2008, 2011; Leroy et al. 2013a).

Figure 5.3 shows that the median $\tau_{\rm dep}^{\rm mol}$ is $\sim 2-3$ Gyr at the highest resolution of 20 pc. The molecular gas depletion time changes with resolution because the peaks in the molecular gas are physically separated from the peaks in the star formation rate at scales where the star-forming regions are spatially resolved. The tendency of low star formation rates at the peaks in the molecular gas and low to no molecular gas at the peaks in the star formation rate ($\tau_{\rm dep}^{\rm mol}$ is only defined for regions with $\Sigma_{\rm mol}$) biases $\tau_{\rm dep}^{\rm mol}$ at high resolutions biased towards longer times. A scale of 200 pc is typically large enough to include both the recent star formation and the molecular gas and sample star-forming regions at a range of evolution stages (Schruba et al. 2011). While the molecular gas depletion time gets closer to the integrated $\tau_{\rm dep}^{\rm mol}$ value at a scale of 200 pc, the median $\tau_{\rm dep}^{\rm mol}$ reaches the integrated value at ~ 500 pc in the LMC and SMC.

The lower metallicities of the SMC and LMC and the lack of a metallicity bias in our dust-based molecular gas estimate allow us to investigate whether there is any trend in $\tau_{\rm dep}^{\rm mol}$ with metallicity. Figure 5.4 shows that there is no clear trend in the average molecular gas depletion times when comparing the LMC and SMC to the HERACLES sample of galaxies. Leroy et al. (2013a) also saw no trend with

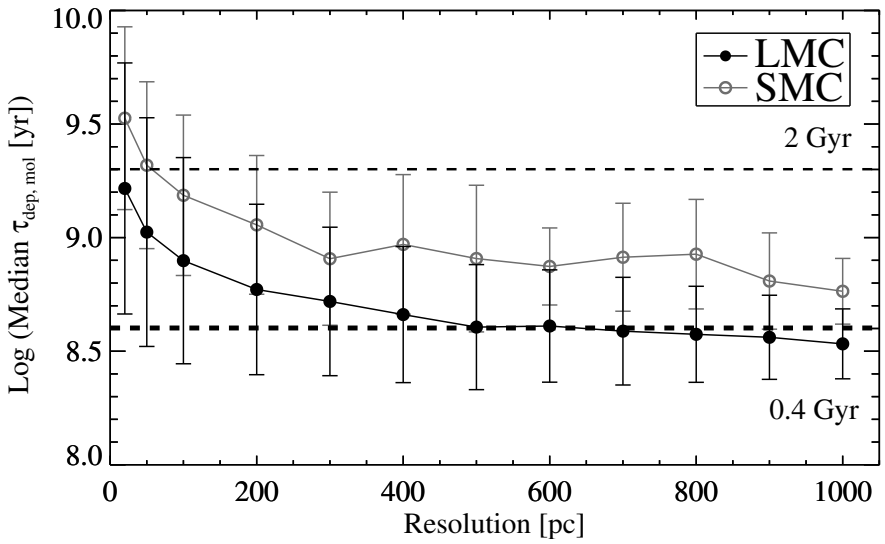

Figure 5.3 Median molecular gas depletion time as a function of resolution. Black filled and open grey circles show the data for the LMC and SMC, respectively. The error bars show 1σ on the mean. The upper dashed line shows $\tau_{\rm dep}^{\rm mol} = 2$ Gyr, the average for normal galaxies, and the lower dashed line shows $\tau_{\rm dep}^{\rm mol} = 0.4$ Gyr, the integrated depletion time for both the LMC and SMC. The LMC and SMC $\tau_{\rm dep}^{\rm mol}$ reach the integrated value of ~ 0.4 Gyr and ~ 0.6 Gyr, respectively, at large (> 500 pc) scales.

metallicity as long as they allowed for a variable CO-to-H_2 conversion factor. We also compare our measurements to the integrated $\tau_{\rm dep}^{\rm mol}$ using a metallicity dependent CO-to-H_2 conversion factor for the *Herschel* Dwarf Galaxy Survey (DGS; Cormier et al. 2014). Over the range of metallicities studied, the main cause of variations in the molecular gas depletion time does not appear to be metallicity.

5.4.2 Correlation Between Gas and Star Formation Rate from 20 pc to 1 kpc Size Scales

We use the Spearman's rank correlation coefficient to quantitatively gauge how well the gas correlates with star formation rate at different size scales. Spearman's rank correlation coefficient (r_s) measures the degree to which two quantities monotonically increase ($r_s > 0$) or decrease ($r_s < 0$). We computed the 3σ confidence intervals using the Fisher z-transformation, which is appropriate for bivariate normal distributions. Figure 5.5 shows the rank correlation coefficient as a function of resolution for the relationship between star formation rate and molecular gas and atomic gas.

The change in the rank correlation coefficient with resolution is similar for both the LMC and SMC. As expected for atomic-dominated galaxies, the correlation of $\Sigma_{\rm gas}$ vs. $\Sigma_{\rm SFR}$ follows that of $\Sigma_{\rm HI}$ and $\Sigma_{\rm SFR}$, therefore we only show $\Sigma_{\rm HI}$ vs. $\Sigma_{\rm SFR}$ in Figure 5.5. The correlation between $\Sigma_{\rm HI}$ vs. $\Sigma_{\rm SFR}$ in both the LMC and SMC is high ($r_s \sim 0.6 - 0.7$) at the smallest size scale of 20 pc and remains high across all size scales. The correlation of H I with the star formation rate, even at small spatial scales, is due to the extended nature of both components combined with the

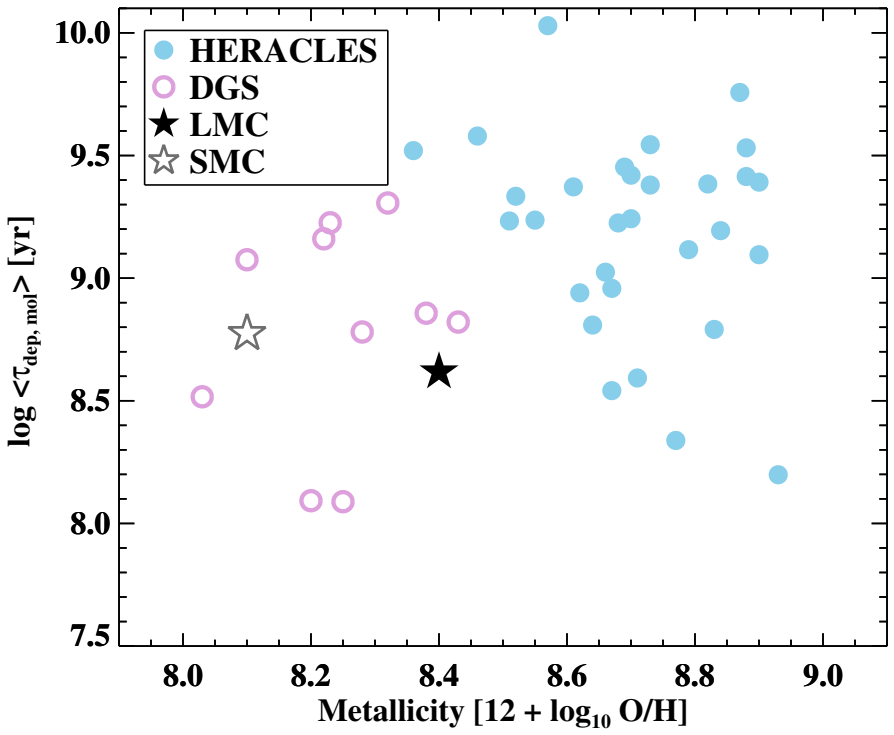

Figure 5.4 The galaxy-averaged molecular gas depletion time ($< \Sigma_{\rm mol} > / < \Sigma_{\rm SFR} >$) with metallicity for the HERACLES sample (light blue points), LMC (black filled stars), and SMC (grey open stars). We have taken the average $\Sigma_{\rm mol}$ and $\Sigma_{\rm SFR}$ of the 1 kpc LMC and SMC data, which are comparable measurements to the $\sim$ 1 kpc resolution HERACLES data. We also include the integrated molecular gas depletion times ($M(\rm H_2)$/SFR) from the Dwarf Galaxy Survey (DGS) using a metallicity dependent CO-to-$\rm H_2$ conversion factor from Cormier et al. (2014). While there is a large amount of scatter, there does not appear to be any strong trend with metallicity.

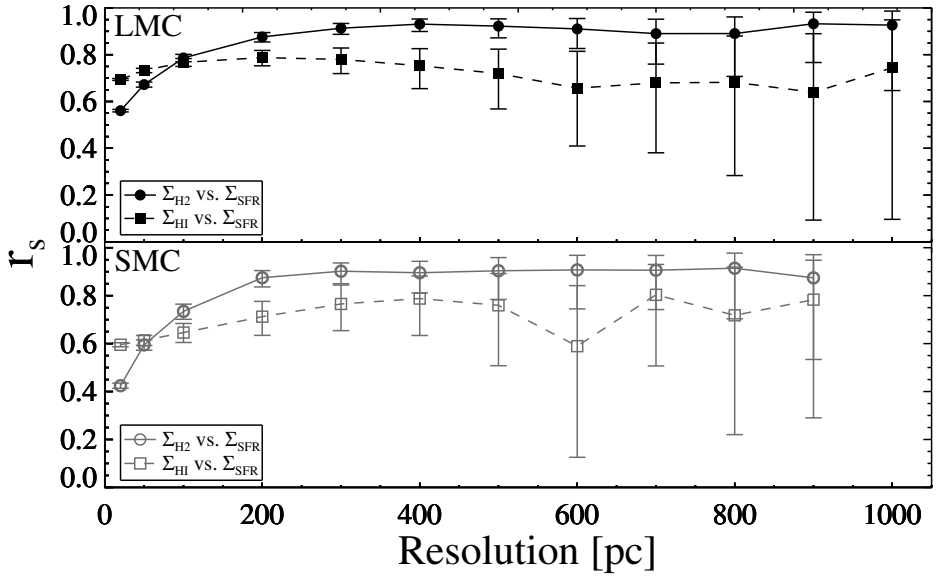

Figure 5.5 The Spearman rank correlation coefficient (r_s) as a function of image resolution for the $\Sigma_{\rm H_2}$ vs. $\Sigma_{\rm SFR}$ (circles with solid line) and $\Sigma_{\rm HI}$ vs. $\Sigma_{\rm SFR}$ (squares with dashed line) distributions. The top plot shows the rank correlations for the LMC and the bottom show those for the SMC. The error bars show the 99.75% confidence interval ($\sim 3\sigma$) of the measured rank correlation coefficient. The correlation between H I and SFR remains at a constant, high level of $\rm r_s \sim 0.7$ across size scales in part due to the extended nature of both the H I gas and Hα emission that dominates the SFR. The correlation between H_2 and SFR reaches a maximum value of $\rm r_s \sim 0.9$ at a size scale of 200 pc, which is the expected size scale to average over enough individual star-forming regions to sample a range of evolutionary states.

general trend that regions with more total gas have more star formation and more molecular gas.

The $\Sigma_{\rm H_2}$ vs. $\Sigma_{\rm SFR}$ distribution reaches the maximum correlation coefficient of $r_s \sim 0.9$ at a size scales ~ 200 pc, past which it is better correlated than the relationship with H I. While the H I is correlated with the star formation rate tracer, we see that molecular gas is best correlated with recent star formation in the LMC and SMC at size scales $\gtrsim 200$ pc. The 200 pc scale indicates the average size scale where both molecular gas and the star formation rate tracer, Hα, are found together and enough independent star-forming regions at different evolutionary stages (i.e., different ratios of Hα to molecular gas) are averaged together. While the correlation peaks at 200 pc, the average molecular gas depletion time decreases until it reaches the integrated value at a size scale of $\sim 500 - 700$ pc in the LMC and SMC. The molecular gas and star formation rate tracer have a strong positive correlation, stronger than that with H I, supporting the physical connection between molecular gas and recent massive star formation.

5.5 Discussion

We discuss our findings on the relationship between gas and star formation in the Magellanic Clouds using our new dust-based molecular gas maps. By comparing our results to existing observational studies of mainly massive, high metallicity, molecular-dominated galaxies, simulations, and theoretical models of star formation, we provide insight into the physical mechanisms that drive star formation.

5.5.1 $\tau_{\rm dep}^{\rm mol}$ in the Magellanic Clouds

The range of possible molecular gas depletion times for the LMC and SMC at 1 kpc scales given the systematic uncertainty in our estimate of the molecular gas of $\sim 0.2 - 1.2$ Gyr falls below the average ~ 2 Gyr found for nearby normal disk galaxies. This is consistent with the previous work by Bolatto et al. (2011) that found $\tau_{\rm dep}^{\rm mol} = 1.6$ Gyr at 1 kpc scales in the SMC using similar dust-based molecular gas estimates, with the value being higher due to a higher estimate of the molecular gas. The shorter molecular gas depletion times do not appear to be directly due the lower metallicities as there is no trend in $\tau_{\rm dep}^{\rm mol}$ with metallicity (see Figure 5.4).

The other remaining environmental factors, besides metallicity, that could affect the ratio of the amount of molecular gas to the amount of current star formation are the lower galaxy masses of the Magellanic Clouds and the interaction between the LMC, SMC, and Milky Way (Besla et al. 2012). Lower mass galaxies tend to have lower dark matter and stellar densities, making them more susceptible to stochastic bursts of star formation. Both the star formation histories of the SMC and LMC (Harris & Zaritsky 2004, 2009) indicate that there have been recent bursts in star formation in both galaxies. A burst in star formation over a short period of time could lead to a depletion of the molecular gas reservoir combined with higher star formation rates that together can produce low $\tau_{\rm dep}^{\rm mol}$ values.

The molecular gas depletion time in M33 is ~ 0.5 Gyr when the diffuse Hα emission is included (Schruba et al. 2010), which is comparable to our measurements of the Magellanic Clouds. If the diffuse ionized gas is removed from the Hα emission,

then the molecular gas depletion time increases to $\sim$ 1 Gyr. This highlights the importance of understanding the connection between the diffuse ionized gas and recent massive star formation as it represents a significant fraction of the Hα emission and changes $\tau_{\rm dep}^{\rm mol}$. Rahman et al. (2011) found a similar increase in $\tau_{\rm dep}^{\rm mol}$ by a factor of $\sim$ 2 when the diffuse ionized gas was removed in the disk galaxy NGC 4254. If the diffuse ionized component is excluded in the star formation rate determination, the $\tau_{\rm dep}^{\rm mol}$ in M33, LMC, and SMC is $\sim$ 1 Gyr.

Like the Magellanic Clouds, M33 is low mass, atomic dominated, has likely interacted with M31 within the past $0.5 - 2$ Gyr (Davidge & Puzia 2011). The LMC, SMC, and M33 show evidence for bursts in the star formation history within the last Gyr and the most recent epochs show lower star formation rates, which suggest that the star-forming gas reservoir has been depleted. The observed shorter depletion times appear to be caused by catching these galaxies after a period of higher star formation rate and does not necessarily indicate that these low-mass, low-metallicity galaxies are forming stars differently from normal disk galaxies.

Saintonge et al. (2011) also found that for the volume-limited COLD GASS survey, lower stellar mass galaxies ($\sim 10^{10} M_{\odot}$) had shorter depletion times of $\sim$ 0.5 Gyr. While consistent with the integrated depletion times in the LMC and SMC, the data are not completely comparable since a value for the CO-to-H_2 conversion factor has to be assumed and single dish CO observations from the COLD GASS survey will mainly detect the central regions of the galaxies. Saintonge et al. (2011) conjecture that the shorter depletion time is due to the tendency for smaller galaxies to have more "bursty" star formation. Similarly, Cormier et al. (2014) suggest that

the observed short molecular gas depletion depletion times for their DGS sample of dwarf galaxies are due to recent bursts in star formation. Kauffmann et al. (2003) found that low redshift galaxies with stellar mass $< 3 \times 10^{10}\ M_{\odot}$ in the Sloan Digital Sky Survey (SDSS) have younger stellar populations and that the star formation histories are correlated with the stellar surface density, also indicative of recent bursts in star formation like seen in the LMC, SMC, and M33. In Figure 5.6, we show the average $\tau_{\rm dep}^{\rm mol}$ time as a function of the average stellar surface density (Σ_*) for the LMC, SMC, and the HERACLES sample of galaxies and see that all of the low molecular depletion times are found at low Σ_*. The fact that low-mass galaxies are more susceptible to stochastic star formation can produce bursts in star formation (Hopkins et al. 2014) and lead to shorter molecular gas depletion times.

5.5.2 Physical Interpretation of the Scatter in $\tau_{\rm dep}^{\rm mol}$

The scatter in the $\Sigma_{\rm mol}$-$\Sigma_{\rm SFR}$ relationship, which we quantify in terms of the scatter in $\log \tau_{\rm dep}^{\rm mol}$, can be produced by both physical mechanisms and the imperfect nature of the observable tracers of the physical quantities. The previous observational work that focused on the scatter in $\tau_{\rm dep}^{\rm mol}$, or the "break down" of the $\Sigma_{\rm mol}$-$\Sigma_{\rm SFR}$ relationship, by Schruba et al. (2010), Verley et al. (2010), and Onodera et al. (2010) studied the $\Sigma_{\rm mol} - \Sigma_{\rm SFR}$ relationship in M33 over $\gtrsim 100$ pc size scales. Schruba et al. (2010) compared $\tau_{\rm dep}^{\rm mol}$ found for apertures centered on CO peaks to apertures centered on Hα peaks for various aperture sizes from $75 - 1200$ pc and found that the $\tau_{\rm dep}^{\rm mol}$ values differed for CO and Hα peaks for $\lesssim 300$ pc size scales. There are a

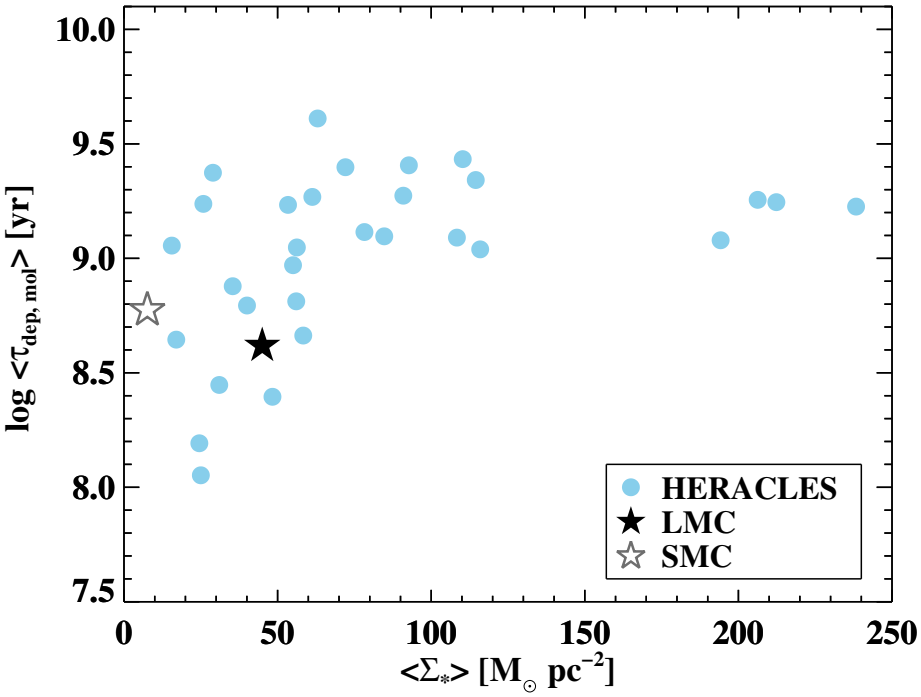

Figure 5.6 Average molecular gas depletion time as a function of the average stellar surface density for the disk-averaged HERACLES sample (Leroy et al. 2013a) in blue with the filled and open stars showing the galaxy-averaged data for the LMC and SMC, respectively. The HERACLES sample data used a Galactic CO-to-H_2 conversion factor and Σ_* was measured for the HERACLES sample, LMC, and SMC using $I_{3.6\mu\mathrm{m}}$ from *Spitzer* and the conversion from Zibetti et al. (2009). We see that the LMC and SMC points agree with the trend of lower average $\tau_{\mathrm{dep}}^{\mathrm{mol}}$ with lower Σ_*.

number of possible causes of the difference between the CO and Hα molecular gas depletions times: difference in evolutionary stage of the star-forming region, drift of the young stars from their parent cloud, actual variation in $\tau_{\rm dep}^{\rm mol}$, differences in how the observables map to physics quantities, and noise in the maps. Schruba et al. (2010) identify the evolution of individual star-forming regions as the likely cause for the variations.

At high resolution (scales of $\sim 20 - 50$ pc), the star formation and molecular gas are resolved into discrete regions that span a range evolutionary stages (e.g., Kawamura et al. 2009; Fukui & Kawamura 2010) and have different ratios of molecular gas to star formation rate tracers. Averaging over larger size scales samples regions at a range of evolutionary stages resulting in a "time-averaged" $\tau_{\rm dep}^{\rm mol}$. The change in the scatter in the molecular gas depletion time (σ) with resolution informs us about whether the star-forming regions are spatially correlated due to synchronization of star formation by a large-scale process. We see this effect in Figure 5.1; the scatter in $\tau_{\rm dep}^{\rm mol}$ decreases as the size scales are increased.

Theoretical studies can be used to explore which mechanism produces the scatter in the $\Sigma_{\rm mol}$-$\Sigma_{\rm SFR}$ relationship. We compare our results in the SMC and LMC to the hydrodynamical simulations of galaxies by Feldmann et al. (2011) and to the analytical model by Kruijssen & Longmore (2014). Both provide predictions of the amount of scatter in the $\Sigma_{\rm mol}$-$\Sigma_{\rm SFR}$ relationship for small size scales (50 pc for predictions from Kruijssen & Longmore 2014, and 300 pc for the simulations from Feldmann et al. 2011) and how the scatter changes with size scale.

The simulations by Feldmann et al. (2011) show that the time-averaging of

the star formation rate (or, our inability to measure the instantaneous star formation rate) combined with $\Sigma_{\rm mol}$ estimates that are instantaneous alone can generate most of the scatter observed in the $\Sigma_{\rm SFR}$-$\Sigma_{\rm H_2}$ relation. If we possessed a perfect, instantaneous tracer of the star formation rate, then we would expect to see high star formation rates while there is still a large amount of molecular gas. As the molecular gas is depleted and destroyed by the previous episode of star formation, both the molecular gas and star formation rate would decrease. Instead, we observe the tracers of the star formation rate (namely Hα) peak when the molecular gas is partially or mostly dissipated because the tracers show the average star formation rate over up to $\sim$ 10 Myr (Kennicutt & Evans 2012). The time evolution of star-forming regions alone does not cause the observed offset between the observed star formation rate and molecular gas, rather the time-averaging of the star formation rate combined with the time evolution of star-forming regions produces different ratios of molecular gas to star formation rate and scatter in $\tau_{\rm dep}^{\rm mol}$. Hony et al. (2015) shows evidence of this effect in the N66 region of the SMC where the star formation rate from Hα disagrees with that from pre-main sequence stars at small ($\sim 6 - 150$ pc) size scales.

Kruijssen & Longmore (2014) quantify how the scatter in the $\Sigma_{\rm gas} - \Sigma_{\rm SFR}$ relationship should change with size scale due to the incomplete statistical sampling of independent star-forming regions, including the effect of the different timescales associated with the gas and star formation tracers discussed by Feldmann et al. (2011), and add the additional scatter associated with incomplete sampling of star formation rate tracers from the initial stellar mass function (IMF), and the spatial

drift between stars between gas and stars. The model requires having an estimate of the lifetime of GMCs (t_{rmgas}), the time scale for the star formation rate tracer ($t_{\rm stars}$), the time where both the gas and star formation rate tracer overlap ($t_{\rm over}$), the typical separation between independent star-forming regions (λ), the flux ratio between peaks in the overlap phase and in isolation for the gas and star formation (β_1, β_2), the scatter due to the time evolution of gas and star formation flux ($\sigma_{\rm evol,1g}$, $\sigma_{\rm evol,1s}$), the scatter due to the mass spectrum ($\sigma_{\rm MF}$), and the observational error ($\sigma_{\rm obs}$). The predictions for the scale dependence of the scatter in the gas depletion time from Kruijssen & Longmore (2014) agrees with the predictions by Feldmann et al. (2011) at size scales $>$ 300 pc where the two are directly comparable. Kruijssen & Longmore (2014) find that the scatter varies from $\sim$ 0.9 dex at 50 pc scales to $\sim$ 0.2 dex at 1 kpc. The trend in the prediction of scatter (valid for their fiducial parameter values for disks and dwarfs) is consistent with the observation from the HERACLES galaxies (Leroy et al. 2013a) and M33 (Schruba et al. 2010).

For the LMC and SMC predictions of the scatter from Kruijssen & Longmore (2014), we use estimates of the input parameters based on observational data when possible. For both the LMC and SMC, we set $t_{\rm stars}$ = 6 Myr based on the lifetime of Hα, make the assumption that β_1, β_2 = 1, and set λ = 150 pc, the typical Toomre length (for $\Sigma_{\rm gas} \sim 10\ M_\odot\ {\rm pc}^{-2}$ and $\Omega \sim 0.03\ {\rm Myr}^{-1}$). In the LMC, we use the results of Kawamura et al. (2009) to set $t_{\rm gas}$ = 26 Myr and $\sigma_{\rm MF}$ = 0.4 dex (the mean logarithmic scatter of the Class I GMC mass). For the upper limit in the LMC, we take $t_{\rm over}$ = 0 Myr and $\sigma_{\rm evol,1g}$, $\sigma_{\rm evol,1s}$ = 0.3 dex, based on a linear time evolution to or from zero. For the lower limit in the LMC, we adopt $t_{\rm over}$ = 3 Myr

(the supernova timescale) and $\sigma_{\rm evol,1g}$, $\sigma_{\rm evol,1s}$ = 0.15 dex; while it can vary from $0-0.3$ dex, half the amount of scatter as linear evolution is a reasonable lower limit since the parameters must be > 0 due to the existence of molecular clouds without massive stars and H II regions without molecular clouds. We note that Kruijssen & Longmore (2014) assume that the galactic star formation rate is roughly constant over the entire lifetime of the GMCs ($\sim$ 30 Myr), which stands in contrast to the multiple bursts over the past $\sim$ 50 Myr identified in the star formation history of the both LMC (Harris & Zaritsky 2009) and SMC (Harris & Zaritsky 2004).

In the LMC, where the morphology is more clearly a disk and the metallicity is not much lower than Solar, we observe scatter at the level of $\sim$ 0.45 dex at $\sim$ 100 pc and $\sim$ 0.18 dex at $\sim$ kpc scales. The Feldmann et al. (2011) simulations show that the behavior of the scatter in $\log \tau_{\rm dep}^{\rm mol}$ with averaging size scale from $\sim 100-1000$ pc for Solar metallicity and radiation field are remarkable similar to the observations for the LMC. The simulations from Feldmann et al. (2011) predict scatter of $\sim 0.4-0.6$ dex at $\sim$ 100 pc scales and $\sim 0.1-0.3$ dex at $\sim$ kpc scales for their fiducial solar metallicity simulations (across the range of their parameter exploration). The Kruijssen & Longmore (2014) model produces a range in the predicted scatter in $\log \tau_{\rm dep}^{\rm mol}$ in the LMC of $0.46-0.51$ dex at 100 pc scales and $0.19-0.23$ dex at 1 kpc scales, which are comparable to the results from the Feldmann et al. (2011) and close to the observed values for the LMC (see Figure 5.7). The dominant source of scatter at large ($>$ 100 pc) size scales for the lower limit predictions (closest to the observations) from the Kruijssen & Longmore (2014) model comes from the Poisson statistics of the number of times each evolutionary phase of star formation is

sampled, which is determined primarily by the timescale of the star formation rate tracer, the lifetime of GMCs, and the separation between star-forming regions. The similarity between our observations and both the Feldmann et al. (2011) simulation and Kruijssen & Longmore (2014) model at large (> 100 pc) size scales, where both are comparable and individual star-forming regions are unresolved, supports the interpretation that the scatter in the $\Sigma_{\rm mol} - \Sigma_{\rm SFR}$ relationship can be largely attributed to star formation rate tracers that time-average the "true" or instantaneous star formation rate.

5.5.2.1 Scatter in $\tau_{\rm dep}^{\rm mol}$as a Function of Size Scale

As a means to quantify the behavior of scatter with different size scales, Feldmann et al. (2011) fit a power law to the relationship between size scale and the scatter in $\log \tau_{\rm dep}^{\rm mol}$. Leroy et al. (2013a) used a subset of nearby HERACLES galaxies to study the scatter in $\tau_{\rm dep}^{\rm mol}$ at linear resolutions of $0.6 - 2.4$ kpc, which we can compare to our results in the Magellanic Clouds spanning linear resolutions of $0.02 - 1$ kpc. Following Feldmann et al. 2011 and Leroy et al. (2013a), we quantify the scale-dependence of the scatter in $\tau_{\rm dep}^{\rm mol}$ in the LMC and SMC by

$$\sigma(l) = \sigma_{100} \left(\frac{l}{100 \text{ pc}} \right)^{-\gamma}$$

where l is the spatial resolution, σ_{100} is the scatter in $\log\left(\tau_{\rm dep}^{\rm mol}\right)$ at 100 pc resolution, and the power-law index γ measures the rate that the scatter changes with resolution

($\gamma = 1$ for uncorrelated star formation in a disk)[1]. We fit only resolutions greater than 100 pc, since below that resolution $\log(\tau_{\rm dep}^{\rm mol})$ will be biased by negative and zero values. Figure 5.7 shows how the scatter in $\tau_{\rm dep}^{\rm mol}$ changes with resolution, including the best fit power-law functions with $\gamma = 0.43$ for the LMC and $\gamma = 0.24$ for in the SMC. Leroy et al. (2013a) find a best fit γ for the scatter in $\log(\tau_{\rm dep}^{\rm mol})$ in the range of 0-0.8 with an average of $\gamma = 0.5$ (shown by the thick dashed line in Figure 5.7).

If a galaxy has a fixed $\tau_{\rm dep}^{\rm mol}$ and star formation proceeds randomly and independently in separate regions within the resolution element, then behaves like Poisson noise and $\sigma \propto \sqrt{N^{-1}}$, where N is the number of star forming regions. For a region of size l, $N \propto l^2$ so that $\sigma \propto l^{-1}$ or a power-law scaling of $\gamma = 1$. Both Feldmann et al. 2011 and Kruijssen & Longmore (2014) find that the scatter in $\log(\tau_{\rm dep}^{\rm mol})$ scales with a rough power-law scaling with an index of $\gamma = 0.5$ at larger ($\gtrsim$ 200 pc) scales. Feldmann et al. (2011) expect this shallow scaling as a result of star formation occuring in a 2D disk galaxy. However, Kruijssen & Longmore (2014) finds similar shallower slopes with uncorrelated, independent star-forming region due to the contribution to the scatter from the time evolution of the star-forming regions and from the underlying distribution of GMC masses. The model from Kruijssen & Longmore (2014) shows that the scatter due to Poisson noise dominates at large size scales that sample multiple star-forming regions ($>$ 100 pc). At small scales, the Poisson noise disappears due to the fact only one star-forming region will be sampled and the scatter from the time evolution of the star-forming regions and

[1]We use γ instead of β (used in Leroy et al. (2013a)) as the variable representing the exponent to avoid confusion with the dust emissivity index β.

from the underlying distribution of GMC masses drives the variation in ratio of star formation rate to molecular gas and $\tau_{\rm dep}^{\rm mol}$.

Figure 5.7 shows the data for the LMC and SMC, the HERACLES galaxies, and the corresponding Kruijssen & Longmore (2014) model predictions. For the SMC model predictions, we set the upper limit to the upper limit values for the LMC and the lower limit the same as for the LMC but with $t_{\rm gas} = 10$ Myr (approximate free-fall time of a GMC) and $\sigma_{\rm MF} = 0.2$ dex (60% of the scatter in GMC masses in the LMC). We see general agreement between the trend in the observed relationship and the model predictions, however, the LMC data fall below the predicted lower limit (see Section 5.5.2) at large size scales (> 200 pc). The most uncertain parameter in Kruijssen & Longmore (2014), due to lack of observational constraints, is the scatter due to the time evolution of the gas flux and star formation rate flux ($\sigma_{\rm evol,1g}$, $\sigma_{\rm evol,1s}$). Decreasing $\sigma_{\rm evol}$ further from 0.15 dex to 0.1 dex brings the model predictions much closer to the LMC observations at scales > 100 pc.

If we apply the interpretation of Feldmann et al. (2011), the shallower decline in the amount of scatter with increasing averaging scale seen in the LMC (and SMC) could be caused by increased spatial correlation between individual star-forming regions. Correlation of star-forming regions, both spatially and temporally, would cause individual star-forming regions to be at similar evolutionary phases throughout large parts of the galaxy and could explain the need for a lower amount of scatter from the time evolution for the gas flux and star formation rate. Large-scale spatial correlation in star formation requires a physical mechanism to synchronize star formation, such as bursts of star formation throughout large parts of the galaxies

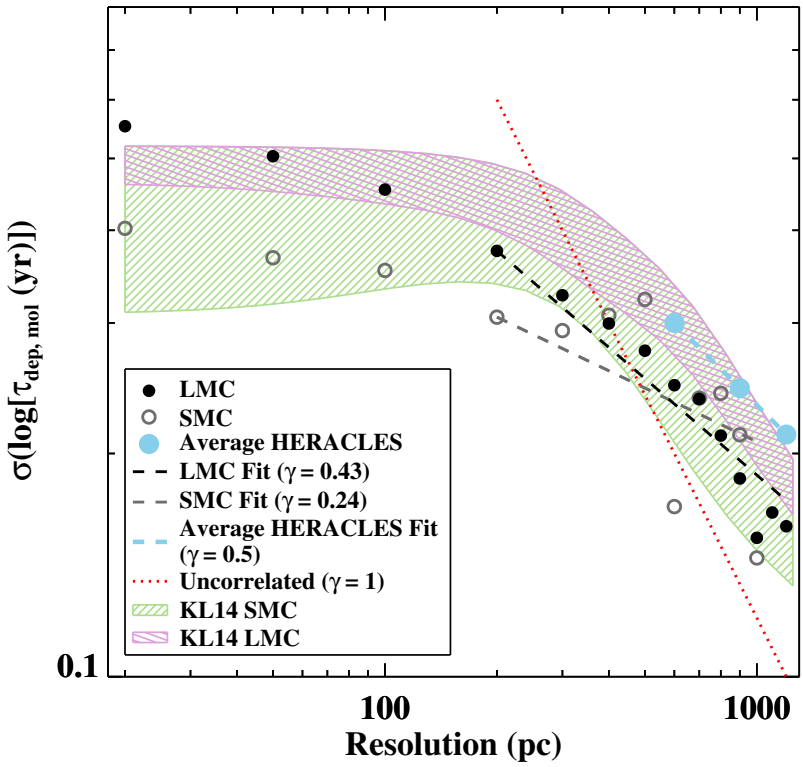

Figure 5.7 We fit power laws (dashed lines) to the change in scatter in the depletion time as a function of scale for the LMC (black filled circles) and SMC (grey filled circles), and find that the power law exponent (γ) is low indicating correlation of star formation throughout the galaxies likely due to synchronization by a large-scale process. The thick light blue line shows the line for $\gamma = 0.5$, the average fit to the 9 HERACLES galaxies that had high enough resolution ($r \sim 400$ pc) and the expected scaling for a disk galaxies from simulations by Feldmann et al. (2011). The purple and green hashed lines show the estimates of the scatter due to independent star-forming regions from the Kruijssen & Longmore (2014) model (KL14) with upper and lower limits for the LMC and SMC, respectively. For comparison, the red dashed line shows how the data would behave if there was no spatial correlation between the star formation and molecular gas at large spatial scales.

driven by tidal interactions or ram pressure. The star formation histories of both the LMC and SMC indicated that there have been recent bursts of star formation throughout large parts of the galaxies, likely due to interaction between the galaxies and the Milky Way, and is possibly driving the shorter molecular gas depletion times. The lower amount of scatter in $\log \tau_{\rm dep}^{\rm mol}$ at larger size scales observed in the LMC (and more tenuously in the SMC) could also be due to large-scale synchronization of star formation.

5.5.3 Comparison to Star Formation Model Predictions

The Magellanic Clouds provide ideal laboratories to test models of star formation given their low metallicity. While higher metallicity, the geometry of the LMC is better understood than the more irregular SMC. There are few nearby low-mass, low-metallicity systems and measuring their molecular gas content is challenging as they are often weakly emitting in CO and, when CO is observed, it is unclear what CO-to-H_2 conversion factor should be applied. The dust-based molecular gas estimates for the LMC and SMC allow us to test metallicity-dependent models of star formation at high resolution. We examine the model predictions from Ostriker et al. (2010, hereafter OML10) and Krumholz (2013, hereafter KMT+), a recent update of the Krumholz et al. (2009) model modified for atomic-dominated regions. Both models take the total gas surface density ($\Sigma_{\rm gas}$) and metallicity (Z') as input parameters and predict the fraction of molecular gas, and from that the star formation rate.

The OML10 model determines the star formation rate based on a balance between vertical gravity in the disk and the pressure of the diffuse ISM, which is controlled by star formation feedback. OML10 relates thermal pressure to $\Sigma_{\rm SFR}$, whereas Ostriker & Shetty (2011) relates turbulence to $\Sigma_{\rm SFR}$. While the star-forming gas in the OML10 model is not strictly molecular gas, but rather bound clouds, we identify our estimate of $\Sigma_{\rm H_2}$ with the model parameter $\Sigma_{\rm gbc}$, the surface density of gas in gravitationally bound clouds (note that in our methodology both H_2 and any optically thick H I are effectively indistinguishable). This ignores the fact that in very dense regions a significant fraction of the molecular gas could be not self-gravitating, a concern that is probably important in starburst environments but unlikely to matter in the Magellanic Clouds. The reverse concern, that H I may make a significant contribution to the cloud bounding mass, is likely a more significant consideration in these sources, although its magnitude is difficult to evaluate. The KMT+ model is based on the assumption that the fraction of molecular gas is mainly determined by the balance between the dissociating UV radiation field and the shielding of the gas. The KMT+ model adds to Krumholz et al. (2009) the condition that in a region with low star formation rate, hence low UV field, the threshold density of the cold neutral medium is no longer set by two-phase equilibrium between the cold and warm neutral medium, but rather by hydrostatic equilibrium.

Both the KMT+ and OML10 model use the mid-plane pressure, which requires an estimate of the density of stars and dark matter in the disk to determine the gravitational pressure. We estimate the stellar surface density by applying the mass-to-light conversion from Leroy et al. (2008) to the 3.6 μm *Spitzer* SAGE images

of the LMC and SMC. The Σ_* is then converted to volume density by assuming a stellar disk thickness of 600 pc for the LMC (van der Marel et al. 2002) and 2 kpc for the SMC (following Bolatto et al. 2011). For the LMC, we use the dark matter density profile from Alves & Nelson (2000), for the SMC we use the profile from Bekki & Stanimirović (2009) to estimate the dark matter density as a function of radius from the centers of the galaxies. We find that the combined stellar and dark matter densities have ranges of $0.6 - 0.1\ M_\odot\ \mathrm{pc}^{-3}$, with the higher values concentrated in the stellar bar and $\sim 10\%$ dark matter contribution in the LMC, and $0.006 - 0.1\ M_\odot\ \mathrm{pc}^{-3}$ with $\sim 20\%$ dark matter contribution in the SMC.

We adopt most of the fiducial model parameter values as described in OML10 and KMT+. The exception is the depletion time in gravitationally bound clouds, $t_{\mathrm{SF,gbc}}$, for which OML10 uses 2 Gyr based on the average observed value in nearby galaxies. This value was also applied in the SMC results in Bolatto et al. (2011) since the observed $\tau_{\mathrm{dep}}^{\mathrm{mol}}$ was not much lower than 2 Gyr. In this study we find a wider range of depletion timescales, and a measurable change in $\tau_{\mathrm{dep}}^{\mathrm{mol}}$ as a function of spatial scale (Fig. 5.3). It is important to note that $t_{\mathrm{SF,gbc}}$ is an input parameter of the OML10 model, obtained from observations rather than theory, and its main impact is to change the relation between Σ_{gbc} and Σ_{SFR} since $\Sigma_{\mathrm{gbc}} = t_{\mathrm{SF,gbc}}\Sigma_{\mathrm{SFR}}$

The self-regulation in the model operates to make Σ_{SFR} insensitive to the choice of $t_{\mathrm{SF,gbc}}$ over a wide range of total gas surface densities. The results we show in Fig. 5.8 are computed for $t_{\mathrm{SF,gbc}} = 0.5$ Gyr, which corresponds approximately to the value of $\tau_{\mathrm{dep}}^{\mathrm{mol}}$ we observe at large spatial scales. The main effect of changing $t_{\mathrm{SF,gbc}}$ from 0.5 to 2 Gyr is to slightly lower the predicted star formation rate, particularly

at high surface densities ($\Sigma_{\rm gas} \gtrsim 50\ M_\odot\ {\rm pc}^{-2}$). The robustness of $\Sigma_{\rm SFR}$ to the choice of $t_{\rm SF,gbc}$ in turn means that $\Sigma_{\rm gbc}$ depends significantly on the value of the depletion timescale. Since we identify $\Sigma_{\rm gbc}$ with $\Sigma_{\rm H_2}$, the consequence is that comparison of our measurements of $\Sigma_{\rm H_2}$ with the model predictions are extremely dependent on the assumed $\tau_{\rm dep}^{\rm mol}$, and on the constancy of $\tau_{\rm dep}^{\rm mol}$ with $\Sigma_{\rm gas}$. In other words, in the context of the model they are very uncertain. Adopting the approximate value observed at large spatial scales, $\tau_{\rm dep}^{\rm mol} \approx 0.5$ Gyr, results in a predicted $\Sigma_{\rm gbc}$ very similar to the observed $\Sigma_{\rm H_2}$.

Figure 5.8 shows the model predictions for the $\Sigma_{\rm SFR}$ for the LMC and SMC. Since both models require averaging over the different gas phases, we only compare the predictions to the data at $r \sim 200$ pc and $r \sim 1$ kpc. While the models can predict the molecular-to-atomic ratio (or, diffuse to gravitationally bound for OML10), the models self-regulate in diffuse gas, which is the dominant regime in the LMC and SMC, and predict similar star formation rates. Both KMT+ and OML10 models predict the general trend observed in the relationship between $\Sigma_{\rm gas}$ and $\Sigma_{\rm SFR}$.

The models do not predict the amount of scatter seen in the higher resolution 200 pc data. This is not surprising since both OML10 and KMT+ predict a time-averaged star formation rate and do not recover variations in the star formation rate based on the details on the star formation rate tracer combined with differences in the evolutionary stages of individual star-forming regions. Assuming that the physical interpretation from Feldmann et al. (2011) is correct, which is supported by the predictions of the amount of scatter in $\tau_{\rm dep}^{\rm mol}$ at ~ 100 pc and 1 kpc scales

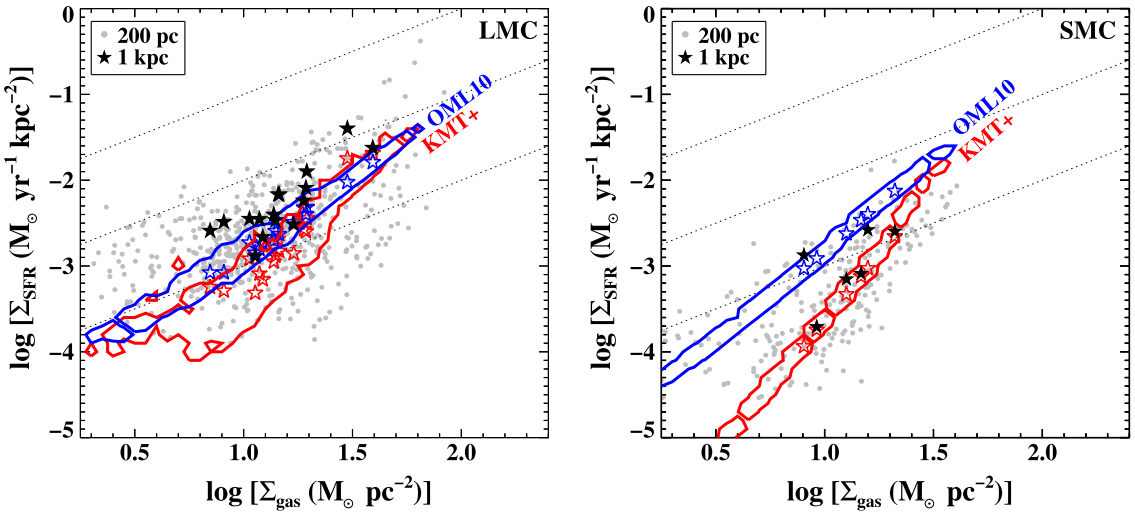

Figure 5.8 Star formation rate predictions from the OML10 and KMT+ models. The grey filled circles show the data at $r = 200$ pc, and the filled stars show the $r = 1$ kpc data. The diagonal dashed lines indicate constant total gas depletion times (from bottom to top: 10 Gyr, 1 Gyr, and 0.1 Gyr). The contours show the full extent of the distribution of points for the model predictions at $r = 200$ pc resolution and the open stars show the $r = 1$ kpc predictions. The KMT+ and OML10 predictions are shown in red and blue, respectively, for the appropriate metallicities for each galaxy and for $t_{\rm SF,GBC} = 0.5$ Gyr for the OML10 model. Both models predict the trend in the data, but do not capture the full extent of the scatter observed.

matching our observations, then an important, possibly the dominant, source of scatter is the time-averaging of the star formation rate (over as little as 10 Myr, Kennicutt & Evans 2012) inherent in using Hα and 24 μm as star formation rate tracers. We think that it is likely that the under-prediction of the amount of scatter in the OML10/KMT+ model predictions at 200 pc is due to the fact that the star formation models do not include the time-averaging effect of the star formation rate tracer (Hα). The scatter present in the OML10/KMT+ model predictions come only from the spatial variation in the stellar and dark matter density, which affects the pressure and therefore the predicted amount of star-forming gas. When averaging over larger ($\sim$ kpc) scales, the difference between the scatter in the data and the scatter in the predictions decreases and the two are comparable. The model predictions are most appropriate at large scales where many independent star-forming regions are averaged over to account for the fact that star formation is treated as a time-averaged process.

The main differences between the star formation rates from OML10 vs. KMT+ appear at high $\Sigma_{\rm gas}$ and low metallicity, where the predictions diverge. All of the KMT+ predictions, independent of metallicity, converge at high $\Sigma_{\rm gas}$ because once the ISM transitions to H_2-rich, which happens past a column density based on the amount of shielding, then the star formation will not behave any differently from high metallicity galaxies. The OML10 model will tend to continue to predict lower $\Sigma_{\rm SFR}$ at high $\Sigma_{\rm gas}$ because the lower metallicity increases the thermal pressure and reduces the star formation at all surface densities. At the same metallicity and at high $\Sigma_{\rm gas}$, OML10 will predict lower $\Sigma_{\rm SFR}$ than KMT+.

5.6 Summary and Conclusions

Using our H_2 maps we study the relationship between gas and star formation without relying on a conversion factor to translate CO emission to the total amount of molecular gas. The high resolution data allow us to study the relationship over 20 to 1000 pc scales. Our main conclusions are as follows:

1. Combining the new molecular gas estimates with the star formation rate from Hα and 24 μm, we find molecular gas depletion times at 1 kpc scales of 0.4 Gyr for the LMC and 0.6 Gyr for the SMC (Figure 5.3). These molecular gas depletion times are shorter than the the average found for normal, nearby star-forming galaxies (Figure 5.1), but are within the scatter found in the STING and HERACLES samples (Rahman et al. 2012; Leroy et al. 2013a, ;Figure 5.2). We show that when we include our dust-based molecular gas depletion time measurements with those using CO from the HERACLES sample (Figure 5.4) we see no trend with metallicity, which suggests the possible trends seen by (Rahman et al. 2012; Leroy et al. 2013a) could be due to the affect of metallicity on the CO-to-H_2 conversion factor. The shorter molecular gas depletion times in the LMC and SMC are similar to that observed in M33 (Schruba et al. 2010) and may be associated with the recent bursts in their star formation history.

2. We measure the rank correlation coefficient of the relationships between $\Sigma_{\rm HI}$ and $\Sigma_{\rm SFR}$ and $\Sigma_{\rm H_2}$ and $\Sigma_{\rm SFR}$ from 20 to 1000 pc size scales (5.5). The correla-

tion between $\Sigma_{\rm HI}$ and $\Sigma_{\rm SFR}$ is scale independent while the correlation between $\Sigma_{\rm H_2}$ and $\Sigma_{\rm SFR}$ increases steadily until flattening out at scales of ~ 200 pc and larger and on those scales is better correlated than $\Sigma_{\rm HI}$ and $\Sigma_{\rm SFR}$.

3. We measure the scatter in the molecular gas depletion time as a function of size scale (Figure 5.7). We have compared the observed scatter in the molecular gas depletion time to the predictions from the simulations by Feldmann et al. (2011) and the model by Kruijssen & Longmore (2014). We find that both can produce the behavior of the scatter with size scale, which suggests that scatter in the $\Sigma_{\rm SFR} - \Sigma_{\rm H_2}$ relation may be driven largely by the time-averaging effect of the star formation rate tracer combined with instantaneous measurements of the molecular gas at large scales (> 100 pc). From comparison with Feldmann et al. (2011) and Kruijssen & Longmore (2014), we see possible evidence of synchronization of star formation in how the amount of scatter changes with size scale in the LMC (and potentially the SMC), perhaps due to star formation on large-scales caused by interactions.

4. We have compared the observed $\Sigma_{\rm SFR}$ to the predictions from OML10 and KMT+ star formation models (Figure 5.8) and find wide agreement, indicating that the inclusion of a diffuse neutral medium is important for predicting the star formation rate in atomic-dominated systems like the Magellanic Clouds. Neither model captures the full extent of the scatter seen in the data at 200 pc scales, which we attribute to the time-averaging effect of the star formation rate tracer (as referred to in our previous conclusion).

Chapter 6: Conclusion

By using dust emission and the combination of [C II]+CO, we have produced estimates of the total molecular gas at low metallicity. In the SMC, we see extended photodissociation regions with higher fractions of warm molecular gas as the main effect of the lower metallicity. While less of the molecular gas is traced by bright CO emission at low metallicity, some of that gas is warm and most of it exists at low A_V in the outskirts of the molecular clouds where it is unlikely to contribute directly to the formation of stars. Using our dust-based molecular gas estimates, we find molecular gas depletion times ($\tau_{\rm dep}^{\rm mol} = \Sigma_{\rm mol}/\Sigma_{\rm SFR}$) that are within the range found for normal disk galaxies, but shorter than the average value of ~ 2 Gyr for nearby galaxies (Rahman et al. 2012; Leroy et al. 2013a), which could be due to recent bursts in star formation. We find no evidence for a strong intrinsic dependence of the molecular gas depletion time on metallicity. We also see evidence for large-scale synchronization of star formation in the way the scatter in $\tau_{\rm dep}^{\rm mol}$ changed with size scale, which may be due to the recent bursts in star formation seen in the star formation histories of the both the SMC and LMC (Harris & Zaritsky 2004, 2009). The comparison of our observations to star formation model predictions demonstrates that the inclusion of a diffuse neutral medium is needed to explain the levels of star

formation observed at the low gas surface densities in the Magellanic Cloud and other low mass galaxies. Our observations and analysis show no indication that star formation proceeds differently in low metallicity, low mass galaxies.

6.1 Future Work

6.1.1 What is the nature of the "CO-faint" gas and its effect on star formation?

How much of the "CO-faint" molecular gas could be optically thick H I in the LMC and SMC? Regardless of whether it is molecular or atomic, how do these extended envelopes around the "CO-bright" contribute to star formation? In Chapter 1 (Jameson et al. 2016), we assume that the excess gas traced by dust is molecular. In fact, some fraction of it may be optically thick H I not accounted for in our optically thin assumption when converting the observed H I line emission to a column density. The H I optical depth estimate using absorption line studies in the SMC (Stanimirović et al. 1999; Dickey et al. 2000) and in the MW (Lee et al. 2015a) showed that correcting for H I optical depth only increased the total H I mass by $\sim 10\%$. Conversely, there are indications of significant optical depth corrections in in M31, M33, and the LMC from fitting line profiles (Braun 2012) and in massive star-forming region W43 in the Milky Way using new absorption line study with VLA data (Bihr et al. 2015). We can begin to address these questions with the existing H I data by stacking spectra in regions with high amounts of excess gas traced by dust (or [C II]) and comparing the dust-based excess gas map with H I peak temperature map. Future absorption line studies using ATCA and ASKAP

(and in the more distant future, SKA) is key to determining how H I optical depth and CNM/WNM changes with environment, which is necessary to understand the nature of the gas surrounding "CO-bright" molecular regions and understand how environment affects the H I-to-H_2 transition and determine whether this has an effect on the dense molecular gas and star formation.

6.1.2 Does Metallicity Affect the Properties of Molecular Clouds and H II regions?

The ALMA observations are the first observations of large regions of the molecular ISM in a very low metallicity environment ($Z_{\rm SMC} \approx 0.2\,Z_{\odot}$) on ~ 2 pc scales (~ 0.5 with future 12m-array data). In conjunction with *Herschel* and *Spitzer* imaging and spectroscopic data these observations will allow us to probe the "CO-bright" and "CO-faint" molecular phase prevalent at low metallicities (see Bolatto et al. 2013 for a review) in two ways: we will obtain direct measurements of optical depths and column densities in bright regions using the CO isotopologues, and we will resolve the photodissociation region (PDR) structure — including the progressive transition from CO-faint to CO-bright emission and the extended CO-faint molecular envelopes of CO-bright clouds (Leroy et al. 2007). At the SMC metallicity and dust-to-gas ratio it takes several parsecs to build up the column density corresponding to $A_V \sim 1-2$ and transition from the CO-faint to the CO-bright regime of molecular gas (e.g., ~ 5 pc for a $n \sim 300$ cm^{-3} cloud).

Are the CO-bright regions of GMCs similar at low and high metallicity? Or, is the structure of the CO-bright portion of a GMC affected by the extended envelope

and the changes in chemistry and thermodynamics? The large-scale characteristics of GMCs appear similar across the local group (Bolatto et al. 2008; Heyer et al. 2009), although there is some indication that the properties depend on local environment (Hughes et al. 2010). However, the available observations do not probe sub-GMC scales. We will address these questions by measuring sizes, column densities, virial parameters, and line profiles of the CO-bright molecular regions for the first time at a resolution of 0.5 pc, bridging the gap between Galactic and extragalactic observations. Heyer & Brunt (2004) find that the size-linewidth relation generated by turbulence is approximately constant throughout the Milky Way and also present on sub-GMC scales. We will test whether turbulence changes from region to region in the SMC, and also with respect to ALMA observations in 30 Doradus in the LMC (Indebetouw et al. 2013) by comparing the scaling exponent and coefficient of the size-linewidth relationship.

Star formation is observed to be an inefficient process (Matzner 2002; Krumholz et al. 2006), likely due to feedback causing this by injecting turbulence into molecular clouds. The ALMA observations allow us to measure the energy injection from star formation and its role at shaping the surrounding molecular gas in the SMC for the first time. The ancillary multi-wavelength data allows us to estimate densities and pressures in H II regions (Lopez et al. 2011, 2014), and compare them to CO kinematics. We will also be able to search for wide CO wings associated with photo-evaporation of the CO-bright molecular material, and resolve high velocity outflows caused by massive embedded star formation.

In addition to measuring the pressures within H II regions, we can learn about

the physical conditions of the ionized gas in low-metallicity H II regions and determine more accurate, local measurements of the gas phase metallicities by modeling the ionic lines found in the mid-IR *Spitzer* IRS spectroscopy. Only two H II regions in the SMC have been studied in detail with *Spitzer* IRS spectroscopy: N66 (Lebouteiller et al. 2008; Whelan et al. 2013) and N88A (Kurt et al. 1999), both are unusual since N66 is the largest H II region in the SMC and N88A is an isolated compact H II region. We will use the latest version of the plasma simulation code CLOUDY (Ferland et al. 2013) to model the ionization, chemical, and thermal state of the gas within the H II regions. With the larger sample of 6 star-forming regions in the S^{4}MC, which overlap the ALMA and *Herschel* coverage, we will study the properties of the ionized gas in low-metallicity across a range of star formation activity and compare the SMC regions with results from similar studies in the nearby SINGS galaxies (Dale et al. 2009), blue compact dwarfs (Wu et al. 2006), and Galactic H II regions.

6.1.3 Can the Star Formation History of Galaxies Explain Variations in $\tau_{\rm dep}^{\rm mol}$?

Determining whether environmental factors affect how molecular gas forms stars throughout galaxies is key part of understanding galaxy evolution. The fact that low-mass galaxies are more susceptible to stochastic star formation can produce bursts in star formation and lead to shorter molecular gas depletion times. To make any statement about the effect of bursts of star formation on the relationship between molecular gas and star formation requires a large sample of nearby galaxies

with resolved molecular gas observations. The Extragalactic Database for Galaxy Evolution (EDGE; PI: A. Bolatto, Co-I: K. Sandstrom) is a molecular gas survey using the Combined Array for Millimeter Astronomy (CARMA) of 125 galaxies based on the Calar Alto Legacy Integral Field Area survey (CALIFA; Sánchez et al. 2012) IFU sample. Having a large sample of resolved ^{12}CO observations remove the bias by unresolved galaxies to only detect the bright central ^{12}CO emission in the galaxies and allows us to compare $\tau_{\rm dep}^{\rm mol}$ values within galaxies to the spatially resolved star formation histories. By using the new EDGE sample of galaxies with ^{12}CO maps from CARMA and star formation histories using the integral field spectroscopy from CALIFA (González Delgado et al. 2014), we can compare the molecular gas depletion times with the star formation history. If bursts are indeed driving the observed differences, then we expect to see a trend towards shorter $\tau_{\rm dep}^{\rm mol}$ with the amount of time since the last major episode of star formation.

Recent cosmological galaxy simulations with explicit treatment of the multi-phase ISM and stellar feedback by (Hopkins et al. 2014) are able to reproduce the $\Sigma_{\rm gas}$ vs. $\Sigma_{\rm SFR}$ relationship and find that the scatter in the relationship can be explained by the variation in the recent star formation history of the individual galaxies. By investigating the effect of star formation history on the molecular gas depletion time, we will be able to test whether the scatter in the relationship is due to variations in the amount of recent star formation in galaxies. Observational verification of predictions by cosmological simulations of galaxy evolution are key to determining whether the simulations include accurate treatment of the relevant physics.

Appendix A: SMC PDR Models

The PDR model we use is based on that of Kaufman et al. (2006), Wolfire et al. (2010), and Hollenbach et al. (2012) but with a modified grain extinction, grain abundances, and gas phase abundances as appropriate for the SMC. For the gas phase metal abundances we use 1/5 of the Galactic values. We use the conversion between optical depth and column density for the average "Bar Sample" from Gordon et al. (2003), $N/A_V = 1.32 \times 10^{22}$ cm^{-2}. For the small grain abundance, which scales the photoelectric heating rate, we use an abundance 1/7.7 of the Galactic value from Sandstrom et al. (2010). The FUV rise of the dust extinction is known to be steeper than the Galactic case (Gordon et al. 2003) which decreases the penetration of FUV photons into the PDR. The general form of the photo-chemical rates is $G_0 \alpha \exp(-\beta A_V)$, where α scales the overall rate and β accounts for the dust attenuation relative to visible wavelengths. We assume that the beta coefficients for the SMC are a factor of 2 higher than for local Galactic grains. This assumption was checked using the Meudon PDR code (Le Petit et al. 2006). First we added an SMC extinction curve to the code using the fits in Gordon et al. (2003) to the Fitzpatrick & Massa (1990) parameterized extinction curves. Second we fit the resulting beta dependence as a function of Av to several key rates calculated by the Meudon PDR

code. We find the factor of 2 results in less than 10% difference in α compared to the Meudon code for the rates that we tested.

Resulting contour plots for [O I] 63 μm/[C II] 158 μm and ([O I] 63 μm + [C II] 158 μm)/FIR as a function of G_0 and n are shown in Figure A.1. For reference, Figure A.2 shows the PDR model results using the models for Galactic conditions from Kaufman et al. (2006). Compared to the Galactic case (Kaufman et al. 1999, 2006) at fixed G_0, the contours of ([OI] 63 + [CII] 158)/FIR are generally shifted to higher density or lower G_0/n ratio. This line-to-continuum ratio can be interpreted as the heating efficiency or the fraction of energy that goes into gas heating compared to the total FUV photon energy (note that the total FIR is approximately twice the FUV energy due to dust heating by optical photons). Theoretical models predict that in low metallicity environments, the reduced abundance of electrons from metals, leads to a higher grain charge and lower heating efficiencies (e.g., Röllig et al. 2006). Increasing n, or lowering G_0/n, leads to more neutral grains and higher heating efficiencies. For low G_0 ($\lesssim$ 10) and low densities n ($\lesssim 10^3$) the [O I] 63 μm/[C II] 158 μm ratio for the SMC deviates from the Galactic curves due to the strong temperature dependence in this region and the effects of metallicity on the heating efficiency. Lower heating efficiency leads to a lower temperature, low [O I] 63 μm line intensity, and low [O I] 63 μm/[C II] 158 μm ratio (we note that at very low G_0 and high density the [C II] line intensity rapidly drops leading to a high ratio of [O I] 63 μm/[C II] 158 μm). At higher density and G_0 the curves are similar to the Galactic case.

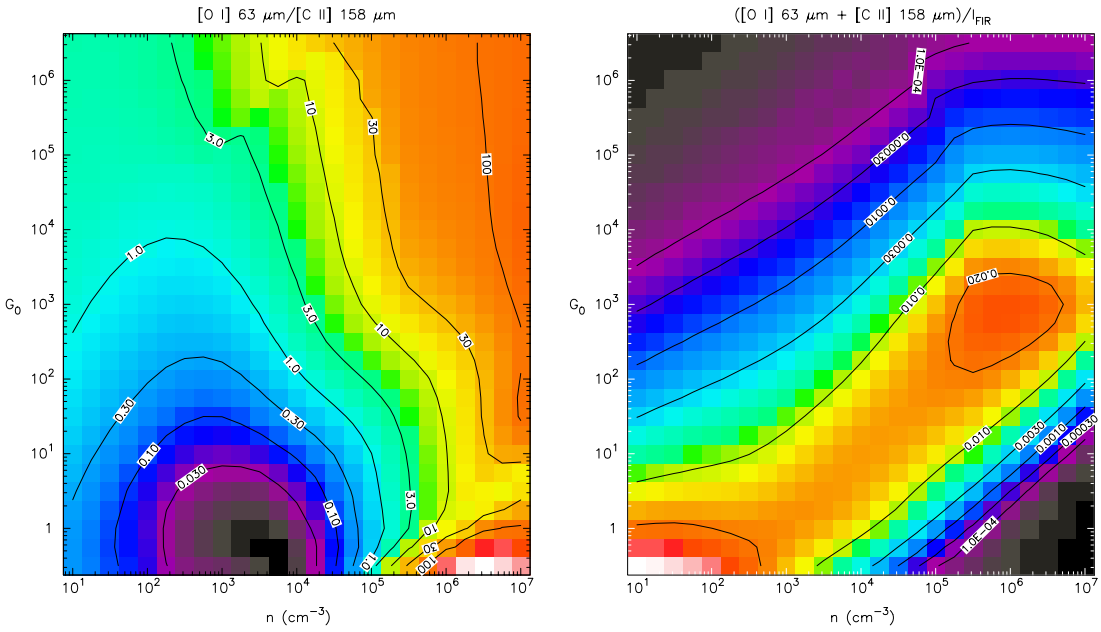

Figure A.1 New SMC PDR model contour plots for the [O I] 63 μm/[C II] 158 μm (left) and ([O I] 63 μm + [C II] 158 μm)/FIR ratios as a function of n and G_0.

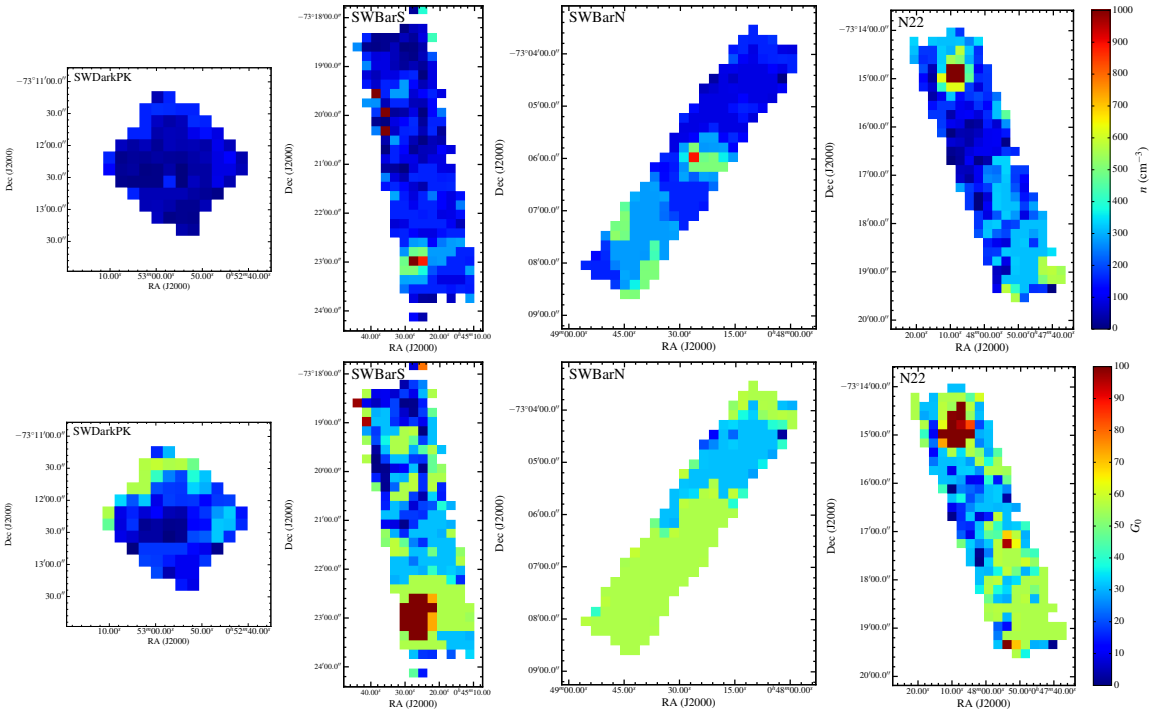

Figure A.2 Images of the results using the previous PDR models for Galactic conditions from Kaufman et al. (2006) for volume density (n; top row), and FUV radiation field strength (G_0; bottom row) for each of the regions using the same [C II], [O I], and TIR data as Figure 3.12. These models indicate similar radiation field strengths, but the densities are a factor of ~ 10 lower than those found using the SMC PDR models.

Bibliography

Alves, D. R., & Nelson, C. A. 2000, ApJ, 542, 789

Aniano, G., Draine, B. T., Gordon, K. D., & Sandstrom, K. 2011, PASP, 123, 1218

Bakes, E. L. O., & Tielens, A. G. G. M. 1994, ApJ, 427, 822

Barinovs, Ğ., van Hemert, M. C., Krems, R., & Dalgarno, A. 2005, ApJ, 620, 537

Bekki, K., & Stanimirović, S. 2009, MNRAS, 395, 342

Bekki, K., Hirashita, H., & Tsujimoto, T. 2015, ApJ, 810, 39

Berkhuijsen, E. M., Mitra, D., & Mueller, P. 2006, Astronomische Nachrichten, 327, 82

Bernard, J.-P., Reach, W. T., Paradis, D., et al. 2008, AJ, 136, 919

Besla, G., Kallivayalil, N., Hernquist, L., et al. 2012, MNRAS, 421, 2109

Bigiel, F., Leroy, A., Walter, F., et al. 2008, AJ, 136, 2846

Bigiel, F., Leroy, A., Walter, F., et al. 2010, AJ, 140, 1194

Bigiel, F., Leroy, A. K., Walter, F., et al. 2011, ApJL, 730, L13

Bihr, S., Beuther, H., Ott, J., et al. 2015, A&A, 580, A112

Blanc, G. A., Heiderman, A., Gebhardt, K., Evans, N. J., II, & Adams, J. 2009, ApJ, 704, 842

Bloemen, J. B. G. M., Deul, E. R., & Thaddeus, P. 1990, A&A, 233, 437

Bolatto, A. D., Jackson, J. M., & Ingalls, J. G. 1999, ApJ, 513, 275

Bolatto, A. D., Simon, J. D., Stanimirović, S., et al. 2007, ApJ, 655, 212

Bolatto, A. D., Leroy, A. K., Rosolowsky, E., Walter, F., & Blitz, L. 2008, ApJ, 686, 948

Bolatto, A. D., Leroy, A. K., Jameson, K., et al. 2011, ApJ, 741, 12

Bolatto, A. D., Wolfire, M., & Leroy, A. K. 2013, ARAA, 51, 207

Bot, C., Boulanger, F., Lagache, G., Cambrésy, L., & Egret, D. 2004, A&A, 423, 567

Boulanger, F., Abergel, A., Bernard, J.-P., et al. 1996, A&A, 312, 256

Brand, J., & Wouterloot, J. G. A. 1995, A&A, 303, 851

Brauher, J. R., Dale, D. A., & Helou, G. 2008, ApJS, 178, 280-301

Braun, R. 2012, ApJ, 749, 87

Bruens, C. 2005, A&A, 432, 45B

Burton, M. G., Hollenbach, D. J., & Tielens, A. G. G. 1992, ApJ, 399, 563

Calzetti, D., Liu, G., & Koda, J. 2012, ApJ, 752, 98

Cormier, D., Madden, S. C., Lebouteiller, V., et al. 2015, A&A, 578, A53

Coupeaud, A., Demyk, K., Meny, C., et al. 2011, A&A, 535, A124

Caldwell, J. A. R., & Coulson, I. M. 1986, MNRAS, 218, 223

Calzetti, D., Kennicutt, R. C., Engelbracht, C. W., et al. 2007, ApJ, 666, 870

Calzetti, D., Wu, S.-Y., Hong, S., et al. 2010, ApJ, 714, 1256

Cohen, R. S., Dame, T. M., Garay, G., et al. 1988, ApJL, 331, L95

Compiègne, M., Verstraete, L., Jones, A., et al. 2011, A&A, 525, AA103

Cormier, D., Madden, S. C., Lebouteiller, V., et al. 2014, A&A, 564, A121

Cox, P., Kruegel, E., & Mezger, P. G. 1986, A&A, 155, 380

Crawford, M. K., Genzel, R., Townes, C. H., & Watson, D. M. 1985, ApJ, 291, 755

Croxall, K. V., Smith, J. D., Wolfire, M. G., et al. 2012, ApJ, 747, 81

Croxall, K. V., et al. 2016, *inprep*

Dame, T. M., Hartmann, D., & Thaddeus, P. 2001, ApJ, 547, 792

Dale, D. A., & Helou, G. 2002, ApJ, 576, 159

Dale, D. A., Smith, J. D. T., Schlawin, E. A., et al. 2009, ApJ, 693, 1821

Dalgarno, A., & Black, J. H. 1976, Reports on Progress in Physics, 39, 573

Davidge, T. J., & Puzia, T. H. 2011, ApJ, 738, 144

Davies, R. D., Elliott, K. H., & Meaburn, J. 1976, MmRAS, 81, 89

de Blok, W. J. G., Walter, F., Smith, J.-D. T, et al. 2016, arXiv:1604.08777

De Looze, I., Cormier, D., Lebouteiller, V., et al. 2014, A&A, 568, A62

Desert, F.-X., Boulanger, F., & Puget, J. L. 1990, A&A, 237, 215

Dickey, J. M., Mebold, U., Marx, M., et al. 1994, A&A, 289, 357

Dickey, J. M., Mebold, U., Stanimirovic, S., & Staveley-Smith, L. 2000, ApJ, 536, 756

Draine, B. T., & Li, A. 2001, ApJ, 551, 807

Draine, B. T. 2003, ARAA, 41, 241

Draine, B. T., & Li, A. 2007, ApJ, 657, 810

Draine, B. T. 2011, Physics of the Interstellar and Intergalactic Medium by Bruce T. Draine. Princeton University Press, 2011. ISBN: 978-0-691-12214-4

Dufour, R. J. 1984, in IAU Symp. 108, Structure and Evolution of the Magellanic Clouds, ed. S. van den Bergh & K. S. D. de Boer (Dordrecht: Reidel), 353

Dupac, X., Bernard, J.-P., Boudet, N., et al. 2003, A&A, 404, L11

Feldmann, R., Gnedin, N. Y., & Kravtsov, A. V. 2011, ApJ, 732, 115

Ferland, G. J., Porter, R. L., van Hoof, P. A. M., et al. 2013, RMxAA, 49, 137

Fitzpatrick, E. L., & Massa, D. 1990, ApJS, 72, 163

Fuente, A., Martín-Pintado, J., Rodríguez-Fernández, N. J., et al. 1999, ApJL, 518, L45

Fukui, Y., Kawamura, A., Minamidani, T., et al. 2008, ApJS, 178, 56

Fukui, Y., Kawamura, A., Wong, T., et al. 2009, ApJ, 705, 144

Fukui, Y., Torii, K., Onishi, T., et al. 2015, ApJ, 798, 6

Fukui, Y., & Kawamura, A. 2010, ARAA, 48, 547

Galametz, M., Hony, S., Galliano, F., et al. 2013, MNRAS, 431, 1596

Galliano, F., Hony, S., Bernard, J.-P., et al. 2011, A&A, 536, A88

Gao, Y., & Solomon, P. M. 2004, ApJ, 606, 271

Gaustad, J. E., McCullough, P. R., Rosing, W., & Van Buren, D. 2001, PASP, 113, 1326

Genzel, R., Tacconi, L. J., Combes, F., et al. 2012, ApJ, 746, 69

Glover, S. C. O., & Mac Low, M.-M. 2011, MNRAS, 412, 337

Goldsmith, P. F., Langer, W. D., Pineda, J. L., & Velusamy, T. 2012, ApJS, 203, 13

González Delgado, R. M., Pérez, E., Cid Fernandes, R., et al. 2014, A&A, 562, A47

Gordon, K. D., Clayton, G. C., Misselt, K. A., Landolt, A. U., & Wolff, M. J. 2003, ApJ, 594, 279

Gordon, K. D., Engelbracht, C. W., Rieke, G. H., et al. 2008, ApJ, 682, 336-354

Gordon, K. D., Meixner, M., Meade, M. R., et al. 2011, AJ, 142, 102

Gordon, K. D., Roman-Duval, J., Bot, C., et al. 2014, ApJ, 797, 85

Groenewegen, M. A. T. 2000, A&A, 363, 901

Grenier, I. A., Casandjian, J.-M., & Terrier, R. 2005, Science, 307, 1292

Griffin, M. J., Abergel, A., Abreu, A., et al. 2010, A&A, 518, L3

Habart, E., Boulanger, F., Verstraete, L., et al. 2003, A&A, 397, 623

Haffner, L. M., Dettmar, R.-J., Beckman, J. E., et al. 2009, Reviews of Modern Physics, 81, 969

Harris, J., & Zaritsky, D. 2004, AJ, 127, 1531

Harris, J., & Zaritsky, D. 2009, AJ, 138, 1243

Haschke, R., Grebel, E. K., & Duffau, S. 2012, AJ, 144, 107

Henize, K. G. 1956, ApJS, 2, 315

Herbst, T. M., Beckwith, S. V. W., Glindemann, A., et al. 1996, AJ, 111, 2403

Herrera-Camus, R., Bolatto, A. D., Wolfire, M. G., et al. 2015, ApJ, 800, 1

Herrera-Camus, R., Bolatto, A., Smith, J. D., et al. 2016, ApJ, 826, 175

Herrer-Camus, R., et al. 2016, *in prep*

Heyer, M. H., & Brunt, C. M. 2004, ApJL, 615, L45

Heyer, M., Krawczyk, C., Duval, J., & Jackson, J. M. 2009, ApJ, 699, 1092

Heyminck, S., Graf, U. U., Güsten, R., et al. 2012, A&A, 542, L1

Higdon, S. J. U., Armus, L., Higdon, J. L., Soifer, B. T., & Spoon, H. W. W. 2006, ApJ, 648, 323

Hindman, J. V. 1967, Australian Journal of Physics, 20, 147

Hollenbach, D. J., Takahashi, T., & Tielens, A. G. G. M. 1991, ApJ, 377, 192

Hollenbach, D. J., & Tielens, A. G. G. M. 1997, ARAA, 35, 179

Hollenbach, D. J., & Tielens, A. G. G. M. 1999, Reviews of Modern Physics, 71, 173

Hollenbach, D., Kaufman, M. J., Neufeld, D., Wolfire, M., & Goicoechea, J. R. 2012, ApJ, 754, 105

Hony, S., Gouliermis, D. A., Galliano, F., et al. 2015, MNRAS, 448, 1847

Hopkins, P. F., Kereš, D., Oñorbe, J., et al. 2014, MNRAS, 445, 581

Houck, J. R., Roellig, T. L., Van Cleve, J., et al. 2004, SPIE, 5487, 62

Hughes, A., Wong, T., Ott, J., et al. 2010, MNRAS, 406, 2065

Hughes, A., Meidt, S. E., Colombo, D., et al. 2013, ApJ, 779, 46

Hunt, L. K., Thuan, T. X., Izotov, Y. I., & Sauvage, M. 2010, ApJ, 712, 164

Indebetouw, R., Brogan, C., Chen, C.-H. R., et al. 2013, ApJ, 774, 73

Israel, F. P., Johansson, L. E. B., Lequeux, J., et al. 1993, A&A, 276, 25

Israel, F. P., Maloney, P. R., Geis, N., et al. 1996, ApJ, 465, 738

Israel, F. P. 1997, A&A, 328, 471

Israel, F. P., Johansson, L. E. B., Rubio, M., et al. 2003, A&A, 406, 817

Israel, F. P., Wall, W. F., Raban, D., et al. 2010, A&A, 519, A67

Israel, F. P., & Maloney, P. R. 2011, A&A, 531, A19

Jager, C., Mutschke, H., & Henning, T. 1998, A&A, 332, 291

Jameson, K. E., Bolatto, A. D., Leroy, A. K., et al. 2016, ApJ, 825, 12

Jenkins, E. B. 2009, ApJ, 700, 1299

Kapala, M. J., Sandstrom, K., Groves, B., et al. 2015, ApJ, 798, 24

Kaufman, M. J., Wolfire, M. G., Hollenbach, D. J., & Luhman, M. L. 1999, ApJ, 527, 795

Kauffmann, G., Heckman, T. M., White, S. D. M., et al. 2003, MNRAS, 341, 54

Kaufman, M. J., Wolfire, M. G., & Hollenbach, D. J. 2006, ApJ, 644, 283

Kawamura, A., Mizuno, Y., Minamidani, T., et al. 2009, ApJS, 184, 1

Keller, S. C., & Wood, P. R. 2006, ApJ, 642, 834

Kennicutt, R. C., Jr., & Hodge, P. W. 1986, ApJ, 306, 130

Kennicutt, R. C., Jr. 1989, ApJ, 344, 685

Kennicutt, R. C., Jr., Bresolin, F., Bomans, D. J., Bothun, G. D., & Thompson, I. B. 1995, AJ, 109, 594

Kennicutt, R. C., Jr. 1998, ApJ, 498, 541

Kennicutt, R. C., Jr., Calzetti, D., Walter, F., et al. 2007, ApJ, 671, 333

Kennicutt, R. C., Jr., Hao, C.-N., Calzetti, D., et al. 2009, ApJ, 703, 1672

Kennicutt, R. C., & Evans, N. J. 2012, ARAA, 50, 531

Kim, S., Staveley-Smith, L., Dopita, M. A., et al. 1998, ApJ, 503, 674

Kim, S., Staveley-Smith, L., Dopita, M. A., et al. 2003, ApJS, 148, 473

Krips, M., Crocker, A. F., Bureau, M., Combes, F., & Young, L. M. 2010, MNRAS, 407, 2261

Kruijssen, J. M. D., & Longmore, S. N. 2014, MNRAS, 439, 3239

Krumholz, M. R., Matzner, C. D., & McKee, C. F. 2006, ApJ, 653, 361

Krumholz, M. R., McKee, C. F., & Tumlinson, J. 2009, ApJ, 699, 850

Krumholz, M. R., Leroy, A. K., & McKee, C. F. 2011, ApJ, 731, 25

Krumholz, M. R., Dekel, A., & McKee, C. F. 2012, ApJ, 745, 69

Krumholz, M. R. 2012, ApJ, 759, 9

Krumholz, M. R. 2013, MNRAS, 436, 2747

Kurt, C. M., & Dufour, R. J. 1998, Revista Mexicana de Astronomia y Astrofisica Conference Series, 7, 202

Kurt, C. M., Dufour, R. J., Garnett, D. R., et al. 1999, ApJ, 518, 246

Lada, C. J., Lombardi, M., & Alves, J. F. 2009, ApJ, 703, 52

Lada, C. J., Lombardi, M., & Alves, J. F. 2010, ApJ, 724, 687

Lada, C. J., Forbrich, J., Lombardi, M., & Alves, J. F. 2012, ApJ, 745, 190

Lada, C. J., Lombardi, M., Roman-Zuniga, C., Forbrich, J., & Alves, J. F. 2013, ApJ, 778, 133

Langer, W. D., Velusamy, T., Pineda, J. L., et al. 2010, A&A, 521, L17

Langer, W. D., Velusamy, T., Pineda, J. L., Willacy, K., & Goldsmith, P. F. 2014, A&A, 561, A122

Lebouteiller, V., Bernard-Salas, J., Brandl, B., et al. 2008, ApJ, 680, 398-419

Lee, C., Leroy, A. K., Schnee, S., et al. 2015, MNRAS, 450, 2708

Lee, C., Leroy, A. K., Schnee, S., et al. 2015, MNRAS, 450, 2708

Lee, M.-Y., Stanimirović, S., Murray, C. E., Heiles, C., & Miller, J. 2015, ApJ, 809, 56

Le Petit, F., Nehmé, C., Le Bourlot, J., & Roueff, E. 2006, ApJS, 164, 506

Leroy, A., Bolatto, A., Stanimirović, S., et al. 2007, ApJ, 658,

Leroy, A. K., Walter, F., Brinks, E., et al. 2008, AJ, 136, 2782

Leroy, A. K., Bolatto, A., Bot, C., et al. 2009, ApJ, 702, 352

Leroy, A. K., Bolatto, A., Gordon, K., et al. 2011, ApJ, 737, 12

Leroy, A. K., Walter, F., Sandstrom, K., et al. 2013, AJ, 146, 19

Leroy, A. K., Lee, C., Schruba, A., et al. 2013, ApJL, 769, L12

Leroy, A. K., Usero, A., Bolatto, A. D., et al. 2016, ApJ, submitted

Leurini, S., Wyrowski, F., Wiesemeyer, H., et al. 2015, A&A, 584, A70

Lopez, L. A., Krumholz, M. R., Bolatto, A. D., Prochaska, J. X., & Ramirez-Ruiz, E. 2011, ApJ, 731, 91

Lopez, L. A., Krumholz, M. R., Bolatto, A. D., et al. 2014, ApJ, 795, 121

Madden, S. C., Poglitsch, A., Geis, N., Stacey, G. J., & Townes, C. H. 1997, ApJ, 483, 200

Madden, S. C., Rémy-Ruyer, A., Galametz, M., et al. 2013, PASP, 125, 600

Marx-Zimmer, M., Herbstmeier, U., Dickey, J. M., et al. 2000, A&A, 354, 787

Matzner, C. D. 2002, ApJ, 566, 302

McKee, C. F., Parravano, A., & Hollenbach, D. J. 2015, ApJ, 814, 13

Meixner, M., Gordon, K. D., Indebetouw, R., et al. 2006, AJ, 132, 2268

Meixner, M., Panuzzo, P., Roman-Duval, J., et al. 2013, AJ, 146, 62

Mizuno, N., Yamaguchi, R., Mizuno, A., et al. 2001, PASJ, 53, 971

Muller, E., Ott, J., Hughes, A., et al. 2010, ApJ, 712, 1248

Nordon, R., & Sternberg, A. 2016, arXiv:1603.02300

Okada, Y., Requena-Torres, M. A., Güsten, R., et al. 2015, A&A, 580, A54

Okada, Y., et al. 2016, *inprep*

Onodera, S., Kuno, N., Tosaki, T., et al. 2010, ApJL, 722, L127

Ossenkopf, V., Röllig, M., Neufeld, D. A., et al. 2013, A&A, 550, A57

Ostriker, E. C., McKee, C. F., & Leroy, A. K. 2010, ApJ, 721, 975

Ostriker, E. C., & Shetty, R. 2011, ApJ, 731, 41

Ott, S. 2010, Astronomical Data Analysis Software and Systems XIX, 434, 139

Padoan, P., Kim, S., Goodman, A., & Staveley-Smith, L. 2001, ApJL, 555, L33

Pagel, B. E. J. 2003, CNO in the Universe, 304, 187

Paglione, T. A. D., Wall, W. F., Young, J. S., et al. 2001, ApJS, 135, 183

Pak, S., Jaffe, D. T., van Dishoeck, E. F., Johansson, L. E. B., & Booth, R. S. 1998, ApJ, 498, 735

Paradis, D., Paladini, R., Noriega-Crespo, A., et al. 2011, ApJ, 735, 6

Pei, Y. C. 1992, ApJ, 395, 130

Pellegrini, E. W., Oey, M. S., Winkler, P. F., et al. 2012, ApJ, 755, 40

Pilbratt, G. L., Riedinger, J. R., Passvogel, T., et al. 2010, A&A, 518, L1

Pineda, J. L., Langer, W. D., Velusamy, T., & Goldsmith, P. F. 2013, A&A, 554, A103

Planck Collaboration, Ade, P. A. R., Aghanim, N., et al. 2011, A&A, 536, A17

Planck Collaboration, Abergel, A., Ade, P. A. R., et al. 2011, A&A, 536, A24

Planck Collaboration, Abergel, A., Ade, P. A. R., et al. 2014, A&A, 566, A55

Poglitsch, A., Krabbe, A., Madden, S. C., et al. 1995, ApJ, 454, 293

Poglitsch, A., Herrmann, F., Genzel, R., et al. 1996, ApJL, 462, L43

Poglitsch, A., Waelkens, C., Geis, N., et al. 2010, A&A, 518, L2

Polk, K. S., Knapp, G. R., Stark, A. A., & Wilson, R. W. 1988, ApJ, 332, 432

Pound, M. W., & Wolfire, M. G. 2008, Astronomical Data Analysis Software and Systems XVII, 394, 654

Requena-Torres, M. A., Israel, F. P., Okada, Y., et al. 2016, A&A, 589, A28

Reynolds, R. J. 1991, ApJL, 372, L17

Reynolds, R. J. 1993, Massive Stars: Their Lives in the Interstellar Medium, 35, 338

Rahman, N., Bolatto, A. D., Wong, T., et al. 2011, ApJ, 730, 72

Rahman, N., Bolatto, A. D., Xue, R., et al. 2012, ApJ, 745, 183

Rigopoulou, D., Kunze, D., Lutz, D., Genzel, R., & Moorwood, A. F. M. 2002, A&A, 389, 374

Röllig, M., Ossenkopf, V., Jeyakumar, S., Stutzki, J., & Sternberg, A. 2006, A&A, 451, 917

Roman-Duval, J., Israel, F. P., Bolatto, A., et al. 2010, A&A, 518, L74

Roman-Duval, J., Gordon, K. D., Meixner, M., et al. 2014, ApJ, 797, 86

Roussel, H., Helou, G., Hollenbach, D. J., et al. 2007, ApJ, 669, 959

Roychowdhury, S., Huang, M.-L., Kauffmann, G., Wang, J., & Chengalur, J. N. 2015, MNRAS, 449, 3700

Rubio, M., Garay, G., Montani, J., & Thaddeus, P. 1991, ApJ, 368, 173

Rubio, M., Lequeux, J., Boulanger, F., et al. 1993, A&A, 271, 1

Rubio, M., Lequeux, J., & Boulanger, F. 1993, A&A, 271, 9

Rubio, M., Lequeux, J., Boulanger, F., et al. 1996, A&AS, 118, 263

Russell, S. C., & Dopita, M. A. 1992, ApJ, 384, 508

Sánchez, S. F., Kennicutt, R. C., Gil de Paz, A., et al. 2012, A&A, 538, A8

Sandstrom, K. M., Bolatto, A. D., Stanimirović, S., van Loon, J. T., & Smith, J. D. T. 2009, ApJ, 696, 2138

Sandstrom, K. M., Bolatto, A. D., Draine, B. T., Bot, C., & Stanimirović, S. 2010, ApJ, 715, 701

Sandstrom, K. M., et al. 2012, ApJ, 744, 20

Saintonge, A., Kauffmann, G., Wang, J., et al. 2011, MNRAS, 415, 61

Schlafly, E. F., & Finkbeiner, D. P. 2011, ApJ, 737, 103

Schmidt, M. 1959, ApJ, 129, 243

Schruba, A., Leroy, A. K., Walter, F., Sandstrom, K., & Rosolowsky, E. 2010, ApJ, 722, 1699

Schruba, A., Leroy, A. K., Walter, F., et al. 2011, AJ, 142, 37

Schruba, A., Leroy, A. K., Walter, F., et al. 2012, AJ, 143, 138

Scowcroft, V., Freedman, W. L., Madore, B. F., et al. 2016, ApJ, 816, 49

Shetty, R., Kauffmann, J., Schnee, S., & Goodman, A. A. 2009, ApJ, 696, 676

Shetty, R., Glover, S. C., Dullemond, C. P., et al. 2011, MNRAS, 415, 3253

Skibba, R. A., Engelbracht, C. W., Aniano, G., et al. 2012, ApJ, 761, 42

Smith, J. D. T., Armus, L., Dale, D. A., et al. 2007, PASP, 119, 1133

Smith, J. D. T., Draine, B. T., Dale, D. A., et al. 2007, ApJ, 656, 770

Smith, R. C., & MCELS Team 1999, New Views of the Magellanic Clouds, 190, 28

Sofia, U. J., Cardelli, J. A., Guerin, K. P., & Meyer, D. M. 1997, ApJL, 482, L105

Solomon, P. M., Sanders, D. B., & Scoville, N. Z. 1979, ApJL, 232, L89

Stacey, G. J., Smyers, S. D., Kurtz, N. T., & Harwit, M. 1983, ApJL, 265, L7

Stacey, G. J., Geis, N., Genzel, R., et al. 1991, ApJ, 373, 423

Stanimirović, S., Staveley-Smith, L., Dickey, J. M., Sault, R. J., & Snowden, S. L. 1999, MNRAS, 302, 417

Stanimirović, S., Staveley-Smith, L., & Jones, P. A. 2004, ApJ, 604, 176

Staveley-Smith, L., Sault, R. J., Hatzidimitriou, D., Kesteven, M. J., & McConnell, D. 1997, MNRAS, 289, 225

Staveley-Smith, L., Kim, S., Calabretta, M. R., Haynes, R. F., & Kesteven, M. J. 2003, MNRAS, 339, 87

Sternberg, A., & Dalgarno, A. 1995, ApJS, 99, 565

Subramanian, S., & Subramaniam, A. 2012, ApJ, 744, 128

Szűcs, L., Glover, S. C. O., & Klessen, R. S. 2016, MNRAS, 460, 82

Tacconi, L. J., Genzel, R., Neri, R., et al. 2010, Nature, 463, 781

Tayal, S. S. 2008, A&A, 486, 629

Tayal, S. S. 2011, ApJS, 195, 12

Teuben, P., et al. 2016, *inprep*

Tielens, A. G. G. M., & Hollenbach, D. 1985, ApJ, 291, 722

van der Marel, R. P., & Cioni, M.-R. L. 2001, AJ, 122, 1807

van der Marel, R. P., Alves, D. R., Hardy, E., & Suntzeff, N. B. 2002, AJ, 124, 2639

van der Marel, R. P., & Kallivayalil, N. 2014, ApJ, 781, 121

Velusamy, T., Langer, W. D., Pineda, J. L., & Goldsmith, P. F. 2012, A&A, 541, L10

Verley, S., Corbelli, E., Giovanardi, C., & Hunt, L. K. 2010, A&A, 510, A64

Walter, F., Brinks, E., de Blok, W. J. G., et al. 2008, AJ, 136, 2563

Walterbos, R. A. M., & Braun, R. 1994, ApJ, 431, 156

Wang, J., Heckman, T. M., & Lehnert, M. D. 1998, apj, 509, 93

Weingartner, J. C., & Draine, B. T. 2001, ApJ, 548, 296

Whelan, D. G., Lebouteiller, V., Galliano, F., et al. 2013, ApJ, 771, 16

Wiesenfeld, L., & Goldsmith, P. F. 2014, ApJ, 780, 183

Wilson, T. L., & Rood, R. 1994, ARAA, 32, 191

Wolfire, M. G., Hollenbach, D., & Tielens, A. G. G. M. 1989, ApJ, 344, 770

Wolfire, M. G., Tielens, A. G. G. M., & Hollenbach, D. 1990, ApJ, 358, 116

Wolfire, M. G., Hollenbach, D., McKee, C. F., Tielens, A. G. G. M., & Bakes, E. L. O. 1995, ApJ, 443, 152

Wolfire, M. G., McKee, C. F., Hollenbach, D., & Tielens, A. G. G. M. 2003, ApJ, 587, 278

Wolfire, M. G., Hollenbach, D., & McKee, C. F. 2010, ApJ, 716, 1191

Wolfire, M. G., et al. 2016, *inprep*

Wong, T., Hughes, A., Fukui, Y., et al. 2009, ApJ, 696, 370

Wong, T., Hughes, A., Ott, J., et al. 2011, ApJS, 197, 16

Wu, Y., Charmandaris, V., Hao, L., et al. 2006, ApJ, 639, 157

Wu, R., Polehampton, E. T., Etxaluze, M., et al. 2013, A&A, 556, A116

Zibetti, S., Charlot, S., & Rix, H.-W. 2009, MNRAS, 400, 1181